Deliverable D3.1

Magnetic studies – Magnetic modeling

Modeling magnetic dynamic properties, laser parameters and impacts on magnetic behaviour

WP3: PHYSICAL STUDIES

Date of Delivery:

30/04/2018 (first submission)

05/08/2019 (1st update)

30/04/2021 (2nd update)

Lead Beneficiary: ESIEE Amiens

Type: Report

Dissemination Level: Public

Version: 2.12

ESSIAL has received funding from the European Union's Horizon 2020 research and innovation program under grant agreement No 766437.

Document identifier: **ESSIAL**-WP3-D3.1

Deliverable leader	ESIEE Amiens
Deliverable contributors	UPJV-LTI, ESIEE Amiens, MULTITEL, IRT-M2P, CRM, UC3M
Related work package	WP3
Author(s)	Manar Nesser Olivier Maloberti Jérôme Fortin
Due date of deliverable	30/04/2018
Actual submission date	30/04/2018
Due date of deliverable update 1	31st of July 2019
Actual submission date	05th of August 2019
Due date of update 2	31/01/2021
Actual submission date	30/04/2021
Approved by	Olivier Maloberti (PC and WL) Paul Bersans
Dissemination level	Confidential
Call	H2020-FoF-06-2017
Project number	766437
Instrument	Research & Innovation Actions
Start date of project	01/11/2017
Duration	54 months

Revision history log

Version number	Date of release	Author	Summary of changes
2.1	23/06/2019	Manar Nesser	Redaction – 1st version
2.2	24/06/2019	Olivier Maloberti	1st corrections
2.3	07/2019	Manar Nesser	2nd version
2.4	20/07/2019	Olivier Maloberti	2nd corrections
2.5	25/07/2019	Manar Nesser	3rd version
2.6	26/07/2019	Olivier Maloberti	3rd corrections
2.7	02/08/2019	Manar Nesser	Last version deliverable update 1
2.8	04/08/2019	Olivier Maloberti	Assembling of first update with the first report
2.9	05/08/2019	Olivier Maloberti	Final Version, submission on 05/08/2018 (1st update of deliverable)
2.10	--/12/2020	Manar Nesser	Last version deliverable update 2
2.11	30/04/2021	Olivier Maloberti	Correction of Lambda model vs laser and correlations
2.12	30/04/2021	Lucie Guilloteau	editing

Version number	Date of release	Author	Summary of changes
1.1	30/04/2018	Manar Nesser	Sections A and B
1.2	30/04/2018	Olivier Maloberti	Section C and Annex
1.3	30/04/2018	Olivier Maloberti	Final Version, submission on 30/04/2018 (Initial deliverable found after page 33 of the 1st update)
1.4	15/07/2019	Olivier Maloberti	Update of section C
1.5	04/08/2019	Olivier Maloberti	Section D
1.6	05/08/2019	Olivier Maloberti	Final Version, submission on 05/08/2018 (Initial deliverable with sections C and D found after page 33 of the 1st update)
1.7	30/04/2021	Olivier Maloberti	Section E

List of variables (m index for the metal, i index for the insulating coating)

f_r	Repetition frequency, kHz
v	Scanning speed, mm/s
P_w	Average power, W
S_p	Spot laser diameter, µm
ρ	Density, kg/m
f	Frequency, Hz
τ	Pulse width, ns; fs
I_c	Confidence interval
E_{pulse}	Pulse Energy, J
e_{pulse}	Pulse Energy density or laser fluence, J/cm^2
e_{cum}	Cumulative energy density, J/cm^2
N	Number of pulses on any single spot
N_{pass}	Number of laser line passes
$\hat{\mathcal{P}}$	Peak power density, W/cm^2
r	Radius of the laser spot, 25 µm
t	Time, s
σ	Electrical conductivity (FeSi), 2e^6 1/(Ω.m)
ϑ	Number between 0 and 1
C	Heat capacitance per unit surface, 713 J/(K.m^2)
$C_{pv,m}$	Volume heat capacity of the metal, 3.39e^6 J/(K. m^3)
q	Laser heat flux per unit surface, W/m^2
G	Thermal conductance per unit surface, W/(K.m^2)
H	Convection heat transfer per unit surface, 10 W/(K.m^2)
λ_m	Thermal conductivity of silicon iron, 25 W/K.m
λ_i	Thermal conductivity of the insulating coating, 0.1 W/K.m
$\alpha_{\lambda,T}$	Metal conductivity constant –0.00075.
e_m	Thickness of the metal
e_i	Thickness of the coating
δ_{dl}	Thermal diffusion length, m
σ_{th}	Thermal stress, Pa
α_m	Thermal expansion coefficient of SiFe, 1.19e^{-5} s.u.
α_i	Thermal expansion coefficient of the insulating coating, 2e^{-5} s.u.
k_{haz}	Constant equal to 24

A_0	Laser absorption coefficient
$\alpha_{\lambda,T}$	Metal conductivity constant, –0.00075
σ_{th}	Thermal stress, Pa
E	Young modulus, $2e^{11}$ Pa
e_{th}	Threshold fluence for ablation, 0.5 J/cm^2
HAZ	Heat affected zone, µm
p	Groove depth, µm
α	Optical penetration depth
ΔHf_e	Specific heat of evaporation of the metal $6.362e^6$ J/Kg
ΔHf_m	Melting enthalpy of the metal $0.18e^6$ J/Kg
ΔHf_m	Melting enthalpy of the Coating $0.012e^6$ J/Kg
T_e	Electron temperature, K
Pr	Pressure, kbar
LP	Long pulse
SP	Short pulse
USP	Ultra short pulse

Table of contents

A) State of the Art 11

I. Magnetic Domain Structure in Soft Magnetic Materials 11

II. Magnetic Domain Refinement by Laser Treatment 13

III. Scalar Models of Magnetic Behavior and Losses 17

(i) Models for Prediction of Losses 17

(ii) Models of Static Hysteresis 18

(iii) Models of Dynamic Hysteresis 20

B) Laser Equipment and Categorization of Laser Treatment 23

I. Optical Images 23

II. Laser Parameters and Energetic Quantities Calculation 27

C) Modeling and Correlations 31

I. Modeling the Impact of Laser Treatment on Surface Physics 31

(i) Reviewing the Modeling of Laser Impacts 31

(ii) Irradiation Process: Estimation of the Induced Thermal Stress and the Heat-Affected Zone 33

(iii) Scribing Process: Estimation of the Induced Thermal Stress and the Groove Depth 38

(iv) Ablation Process: Estimation of the Groove Depth, the Plasma Electron Temperature, and the Peak Surface Pressure 41

II. Bertotti Model: variation of Bertotti coefficient as a function of the laser treatment 47

III. Correlations Between Loss coefficients and Laser Energetic Quantities and physical Impacts 49

(i) Irradiation: Bertotti Loss Coefficients v.s. HAZ and Induced Thermal equivalent Stress. 49

(ii) Scribing: Bertotti Loss Coefficients v.s. the Groove Depth and Induced Thermal Stress 51

(iii) Ablation: Bertotti Loss Coefficients v.s. the Groove Depth, Plasma Electron Temperature and Shock-Wave Peak Pressure 52

D) Modeling and Correlations: Lambda's Model 56

I. Lambda's Model: variation of the dynamic magnetization property Λ and the internal static permeability μ as a function of the laser treatment....56
(i) Lambda's Model Vs. Laser Treatments....56
II. Correlations: Laser Energetic Quantities, Impact, Magnetic Parameters....58
(i) Irradiation: HAZ and Induced and Thermal Stress Vs. Lambda's Model and Bertotti's Coefficients....58
(ii) Scribing: Groove Depth and Induced thermal stress Vs. Lambda's Model 59
(iii) Ablation: Groove Depth, Te, and Peak Pressure Vs. Lambda's Model... 60
Bibliography....62

List of Figures :

Figure 1 Schematic of a Domain Wall Between Two Magnetic Domains. 11
Figure 2 Formation of Domains Reduces the Stray Field (from Left to Right, the Demagnetization Energy is Reduced by the Formation of Domains)[4]. 12
Figure 3 Magnetisation Process and Hysteresis Cycle Showing an Example of Variation in the Domains Structure as a Function of the Applied Field [4]. 13
Figure 4 Diagram showing the different impacts of a laser treatment on the domain structure and loss. 14
Figure 5 Profile Analysis of the Laser Tracing Line on the Sample Surface, an Example of Laser Irradiation on (a) 23M0H sample, and (b) NLCOX21 sample. .. 24
Figure 6 Profile Analysis of the Laser Tracing Line on the Sample Surface, an Example of Laser Scribing on (a) 23M0H Sample and (b) NLCOX21 sample. 25
Figure 7 Profile Analysis of the Laser Tracing Line on the Sample Surface, an Example of Laser Ablation on (a) 23M0H sample and (b) NLCOX21 Sample. 26
Figure 8 Schematic of the Laser Beam and Pulse Characteristics. 28
Figure 9 Irradiation, Scribing and Ablation Zones Defined by the Peak Power Density as a Function of the Pulse Energy Density (on the Left) and as a Function of the Pulse duration (on the Right), Markers Correspond to Laser Configurations Effectively Tried in the Experimental Plan. 30
Figure 10 Equivalent Electrical Diagram and schema of the Thermal Model of Laser Irradiation (h convection heat transfer coefficient, λ_m thermal conductivity of silicon iron and λ_i thermal conductivity of the insulating layer). ... 34
Figure 11 Optical Image Using a Confocal Microscope Showing the 2D Images presenting the measured HAZ on naked SiFe samples with equivalent thermal properties (NGOES), respectively and approximately 100 and 350 μm. 38
Figure 12 Heat Affected Zone as a Function of the Cumulative Energy Density e_{cum} in the case of Laser Irradiation. 38
Figure 13 The Estimated Depth (p) as a Function of the Cumulative Energy Density (e_{cum}) During Laser Scribing. 40
Figure 14 The Calculated Groove Depth as a Function of the Cumulative Energy Density (e_{cum}) in the Case of Laser Ablation. 42
Figure 15 The Electron Temperature as a Function of the Cumulative Energy Density (e_{cum}) in the Case of Laser Ablation. 42
Figure 16 Definition of the ablation problem with the Finite Element Method 43
Figure 17 Computation of the electrons and lattice temperatures. 43
Figure 18 Computation of the groove depth with the numerical ablation model (2 T model). 44
Figure 19 Schematic of Laser Shock Wave Principle[39]. 44
Figure 20 The Peak Pressure as a Function of the Peak Power Density in the Case of Laser Ablation. 45
Figure 21 Variation of Bertotti's Coefficient k_h and k_e as a Function of Peak Induction Level at frequency 50Hz for Different Laser Treatment on GO 23M0H Samples. 48

Figure 22 The variation of Bertotti's Coefficients k_h and k_e as a function of the Heat-Affected Zone (on the left) and the Induced Thermal Stress(on the right) During the Irradiation Process for 1.5T@50Hz. 49
Figure 23 The variation of Bertotti's Coefficients k_h and k_e as a function of the Heat-Affected Zone (on the left) and the Induced Thermal Stress (on the right) in the Case of Laser Irradiation for 0.1T@5000Hz. 50
Figure 24 The Variation of Bertotti's Coefficients k_h and k_e as function of the Measured Depth (on the left) and the Induced Thermal Stress (on the right) in the Case of Laser Scribing for 1.5T@50Hz. 52
Figure 25 The Variation of Bertotti's Coefficients k_h and k_e as a function of the Measured Depth (on the left) and the Induced Thermal Stress (on the right) in the Case of Laser Scribing for 0.1T@5000Hz. 52
Figure 26 The Variation of Bertotti's Coefficients k_h and k_e as a function of the Measured Depth for 1.5T@50Hz (on the left) and 0.1T@5000Hz (on the right) in the Case of Laser Ablation. 53
Figure 27 The Variation of Bertotti's Coefficients k_h and k_e as a function of the Electron Temperature for 1.5T@50Hz (on the left) and 0.1T@5000Hz (on the right) in the Case of Laser Ablation. 54
Figure 28 The Variation of Bertotti's Coefficients k_h and k_e as a function of the Peak Pressure for 1.5T@50Hz (on the left) and 0.1T@5000Hz (on the right) in the Case of Laser Ablation. 54
Figure 29 The Dynamic Magnetization Property Λ (on the left) and the Internal Static Permeability μ (on the right) as a Function of Peak Induction Level for Different Types of Laser Treatment on GO 23MOH Samples. 56
Figure 30 The variation in Lambda's Model Parameters Λ and μ as a Function of Peak Induction Level @50Hz for Different Laser Treatment on GO 23MOH Samples. 57
Figure 31 The variation of Lambda Model parameters as a function of the heat-affected zone (on the left) and the induced thermal stress (on the right) in the case of laser irradiation for 1.5T@50Hz. 58
Figure 32 The variation of Lambda Model parameters as a function of the heat-affected zone (on the left) and the induced thermal stress (on the right) in the case of laser irradiation for 0.1T@5000Hz. 59
Figure 33 The variation of Lambda Model Parameters as a function of the Measured Depth (on the left) and the Induced Thermal Stress (on the right) in the case of Laser Scribing for 1.5T@50Hz. 60
Figure 34 The variation of Lambda Model Parameters as a function of the Measured Depth for 1.5T@50Hz (on the left) and for 0.1T@5000Hz (on the right) in the Case of Laser Ablation. 60
Figure 35 The Variation of Lambda's Model Parameters as a function of the Electron Temperature for 1.5T@50Hz (on the left) and for 0.1T@5000Hz (on the right) in the Case of Laser Ablation. 61
Figure 36 The Variation of Lambda Model Parameters as a function of the Peak Pressure for 1.5T@50Hz (on the left) and for 0.1T@5000Hz (on the right) in the Case of Laser Ablation. 61

List of Tables :

Table 1 Laser Characteristics. 23
Table 2 Quantitative Results of the Impact of the Laser Parameters on the Surface, in Red the Eliminated Parameters are According to the Optical Images. 27
Table 3 Laser Parameters and Energy Contributions Used in the Case of Laser Irradiation for a Fixed Pattern Perpendicular to the Rolling. 37
Table 4 The Estimated Thermal Stress Induced for Each Irradiation Configuration. 37
Table 5 Laser Parameters and Energy Contributions Used in the Case of Laser Scribing for a Fixed Pattern Perpendicular to the Rolling Direction. 40
Table 6 The Estimated Induced thermal stress for each Scribing Configuration. 40
Table 7 Laser parameters and energy contributions used in the case of laser ablation for a fixed pattern perpendicular to the rolling direction. 42
Table 8 The Estimated electron temperature, groove depth and peak pressure under a laser ablation. 46

A) State of the Art

I. Magnetic Domain Structure in Soft Magnetic Materials

Magnetic materials are divided into two classes: soft magnetic and hard magnetic materials. Soft magnetic materials can be magnetized with weak magnetic fields. Their use in electrical machines is to channel the magnetic flux. While, hard magnetic materials retain their initial magnetized state under high magnetic field. They are used in electrical machines as a source of magnetic field. They also differ in their coercivity, i.e. the amount of external reverse magnetic field that must be applied to demagnetize a material after saturation. Soft materials have a low coercivity while hard magnetic materials have a much higher coercivity[1], [2].

The importance of soft magnetic materials is their ability to be magnetized and demagnetized easily under an applied magnetic field. Indeed, at the macroscopic scale, the spontaneous magnetization observed at the microscopic scale cannot be observed. The Weiss's theory [3] explains the existence of a demagnetized state and that a ferromagnetic material is divided into several domains called Weiss domains. Along these domains the magnetization is uniform and oriented in the same direction for each domain, but differs from one domain to another. These domains are separated by walls (Figure 1).

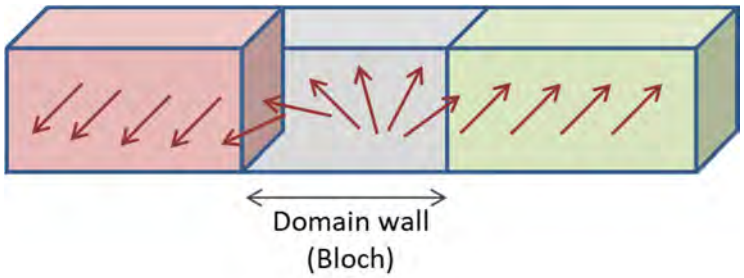

Figure 1 Schematic of a Domain Wall Between Two Magnetic Domains.

The main energy contributions responsible for the distribution domains and walls within the magnetic structure are:

- The magnetic exchange energy is microscopic energy resulting from the interaction between the electron clouds of two neighboring atoms. This exchange energy tends to align the microscopic magnetic moments of each atom in the same direction [3].

- The magnetocrystalline anisotropy comes from the distribution of atoms in the crystal lattice that sets the directions of minimum energies for magnetization. The directions corresponding to minimum energies are called easy magnetization axes and those corresponding to maximum energies are the so-called difficult magnetization axes. The magneto-crystalline anisotropy between the crystals enforces the magnetization to follow the easy magnetization axes.

- The magnetostatic stray-field energy (demagnetizing energy) tends to always close the magnetic flux ensuring its divergence-free condition. It is related to the formation of magnetic charges at some defects, inclusions, grooves, on the surface and at the edges of the sample, which causes a demagnetizing field. In macroscopic materials, it enforces the

magnetization to be tangential to the surface of the material, thus reducing the creation of magnetic poles.

- The magnetoelastic and magnetostriction energy: Within the crystal structure, the distance between each atom is naturally regulated according to a state of equilibrium of electron pool between the atoms that are physically the closest as possible to each other. Magnetoelastic energy is the mechanical energy required by the material to change the electron pool. Mechanical stress can change significantly the distance between the atoms and thus the electron pool, resulting in a change of the energy state and the anisotropy called stress induced anisotropy. The magnetization in each domain leads to a distortion of the electron pool and thus can also change the distance between the atoms, resulting in a strain called magnetostriction equivalent to stress that also changes the energy state and the anisotropy. Both the stray field energy and the stress induced anisotropy contribute to the creation of closure domains with various orientations at some defects, inclusions, grooves, at borders, on the surface, and at the edges of the sample.

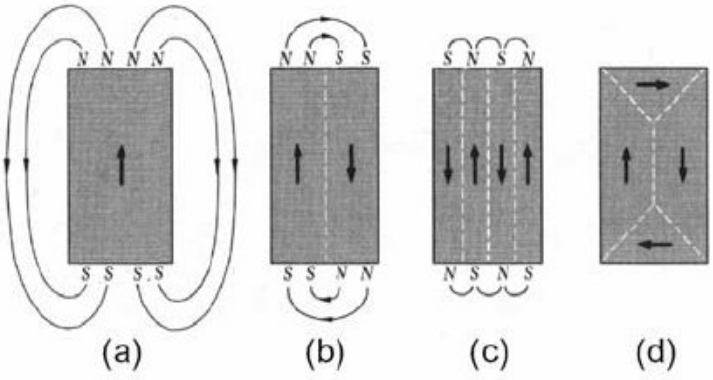

Figure 2 Formation of Domains Reduces the Stray Field (from Left to Right, the Demagnetization Energy is Reduced by the Formation of Domains)[4].

The structure and size of the magnetic domains in a material is naturally distributed in a way that minimizes all these energies (Figure 2).

The magnetisation processes are dominated by walls displacements first and then magnetisation rotations under the action of an external magnetic field (Figure 3). Thus, the magnetic domain structure influences the macroscopic behavior of the material and its magnetization processes and then its hysteresis loop. The hysteresis cycle is the response curve of magnetic materials, through which they keep the memory of all their previous magnetization states via the elementary domains. The hysteresis cycle of a ferromagnetic material depends on the walls density and mobility, which is itself a function of the magnetic energies and the applied field.

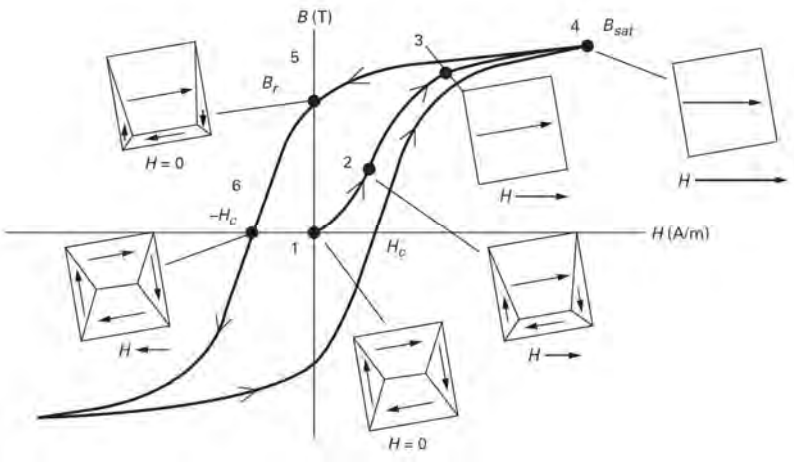

Figure 3 Magnetisation Process and Hysteresis Cycle Showing an Example of Variation in the Domains Structure as a Function of the Applied Field [4].

II. Magnetic Domain Refinement by Laser Treatment

Grain-oriented steels are formed by grains of large sizes, resulting in large magnetic domains. These domains produce losses resulting from the motion of the domain's wall under an applied alternating field. Losses are proportional to the number of walls but also their speed at the power of two. Thus, the domain refinement minimizes the speed and displacement of walls necessary to achieve the same magnetic state and therefore less energy is lost. The first studies on domain refinement were carried out using a mechanical scratching method to reduce energy losses in electrical steels. Researchers, therefore, sought to save energy and studied different domain refinement techniques (mechanical scratching [5], plasma irradiation [6], spark ablation [7], and laser surface treatment) to understand their influence on energy losses.

Among these techniques, surface laser treatment is an elegant non-contact method that gives good results for 180° domain refinement and then for core loss reduction [8]. Let's start by understanding the relationship between laser treatment and loss reduction (Figure 4). During the laser irradiation process, the energy received by the sample is used to heat the surface thus generating thermal-induced stresses that can change the energy state of the magnetic domains, especially affecting the magnetoelastic energy. Thus, to minimize their energies, some misoriented closure domains can be generated and at the same time, the domains are refined. The thermal induced stress and misoriented closure domains around the laser spots may have an impact on the quasi-static hysteresis losses and the main domains refinement contributes to the dynamic losses reduction[9]. In the case of etching a material with small grooves, two phenomena can occur: the presence of a groove approaches the magnetic poles and changes the energy state of the domains so that they must be refined to minimize their energies. On the other hand, a groove is a surface defect that can in a favorable case (i.e. with no heat affected zone) create well-oriented closure domains (“spike-like” domains, see chapter 4) and thus nucleation centers of walls with enhanced mobility which facilitates the process of magnetization and de-magnetization in the frequency domain, thus reducing the dynamic losses. However, the difficulty to cancel the magnetic poles thanks to misoriented closure domains in this case can be a drawback at a high induction level for the permeability. Nevertheless, it might stay an advantage in

terms of magnetic induced strain through the magnetostriction effect (reference thèse de Elias Salloum). In any case, there must be a limitation for both the thermal stress induced and the groove depth and width, that may become detrimental to the power losses rather than beneficial. This work aims to analyze in detail these differences between laser parameters and conditions that lead to either heating or engravement processes and to find the limitations and the optimal conditions for each.

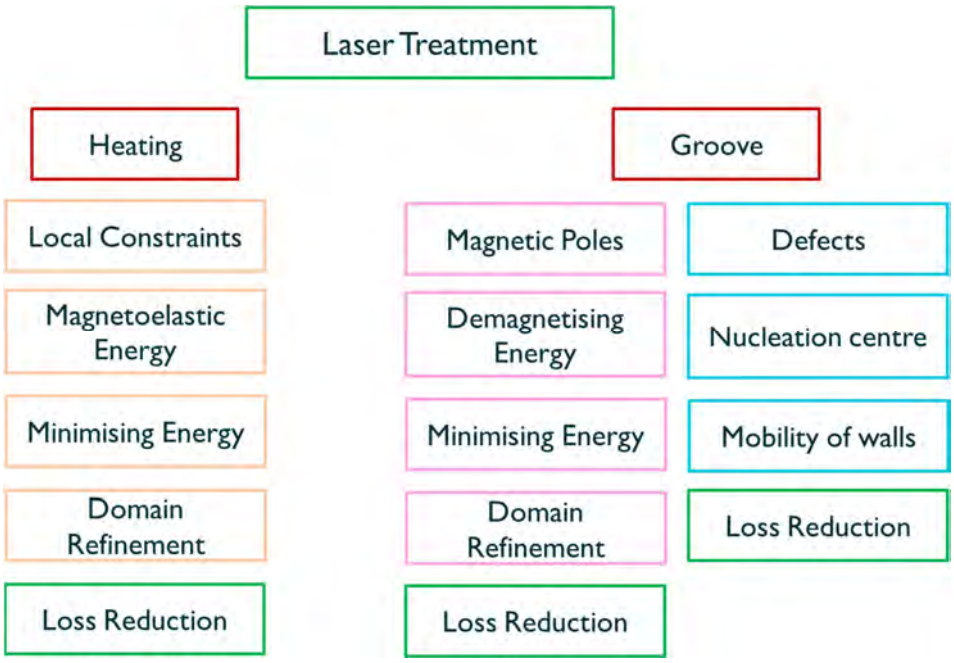

Figure 4 Diagram showing the different impacts of a laser treatment on the domain structure and loss.

In order to select the first appropriate laser parameters leading to improved magnetic properties, we based our investigations on previous researches presenting parametric studies on the magnetic structure and losses as a function of laser energetic quantities.

Laser's pulse mode:

Petryshynets et al.[10] showed an improvement of 16% (maximum value) at induction level 1.5 T for frequency 50 Hz for grain-oriented Fe-3%Si steel (a sheet of 30mm width, 80mm length, and 0,28mm thickness) scribed by a fiber laser in pulse regime while the continuous regime gives a better improvement (38% maximum value) for the same scribe lines distances (for line distance 4 mm). Noting that the power density of the laser beam in case of the continuous regime was in the range from 12W up to 30W with a step of 6W, the laser beam spot size was 30µm and the scan speed was 100mm/s. For the pulse mode, the input power of the laser beam varied from 30 W to 240 W with a pulse duration of 100µs and 100Hz frequency. The distance between the neighboring spots was 0.3mm.

In a comparison between the use of a continuous CO_2 laser and the use of a pulsed fiber laser for scribing grain-oriented electrical steel (sheet dimensions 300mm × 30mm × 0.3 mm), Rauscher et al.[11] found the reduction in core loss for the sample treated with pulsed fiber laser (14.5% mean value) higher than for that treated with continuous CO_2 laser (12.5% mean value) for the same line spacing. Also, using an Nd-YAG laser set to Q-

mode, Huang et al.[12] verified a reduction rate of 13.12% in core loss for grain-oriented silicon steel (30Q130, thickness 0.3mm) for optimized laser conditions (a combination of pulse energy of 2.52 mJ, small spot spacing of 0.22 mm, and line spacing of 3.03 mm).

Therefore, Ponnaluri et al.[13] demonstrated that the use of an excimer laser scribing process gives beneficial effects in reducing core loss more than the use of Nd-YAG or CO_2 lasers. They was able to achieve a maximum core loss reduction of 26% for grain-oriented silicon steel (M-4 of thickness 0.3mm) scribed by the excimer laser (energy = 64 mJ, repetition rate =50 Hz, spot size =1.2mm×0.7mm, which is very large). However, the use of an excimer laser is not favorable due to his multimode aspect also the profile and the beam energy of this type of lasers are usually inhomogeneous so it makes it hard to been correctly focalized.

Pulse Energy and Energy rate:

Iuchi et al.[8] studied the optimum value of the pulse energy of their irradiation laser for a better reduction in core loss. So, they figure out an experimental relation between the energy pulse and the reduction of core loss by the expression:

$\Delta W = \frac{c_1 u}{1+c_2 u} - c_3 u$, where c_1, c_2 and c_3 are constants, ΔW is the reduction of core loss, and u the energy irradiated per unit surface. The optimum condition for u was between 0.2 and 0.3 J/cm^2 with a reduction in core loss of more than 10%.

By comparing two laser sources used on grain-oriented electrical steel, Rauscher et al.[11] found a non-significant improvement (3%) of core loss at low laser pulse energy per length (E<4 J/m) as well as at a high energy (E>50 J/m) for both CO_2 laser and fiber laser source. On the contrary, the core loss was reduced by 12.5% (mean value) for the sheet treated by the CO_2 laser and 14.5% (mean value) for the other within the optimal energy E (5 J/m<E<45 J/m). A maximum value of the reduction in core loss was achieved for an energy E=13 J/m and E= 9 J/m respectively for the CO_2 laser and the fiber laser.

Huang et al.[12] showed an increasing rate of core loss reduction (sheet thickness 0.3 mm) with the increase of pulse energy and they achieved a maximum reduction rate of 13 % for a pulse energy that equals 2.52 mJ (at optimum conditions of an Nd-YAG laser Q-mode: 0.22 mm spot spacing and 3.03 mm line spacing).

New research was done by Puchy et al.[14] on a sample of Fe 3.2Si grain-oriented electrical steel (dimensions 30 mm ×10 mm×0.35 mm) treated by a fiber pulsed laser with a wavelength of 1064 nm where the scan direction was oriented perpendicularly to the rolling direction. It shows the effects of the laser treatment at the microscale (magnetic domain width) and the macroscale (coercivity) on the sample magnetic structure. In the process of laser-scribing, they used different numbers of pulses (1, 5, 10, 50, and 100 pulses) and for each number of pulses, they varied the single pulse energy. They showed that the increase of the single energy pulse for the same number of pulses increases the magnetic domain width as well as for the coercivity. So, the lowest pulse energy used (0.6 mJ) was the optimum energy for decreasing the magnetic domain width and coercivity then for decreasing the core loss. Also, they examined the effect of increasing the number of pulses on the sample for the same single pulse energy, for a single pulse the surface engravement is negligible while for 100 pulses and 100 modulated pulses laser regime a significant surface engravement occurs. At the macroscale, for the same single pulse energy the coercivity H_c decreased by increasing the pulse numbers from single pulse to 5 pulses with

an optimum value of H_c = 0.035 A/cm for a single pulse energy of 0.6 mJ (coercivity before laser-scribing was 0.057 A/cm), but then the increase of the pulse numbers increased the coercivity.
In the like manner, at the microscale, the magnetic domain width decreased by increasing the number of pulses to 5 pulses and 10 pulses with an optimum value of 15±1.9 μm at for a single pulse energy of 0.6 mJ (magnetic domain width before laser-scribing was 45±4.2 μm), but when they increased the number of pulses the decrease in domain width becomes less significant.

Lines Spacing:

Besides their study on the influence of pulse energy, Huang et al.[12] examined the suitable value of the lines spacing scribed with the Nd-YAG laser process for a maximum core loss reduction in grain-oriented silicon steel (30Q130 sheet thickness 0.3 mm). They found that increasing too much the lines spacing leads to more core loss and they selected a spacing of 3.03 mm (pulse energy of 2.52 mJ and spot spacing of 0.22 mm) as an optimum value for the reduction of core losses, *i.e.* 13 %.

Furthermore, Petryshynets et al.[10] studied the effect of laser-scribing with a fiber laser in continuous mode on magnetic properties of grain-oriented steel. So, they showed a deterioration of coercivity for the sample scribed by the laser with a scribing spacing of 3 mm and that is due to the high intensity of thermal stress on the sample. By increasing the lines spacing the coercivity decrease, the lowest value of coercivity was reached for a lines spacing of 7.5 mm and a laser power beam of 24 W. In the same paper, they showed the effect of the laser scribing for these optimal conditions on the refinement of magnetic domains and the texture of the sample: They presented a formation of complex domain structures in the vicinity of the laser lines and it can be assumed that the disturbance of domains took place around the heat affected zone. On the other hand, the sharpness of the Goss texture of the sample wasn't significantly affected by the laser-scribing because the laser beam power of 24 W induces a slight variation of the substructure parameters on the surface so the texture of the sample was unchanged.

Scribing Direction:

The scribing of a sample could be realized either in the longitudinal direction it means in the rolling direction of the manufactured sample or the transversal direction it means perpendicularly to the rolling direction. Ponnaluri et al.[13] examined the effect of each scribing direction of a grain-oriented silicon steel sheet on the reduction of core loss.

So, they found that the scribing in the transversal direction improves the core loss much better than in the longitudinal direction. Also, Kajiwara and Enokizono[15] conclude the same result that the iron loss decreases with using a scribing in the longitudinal direction but this reduction is higher in the case of transversal direction. Much more they tested the effect of the scribing in both directions and they found a better improvement in iron loss up to 12.9%. The transverse direction of scribing creates better refinement in domain structures than that in the longitudinal direction.

In order to investigate the influence of laser scribing on static, dynamic, high and low loss component of laser scribed electrical steel, Weidenfeller and Anhalt[16] were based on the theoretical formula of loss that relates the dynamic losses with the classical losses (eddy currents) with an anomaly factor η dependent on the frequency $P_{dyn}(f) = \eta\,(f)\,P_{cl}(f)$.

They tested the effect of laser scribing on the behavior of the anomaly factor as a function of frequency for different laser beam intensities: for the high-intensity anomaly factor η(f) increases, which increases the dynamic losses generated by the domain wall motion. Then, as they reduce the laser intensity, the anomaly factor decreases for frequencies between 1 and 100 Hz, but then increases for a higher frequency. In addition, they showed that high induction losses that represent the annihilation-recreation of the domain wall and the rotation of magnetic moments were increased by laser scribing while low induction losses that represent the mobility of the domain wall were decreased after laser scribing at low intensity. Thus, the reduction of total power losses can be achieved when the increase in high induction losses is negligible compared to the decrease in low induction losses.

III. Scalar Models of Magnetic Behavior and Losses

To analyze the magnetization and iron loss behavior in grain-oriented silicon steel, it is very useful to understand some hysteresis and loss models. In this paragraph, we will focus on the magnetic parameters defined in the different models to correlate them with the magnetic structures. It will then be proposed to study the relationship between these magnetic structures and the conditions of laser treatments with the aim to optimize laser parameters in a way to control the parameters of the magnetic structure responsible for the iron losses.

(i) Models for Prediction of Losses

Steinmetz [17] considered the core loss as sum of two components: hysteresis loss and eddy current loss. The total loss is given by an empirical formula:

Equation 1

$$P_{tot} = k_h \,.f.\, B^{n} \;+\; k_c \,.\, f^2 .\, B^2$$

where n is the exponent of the flux density for the hysteresis loss that is dependent on the type of material and k_c is the eddy current loss coefficient proportional to the electrical conductivity σ and the rolling thickness e and inversely proportional to the material density ρ according to the following relationship:

Equation 2

$$k_c = \frac{e^2\,\pi^2\sigma}{6\,\rho}$$

This model was limited because it only handles sinusoidal flux waveforms. Subsequently, many modifications were proposed for the Steinmetz model to overcome the various limitations[18][20]. For several years, the Steinmetz equation and its modifications have been used as good examples for iron loss prediction, but these equations do not take into account the domains structure and its parameters. Thus, it is not able to provide a relationship between the macro-scale parameters and the magnetic structure using this model.

Bertotti[21] has proposed a loss model which is commonly used nowadays, based on the separation of the total iron losses per unit mass P $[W/kg]$ into three categories: hysteresis losses (static losses), eddy current losses (classical losses), and excess losses as follows:

Equation 3

$$P\,[W/kg] = P^{(hyst)} + P^{(class)} + P^{(exc)} = k_h\, f\, B_m^2 + k_c\, f^2\, B_m^2 + k_e\, f^{1.5}\, B_m^{1.5}$$

The hysteresis loss coefficient k_h is linked to the coercive field H_c, mainly dependent on the volume density of defects that pin the walls, including for example the number of dislocations per grains n_d and the volume density of grain boundaries inversely proportional to the grains' average volume V_G. However, the original Bertotti loss model contains and excess static contribution that depends on the magnetic flux density $\tilde{B}$ through n_0 the limiting number of magnetic objects that are active when the frequency tends to zero.

Equation 4

$$k_h \approx \frac{1}{\rho}\frac{1}{|\tilde{B}|^2}\left(\frac{n_d \varepsilon_p}{V_G} - 2n_0 V_0 |\tilde{B}|\right)$$

Where ρ is the mass density, V_0 is an intrinsic magnetic field related to the microstructure of the material, ε_p is the average energy of pinning centers (grains boundaries, dislocations …). n_0 and V_0 are closely dependent on $\frac{n_d}{V_G} and\ \varepsilon_p$, even if it is difficult to express the relationship.

The classical loss coefficient k_c is related to the classical eddy currents occurring within the thickness of the steel sheet. It can be approximated by calculation using the Equation 2.

Bertotti has developed a statistical model for the interpretation of eddy current losses[22] which are due to the so called reversal mechanisms of microscopic magnetic objects (MO): the characteristic groups of active walls grouped by the effect of internal correlation of fields between the walls. Resultantly, he considered the structure of the domains with number ñ which counts independent statistical magnetic objects. Moreover, for grains-oriented silicon steel, as in our case, only Bloch walls were considered as MO.

The excess loss coefficient k_e is due to magnetization reversal processes and associated with microscopic eddy currents around active magnetic objects [1], [22]. The equation of the excess loss component is the following:

Equation 5

$$\frac{P^{exc}}{f} = 8 \cdot \frac{B_m}{\rho}\left(\sqrt{\sigma \cdot G \cdot S \cdot V_0 \cdot B_m \cdot f}\right)$$

Where, V_0 is still the intrinsic magnetic field related to the microstructure of the material, G is the coefficient of friction between the magnetic domains taken as a constant equal to 0.1357 [n.u.] for the GO SiFe magnetic structure. S=we is the cross-sectional area of the magnetic sheet, i.e. w is the width and e the thickness.

(ii) Models of Static Hysteresis

The Jiles-Atherton model[23] is a static hysteresis model based on the physical behavior of magnetic materials, in particular on the energetic considerations in connection with the displacement and deformation of the Bloch walls. The total magnetization is regarded as two contributions: the reversible component M_{rev} due to domain wall bending and the irreversible component M_{irr} due to the displacement of the walls.

Equation 6

$$M = M_{rev} + M_{irr}$$

The reversible magnetization can be written as a function of the anhysteretic magnetization M_{anh} by the expression:

Equation 7

$$M_{rev} = c\,(M_{anh} - M_{irr})$$

Equation 8

$$M_{anh}\ (H_e) = M_s\ .L\left(\frac{H_e}{a}\right)$$

where M_s represents the saturation magnetization, H_e the effective field: $H_e = H + \alpha \cdot M_{anh}$ and $L\left(\frac{H_e}{a}\right)$ the Langevin equation. The variation of the irreversible magnetization is then given by the following equation:

Equation 9

$$\frac{dM_{irr}}{dH_e} = \frac{(M_{anh} - M_{irr})}{k\delta}$$

with δ which symbolizes a coefficient of value +1/-1 depending on the increasing/decreasing evolution of the field. Finally, the variation of the total magnetization is expressed by the differential equation:

Equation 10

$$\frac{dM}{dH} = \frac{(1-c)\frac{dM_{irr}}{dH_e} + c\frac{dM_{anh}}{dH_e}}{1 - \alpha c\frac{dM_{anh}}{dH_e} - \alpha(1-c)\frac{dM_{irr}}{dH_e}}$$

To use this hysteresis model, 5 parameters, among which some are directly related to the microstructures, should be determined:

α: mean-field parameter representing interdomain coupling, affects the remanence magnetization.

M_s: saturation magnetization of the material.

a: parameter related to the temperature: $a = \frac{k_B T}{M_s \mu_0}$, affects the shape of the loop.

c: coefficient representing the rate of domain wall bending, affects the initial magnetization.

k: parameter representing the static mobility of the walls (related to the number of pinning sites), affect the width and slope of the loop (coercive field and the remanence magnetization).

The coercivity is determined by the amount of pinning centers, and hence by the parameter *k*. For this reason, the definition of this pinning parameter in units of A.m^{-1} is preferred since the pinning force acts like a field opposing the prevailing magnetic field H.

Jiles proposed a numerical method [24] for the determination of these parameters calculated from the experimental measurements of coercivity, remanence, saturation magnetization, initial anhysteretic susceptibility, initial normal susceptibility, and maximum differential susceptibility.

The researchers attempted to understand the influence of the microstructure on the parameters of Jiles-Atherton's model, they observed that a change in grain size (ϕ) or dislocation density (ζ_d)corresponds to a variation in the parameters k and a is ought to vary linearly with $\frac{1}{\phi}$ and must both be proportional to $\sqrt{\zeta_d}$. The other parameters M_s, $c_j$and α_j are compelled to remain constant.

The reason why parameter k is considered as a parameter dependent on grain size and dislocation density is that k is proportional to the coercivity Hc, and the coercivity depends predominantly on grain size and dislocation density. Also, as for parameter a, which should be a material constant, it is dependent on the microstructure[25]. According to the literature, it must be proportional to the domain density in the demagnetized state which in turn must be proportional to the density of the binding site. Finally, all these binding sites are successively proportional to k. This dependence is indicated by the following relationship:

Equation 11

$$k_j = k_{j0}(G_1 + \frac{G_2}{\phi})\sqrt{\zeta_d}$$

Equation 12

$$a_j = a_{j0}(G_1 + \frac{G_2}{\phi})\sqrt{\zeta_d}$$

were G_1 and G_2 are constants, k_{j0} and a_{j0} are constants chosen in a way that k_j and a_j vary over a range that realistically corresponds to fits to known steels[25].

(iii) Models of Dynamic Hysteresis

The LS model is based on the work of T. Chevalier and A. Kedous-Lebouc[26], it models the dynamic behavior which strictly demands the knowledge of the surface response after a considerable number of measurements; it is based on three parameters to represent the magnetic behavior of the sheet: the induction peak, the instantaneous value of the induction, and its speed of evolution over time. The measurements allow to build or draw a surface *H(B_m, B, dB/dt)* under triangular induction with different magnitudes, knowing the pair of values *(B, dB/dt)* it is possible to build the *B(H)* cycle. The next step has been a thorough analysis of the dynamic phenomena which gives a physical interpretation for the expression of the variation of the dynamic magnetic field. Therefore, the hysteresis cycle is reconstructed by distinguishing a static and a dynamic contribution of the magnetic field as indicated in the expression:

Equation 13

$$H(B,\frac{dB}{dt}) = H_{stat}(B,historical) + H_{dyn}(B,\frac{dB}{dt})$$

where H_{dyn} is an analytical function, approached by portions of polynomials, and it is dependent on $\frac{dB}{dt}$ and B, then the energy loss per unit volume and per cycle $\mathcal{E} = \rho P/f$ is obtained by a simple integration in the volume during one hysteresis cycle:

Equation 14

$$\mathcal{E}[\boldsymbol{J}.\boldsymbol{m}^{-3}] = \int_{cycle}\iiint_{volume} H\, dB$$

The comparison between the calculated hysteresis loops and the measured loops gives a good agreement. Also, due to its significance, this model has been implemented in the 2D/3D post-processing code of the FLUX finite element calculation for some types of ferromagnetic materials. However, no separation of the dynamic contributions was carried out. Necessarily, these dynamic contributions involve the classical losses caused by macroscopic eddy currents and the excess losses due to microscopic local eddy currents which are generated by both, the structure of the magnetic domains in the material and the Bloch walls displacements.

In the dynamic LS model, the coefficients of the polynomial function used for the dynamic magnetic field are not easily and physically related to the microscopic magnetic structure. Some microscopic parameters such as grain size, sheet thickness, and domains, are very crucial because they must be related to the laser marking parameters to control the microstructure.

Raulet and Masson[27] have proposed a behavioral model of the dynamic properties of magnetic materials called DSF (Dynamic Static Feedback Model). They introduced a dynamic parameter γ linked to the geometry of the sheet on one hand, and the conductive dynamic properties of the magnetic material on the other hand. The dynamic field is expressed by the following equation:

Equation 15

$$H_{dyn} = H_{stat}(B_m) + \gamma \cdot \frac{dB_m}{dt}$$

Subsequently, Raulet improved a DWM "Diffusion & Wall Motion" magnetic diffusion model [28]. The idea of the DWM model is to replace the static characteristic of the material in the classical magnetic diffusion model with a dynamic parameter that takes into account the dynamic effects due to the domain walls motion. The expression of the magnetic field is similar to the DSF model but the dynamic parameter β of the DWM model is related to the structure of the magnetic domains and the walls motion. The dynamic behavioral law of the material is expressed by the following equation:

Equation 16

$$\frac{\partial B(y,t)}{\partial t} = \frac{1}{\beta}\left[H(y,t) - H_{stat}(B(y,t))\right]$$

where the dynamic parameter β is identified with a single dynamic characteristic B(H) performed under experimental conditions. As a consequence, this material law represents a statistical behavior of the wall motion and considers it as isotropic and characteristic of the material.

To correlate the macroscopic measurements with the microscopic observations, we used the dynamic hysteresis model developed by Maloberti [29] which led to the expression of two important observables: the dynamic contribution of power loss and the apparent permeability as a function of two intrinsic properties: a dynamic magnetization property, called Λ, which comprises parameters related to the microscopic magnetic structures with domains and walls and the magnetization reversal mechanisms and an internal static permeability, called μ. The law of magnetic behavior used includes a static component related to the an-hysteresis loop. Accordingly, this term is represented by μ which is the internal static permeability ($H_s = \mu^{-1}B$). The dynamic component is represented by Λ the dynamic magnetization property. The static hysteresis is not taken into account in this model but it is possible to add a static hysteresis contribution to the static magnetic field H_s and the corresponding losses (like in the loss model of Bertotti):

Equation 17

$$H = H_s + \sigma \Lambda^2 \partial_t B$$

Equation 18

$$\Lambda = \sqrt{\frac{1}{2\sigma\vartheta J_s n_\omega m_\omega S_\omega}}$$

where J_s is the saturation magnetic polarization, ϑ is the number between 0 and 1 (depending on the polarization direction inside domains), and lambda (Λ)the unit of length (meter) which represents a structural dynamic property summarizing the parameters of the domain wall structure ($s_\omega, m_\omega, n_\omega$): s_ω is the walls surface, m_ω is the walls mobility and n_ω is the volume density of walls.

The calculation of the field diffusion with the conductivity σ, led to the expression of the dynamic power loss per unit mass (P_{mf}) as a function of this dynamic magnetization property with the following equation:

Equation 19

$$P_{mf}(\Lambda,\omega) = \frac{\omega\xi B_{max}^2}{4\mu\rho}\left(\frac{\cosh(ek_+)+\cos(ek_-)}{sinh^2(ek_+)+sin^2(ek_-)}\right) \times (\sigma\Lambda^2\mu\omega k_+ + k_-)\, sinh(ek_+) + (\sigma\Lambda^2\mu\omega k_- - k_+)\, sin(ek_-)$$

Equation 20

$$k_\pm(\Lambda,\omega) = \sqrt{\frac{1}{2}\left(\frac{\sigma\mu\omega}{1+(\sigma\Lambda^2\mu\omega)^2}\right)} \times \sqrt{(\pm\sigma\Lambda^2\mu\omega + \sqrt{1+(\sigma\Lambda^2\mu\omega)^2}\,)}$$

where *e* is the sheet thickness (in our case e_m = 0.23mm), *ρ* is the mass per unit volume of the material, and μ is the static internal permeability characteristic of the static magnetic field ($H_s = \mu^{-1}B$) independent on the frequency $f = \omega/2\pi$. The average magnetic induction within the sample cross-section is given by the equation:

Equation 21

$$\langle B\rangle = \frac{2\mu H_a}{e}\,\frac{\tanh\left((k_+ + jk_-)\,e/2\right)}{(1+j\sigma\Lambda^2\mu\omega)(k_+ + jk_-)} \quad \text{where} \quad \langle B\rangle = B_{max}\cos(\omega t+\varphi)$$

At time $t = \frac{-\varphi}{\omega}$: $\langle B\rangle = B_{max}$ and $H_{max} = H_a\cos\varphi$

Where H_a is the magnitude or peak value of the magnetic field applied on the sample surface. In this model, both the field diffusion process and the wall's motion are taken into account. Therefore P includes both the losses due to macroscopic classical eddy currents and microscopic eddy currents around magnetic objects, but with no separation possible (unlike the Bertotti model but like in the L-S model).

The apparent permeability ("amplitude permeability") is then expressed as:

Equation 22

$$\mu_{app} = \frac{B_{max}}{H_{max}} = \frac{B_{max}}{H_a\cos\varphi}$$

Based on this state of the art a distinction between laser processing impacts will be presented in the following. Initial adjustments of the laser parameters and pattern were also inspired by the work presented in the bibliography. Among the magnetic models, Bertotti model is considered in the following to separate the losses and understand the physical origins behind the changes in magnetic properties under laser treatment.

B) Laser Equipment and Categorization of Laser Treatment

Laser treatments presented in this study were executed by MULTITEL, one of our partners in the ESSIAL project. For these treatments, they used two laser equipment with pulse durations of different orders of magnitude ranging from nanosecond to femtosecond (Table 1).

The nanosecond laser is a pulsed IPG ytterbium fiber laser that operates at a wavelength equal to 1064 nm. It delivers a maximum optical average power of 20 Watts and pulses energy up to 1 mJ. The laser pulse width can be changed in a range between few nanoseconds (short pulse SP) and hundreds of nanoseconds (long pulse LP).

On the other hand, the Amplitude Ytterbium (USP) femtosecond laser operates at a wavelength equal to 1030 nm with adjustable pulse widths from 10 ps to hundreds of femtoseconds [34].

For steel, an infrared wavelength of around 1 µm is recommended according to the absorption coefficient as a function of wavelength. At this wavelength, the absorption rate of ferrous metal is about 35% [35].

	Wavelength	**Pulse duration**
Laser **LP**	1.064 µm	Hundreds of Nanoseconds
Laser **SP**	1.064 µm	Few Nanoseconds
Laser **USP**	1.03 µm	Femtosecond

Table 1 Laser Characteristics.

I. Optical Images

Following each laser treatment with a particular set of parameters, our partners in MULTITEL performed a surface analysis and characterization of the treated sample by a confocal microscope, type Keyence series VK-X. They visualized the topography of laser line engraving on the surface to measure its depth, height, and/ or relief width.

In the first stage, we have eliminated laser configurations that deteriorate the sample. For instance, the ones that induce severe damage to the surface coating, significant droplet formation (deposits of molten metal around the edges of the laser spot), or very deep engravings that deform and bend the sample. Furthermore, optical images were used to measure the groove's depth as well as the peak and width of the relief (if any). The measured heat-affected zone was estimated only visually, thanks to the colorization and dark marks on the edges of the laser line (Figure 11). Then, the selection of laser configurations was updated according to the set of measurements and models carried out.

Different laser effects were observed on the samples (engravings, thermal effects or both). These effects vary according to the set of parameters adjusted during the process. These

laser input parameters are the pulse duration, its average power, the scanning speed and the repetition frequency together change the shape and depth of the groove depending on the amount of pulse overlap (continuous line or dots). The adjustment of these combined parameters changes the effect of the laser spot on the sample surface (see optical images Figure 5, Figure 6, Figure 7) which allowed us to distinguish three different types of laser effect in which each configuration will be categorized: laser irradiation, laser scribing, and laser ablation.

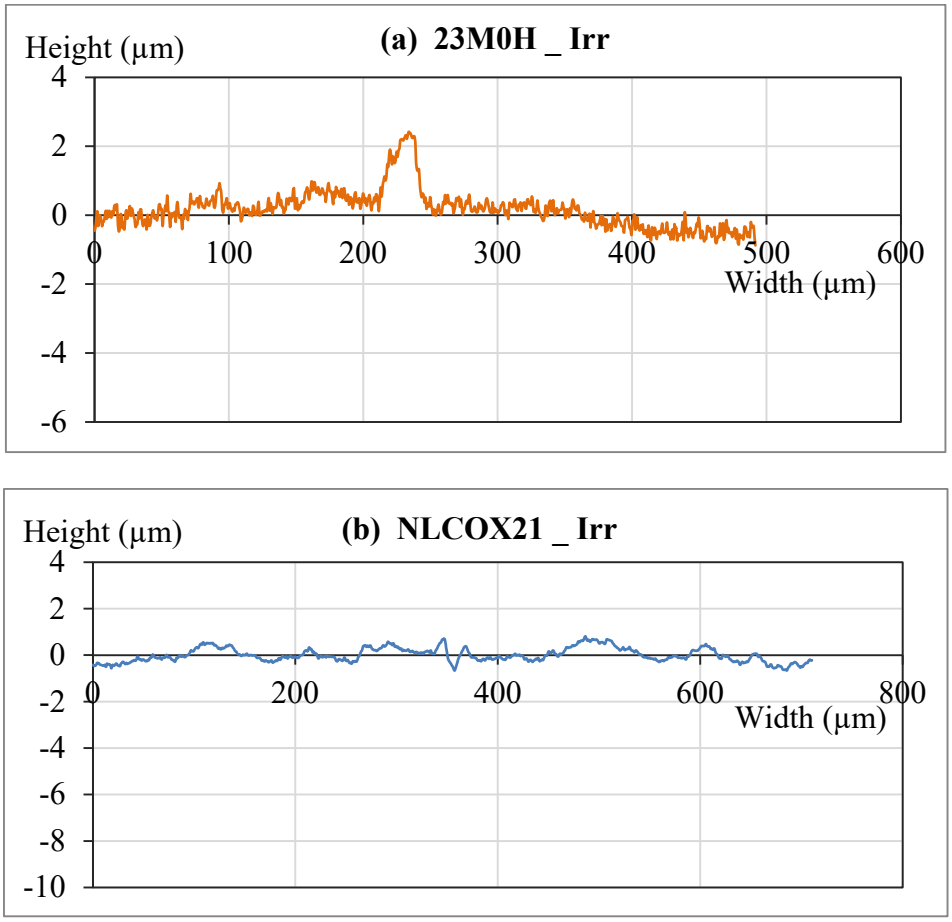

Figure 5 Profile Analysis of the Laser Tracing Line on the Sample Surface, an Example of Laser Irradiation on (a) 23M0H sample, and (b) NLCOX21 sample.

- **Laser Irradiation:**

Laser irradiation designates a laser process with thermal effect dominance, the effect of the laser is mostly thermal heating of the surface with neither coating removal nor significant surface deformation or degradation (less than the coating thickness (< 2 µm). The coating is locally heated and at a certain temperature reached, the coating can then be melted and redeposited on the surface. This thermal effect can lead to internal stresses modification. It can be achieved thanks to pulsed lasers with sufficiently long pulses (nanosecond). The coating is locally heated and can slightly be deformed, but it is not removed from the surface. As shown in Figure 5, the zone with a slight coating deformation representing the width of the measured heat affected zone was around 100 µm. Figure 5

(a) shows a relief formation between 1 and 2 µm on GO 23M0H sample under laser irradiation while it resulted in almost no deformation (between 1µm and −1µm) on a thicker sample (NLCOX21) Figure 5 (b).

- **Laser Scribing:**

In this process, we have both thermal effects inducing thermal stresses and grooves engraved inside the material. The mark of the laser line sinks by some micrometers into the surface of the sample with a formation of relief edges (melted material is ejected from the scribing area which falls and solidifies on or around the grooves). Inevitably, the coating is damaged and removed locally by this process. A thin layer of metal particles underneath can also be melted and removed by this process. As shown in Figure 6 (a and b), a groove's depth was 1.26 µm, with a relief height of less than 1 µm for the 23M0H sample while on the NLCOX21 sample, the groove's depth was 2.3 µm with a relief height of less than 1.2 µm.

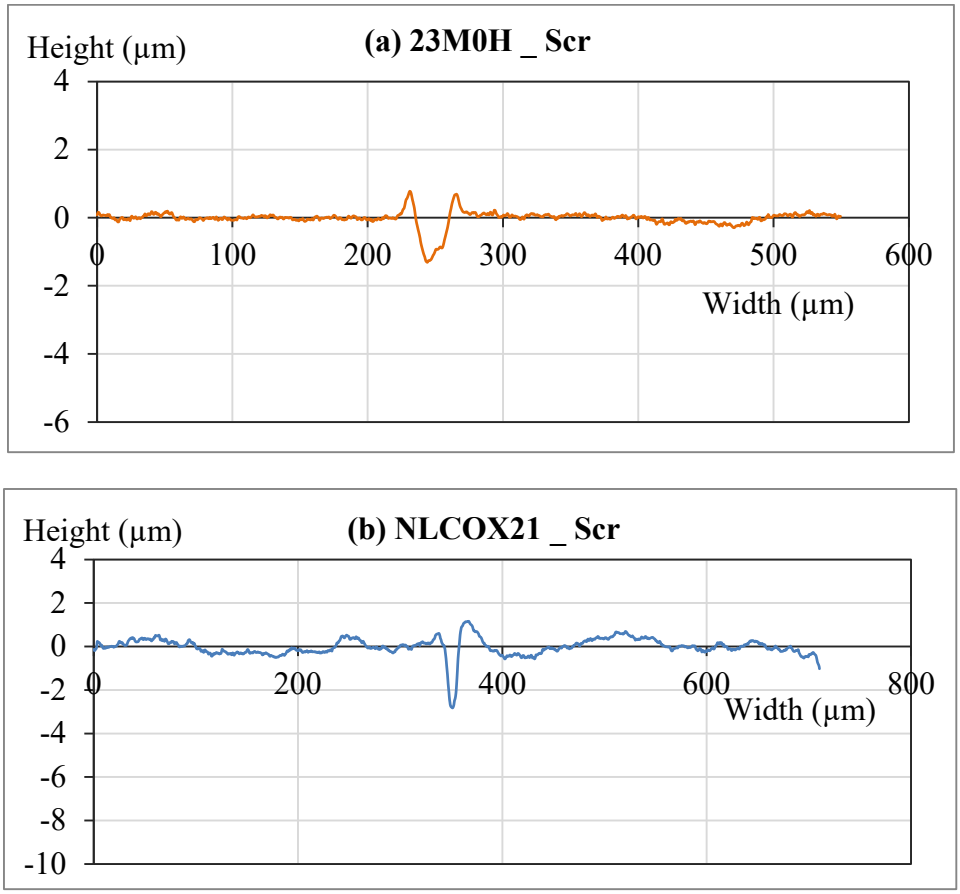

Figure 6 Profile Analysis of the Laser Tracing Line on the Sample Surface, an Example of Laser Scribing on (a) 23M0H Sample and (b) NLCOX21 sample.

- **Laser Ablation:**

The ultra-short pulse laser permits the removal of material by sublimation with a spot scanning without any thermal effect observation around the holes. Both the coating and the metal can be removed by the ablation process. As shown in Figure 7 (a), the metal ablation depth was 5.2 µm on the 23M0H sample, however, it was deeper on thicker sample NLCOX21 (9.02 µm). To increase the ablation depth, multi-pass laser processes, or reduced speed (overlapped pulses) could be used.

The ultra-short pulse provides a very high peak pulse power located at the laser spot. This very powerful laser pulse induces a surface shock wave with a very high peak pressure. This contributes to the ejection of metal particles and the generation of a surface plasma between the metal and the laser beam. However, the energy density of the pulse must be higher than the ablation threshold (~ 0.3 - 3 $J.cm^{-2}$)[36] for the laser pulse to engrave the metal by removing the particles by sublimation.

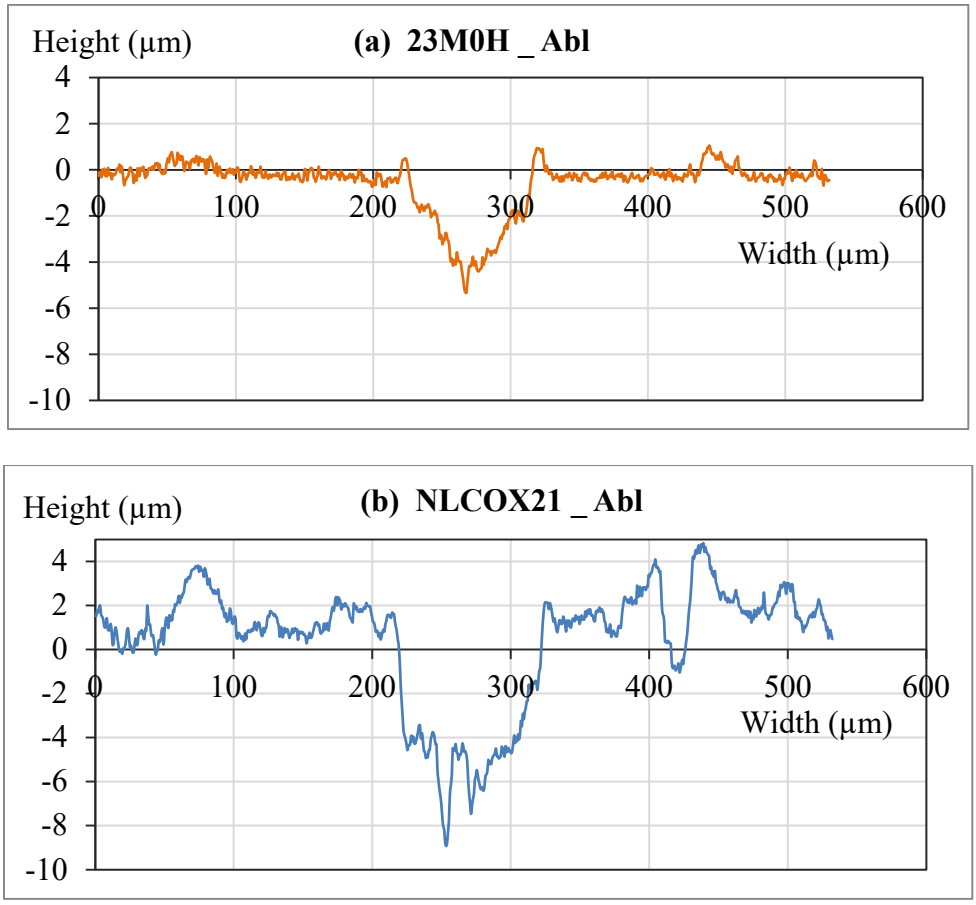

Figure 7 Profile Analysis of the Laser Tracing Line on the Sample Surface, an Example of Laser Ablation on (a) 23M0H sample and (b) NLCOX21 Sample.

II. Laser Parameters and Energetic Quantities Calculation

The standard roughness of the sample 23M0H is 0.75 µm with a coating thickness of approximately 2 µm. Laser parameters that cause a high surface relief (>3 µm) due to the melting and cooling of metals, including the laser parameter below the ablation threshold were discarded. The sheets shouldn't have any large deformations or reliefs once they are stacked to form the core of a transformer core. An example of the first parameters selection according to optical images is listed in Table 2 where different configurations were tested on the GO 23M0H sample using the nanosecond to select the set of parameters. The line spacing is fixed and laser lines were done in a direction perpendicular to the sheet rolling direction and the spot size is fixed at 50 µm. The mean powers tested between 1 and 10 W. The configurations giving a high relief (> 3 µm) were rejected (colored in red).

Configurations	Groove width (µm)	Groove depth (µm)	Heat Affected Zone (µm)	Relief (µm)
Conf_1	59	19	351	14.8
Conf_2	56	2.5	488	3.1
Conf_3	48.5	1.9	334	1.4
Conf_4	36	1.7	138	1.5
Conf_5	35	0.9	119	0.8
Conf_6	0	0.9	98	0

Table 2 Quantitative Results of the Impact of the Laser Parameters on the Surface, in Red the Eliminated Parameters are According to the Optical Images.

For each laser processing test, a configuration is defined by a set of parameters (Figure 8):

- Pulse width τ
- Average power (P_w in Watt)
- Scanning speed (v in mm/s)
- Spot size (S_p in µm)
- Repetition frequency (f_r in kHz)
- Angle between the laser lines and the rolling direction of the sheet (in °)
- Laser lines spacing (d in µm)

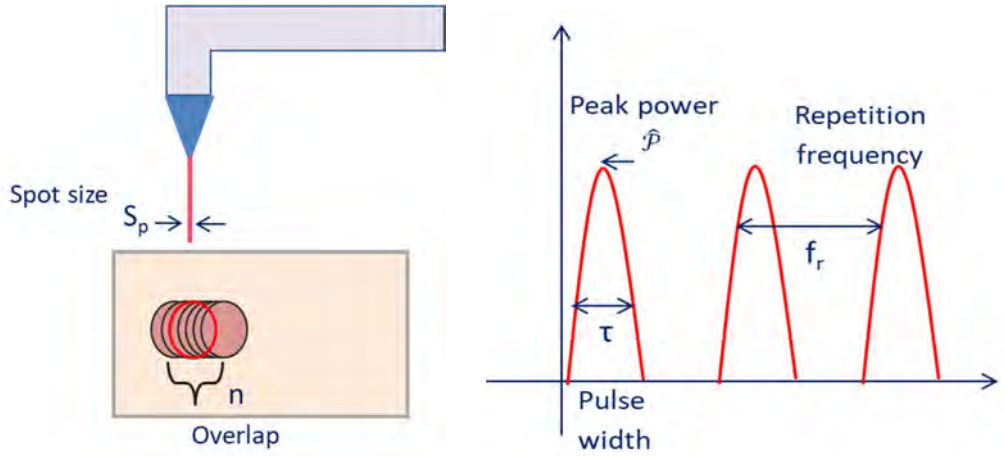

Figure 8 Schematic of the Laser Beam and Pulse Characteristics.

To give physical meaning and reduce the number of laser parameters, we preferred to characterize a laser configuration in the term of energy quantities that include all these parameters. Thus, for each configuration, we calculated the corresponding values of the pulse energy (E_{pulse}), the pulse energy density (e_{pulse}), the peak power density ($\hat{\mathcal{P}}$) and the cumulative energy density (e_{cum}) which represents the amount of energy received along an area of the sample equal to the laser spot size taking into account the overlap, or equivalently the number of pulse per single spot (n) and the number of laser passes (N_{pass}) using the following equations:

Equation 23 Pulse Energy $\boldsymbol{E_{pulse}} = \frac{\boldsymbol{Pw}}{\boldsymbol{fr}}$ [J]

Equation 24 Pulse Energy density or laser fluence $\boldsymbol{e_{pulse}} = \frac{\boldsymbol{E_{pulse}}}{\boldsymbol{\pi \times (Sp/2)^2}}$ [J/cm^2]

Equation 25 Peak power density $\hat{\boldsymbol{\mathcal{P}}} = \frac{\boldsymbol{Pw}}{\boldsymbol{\tau \times fr \times \pi \times (Sp/2)^2}}$ [W/cm^2]

Equation 26 Number of pulses on any single spot $\boldsymbol{N} = \frac{\mathbf{Sp \times fr}}{\boldsymbol{v}}$

Equation 27 Cumulative energy density $\boldsymbol{e_{cum}} = \boldsymbol{N_{pass} \times N \times E_{pulse}}$ [J/cm^2]

According to the influence of each configuration on the sample surface visualized by the optical images, we defined an operating area for each type of laser treatment defined by a range of peak power density values as a function of the energy density or the laser fluence.

From the above equations, the peak power density is proportional to the fluence where the pulse duration is the proportionality coefficient. Hence, it is logical that irradiation is standardly obtained with long pulses, scribing with shorter pulses, and ablation with ultra-short pulses. Therefore, for the same fluence, irradiation corresponds to a peak power lower than scribing which itself has a peak power much lower than ablation.

These areas are presented in Figure 9. The irradiation effect corresponds to laser fluence lower than 2.7 J/cm^2 for a peak power density up to 100 MW/cm^2 or a fluence between 2.7

and 4 J/cm^2 for a peak power between 30 and 100 MW/cm^2 or a fluence higher than 4 J/cm^2 for a peak power below 25 MW/cm^2. Then, the scribing effect corresponds to laser fluence lower than 1 J/cm^2 with a peak power density higher than 100 MW/cm^2 or a fluence higher than 2.7 J/cm^2 with a peak power density above 25 MW/cm^2. The limit of the irradiation zone is superimposed by the beginning of the scribing zone.

The ablation fluence threshold is about ~ 0.5 J/cm^2. Correspondingly, the peak power density of the ablation effect is greater than that of the irradiation and scribing effect by an order of magnitude of 4.

The analysis and comparisons between these different energy quantities can be understood as follows:

- The peak power density determines the strength and speed of the laser impact as it is inversely proportional to the pulse duration and the spot size. At equal fluences, it permits the estimation of the degree of physical impact and phase change on the sample surface: the lowest peak power density corresponds to irradiation (heat-fusion effect). Gradually, by increasing this density, the phenomenon of scribing (fusion-evaporation effect) takes place. Finally, with the highest peak power density, an ablation (evaporation-sublimation effect) occurs.

- The fluence (pulse energy density) determines the amount of matter impacted and the phase change per pulse. At equal power densities, this allows measuring the area affected either by heating (case of irradiation) or by a phase change above a certain threshold (case of scribing and ablation) during each pulse.

- Lastly, the cumulative energy density represents the sum of the energies of all the delivered pulses at a single point taking into consideration the overlap. At equal energy densities, this enables counting the number of the equivalent pulses seen by each laser-treated spot.

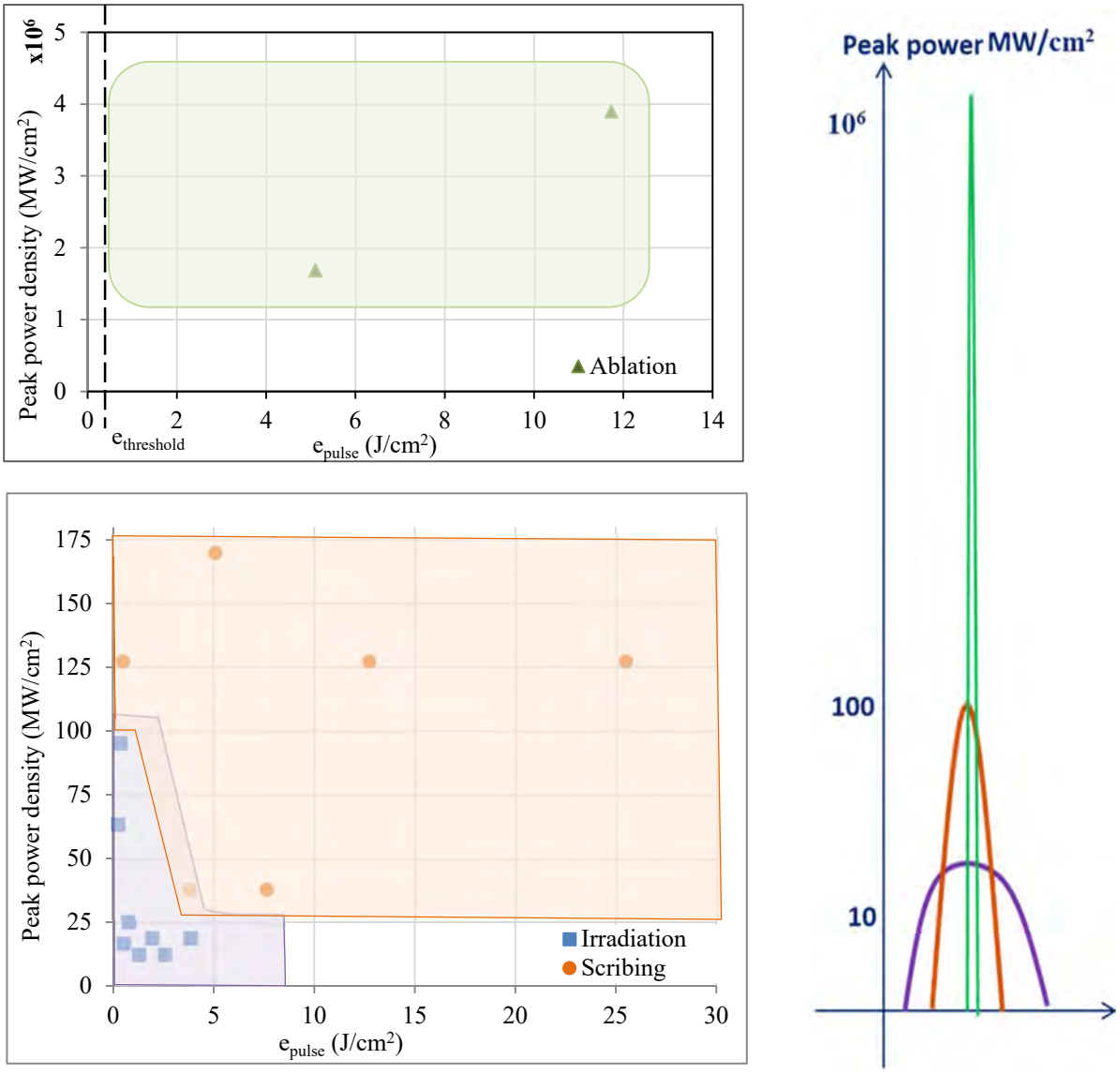

Figure 9 Irradiation, Scribing and Ablation Zones Defined by the Peak Power Density as a Function of the Pulse Energy Density (on the Left) and as a Function of the Pulse duration (on the Right), Markers Correspond to Laser Configurations Effectively Tried in the Experimental Plan.

C) Modeling and Correlations

In this chapter we presented theoretical models and parameter identifications based on the experimental results in order to understand the physical phenomena that can lead to and thus explain the obtained results.

First, to understand the influence of the surface laser treatment on the material properties, we have established the relationships between the laser energy parameters and its effects on the surface; in terms of the thermal affected zone, the groove depth, the induced thermal stress (nanosecond pulse duration creates significant thermal effects), and the plasma electron temperature and peak pressure (femtosecond pulse duration) according to each treatment type. We used simple models to estimate the impact of each type of treatment on the surface of the sheet as a function of the amount of energy delivered by the laser:

- Irradiation: Induced Thermal Stress (σ_{th}) and thermally Heat Affected Zone (*HAZ*).

- Scribing: Induced thermal stress (σ_{th}), Heat Affected Zone (*HAZ*), and groove depth (p).

- Ablation: Groove depth (p) and electron temperature (T_e) or/and peak wave pressure (Pr).

These models are detailed in the first paragraph of this chapter and the evolution of each impact is presented as a function of the laser energy quantities.

Secondly, to interpret the origin of the change due to the magnetic observables we used the Bertotti model based on loss separations. The behavior of the Bertotti coefficients under different laser treatment helps to explain the physical phenomena that occurred as a result of the laser treatment.

Finally, the estimated impacts are used in the rest of the chapter to study their direct influence on the magnetic properties in order to determine optimal values that can be used to control and improve the effect of the laser treatment.

I. Modeling the Impact of Laser Treatment on Surface Physics

(i) Reviewing the Modeling of Laser Impacts

Researchers considered mechanical scratching among the first techniques to refine magnetic domains in grain-oriented steel sheets. They demonstrated that techniques such as ball-point scratching induced stress on the surface of the sheet, resulting in a refinement of the magnetic domains due to local surface deformation [37]. They proved the existence of compressive stress in the vicinity of the scratch and a tensile stress perpendicular to the scratch line. With the same analogy, Imafuku and Suzuki [38] presented a comparison between the impact of a laser-irradiation and a gear-rolling on grain-oriented Fe-3% silicon samples. They measured the stress distribution in the sheet using the X-Ray technic. Besides, they measured the tensile residual stress only near the laser-irradiated line resulting in a magnetic domain refinement.

This residual stress was released after annealing at 1027 K for 2 hours in a pure hydrogen atmosphere when the domain-refining effect vanished; the magnetic domain width returned to its initial value in the standard sample. In the case of gear rolled samples, they

observed complex states of compressive and tensile stresses in the vicinity of the groove. Therefore, after the same annealing, the residual stresses around the groove were released but the domain refinement was maintained. When we assimilate the groove effect resulting from laser ablation and laser scribing with the one resulting from the mechanical scratching, we realize that each type of laser treatment behaves uniquely on the metal surface.

A shock wave model developed by Peyre and Fabbro [39] to estimate the change in a sheet under laser ablation illustrates that the pressure generated by the plasma in the metallic substrate during the laser treatment induces superficial residual stress. They assumed that the plasma layer formed during the ablation process induces compressive pressure and a shock wave resulting in local plastic deformation and a residual stress field in the localized volume of the sheet. The value of the pressure generated is proportional to the power density of the laser. Plastic deformation and the creation of dislocations in the material only occur if the amplitude of the primary shock wave is greater than the dynamic yield point called the Hugoniot limit. During the propagation of the wave, the affected volume is plastically strained. Post the interaction, the surrounding material induces biaxial compressive residual stresses in the plane parallel to the surface, which only counteracts the deformation if the value of the peak stress exceeds the Hugoniot limit. In addition to this condition, the pulse duration has to be in a few nanoseconds to allow the propagation of the generated wave throughout a certain depth in the material. Taking an example of the laser treatment with a femtosecond pulse duration, the pressure generated is quite high, but since the pulse duration is very short, the pressure generated should not propagate through any significant depth in the material.

In their studies, Li et al.[18] revealed two types of lasers used for surface treatment: a continuous laser and a pulsed laser. They explained that during laser treatment a small amount of plastic deformation and high-density dislocation is produced in the heat-affected zone. Then, due to subsequent heating and cooling, the magneto-elastic energy of the specimen changes, and the width of the domain walls is reduced. Thus, the residual tensile stress produced by plastic deformation refines the domains and reduces core loss. For the estimation of the residual stress induced during a laser surface treatment, they first calculated the temperature variation as a function of the heating time by considering the laser as a pulsed heat source, then solved the simplified classical heat transfer equation. Accordingly, for ultra-short laser pulses, these models lost their validity. To describe the heat transfer, it is substantial to use the two-temperature model distinguishing between lattice temperature and electron temperature [36]. This model is explained in the paragraph below.

Further, Naqavi and Yilbas[40] studied the heat transfer and stress distribution during laser irradiation they explained the mechanism of heating during laser irradiation. The laser irradiation is controlled by the process of absorption. The absorption of the laser energy occurs through the interaction between the lattice and the free electrons, during which the energy of these electrons is raised to high energy levels.

The energy transfer from excited electrons to the lattice occurs due to successive collisions. The average free collision time is 10^{-14}s. Since the duration of the interaction is short compared to the irradiated time, the energy transport between the electrons and the atomic site mesh is unbalanced. Thus, the temperature of the electron is higher than that of the lattice sites. The absorbed laser energy is converted instantaneously by heating to the point where absorption occurs.

To understand the effect of surface laser treatment on the sample properties, we sought to first analyze the impact of laser parameters of each configuration on magnetic properties (loss separation), then on macroscopic magnetic observables (especially the losses and apparent permeability) of the sample. The best way was to start expressing laser parameters in terms of energy quantities and relating them to main physical effects on the sample: the Heat-Affected Zone (HAZ), the groove depth (p) and the induced thermal stress (σ_{th}) or peak wave pressure (Pr) for each kind of laser process [39] [18] [41]. Using main considerations partly found in the literature, we presented simple adjusted models to estimate the impact of each type of treatment on the sheet surface as a function of energy quantities delivered by the laser: more precisely the induced thermal stress and heat-affected zone due to laser irradiation, the induced thermal stress and groove depth due to laser scribing and the groove depth, plasma maximum temperature or/and peak surface wave pressure due to laser ablation. Then these new physical parameters describing the impacts of laser pulses will be correlated to local magnetic properties presented afterwards.

(ii) Irradiation Process: Estimation of the Induced Thermal Stress and the Heat-Affected Zone

The laser beam forms a heat source that will locally heat up the surface of the sample and the temperature variation in the material will generate thermal stress, a zone is thermally affected with located and partial coating melting for some delivered quantities of energy. All values of temperature variations reached during the laser treatment depend on the laser setting parameters (peak power density, cumulative energy density, pulse energy, the scanning speed...) used during the laser process. We presented the variation of the thermal-induced stress, the heat-affected zone, and the affected depth and area as a function of the energy quantities involved during each laser irradiation and laser scribing. Inspired by the work of Li et al.[18], we developed a simple model estimating the local thermal-induced stress under a laser irradiation process. In this model, the total thermally conducting area in the metal is considered defined by the space between two coaxial cylinders with a height that equals the sheet thickness: one represents the area affected directly by the laser spot of radius r and the other represents the area affected by conductive heat transfer of radius that equals r plus the thermal diffusion length (considered isotropic in plane and cross-section) calculated below.

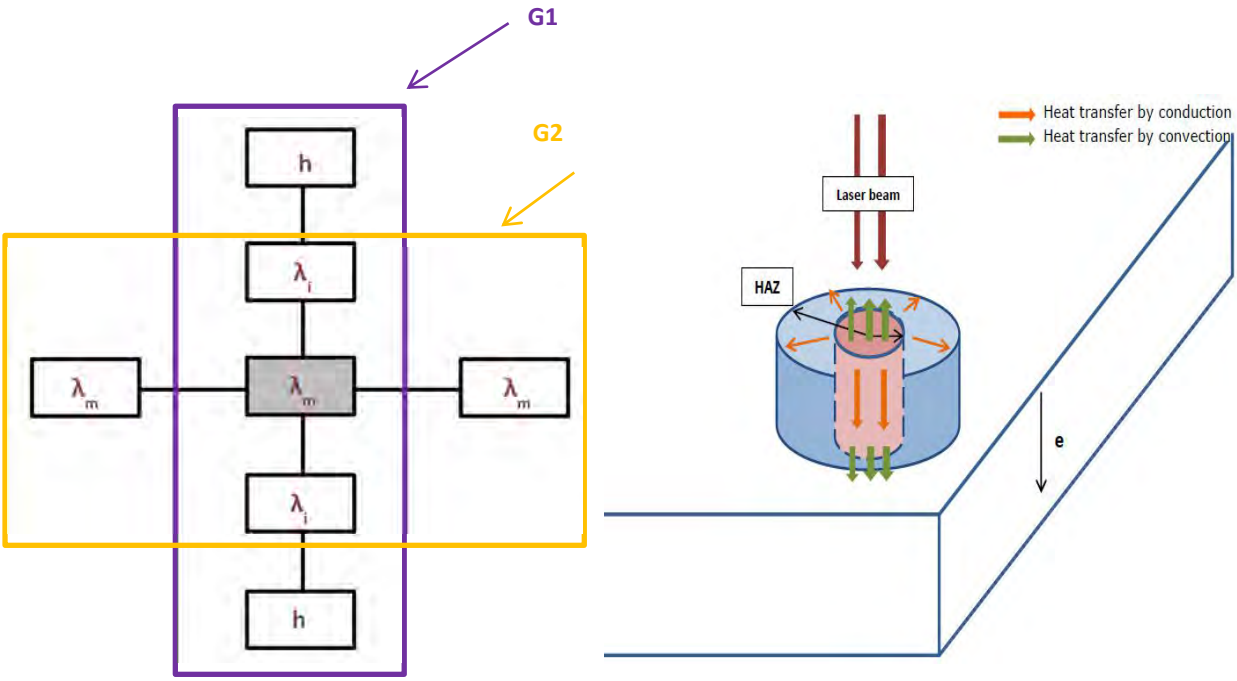

Figure 10 Equivalent Electrical Diagram and schema of the Thermal Model of Laser Irradiation (h convection heat transfer coefficient, λ_m thermal conductivity of silicon iron and λ_i thermal conductivity of the insulating layer).

The variation in the metal of the spot area temperature (ΔT) is estimated by the linear thermal Equation 28 which is written per unit surface:

Equation 28

$$C\ \partial_t \Delta T + (G_1 + G_2)\,\Delta T = A_0 \cdot q$$

where C [$J.K^{-1}.m^{-2}$] is the heat capacitance per unit surface (product of the mass-specific heat [$J.K^{-1}.kg^{-1}$], the density of the metal [$kg.m^{-3}$], and the metal thickness e_m [m]), q [$W.m^{-2}$] is the laser heat flux per unit surface which corresponds to the peak power density of the laser pulse ($\hat{\mathcal{P}}$), G_1 [$W.K^{-1}.m^{-2}$] is the thermal conductance per unit surface due to heat transfer by convection (between the air, the coating layer, and the metal layer, and G_2 [$W.K^{-1}.m^{-2}$] is the thermal conductance per unit surface of the heat transfer by conduction between the two cylinders with a height e_m equal to the metal thickness; the internal radius equals the radius of the laser spot and the external radius equals the radius plus the thermal diffusion length. The laser heat flux q equals the peak power over the disc surface of radius r. The laser absorption coefficient used in the irradiation case is A_0 equal to 0.35 [35]. The first values of G_1 and G_2 are calculated using the following equations (the value of G_1 (order of magnitude ~ 10) is negligible compared to the value of G_2 (order of magnitude ~ 10^5):

Equation 29

$$G_1 \cong \frac{h\cdot\left(\frac{\lambda m}{e_m}\right)\cdot\left(\frac{\lambda_i}{e_i}\right)}{\left(h\cdot\left(\frac{\lambda m}{e_m}\right)+h\cdot\left(\frac{\lambda_i}{e_i}\right)+\left(\frac{\lambda m}{e_m}\right)\cdot\left(\frac{\lambda_i}{e_i}\right)\right)}$$

Equation 30

$$G_2 \cong \frac{2\cdot\lambda_m\cdot e_m}{(r+\delta_{dl})^2\cdot \ln\left(\frac{r+\delta_{dl}}{r}\right)}$$

where *h* is the convection heat transfer coefficient per unit surface between the surface and the ambient air [$W.K^{-1}.m^{-2}$], λ_m is the thermal conductivity of silicon iron [$W.K^{-1}.m^{-1}$], λ_i is the thermal conductivity of the insulating coating [$W.K^{-1}.m^{-1}$], e_m [m] and e_i [m] are respectively the metal and the coating thickness, and δ_{dl} [m] is the thermal diffusion length in frequency domain determined by the following equation [42]:

Equation 31

$$\delta_{dl} \cong k_{haz}\sqrt{\frac{\lambda_m / C_{pv,m}}{\pi \cdot fr}}$$

where k_{haz} is a fixed constant equal to 24 (coefficient adjusted empirically to maintain consistency for the groove depth engraved in the scribing case between the observations and the measurements, refer to the following), $C_{pv,m}$ [$W.K^{-1}.m^{-3}$] is the volume heat capacity of the metal (it equals the product between the specific heat per unit mass in [$J.K^{-1}kg^{-1}$] and the mass density of the metal [$kg.m^{-3}$]) and f_r [Hz] is the laser repetition frequency.

The solution of the thermal equation allows us to express the temperature following the heating and cooling process for each pulse as follows:

Equation 32

$$\Delta T(\tau) = \Delta Tc \cdot (1 - \exp(-\kappa \cdot \tau)\,)\exp(-\kappa \cdot t_{down})$$

with $\Delta Tc = (A_0 \cdot q) / (G_1 + G_2)$ and $\kappa = (G_1 + G_2) / C$, using this equation we calculate the temperature variation of the metal. The first value of the insulating coating temperature variation is considered extremely close to the metal temperature variation.

The heating duration ($t_{up} = \tau$) is the duration of one laser pulse and the cooling duration ($t_{down} = (1 / f_r) - t_{up}$) is the duration between two successive pulses. Then, to include the dependence of the thermal conductivity coefficient of the metal on temperature, this conductivity is recalculated according to the following relationship as well as the recalculation of all other conductivity-dependent parameters[43]:

Equation 33

$$\lambda_m(\Delta T) = \lambda_m \cdot (1 - \alpha_{\lambda,T} \cdot \Delta T)$$

Where $\alpha_{\lambda,T}$ equals −0.00075 is the metal conductivity constant. The calculation of ΔT is repeated using the same equation considering that the temperature after each pulse is the new initial temperature of the metal to account for the overlap.
The cumulative energy density (e_{cum}) is calculated using the following equation (N is the number of laser line passes):

Equation 34

$$e_{cum} = A_0 \,.\, q \cdot N \cdot t_{up}$$

If the calculated coating temperature is below its softening and melting temperature (< 600°C), then there is no visible change occurring in the coating layer except an induction of an isotropic thermal stress in-plane (σ_{th}, tangential to the surface) during the process (not necessarily maintained after the process) calculated in the following equations:

Equation 35

$$\sigma_{th} = (\alpha_i \cdot \Delta T_i - \alpha_m \cdot \Delta T_m\,) \cdot E$$

where *E* is the quasi-linear Young modulus of the metal and a_i and a_m are the thermal expansion coefficient of the insulating coating and the metal respectively. It is important here to mention that neither viscous nor plastic mechanical properties are taken into account in case the thermal stress exceeds the yield stress with nonlinear behaviour. As a consequence, this equation only gives an estimation of the thermal equivalent stress

induced very locally during the process and not the permanent residual stress effectively maintained after the process. In order to estimate both the effective mechanical stress during the process and the residual stress after the process, a nonlinear behavioral for $E(\sigma)$ is required.

From the literature, in the absence of any coating,; during the heating process the part of metal located in the *HAZ* tends to expand along the three directions of space (perpendicular and parallel to the plane). Due to the cold metal around, the thermal expansion of the metal generates compression stresses in the in-plane or radial direction (parallel to the plane) and tensile stress in the out-of plane or axial direction (perpendicular to the plane)[40]. The magnitude of the normal or axial stress decreases as it propagates along the volume. The tangential or radial stress component is compressive near the axis of symmetry of the cylindrical *HAZ* and it becomes tensile, then compressive again and vanishing away from this axis. In the presence of a coating, and if and only if this coating doesn't become soft or melt, then the relative induced equivalent stress located at the interface between the metal and the coating can be radial tensile (in-plane) or axial compressive (out-of plane) at the laser spot and radial compressive (in-plane) and axial tensile (out-of-plane) away from the spot due to the thermal expansion of coating, before vanishing further again from the spot. In the following we estimated the tensile respectively compressive equivalent thermal stress induced parallel the plane by the long or short pulse located within the laser spot and only during the process. The question relative to the residual stress effectively maintained after the process can't be solved with such simple models (elastic mechanical behaviour, constant thermal and mechanical properties with temperature ...).. However, what we know from the literature on laser welding is that usually:

i) The generation of residual stress after a process inducing a thermal stress is possible if and only if the stress induced during the process is higher than the yield stress (~300 MPa).
ii) The actual value of residual stress is much lower than the process stress but its absolute value increases when the induced thermal stress increases during the process. Even low values of stress (tens of MPa) can have an extremely significant effect on magnetic properties.
iii) When the stress induced during a process is compressive (respectively tensile), then the residual stress that is maintained after the process will probably be tensile (respectively compressive) on the same locations.

If the calculated temperature variation of the coating layer achieves the softening temperature or melting point (600°C), under this circumstance the coating layer became soft or melted and then redeposited on the surface. The thermal conductance G_1 is replaced by G_1'; the heat transfer by convection is considered only between the air and the metal layer in this case. Part of the delivered laser energy corresponds to the coating melting enthalpy and the rest to the energy that heats the metal. The coating softening temperature is fixed at 600°C, the metal temperature variation and the thermal-induced stress are recalculated.

Equation 36

$$G_1' \cong \frac{h \cdot \left(\frac{\lambda_m}{e_m}\right)}{\left(h + \left(\frac{\lambda_m}{e_m}\right)\right)}$$

For both cases, we measured the value of the heat-affected zone HAZ under laser irradiation from the optical images (visual estimation, corresponding to a slight coating deformation). The behavior of the measured HAZ (Figure 11) as a function of the cumulative energy density is presented in Figure 12.

The laser parameters with their corresponding energy quantities studied in the case of laser irradiation are listed in the table below (Table 3):

Symbol	$\hat{\mathcal{P}}$ (MW/cm^2)	e_{pulse} (J/cm^2)	e_{cum} (J/cm^2)	N_{pass}
Irr_1	12.73	2.55	509.3	1
Irr_2	**12.73**	**1.27**	**509.3**	**1**
Irr_3	12.73	1.27	50.93	1
Irr_4	16.98	0.51	509.3	1
Irr_5	16.98	0.51	50.93	1

Table 3 Laser Parameters and Energy Contributions Used in the Case of Laser Irradiation for a Fixed Pattern Perpendicular to the Rolling.

For each irradiation configuration, we estimated the values of the induced thermal stress and the heat-affected zone. The results of the heat affected zone are presented in Figure 12. The heat-affected zone increased by increasing the cumulative energy density. Moreover, we limited the cumulative energy density (e_{cum}) of the laser by keeping constant the spot size Sp, the scan velocity v, the repetition frequency fr, the pulse duration τ and the total number of pulses N with the corresponding overlap. In the x-axis of each curve, we vary the laser average power P_w, from 0 to its nominal value and thus we vary the peak power density and energy density of each pulse and finally the cumulative energy density e_{cum} after *N* pulses. At higher cumulative energy density, the *HAZ* exceeds the thickness of the sheet, which can lead to sheet deformation and magnetic deterioration. The values of the induced thermal stress estimated are listed in Table 4. Irr_2 and Irr_1 correspond to cases with softening or/and melting of the coating whereas in Irr_3, Irr_4 and Irr_5 the coating is kept cold enough.

Configuration	Induced thermal stress σ_{th} (MPa)
Irr_1	-1285.7
Irr_2	-508.8
Irr_3	373.4
Irr_4	913.4
Irr_5	328.7

Table 4 The Estimated Thermal Stress Induced for Each Irradiation Configuration.

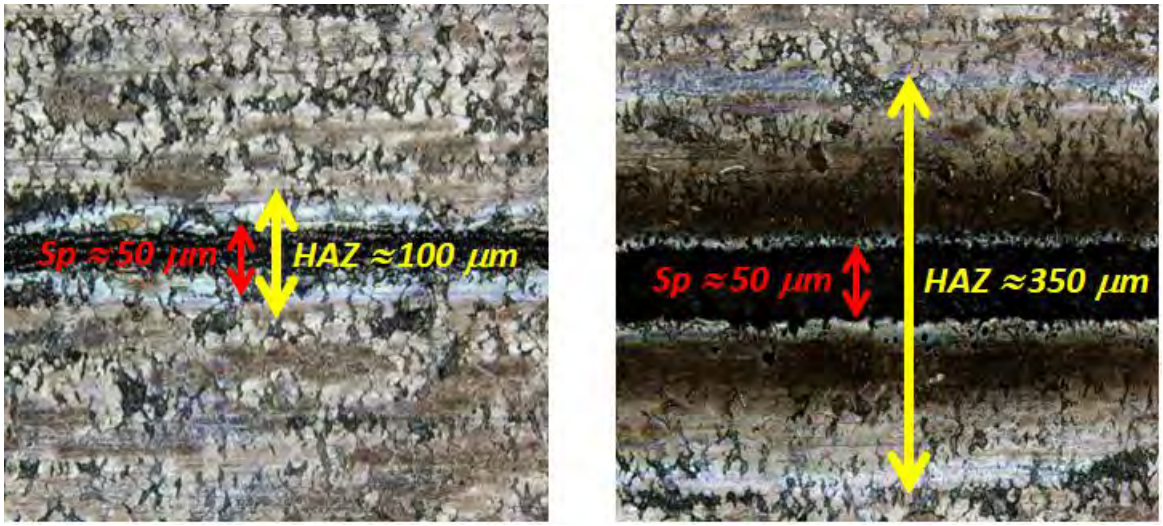

Figure 11 Optical Image Using a Confocal Microscope Showing the 2D Images presenting the measured HAZ on naked SiFe samples with equivalent thermal properties (NGOES), respectively and approximately 100 and 350 µm.

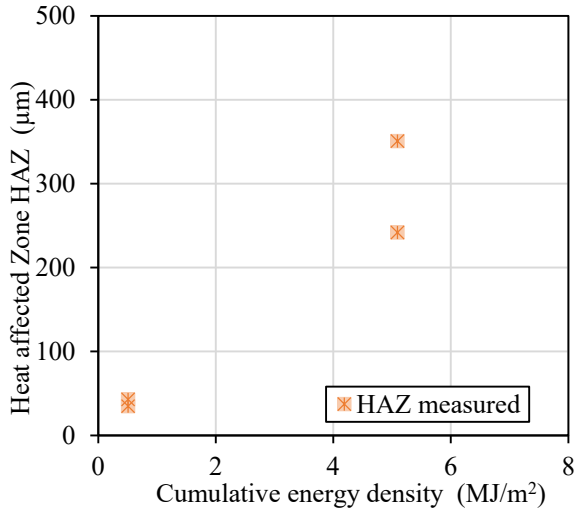

Figure 12 Heat Affected Zone as a Function of the Cumulative Energy Density e_{cum} in the case of Laser Irradiation.

(iii) Scribing Process: Estimation of the Induced Thermal Stress and the Groove Depth

To estimate the induced thermal stress, the heat-affected zone and the groove depth due to laser scribing, we used the same estimation model as the one for laser irradiation explained in the previous paragraph but with some modifications to include the engraving effect. First, due to quite higher laser power and metal phase transformations, an adjustment of the probably non-linear absorption coefficient A_0 close to 98% has been considered, by fitting the groove depth measured with the present estimation.

Then, the temperature variation of the metal increases and exceeds either the coating softening/melting temperature or/and the metal melting point in case of scribing leading to small grooves into either the coating only or/and both the coating and the metal. Some of the scribing cases that do not theoreticaly lead to a groove because the temperature achieved is not high enough should only lead to thermal stresses and be reclassified at the limit between irradiation and scribing.
To adjust the model, when the temperature achieved is high enough, the temperature of the coating layer is fixed at its melting temperature (600 °C), the temperature of the metal is fixed at its melting temperature too (1535 °C) and the radial compressive stress ($\sigma_{th} = \sigma_r$) induced during the laser scribing process is calculated using Equation 35.

Below 600 °C, none engravement is possible, the scribing can only lead to a tensile thermal stress. The whole energy is used for the heating process. Between 600 and 1535 °C at the laser spot, the scribing process removes the coating layer and can also lead to a tensile thermal stress in the heated metal in the *HAZ* around the laser spot still below 600 °C. Part of the delivered laser energy corresponds to heating process of the coating and metal from ambient up to 600 °C for the coating and up to a temperature between 600 °C and 1535 °C for the metal, part corresponds to the coating melting enthalpy (ΔHf_i = 12 kJ/kg) and the last part corresponds to the heating process of metal in the *HAZ* from the ambient up to a temperature below 600 °C. Above 1535 °C at the laser spot, the scribing process removes the coating layer, engrave the metal by removing some droplets of metal, but can now lead to a compressive thermal stress in the heated metal in the *HAZ* around the laser spot with a temperature between 600 °C and 1535 °C. The process used two additional energies which are the metal melting enthalpy (ΔHf_m = 180 kJ/kg) and the energy used to engrave the metal by melting. For this last case, involving the metal engraving process, considering the volume of a cylinder of radius R (R = r + δ_{dl}) and height p (the total groove depth: coating + metal), we estimated the value of the groove depth p in the metal thanks to the Equation 37.

Equation 37

$$p = \begin{cases} 0 & \Delta T < 600°C \\ e_i & 600°C < \Delta T < 1535°C \\ e_i + \left(\frac{r^2}{R^2}\right) \cdot \frac{e_{cum} - e_{cumTh}}{(\Delta Hf_m \cdot \rho)} & \Delta T > 1535°C \end{cases}$$

Where e_i is the coating thickness and e_{cumTh} is the cumulative energy density threshold corresponding to the sum of the total energy used for the heating process from the ambient to 600 °C and from 600 °C to 1535 °C plus both the coating melting enthalpy (ΔHf_i) used to melt the coating at 600 °C and the metal melting enthalpy (ΔHf_m) used to melt the metal at 1535 °C and ρ is the mass density of the metal. The scribing parameters considered are listed in Table 5. The depth estimated presented in Figure 13 increases with the increase of cumulative energy density; for a cumulative energy density between 0 and 1 MJ/m^2 the estimated depth is smaller or equal to the coating layer thickness (2 µm). On this account, for higher cumulative energy density, the metal layer is attacked and some metal particles are engraved. The metal starts to melt and to be engraved, some droplets of material can be removed. It should be noted that due to the non-reliability of optical measurements (irregular grooves) and the non-reproducibility of the nanosecond laser and the random laser-material interactions in the case of scribing due to the melting of the coating and/or the metal and its redeposition on the surface after cooling, the error between the measured and calculated values is important. For this reason, we decided to use the theoretical model for the parametric of study magnetic parameters as a function

of the theoretical depth behavior (dependent on the laser energy).On the other hand, the estimated induced thermal stress during laser scribing also increased as a tensile stress (> 0) with the increase of the cumulative energy density to a maximum of 1000 MPa and then decreased to become a compressive stress (< 0) when the metal scribing took place due the change in the remaining constraint when the coating is engraved (Table 6).

Symbol	$\hat{\mathcal{P}}$ (MW/cm^2)	e_{pulse} (J/cm^2)	e_{cum} (J/cm^2)	N_{pass}
Scr_1	**127.32**	**0.51**	**509.3**	**1**
Scr_2	127.32	0.51	50.93	1
Scr_3	38.20	7.64	30.56	1
Scr_4	127.32	12.73	50.93	1
Scr_5	38.20	3.82	15.28	1
Scr_6	169.77	5.09	101.8	1
Scr_7	169.77	5.09	50.93	1

Table 5 Laser Parameters and Energy Contributions Used in the Case of Laser Scribing for a Fixed Pattern Perpendicular to the Rolling Direction.

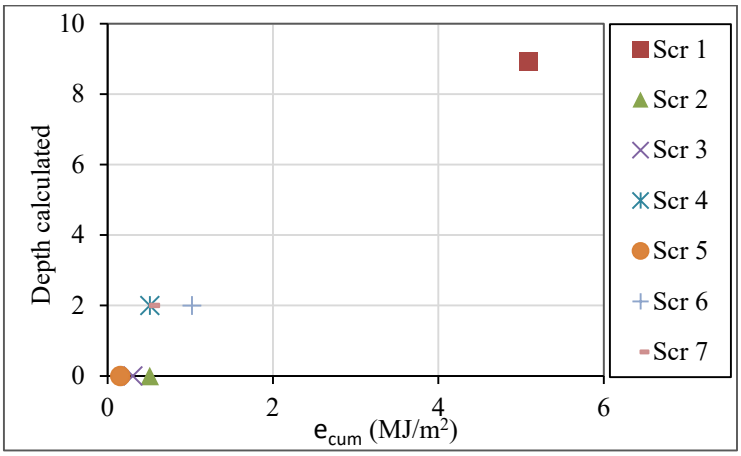

Figure 13 The Estimated Depth (p) as a Function of the Cumulative Energy Density (e_{cum}) During Laser Scribing.

Configuration	Induced thermal stress σ_{th} (MPa)
Scr_1	-1285.7
Scr_2	917.5
Scr_3	840.7
Scr_4	263.4
Scr_5	420.1
Scr_6	-862.1
Scr_7	534.7

Table 6 The Estimated Induced thermal stress for each Scribing Configuration.

(iv) Ablation Process: Estimation of the Groove Depth, the Plasma Electron Temperature, and the Peak Surface Pressure

Considering the femtosecond laser-matter interaction, the energy accumulated by the free electrons is transferred to the lattice by collisions, causing it to heat up to the sublimation point. Free electrons absorbs the laser energy very quickly, it lasts a few tens of femtoseconds, while their relaxation in the lattice varies between 1 and 10 ps. The pulse duration is shorter than the cooling time of the electrons. The use of ultrashort pulses shorter than these transfer times implies a decoupling between the thermal behaviour of the electrons at the temperature T_e and the thermal behaviour of the lattice at the temperature T_l . Thus, the classical approach to estimate a temperature is not valid. This non-equilibrium temperature state is expressed by the two-temperature model that involves both the electrons' temperature T_e and the temperature of the lattice T_l [41],[46].

Equation 38

$$\rho_e C_e(T_e)\frac{\partial T_e}{\partial t} = \nabla[K_e(T_e)\nabla(\mathrm{T_e})] - \kappa(T_e - T_l)$$

$$\rho_l C_l(T_l)\frac{\partial T_l}{\partial t} = \nabla[K_l(T_l)\nabla(\mathrm{T_l})] + \kappa(T_e - T_l)$$

with ρ the density, C the heat capacity , e refres to the electron, l refers to the matrix, λ the thermal conductivity, κ the constant of electron-phonon coupling.

Based on the literature[41], we used the expressions estimating the impacts of ablation to calculate the electron temperature and the ablation depth from the energy quantities of each laser configuration used. First, the electron temperature achieved during the laser ablation process, is estimated using the equation:

Equation 39

$$T_e \simeq \left(\frac{2 \cdot A_0 \cdot e_{pulse} \cdot \alpha}{C_e'}\right)^{\frac{1}{2}}$$

C_e' is the electron heat capacity coefficient per unit volume ($C_e = C_e' T_e$, $C_e' \approx 84\, J.m^{-3}.K^{-2}$).

Further, the ablation depth of *N* pulses ($N_{pass}=1$ for single pass and $N_{pass}=2$ for double pass) as a function of the laser fluence is estimated using the following expression:

Equation 40

$$\boldsymbol{p \simeq e_i + N * N_{pass} * \alpha^{-1} ln\,(A_0 * e_{pulse}/e_{th})}$$

e_{pulse} is the laser fluence, e_{th} is the threshold fluence for ablation (it equals approximately 0.5 J/cm^2 for FeSi [36]) and α is an optical penetration depth $\alpha = \frac{\rho \cdot \Delta Hfe}{e_{th}}$ [m^{-1}] with ρ the metal density and ΔHf_e is the specific heat of evaporation.
The behavior of the groove depth and the electron temperature is presented in Figure 14 and Figure 15, it is shown that these parameters increased as function of the cumulative energy density and the pulse energy.

Symbol	$\hat{\mathcal{P}}$ (M/cm^2)	e_{pulse} (J/cm^2)	e_{cum} (J/cm^2)	N_{pass}	*N*
Abl_1	**23.4 e^6**	**11.71**	**1171.3**	**1**	**100**
Abl_2	23.4 e^6	11.71	2342.7	2	100
Abl_3	23.4 e^6	5.09	509.30	1	100
Abl_4	10.2 e^6	5.09	50.93	1	10
Abl_5	30.5 e^6	15.28	1527.8	1	100

Table 7 Laser parameters and energy contributions used in the case of laser ablation for a fixed pattern perpendicular to the rolling direction.

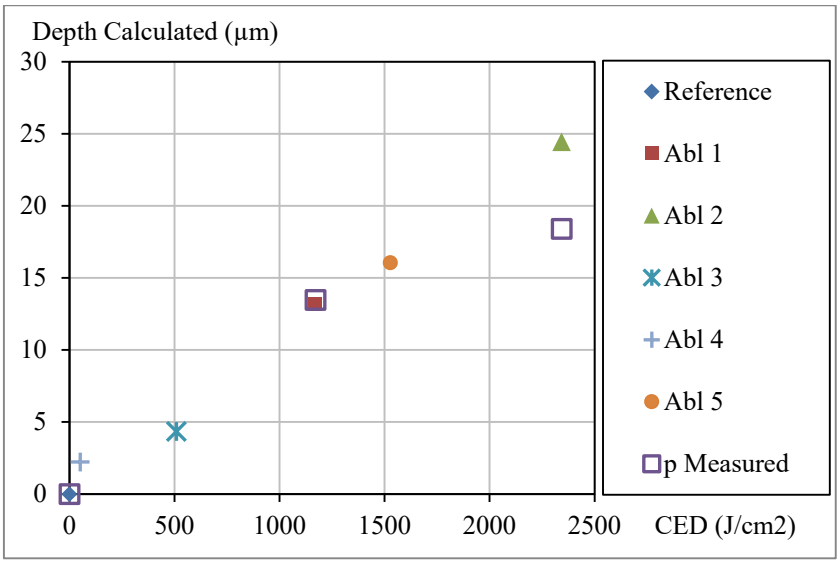

Figure 14 The Calculated Groove Depth as a Function of the Cumulative Energy Density (e_{cum}) in the Case of Laser Ablation.

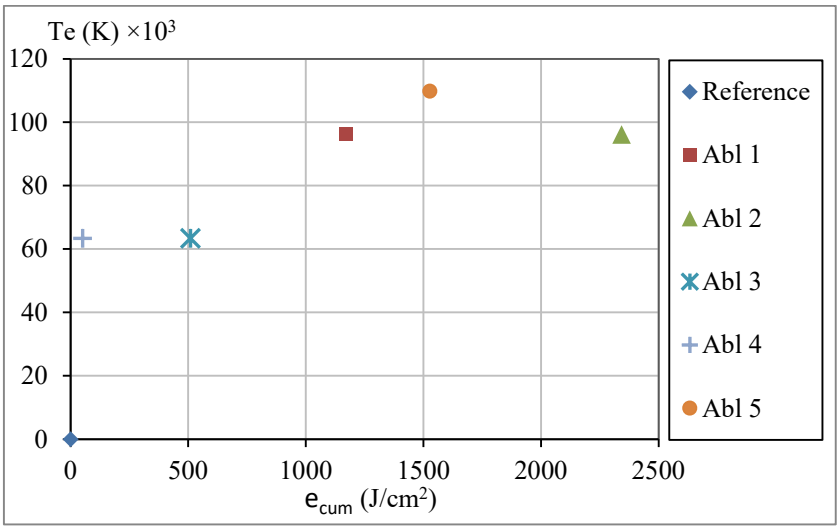

Figure 15 The Electron Temperature as a Function of the Cumulative Energy Density (e_{cum}) in the Case of Laser Ablation.

The estimation model for the ablation can also be compared to accurate numerical prediction performed by implementing the two-temperature model of equation 38. The definition of the problem can be simplified as in *Figure **16***.

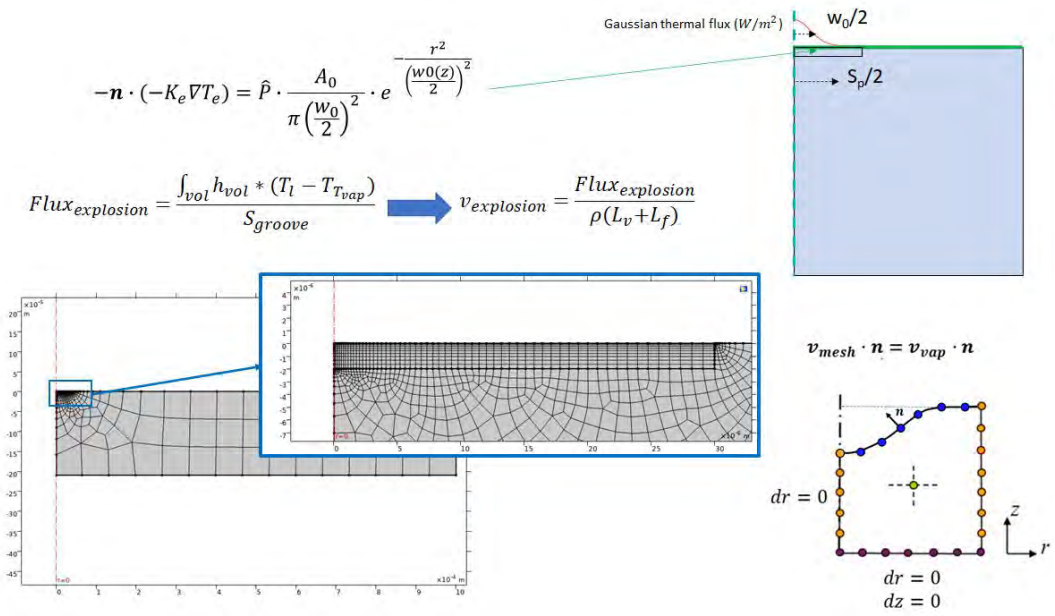

Figure 16 Definition of the ablation problem with the Finite Element Method

Results obtained for both the electrons temperature (***Figure 17***) and the groove depth measured and previously estimated (***Figure 18***) are in complete accordance one to each other.

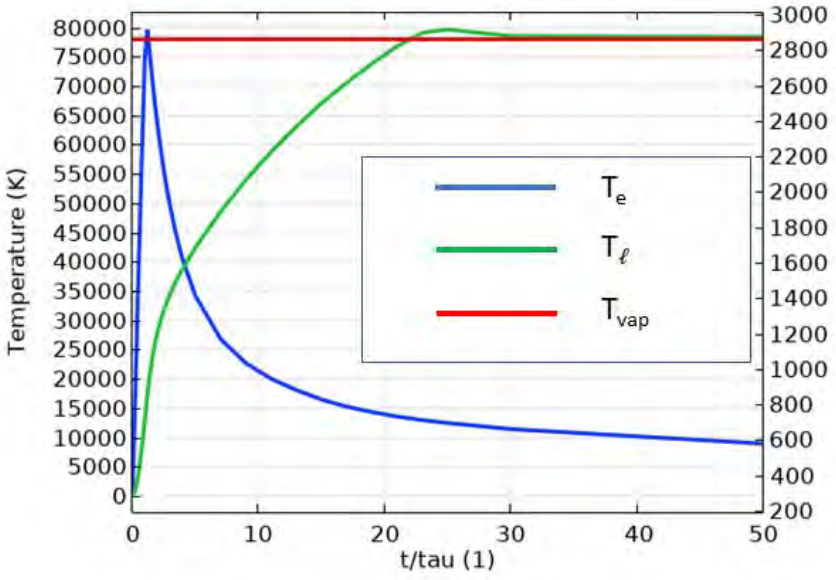

Figure 17 Computation of the electrons and lattice temperatures.

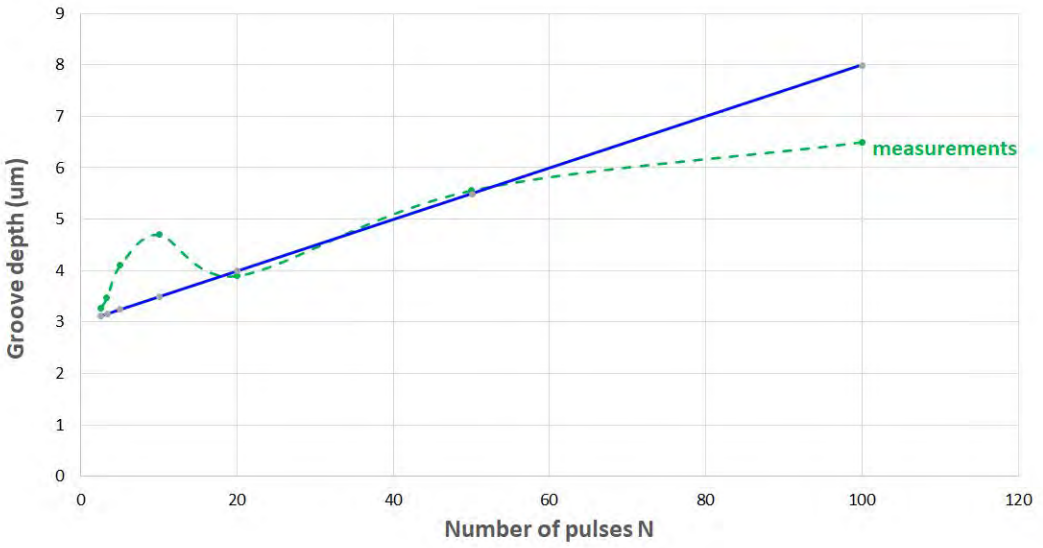

Figure 18 Computation of the groove depth with the numerical ablation model (2 T model).

Besides the groove depth and the electron temperature, we estimated the surface peak pressure as a function of the laser peak power with a shock wave model. A simple model of shock waves is developed by Peyre and Fabbro[39] to estimate the residual stress induced in the sheet submitted to laser short pulse with specified laser power density, pulse width, and spot size. In this model, they estimated the pressure generated by the plasma in the metallic substrate during the laser ablation process. And then they deduced the superficial residual stress assuming that the plasma layer formed during the ablation process induces a shock wave and a compressive pressure resulting in local plastic strain and residual stress field in the localized volume of the sheet.

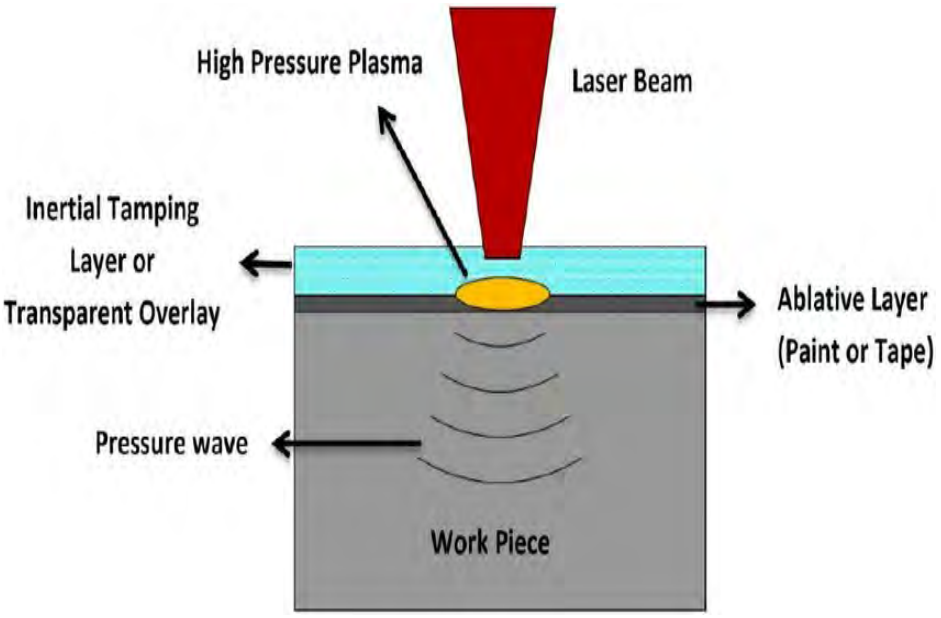

Figure 19 Schematic of Laser Shock Wave Principle[39].

In their experiment (Figure 19), the laser beam passes through a layer of confinement medium (water or glass to eliminate the thermal effect), the value of the pressure (*Pr*) generated is proportional to the square root of the laser peak power density ($\hat{P}$):

Equation 41

$$\mathbf{Pr} = \mathbf{BC} * \hat{\boldsymbol{P}}^{\frac{1}{2}}$$

Pr in kbar and $\hat{P}$ in $GW.cm^{-2}$, BC is a constant depending on the confinement layer (BC=10 for water confinement). The pressure generated in the case of ablation with a confinement layer is greater than one order of magnitude than for direct ablation. In our case, the laser beam is applied directly on the material surface, so the value of BC is considered equal to 1.

The plastic deformation and the creation of dislocations in the material occur only if the magnitude of the primary shockwave is higher than the dynamic yield strength or the Hugoniot Limit. During the propagation of the wave, the volume affected is plastically strained, thus after the interaction, the surrounding material induces biaxial compressive residual stresses on the plane parallel to the surface, to oppose the straining only if the value of peak stress exceeds the Hugoniot limit. To estimate the residual stress induced in the material, they calculated the value of the plastically affected zone (L_p) depending on the pressure Pr and P_h the Hugoniot limit (the yield strength under uniaxial shock condition). The plastically affected zone (L_p) is the distance covered by the shock wave before its peak stress value decreases to a value lower than the Hugoniot Limit.

Using the femtosecond laser with high peak power induces a peak pressure that exceeds the Hugoniot limit but the theoretical value of the plastically affected depth is very low and not significant due to the very short pulse duration. Thus, the shock wave created does not propagate into the material. While we still can estimate the surface peak pressure and study its behavior as a function of the laser peak power density (Figure 20). In the next paragraph we studied the behavior of the magnetic parameters as a function of this peak pressure.

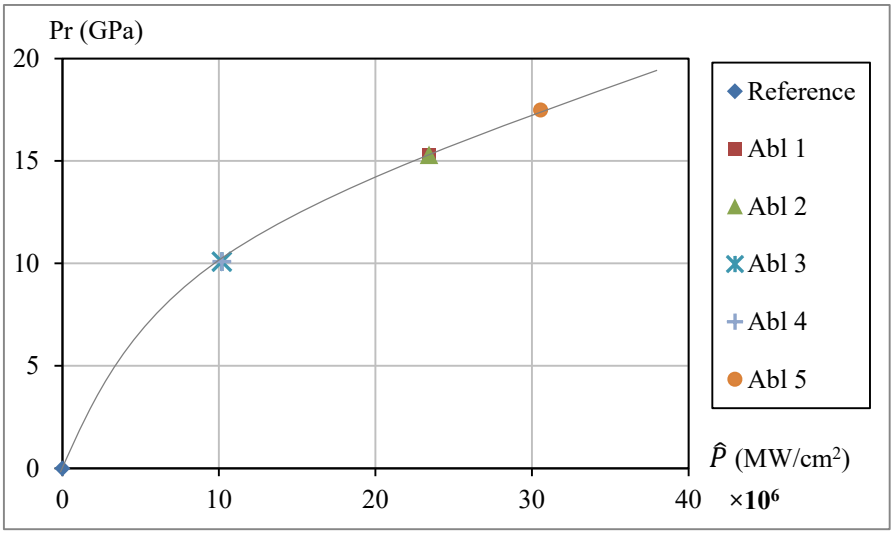

Figure 20 The Peak Pressure as a Function of the Peak Power Density in the Case of Laser Ablation.

Symbol	T_e *(K)* $\times 10^3$	*p (μm)*	*Pr (GPa)*
Abl_1	96.1	13.2	15.3
Abl_2	96.1	24.4	15.3
Abl_3	63.3	4.3	10.1
Abl_4	63.3	2.2	10.1
Abl_5	109.7	16.0	17.5

Table 8 The Estimated electron temperature, groove depth and peak pressure under a laser ablation.

II. Bertotti Model: variation of Bertotti coefficient as a function of the laser treatment

The chief parameters of Bertotti's model are the hysteresis loss coefficient k_h, the eddy current coefficient k_c, and the excess loss coefficient k_e. Bertotti suggested that the eddy current coefficient k_c is a constant that is identified by the material properties and thickness known from the manufacturer's datasheet (see Equation 2). We deduced the hysteresis loss coefficient k_h by measuring the losses at a very low frequency (3 or 5 Hz) for which both the classical eddy current loss and the excess loss are negligible.

Then with the equation of loss separation Equation 1, we identified the excess loss coefficient ke depending on the induction level and frequency using the corresponding power loss provided by the from experimental data.

In Table 3, Table 5 and Table 7 of the previous paragraphs, we have listed several laser configurations for each type of treatment tested on GO 23M0H sheets. The impact of these configurations on the identified Bertotti coefficients is presented in the next paragraph. In this paragraph, we focus on the comparison between one irradiation (Irr_2), scribing (Scr_1) and two ablations (Abl_1 and Abl_2(1side)) configurations that are mostly recommended for certain induction and frequency levels. The contribution of each loss component varies according to the level of induction and frequency. Respectively, to know at a given level of induction and frequency which component among hysteresis loss and excess loss is in the majority, it is required to compare the products $k_h\sqrt{B}$ to $k_e\sqrt{f}$.

We calculated the rate of change in percentage of the hysteresis loss coefficient k_h and the excess loss coefficient k_e of the treated sample compared to the sample itself before laser treatment, then we displayed the results in Figure 21.

Notably, the use of laser irradiation configuration "Irr 2" reduced significantly the hysteresis loss coefficient k_h at different induction levels for frequency 50 Hz whereas it slightly decreased the excess loss coefficient. It must be pointed out that the scribing configuration behaves in a like manner as the irradiation configuration with a higher reduction for the excess loss coefficient. However, for ablation, we deduced that if the treatment is done on both sides with one pass the effect on the hysteresis loss and the excess loss coefficients was similar at high induction, both were reduced. While, the ablation in two passes on one side resulted in the highest decrease in both coefficients, especially that of excess loss.

The variation of the hysteresis and excess loss coefficients is dependent on the type of laser treatment. Which asserts that a laser treatment acts differently on the sample surface depending on the laser type and its pulse duration:

The long pulses of the order of nanoseconds with small grooves and located induced thermal stresses could allow the generation of misoriented 90° closure domains at the vicinity of the laser spots which shows a significant reduction of the hysteresis loss coefficient without a significant impact on the excess loss coefficient related to the dynamics and mobility of the wall. The hysteresis loss coefficient is proportional to the defect density responsible for the wall pinning effect, partly due to the magnetic poles and demagnetizing effect around these defects. In the cases of irradiation and scribing, magnetic poles and demagnetizing effect are minimized thanks to the misoriented 90° closure domains appearing due to the thermally induced stress anisotropy.

On the other hand, ultra-short pulses of the order of a few hundred femtoseconds with an ablation effect that produces a deep groove in the sheet (especially in the case of two-pass treatment) can create different kinds of defects with magnetic poles that can pin the walls which is not favourable to the hysteresis coefficient especially at low induction levels. However, it can help the domain wall nucleation and 180° closure domains multiplication at the vicinity of the laser lines and facilitate the process of magnetization at higher induction levels. The most typical effect is also the 180° magnetic domain refinement and a change in the wall's mobility. The excess loss coefficient is proportional to wall density and mobility and therefore shows a greater reduction after ablation. Finally, it must also be mentioned that the ablation process can increase the permeability at low induction levels but reduce it significantly at high induction levels, effects that are stronger for the ablation than for the irradiation and scribing processes. The orientation of domains at the vicinity of the laser spots is closer to the rolling direction in case of ablation in comparison to the irradiation and scribing processes, it may lead to a significant increase of the permeability at a low induction level. In the case of ablation, this same orientation will generate large magnetic poles at high induction levels; whereas they are reduced and minimized in the case of irradiation and scribing. As a consequence, the demagnetizing effect added due to the laser process, which reduces the permeability at high induction levels, will be stronger for ultra-short pulses rather than for simply short or long pulses.

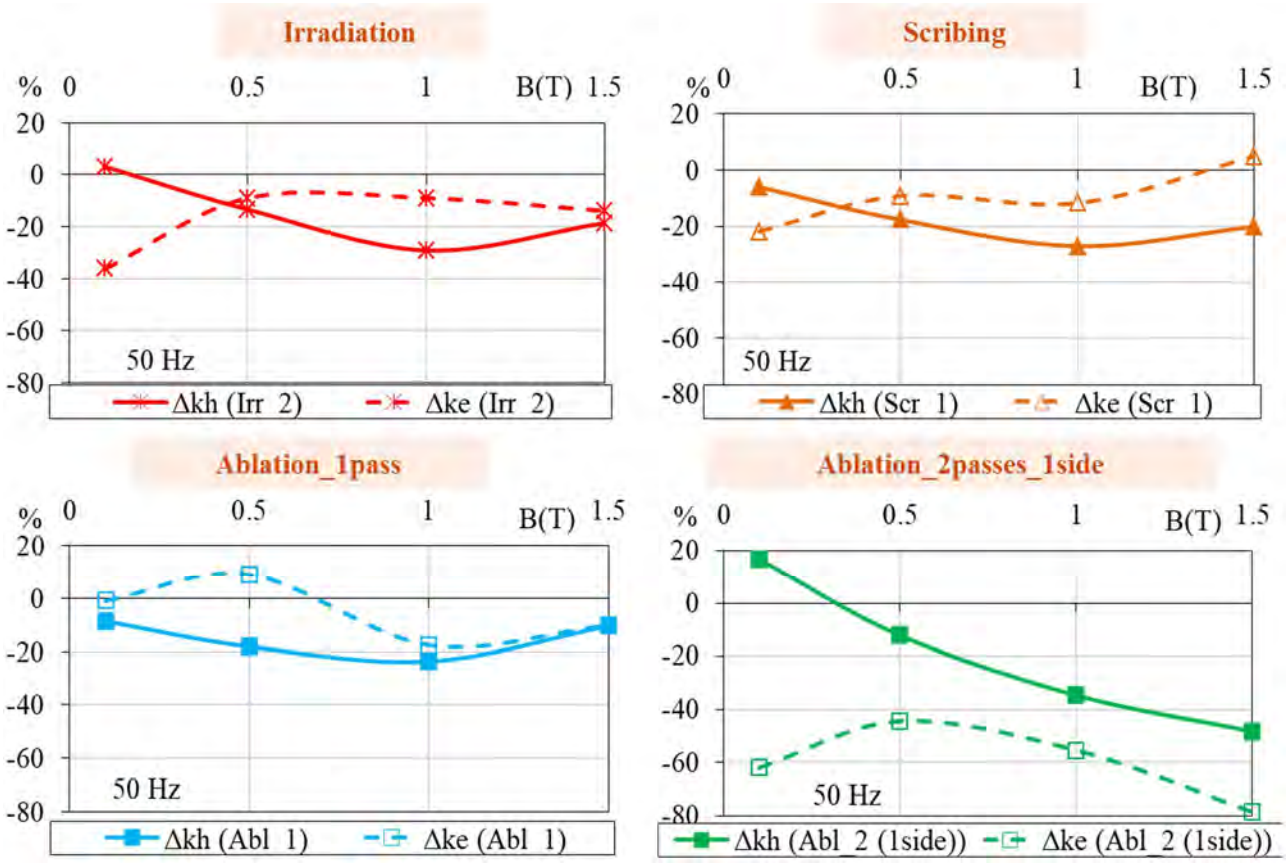

Figure 21 Variation of Bertotti's Coefficient k_h and k_e as a Function of Peak Induction Level at frequency 50Hz for Different Laser Treatment on GO 23M0H Samples.

III. Correlations Between Loss coefficients and Laser Energetic Quantities and physical Impacts

In this paragraph, we presented a correlation between the estimated laser impacts (topography, temperature, stresses...) and the identified magnetic properties (Bertotti coefficients) in order to study their behavior and to determine their optimum as a function of the laser impacts, the latter being directly related to the energetic quantities of a laser configuration.

In the case of laser irradiation, we related the identified Bertotti coefficients to the thermally affected zone and the induced thermal stress. Similarly, in the case of laser scribing, we related these loss coefficients to the groove depth and the induced thermal stress. Finally, in the case of laser ablation with an ultra-short ablation time, we presented the behavior of the Bertotti coefficients as a function of the groove depth, the electron temperature or/and the shock wave peak pressure generated during the process.

(i) Irradiation: Bertotti Loss Coefficients v.s. HAZ and Induced Thermal equivalent Stress.

Once the thermal affected zone and the thermal-induced stress were estimated as a function of the cumulative energy density for each laser irradiation configuration, we correlated these quantities to the magnetic properties. We should mention that the estimated induced stress is tensile when the temperature of the coating stays below the softening/melting temperature. Whereas, this stress is compressive when the temperature of the coating becomes higher than its softening/melting temperature, meaning that the coating becomes soft or melts and is partially removed or/and redeposited.

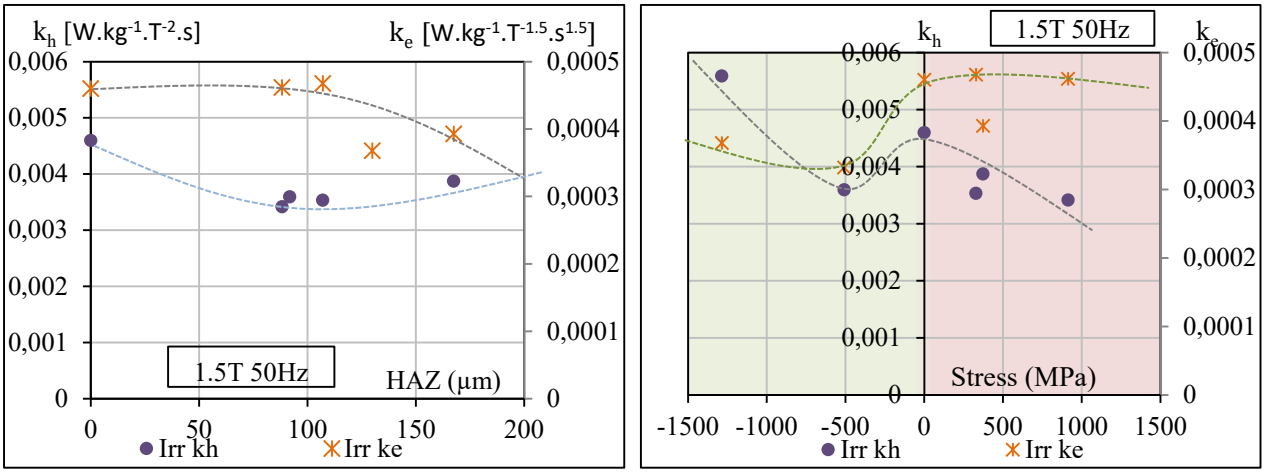

Figure 22 The variation of Bertotti's Coefficients k_h and k_e as a function of the Heat-Affected Zone (on the left) and the Induced Thermal Stress(on the right) During the Irradiation Process for 1.5T@50Hz.

Since the initial residual stress was not known, the residual stress couldn't be deduced. The stress presented was only the thermal equivalent stress induced locally during the irradiation process. We just can say that if this induced thermal stress has got an absolute

value higher than the yield stress of the metal, then it will add permanent residual stress with a lower value and the opposite sign after the process. Therefore, a compressive/tensile thermal stress during the process will add a tensile/compressive residual stress after the process.

The variation of Bertotti coefficients as a function of the heat-affected zone and the thermal-induced stress is presented in Figure 22 and Figure 23. At the peak induction 1.5 T for frequency 50 Hz, it is shown that by increasing the *HAZ*, the behavior of the loss coefficients k_h and k_e are contradictory. Thus, the need to find a compromise between the two values resulting in an optimum total loss result. This optimum was reached for a *HAZ* that equals 100 µm. This value corresponds to half of the sheet thickness, which seems coherent with the conclusion presented in the experimental part, recommending a laser treatment at both sides of the sheet in the case of an irradiation process so that the impact of the treatment can propagate throughout the whole volume of the sheet.

Meanwhile, the hysteresis and excess loss coefficients showed a similarity in their behavior as a function of compressive thermal-induced stress; the increase in compressive stress decreased both coefficients up to an optimal value around -500 MPa at peak induction 1.5T for frequency 50 Hz and at 0.1 T for 5000 Hz. This could refer to the persistence of a specific local tensile residual stress on the laser spot, and a specific compressive residual stress at the vicinity, acting on the energy state of domains through a magnetostrictive induced stress anisotropy which allow the nucleation of various differently shaped domains: 90° in-plane or out-of-plane closure domains within the laser spot and Lancet out-of-plane domains at the vicinity (see next chapter).

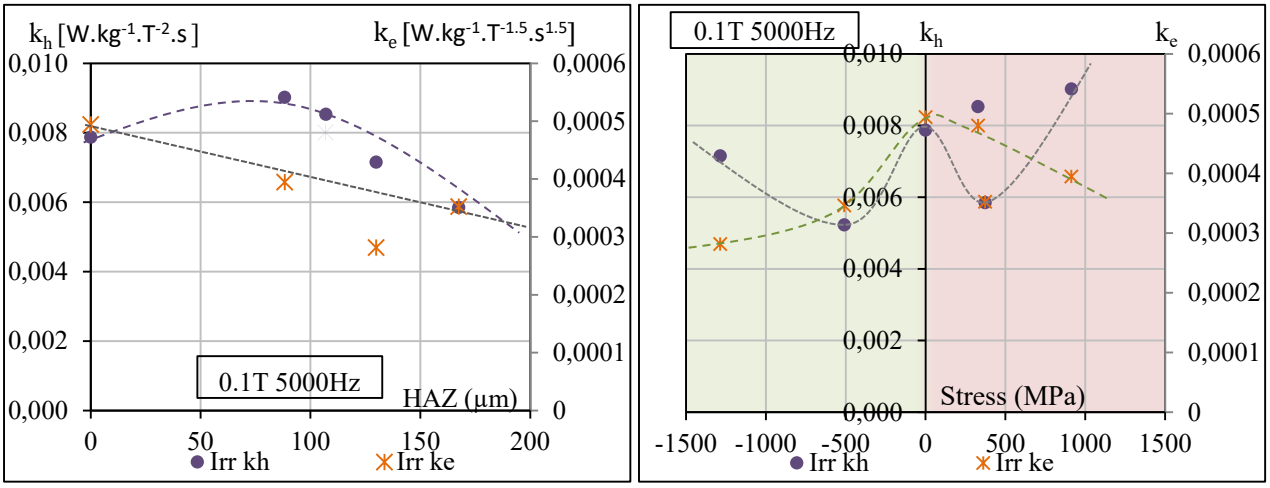

Figure 23 The variation of Bertotti's Coefficients k_h and k_e as a function of the Heat-Affected Zone (on the left) and the Induced Thermal Stress (on the right) in the Case of Laser Irradiation for 0.1T@5000Hz.

The first lead the material to minimize its total energy by refining the domains' structure, especially at low and mid induction; and the second improve the static reversal mechanisms especially at high induction. When the thermal-induced stress is tensile, the behaviour of k_h and k_e are contradictory. At high induction, this stress is interesting to reduce k_h but not k_e, whereas at low induction and high frequency, it is more interesting to k_e rather than k_h. A good compromise is more difficult to find in this case and the most

favorable situation rather corresponds to a compressive thermal-induced stress during the process.

(ii) Scribing: Bertotti Loss Coefficients v.s. the Groove Depth and Induced Thermal Stress

In the case of laser scribing, we have also presented the correlation between the hysteresis and excess loss coefficients and the estimated scribing impacts in terms of measured groove depth and the induced thermal stress. When the temperature achieved is sufficient to melt the coating but not the metal, the groove depth corresponds to the coating thickness, and the thermal stress induced in the *HAZ* where the temperature stays below the softening temperature of the coating still be tensile stress during the process.
When the temperature achieved is sufficient to melt the metal in addition to the coating, the groove depth corresponds to Equation 46, and the thermal stress induced in the *HAZ* where the temperature is between 600 °C and the metal melting point is necessarily compressive during the process.

Figure 24 gives the variation of coefficients k_h and k_e as a function of the measured groove depth at induction level 1.5 T for 50 Hz. At this induction level, it showed that deep grooves with depth higher than the coating thickness can be viewed as defects that pinned the walls and which are detrimental to the quasi-static behavior. Even if the hysteresis loss coefficient slightly decreases for grooves depth below 2 mm, it becomes higher than the reference for deeper grooves. Increasing the groove depth makes it possible to decrease more the excess loss coefficient which is related to the dynamic losses. This is probably due either to the size of closure and main domains near the laser lines, to the domains' walls mobility, or the proximity of the magnetic poles after treatment. Besides, the inclusion of laser lines may form a kind of new edge for the magnetic domains that promote the dynamic walls' mobility, nucleation or multiplication near the groove. However, the improvements become less significant for a depth greater than 2 µm for k_h and approximately 5 µm for *ke*. In a scribing process, grooves are always accompanied by a *HAZ* and various thermal induced stresses. It might then generate closure domains that are not optimal for the refinement effect and wall mobility at this induction level.

Thus, it is necessary to study the dependence of magnetic properties on the thermal stress. In most of the cases, the behaviors of k_h and *ke* are contradictory, meaning that it is not possible to choose a stress configuration that can minimize both k_h and k_e at the same time, except at low induction and high frequency for which a strong but located compressive thermal-induced stress up to -1500 MPa seemed to be beneficial. At high induction, when the hysteresis loss coefficient k_h shows two maxima, the excess loss coefficient k_e seemed to show two minima (Figure 24 and Figure 25) as a function of the thermal-induced stress, both correspond to a tensile stress value or a compressive stress value between 700 and 1000 MPa. k_e can decrease regardless of the sign of the stress as long as the stress is not too high (between 250 and 1000 MPa for the stress induced during the process, which could indicate that a local perturbation of the mechanical state gives birth to closure of any kind to refine the main magnetic structure and reduce excessive dynamic losses, but also to walls pinning centers. Having more stress might turn these pinning centers into nucleation centers in the quasi-static working conditions, but it also apparently jeopardize the excess loss reduction in the dynamic working conditions. An

optimum can be found around 1000 MPa for intermediate frequencies like 50 Hz. However, it has been shown in the previous paragraph, that the optimum for the loss coefficients requires a groove in the metal, which is necessarily accompanied by a compressive thermal induced stress, to be specified now not too far from -1000 Mpa.

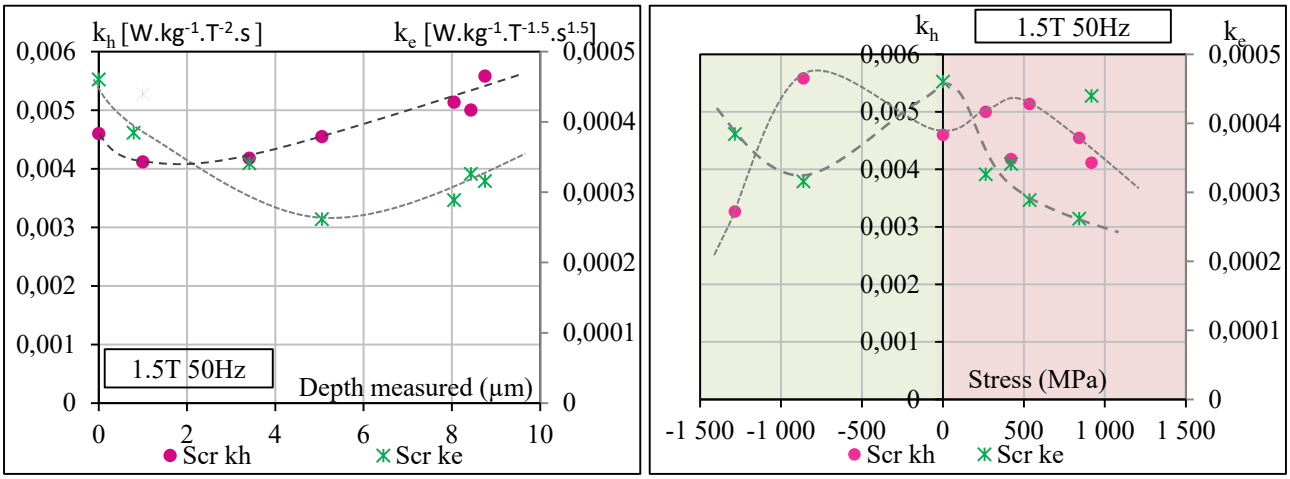

Figure 24 The Variation of Bertotti's Coefficients k_h and k_e as function of the Measured Depth (on the left) and the Induced Thermal Stress (on the right) in the Case of Laser Scribing for 1.5T@50Hz.

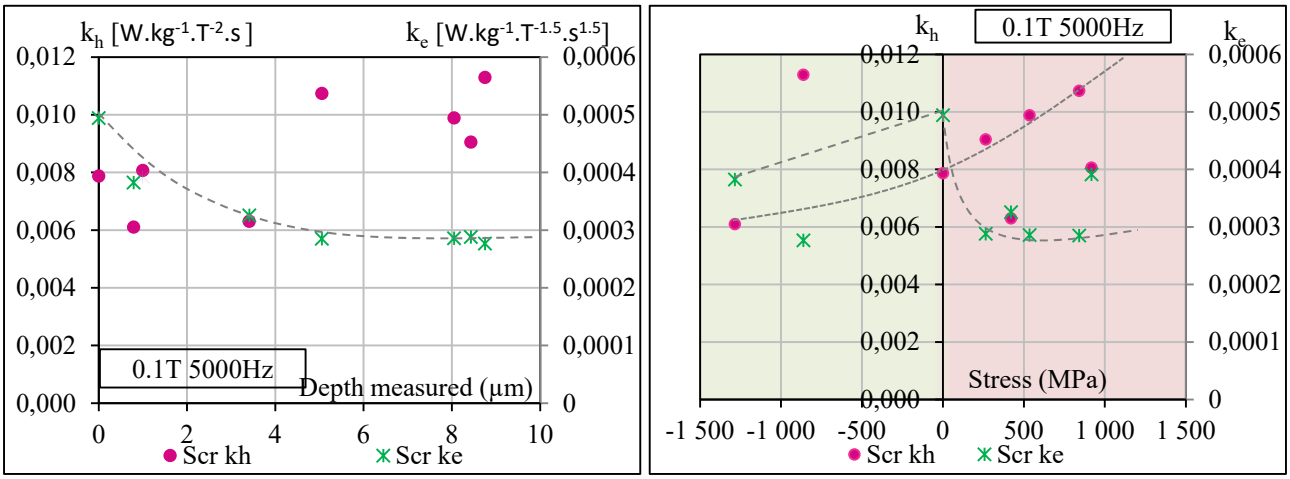

Figure 25 The Variation of Bertotti's Coefficients k_h and k_e as a function of the Measured Depth (on the left) and the Induced Thermal Stress (on the right) in the Case of Laser Scribing for 0.1T@5000Hz.

(iii) Ablation: Bertotti Loss Coefficients v.s. the Groove Depth, Plasma Electron Temperature and Shock-Wave Peak Pressure

In the case of laser ablation, we presented the variation of Bertotti coefficients as a function of calculated groove depth (p), the plasma electron temperature (T_e) and the shock wave peak pressure (Pr).

Since the electron temperature is proportional to the square root of the fluence and the peak pressure is proportional to the square root of the peak power density, *i.e.* also the fluence, the study as a function of these two parameters is similar and the magnetic properties showed the same behaviour as a function of these physical impacts (Figure 27 and Figure 28). This observation has been physically coherent since there might was a close relationship between the temperature and the pressure even within a plasma gaz.

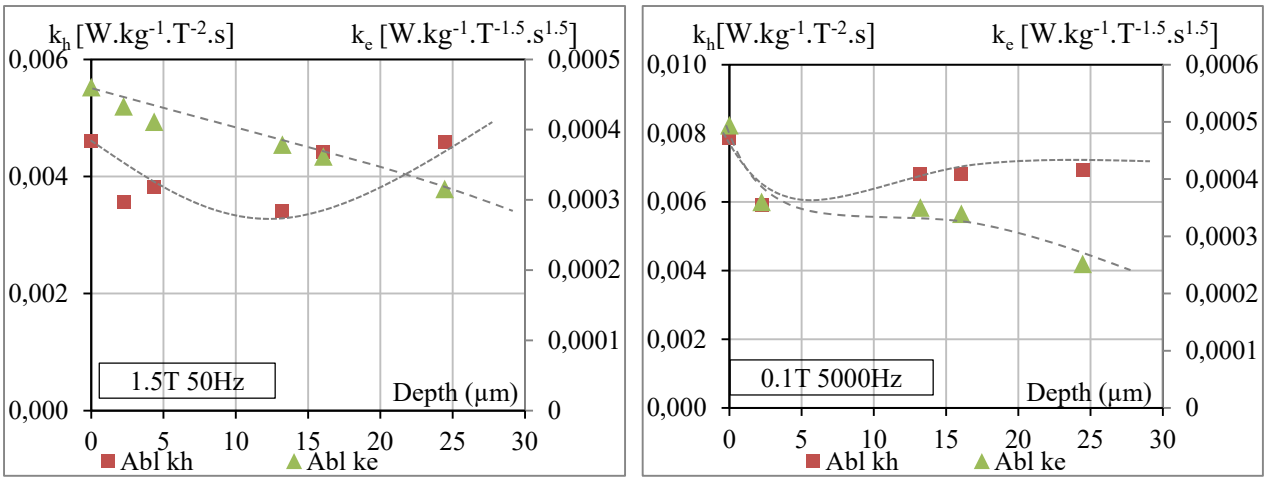

Figure 26 The Variation of Bertotti's Coefficients k_h and k_e as a function of the Measured Depth for 1.5T@50Hz (on the left) and 0.1T@5000Hz (on the right) in the Case of Laser Ablation.

However, at 0.1 T induction for higher frequencies, both hysteresis and excess loss coefficients decreased as a function of groove depth without showing an optimal value. For a peak induction of 1.5 T at a frequency of 50 Hz, the groove depth dependent excess loss coefficient seemed to be monotonously decreasing function (Figure 26), but the hysteresis loss coefficient has got a minimum at 13 µm and so increased for deeper grooves. Grooves in the metal previously meant defects and wall pinning effects with always an increase of hysteresis loss coefficients. On the contrary, in the case of ablation, grooves in the metal can act in this case as nucleation centers rather than pinning centers, probably thanks to the engravement done with ultra-short pulses and without thermal effect. Such "clean" grooves might give birth to located magnetic poles and 180° spike-like domains rather than various misoriented 90° closure domains and Lancet domains.

Therefore, deep grooves in the metal refine the magnetic domains significantly while reducing the dynamic losses, while the inclusion of such deep grooves adds defects increasing the hysteresis losses. As a consequence, a compromise with a specific optimal depth between 18 and 21 µm for the grooves must be found. At this level of induction, the behavior of the Bertotti loss coefficients was similar for the three laser processes studied. The main advantage of the ablation process seems to be the minimization of thermal effect which permits to reduce further and more significantly the excess loss coefficient. For the same reasons, the main corresponding drawback is that the permeability at high induction is also more significantly weakened.

However, at 0.1 T induction for higher frequencies, both hysteresis and excess loss coefficients decreased as a function of groove depth without showing an optimal value.

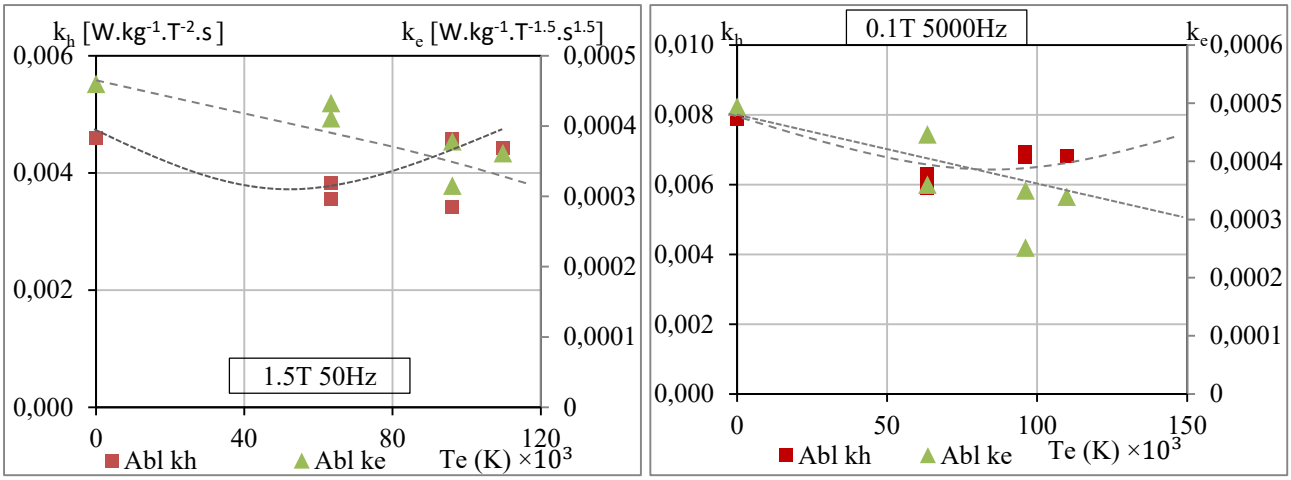

Figure 27 The Variation of Bertotti's Coefficients k_h and k_e as a function of the Electron Temperature for 1.5T@50Hz (on the left) and 0.1T@5000Hz (on the right) in the Case of Laser Ablation.

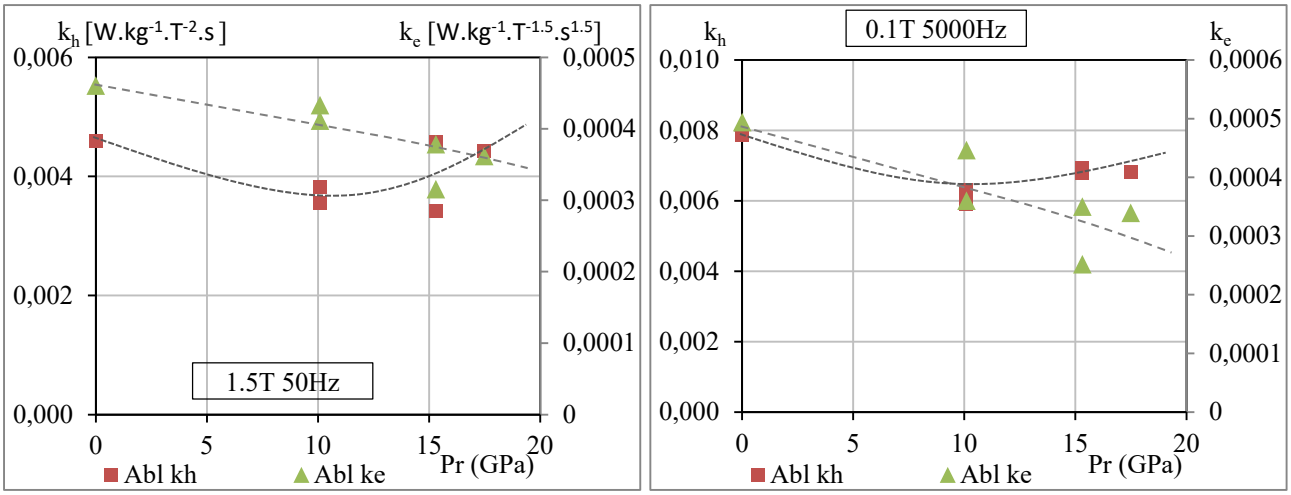

Figure 28 The Variation of Bertotti's Coefficients k_h and k_e as a function of the Peak Pressure for 1.5T@50Hz (on the left) and 0.1T@5000Hz (on the right) in the Case of Laser Ablation.

It should always be possible to engrave two identical grooves with two different ultra-short pulses. Therefore, the dependence of the magnetic properties should be studied not only on the groove depth but also on the electronic plasma temperature T_e or the peak pressure of the shock wave. It showed an optimal value for a temperature around 90000 K and a peak pressure close to 15 GPa beyond which thermal and mechanical induced effects start to appear increasing the hysteresis loss coefficient higher than the dynamic losses at 50 Hz. Having higher temperature or pressure may be interesting only at lower induction and higher frequencies for which the static hysteresis loss is negligible in front of the dynamic losses. In this case, the limitation is either the necessity to magnetize the material up to 1.5 T because the permeability can be then lower than initially or the mechanical weakening or deformation of the sheet.

Conclusion

The laser-matter interaction using a laser with a long or short pulse duration of the order of nanoseconds means melting and ejection of metallic droplets phenomena, once the temperature reached, exceeds its melting temperature. This interaction can be simulated with a classical heat transfer model. Using this model, we have estimated the thermal affected zone, the induced thermal stress, and the groove depth (if any).

However, in the case of an ultrashort pulse laser, the interaction is no longer in the classical domain due to the short pulse duration of the order of femtoseconds. This interaction is estimated by a two-temperature model allowing to deduce the groove depth and the electron temperature. All these impacts were presented as a function of the laser energy quantities.

On the other hand, using the Bertotti loss separation model, we identified the loss coefficients based on the experimental results. The results show a difference in the impact of each type of laser treatment (irradiation, scribing, and ablation). Laser ablation showed the highest reduction rate for the dynamic loss component.

Finally, a correlation between the estimated impacts and the identified coefficients is made resulting in optimal values ensuring a reduction of the total losses: For the case of irradiation the optimal thermal affected zone value is 100 µm (half the thickness), and the optimal induced thermal stress value is tensile around 500 MPa for induction level 1.5 T at 50 Hz. For scribing, the optimal value of the groove depth is between 2 and 4 µm (coating layer mainly), and the optimal induced thermal stress value is compressive around -1000 MPa for induction level 1.5 T at 50 Hz.. For ablation, however, For ablation, however, the optimal depth for one pass is between 8 and 16 µm (between 16 and 24 µm for two passes, only one side) without thermal effect as long as the pulse duration is shorter than 1 ps, the plasma electron temperature is close to 90000 K, and the shock wave peak pressure to 15 GPa at the metal surface.

D) Modeling and Correlations: Lambda's Model

I. Lambda's Model: variation of the dynamic magnetization property Λ and the internal static permeability μ as a function of the laser treatment

(i) Lambda's Model Vs. Laser Treatments

To determine Λ and μ, we applied the values of the dynamic power loss and the apparent permeability from the results measured by the SST. The dynamic power loss (P_{mf}) is deduced from the experimental data; its value is the difference between the value of the total power loss and the static power loss.

Furthermore, the apparent permeability (μ_{app}) is deduced from the experimental data: the value μ_{app} is equal to the ratio between the maximal induction level and its corresponding value of the applied magnetic field at the specified frequency. By solving the system of two equations with two unknowns, we attained the values of Λ and μ that give the same power loss and apparent permeability at specified frequency f and induction B_{max}.

Another method could also be used to identify Λ and μ which requests identifying μ as the apparent permeability at very low frequency from static hysteresis and then deducing lambda using the experimental value of the dynamic loss. Both methods provide the same values of the parameter lambda. Whereas the value of the property μ depends steadily on the selected method, the second one describes only the losses and not the apparent permeability in dynamics.

In summation, we have studied the variation of the dynamic magnetization property Λ and the internal static permeability μ as a function of the frequency and the induction level on one hand, plus the impact of each laser treatment on these properties on the other hand.

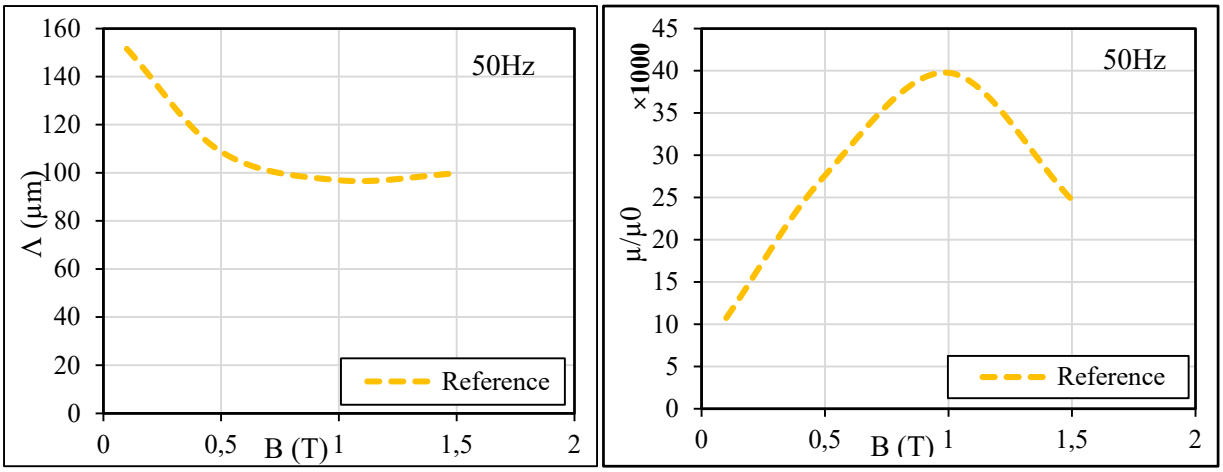

Figure 29 The Dynamic Magnetization Property Λ (on the left) and the Internal Static Permeability μ (on the right) as a Function of Peak Induction Level for Different Types of Laser Treatment on GO 23MOH Samples.

First, we started by studying the behavior of the dynamic magnetization property Λ and the internal static permeability μ as a function of the induction level for specified frequency 50 Hz, as shown in Figure 29, the value of Λ decreased by increasing the induction level to achieve a minimum value at mid-induction level (B ~ 1 T) then it started to increase at a higher induction level. This outcome is due to the increase in the wall's density, surface,

or mobility at mid-induction. In fact, at lower induction, the flux density variation is not elevated enough to ease the walls bowing and multiplication. Conversely, the higher induction near the saturation, the density of the wall decreases significantly. As a consequence, this minimum value for Λ might depend on the product f·B. Therefore, the internal permeability μ increased by increasing the induction level to achieve a maximal value at mid-induction level (1 T), then it decreased again near the saturation at a high induction level.

A comparison between the Lambda's model parameters Λ and μ of treated samples and that of the average of standards samples presented in Figure 30 showed that the laser ablation decreased the dynamic magnetization property the most. This result was consistent with the impact of ablation on the coefficient of excess loss as lambda is inversely proportional to the density, surface, and mobility of the walls. Thus, it is related to the dynamic losses, especially excess loss. Meanwhile, the scribing configuration (Scr_1) didn't show a significant change in the value of lambda Λ.

All laser treatment types improved the static permeability at different induction levels for a frequency of 50 Hz except at induction 1.5T where the laser scribing and ablation decreased the static permeability. This could refer to the addition of laser tracing lines in the case of laser treatment with a metal engraving (ablation and scribing) that favors the formation of narrow magnetic poles disturbing the magnetization near saturation. This phenomenon is compromised in cases where the laser treatment favors the formation of closure domains near the laser tracing lines.

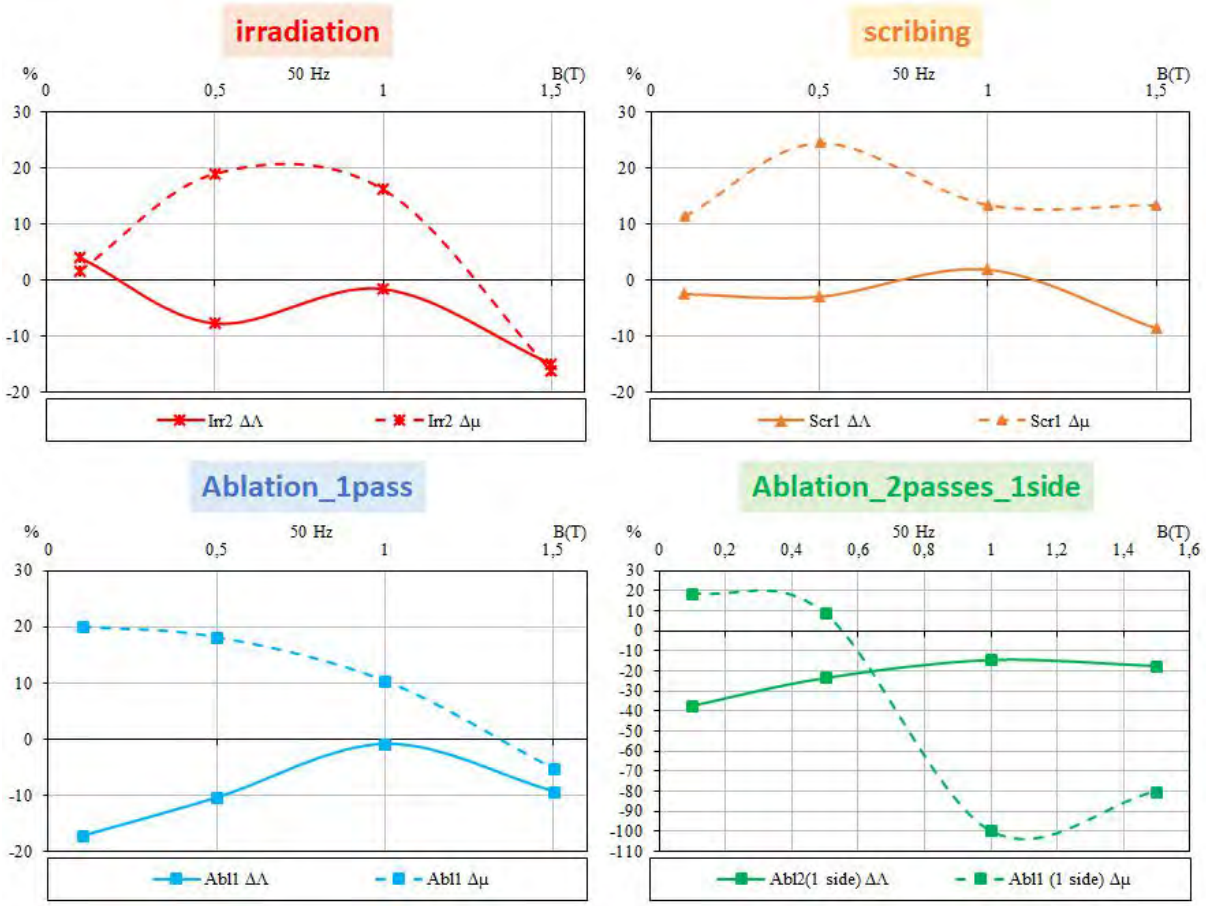

Figure 30 The variation in Lambda's Model Parameters Λ and μ as a Function of Peak Induction Level @50Hz for Different Laser Treatment on GO 23MOH Samples.

II. Correlations: Laser Energetic Quantities, Impact, Magnetic Parameters

In this chapter, we have correlated the laser impact (topography, temperature, constraints...) to the identified magnetic properties in order to study their behavior and determine their optimum as a function of the laser impacts, the latter are directly related to the energetic quantities of a laser configuration.

In the case of laser irradiation, we have related the magnetic parameters (lambda coefficients and Bertotti's model) to the heat-affected zone and the induced thermal stress. Similarly, in the case of laser tracing, we have related the groove depth and the induced thermal stress to the magnetic parameters. Lastly, in the case of laser ablation, we studied the behavior of the magnetic parameters as a function of the groove depth, electron temperature, and peak pressure.

(i) Irradiation: HAZ and Induced and Thermal Stress Vs. Lambda's Model and Bertotti's Coefficients

The increase in the heat-affected zone brought the static permeability to an optimal value for a HAZ between 80 µm and 120 µm. A higher HAZ damaged the static permeability as the heat-affected area increases the state of the induced and then residual stresses changes. The variation in the dynamic magnetization property Λ at high induction was negligible as a function of the HAZ. However, at low induction and for high frequency, Λ decreased with the increase of the HAZ (Figure 31 and Figure 32). This may be due to the formations of closure domains in the vicinity of the treated area facilitating the mobility or increasing wall density.

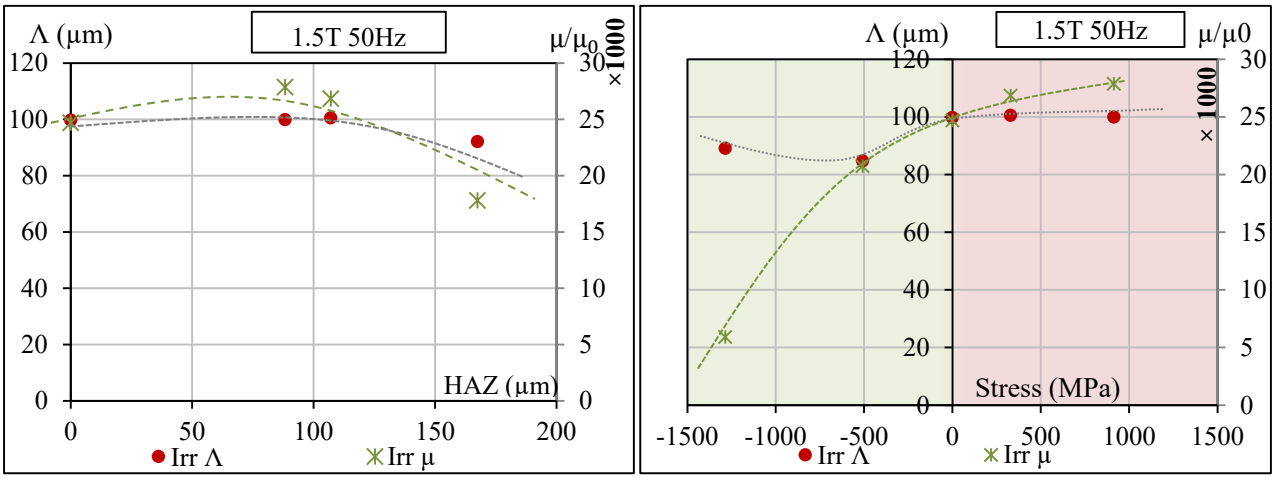

Figure 31 The variation of Lambda Model parameters as a function of the heat-affected zone (on the left) and the induced thermal stress (on the right) in the case of laser irradiation for 1.5T@50Hz.

The estimated induced stress is tensile in cases where the temperature of the coating has not exceeded its melting temperature, with no melting of the coating. Therefore, this stress is compressive when the temperature of the coating becomes higher than its melting temperature, the coating melts and begins to partially evaporate. Since the initial residual

stress was not known, the residual stress couldn't be deduced. The stress presented was only the thermal stress induced locally during the irradiation. The decrease in induced stress has reduced lambda at a low and high level of induction. Local induced stress has altered the energy state domains which, in turn, tend to minimize their energy by refining or creating differently shaped domains (closure or peak-shaped domains), resulting in higher wall mobility or different density or wall surface.

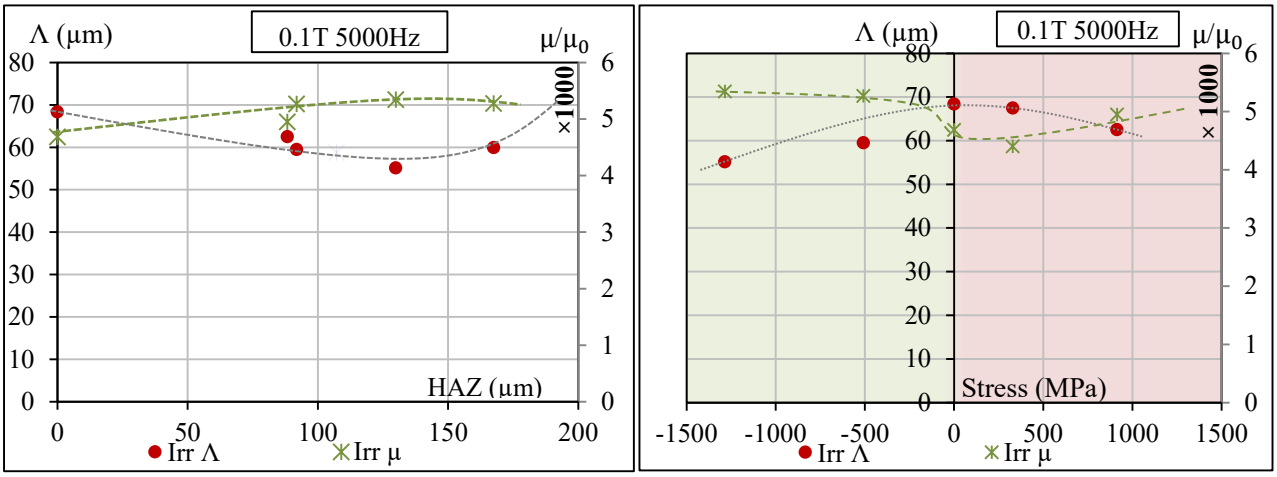

Figure 32 The variation of Lambda Model parameters as a function of the heat-affected zone (on the left) and the induced thermal stress (on the right) in the case of laser irradiation for 0.1T@5000Hz.

The result is similar to the one deduced by analyzing the parameters lambda and µ of the Lambda model by relating the behavior of k_h to that of µ and the behavior of k_e to that of Λ including the notion of wall dynamics during magnetization. The increase in compressive stress decreased both coefficients to an optimal value at -500MPa.

(ii) Scribing: Groove Depth and Induced thermal stress Vs. Lambda's Model

In the case of laser scribing, we presented the variation of Λ and µ as a function of the depth measured from the optical image of the laser pattern on the sheet (Figure 33). At a peak induction of 1.5T for frequency 50 Hz, Λ showed a minimum value corresponding to a depth of 5 mm. While, at a low-induction level, Λ showed a slight decrease with the increase of the depth.

This result could refer to the domain refinement effect associated with the increase in density and/or mobility of the walls. However, the engraved lines that are used to refine the domains can induce significant changes in the configuration of the closure domains and thus in the refinement effect and walls mobility, depending on the groove depth. A deeper groove seems to generate closure domains that are not optimal for the refinement effect and wall mobility at this level of induction. While, at a low-induction level, Λ showed a slight decrease with the increase of the depth with an asymptotic behavior towards a limit around Λ equal to 55 µm. Without considering the permeability, a deeper groove was more suitable for reducing Λ in this case. However, improvements become weak for depth above 5 µm.

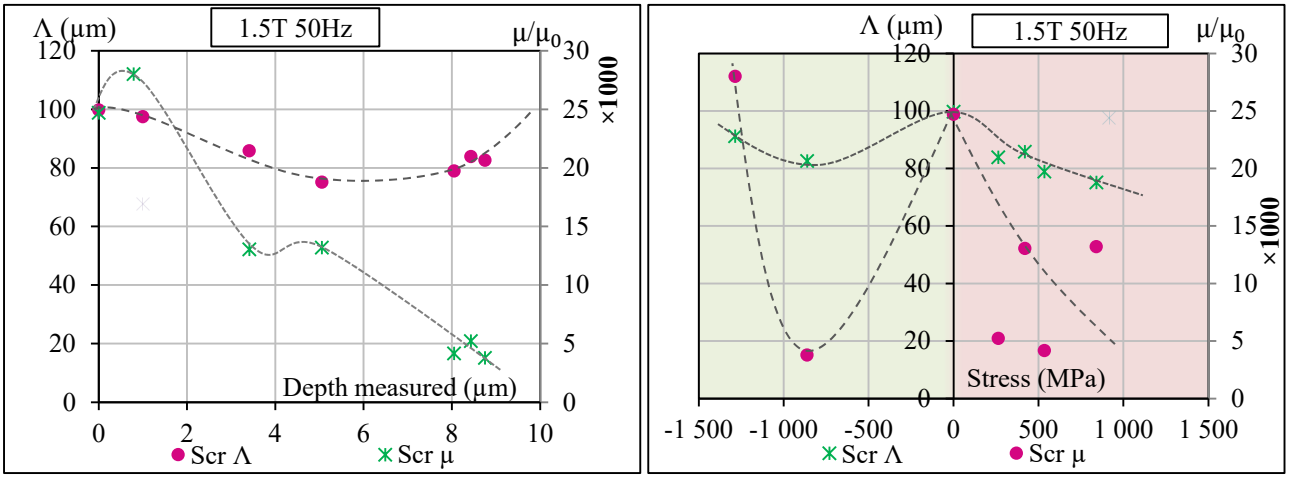

Figure 33 The variation of Lambda Model Parameters as a function of the Measured Depth (on the left) and the Induced Thermal Stress (on the right) in the case of Laser Scribing for 1.5T@50Hz.

The increase in the compressive stress reduced the value of lambda to an optimum for a value of stress between 700MPa and 850MPa, but it also decreased the static permeability.

.

(iii) Ablation: Groove Depth, Te, and Peak Pressure Vs. Lambda's Model

In the case of laser ablation, we presented the variation of Λ as a function of the depth calculated, the electron temperature and the peak pressure.

A very deep groove between 10µm and 20 µm resulted in the best reduction of parameter Λ for high induction level but the corresponding static permeability was damaged. While, at low induction level and for high frequency Λ showed a slight decrease with the increase of the depth (Figure 34).

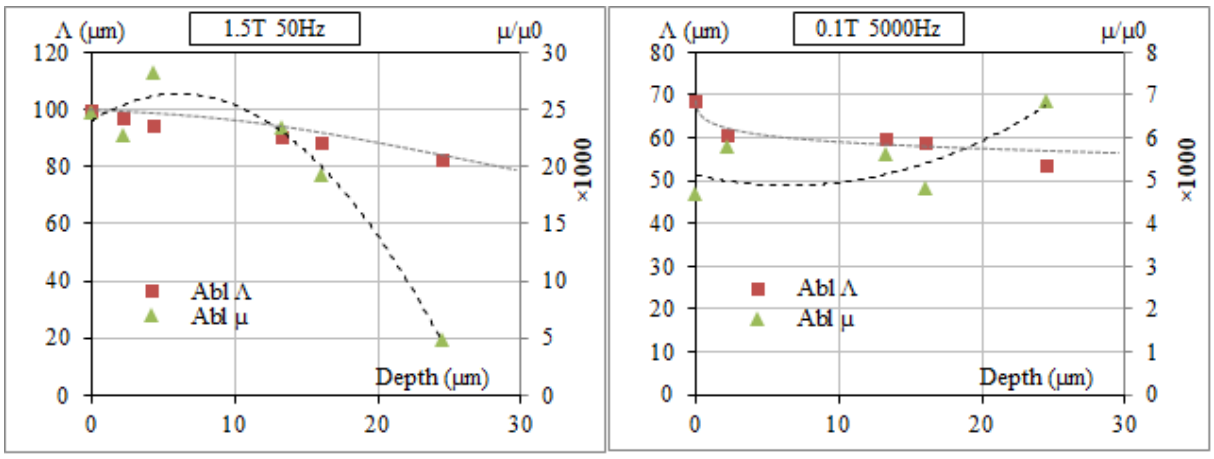

Figure 34 The variation of Lambda Model Parameters as a function of the Measured Depth for 1.5T@50Hz (on the left) and for 0.1T@5000Hz (on the right) in the Case of Laser Ablation.

We decided to correlate the variation Lambda's model parameters as a function of the electron temperature and the peak pressure, both quantities are proportional to the peak power density, thus they showed similar behavior. It showed that the increase in the electron temperature decreased the value of lambda while the static permeability showed an optimum for mean value of T_e. Similarly, the increase in the electron temperature decreased the excess loss and hysteresis loss and coefficient. The latter presented an optimum for mean value of T_e.

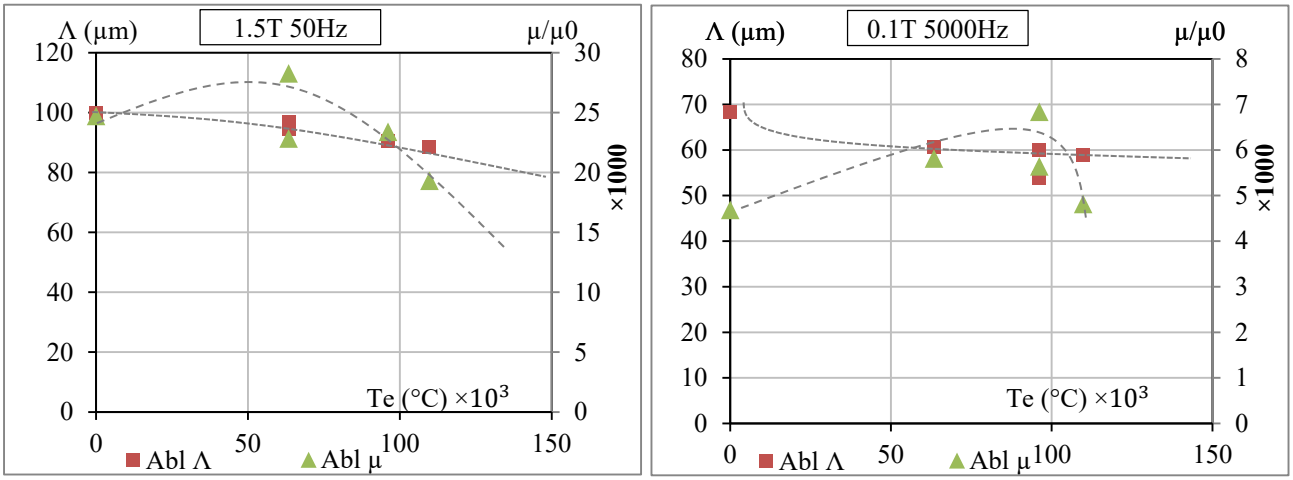

Figure 35 The Variation of Lambda's Model Parameters as a function of the Electron Temperature for 1.5T@50Hz (on the left) and for 0.1T@5000Hz (on the right) in the Case of Laser Ablation.

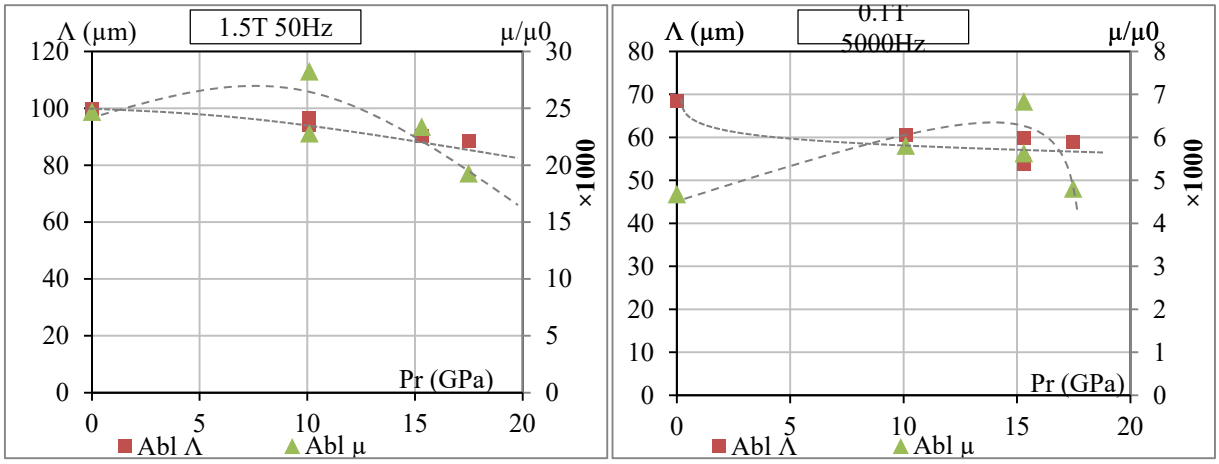

Figure 36 The Variation of Lambda Model Parameters as a function of the Peak Pressure for 1.5T@50Hz (on the left) and for 0.1T@5000Hz (on the right) in the Case of Laser Ablation.

Bibliography

[1] K. Fukawa et T. Yamamoto, « Domain structures and stress distributions due to Ball-Point Scratching in 3% Si-Fe single crystals with orientation near (110) [001] », IEEE Trans. Magn., vol. MAG-18, nº 4, 1982, doi: 10.1109/TMAG.1982.1061948.

[2] M. Imafuku et T. Suzuki, « Residual stress distribution in grain-oriented silicon steel », Int. Cent. Diffr. Data 2004 Adv. X-Ray Anal., vol. 47, p. 402-409, 2004.

[3] P. Peyre et R. Fabro, « Laser shock processing: a review of the physics and applications », Opt. Quantum Electron., vol. 27, p. 1213-1229, 1995, doi: 10.1007/BF00326477.

[4] J. Li, Y. Gu, et Z. Guo, « Decreasing the core Loss of grain-oriented silicon steel by laser processing », J. Mater. Process. Technol., vol. 69, p. 180-185, 1996, doi: https://doi.org/10.1016/S0924-0136(97)00015-0.

[5] K. H. Leitza, B. Redlingshöfer, Y. Reg, A. Otto, et M. Schmidt, « Metal Ablation with Short and Ultrashort Laser Pulses », Phys. Procedia, vol. 12, p. 230-238, 2011, doi: 10.1016/j.phpro.2011.03.128.

[6] I. Z. Naqavi et B. S. Yilbas, « Laser Nanosecond Pulse Heating of Surfaces and Thermal Stresses », Numer. Heat Transf. Part Appl., vol. 40, nº 3, p. 295-316, août 2001, doi: 10.1080/10407782.2001.10120638.

[7] Yu. N. Dragoshanskii, L. S. Karenin, V. D. Solovei, et R. B. Puzhevich, « Development of Stresses in Grain Oriented Electrical Steel during Laser Treatment », Phys. Met. Metallogr., vol. 112, 2011, doi: https://doi.org/10.1134/S0031918X11020190.

[8] A. H. Hamdani, W. Ahmed, A. Ansar, R. Akhter, W. A. Farooq, et M. Aslam, « Parametric Study of Ablation Depths for Different Optical Glasses Using High Fluence Laser Induced Plasma Assisted Ablation (LIPAA) », Key Eng. Mater., vol. 442, p. 172-177, 2010, doi: 10.4028/www.scientific.net/KEM.442.172.

[9] B. N. Chichkov, C. Momma, S. Nolte, F. Alvensleben, et A. Tünnermann, « Femtosecond, picosecond and nanosecond laser ablation of solids », Appl. Phys. Mater. Sci. Process., vol. 63, nº 2, p. 109-115, août 1996, doi: 10.1007/BF01567637.

[10] C. P. Steinmetz, « On the law of hysteresis », Proc. IEEE, vol. 72, nº 2, p. 197-221, 1984, doi: 10.1109/PROC.1984.12842.

[11] J. Reinert, A. Brockmeyer, et R. W. A. A. De Doncker, « Calculation of losses in ferro- and ferrimagnetic materials based on the modified Steinmetz equation », IEEE Trans. Ind. Appl., vol. 37, p. 1055-1061, 2001, doi: 10.1109/28.936396.

[12] K. Venkatachalam, C. R. Sullivan, T. Abdallah, et H. Tacca, « Accurate prediction of ferrite core loss with nonsinusoidal waveforms using only Steinmetz parameters », Proc. 2002 IEEE Workshop Comput. Power Electron., vol. 3-4, p. 36-41, 2002, doi: 10.1109/CIPE.2002.1196712.

[13] G. Bertotti, « General properties of power losses in soft ferromagnetic materials », IEEE Trans. Magn., vol. 24, p. 621-630, 1988, doi: 10.1109/20.43994.

[14] G. Bertotti, « Physical interpretation of eddy current losses in ferromagnetic materials I:Theoretical considerations », J. Appl. Phys., vol. 57, p. 2110, 1985, doi: https://doi.org/10.1063/1.334404.

[15] D. C. Jiles, J. B. Thoelke, et M. K. Devine, « Numerical Determination of Hysteresis Parameters for the Modeling of Magnetic Properties Using the Theory of Ferromagnetic Hysteresis », IEEE Trans. Magn., vol. 28, p. 27-35, 1992, doi: 10.1109/20.119813.

[16] M. J. Sablik et D. C. Jiles, « Coupled Magnetoelastic Theory of Magnetic and Magnetostrictive Hysteresis », IEEE Trans. Magn., vol. 29, 1993, doi: 10.1109/20.221036.

[17] L. Dupré, M. J. Sablik, R. Van Keer, et J. Melkebeek, « Modelling of microstructural effects on magnetic hysteresis properties », J. Phys. App Phys., vol. 35, p. 2086-2090, 2002, doi: https://doi.org/10.1088/0022-3727/35/17/303.

[18] T. Chevalier, B. Kedous-Lebouc, B. Cornut, et C. Cester, « A new dynamic hysteresis model for electrical steel sheet », Phys. B Condens. Matter, vol. 275, p. 197-201, 2000, doi: https://doi.org/10.1016/S0921-4526(99)00768-1.

[19] M. A. Raulet, J. P. Masson, et D. Gaude, « Presentation and experimental validation of a behavioral model of dynamic properties for magnetic materials », J Phys IV Fr., vol. 08, p. Pr2-619-Pr2-622, 1998, doi: https://doi.org/10.1051/jp4:19982143.
[20] M. A. Raulet, « Contribution à la modélisation des matériaux magnétiques liés à leur environnement en génie électrique », Phd Thesis Univ. Claude BernardLyon, 2011.
[21] O. Maloberti, « Contribution à la modalisation de la dynamique d'aimantation dans les matériaux magnétiques doux: Caractérisation et simulation », PhD Thesis Grenoble 2006.

Deliverable D3.1 (Version 1 at M6, update 2 at M39)

Magnetic Studies – Magnetic Models

Investigation on magnetic structures, magnetic properties and gradients on oriented soft magnetic materials submitted to surface laser treatments

WP3: PHYSICAL STUDIES

Date of Delivery: 30/04/2018 (initial report)

05/08/2019 (1st update), 30/04/2021 (2nd update)

Lead Beneficiary: ESIEE Amiens

Type: Report

Dissemination Level: Public

Version: 1.7

ESSIAL has received funding from the European Union's Horizon 2020 research and innovation programme under grant agreement No 766437.

Document identifier: ESSIAL-WP3-D3.1

Deliverable leader	ESIEE Amiens
Deliverable contributors	UPJV-LTI ESIEE Amiens
Related work package	WP3
Author(s)	Manar Nesser Olivier Maloberti Jérôme Fortin
Due date of deliverable	30/04/2018
Actual submission date of deliverable	30/04/2018
Due date of update 1	31/07/2019
Due date of update 2	M39
Actual submission date of update 1	05/08/2019
Actual submission date of update 2	30/04/2021
Approved by	Jérôme Fortin Olivier Maloberti
Dissemination level	Public
Call	H2020-FoF-06-2017
Project number	766437
Instrument	Research & Innovation Actions
Start date of project	01/11/2018
Duration	48 months

Revision history log

Version number	Date of release	Author	Summary of changes
1.1	30/04/2018	Manar Nesser	Sections A and B
1.2	30/04/2018	Olivier Maloberti	Section C and Annex
1.3	30/04/2018	Olivier Maloberti	Final Version, submission on 30/04/2018 (Initial deliverable)
1.4	15/07/2019	Olivier Maloberti	Update of section C
1.5	04/08/2019	Olivier Maloberti	Section D
1.6	05/08/2019	Olivier Maloberti	Final Version, submission on 05/08/2018 (Initial deliverable with updates of sections C and D)
1.7	30/04/2021	Olivier Maloberti	Section E

Table des Matières

A) Bibliography – State of the Art 14
I. Scalar magnetic models, taking the magnetic structure into account: 14
II. Scribing, domains refinement and models of magnetic structures 19
B) First Modelling of the Magnetic Behaviour: 26
C) First modelling of the Surface Magnetic Structure – Surface magnetic model 1 34
I. Context and brief summary of the state of the art for the laser irradiation refinement process 34
II. Soft magnetic materials and the laser scribing or irradiation process 36
III. Energy contributions and magnetic properties involved 43
IV. First test case and modelling 49
V. Sensitivity analysis with constraints 54
D) First modelling of the Volume Magnetic Structure – Tensor Magnetic Phase theory 65
I. Context and brief summary of the state of the art 65
II. Tensor State Variable 65
III. Quasi-Static Energy tendencies 68
IV. Formulation 70
V. Static and dynamic Magnetization 72
VI. Computation and theoretical results – test cases 74
VII. Partial conclusions, critics and forthcomings 85
E) Tensor Magnetic Phase Formulation and couplings (TMP) – Coupling between the volume and the surface magnetic structure 86
I. State variable 86
II. Governing Equations 86
III. Bulk and Boundary conditions 86
IV. Coupling formulations: *TMP(MF) couplings* 87
V. Observables 88
VI. Result: 2D test case with GO material 89
VII. FORTHCOMING 91
Bibliography 92

List of Figures :

Figure 1: Variation of excess losses for Λ = 0, 75, 112, 150 and180 µm as a function of the frequency [17] 19

Figure 2: The domains structure of 3% Si-Fe single sheet before and after laser treatment observed by SEM) [23] 19

Figure 3: Dependence of the core reduction on (a) continuous and (b) pulse laser beam power and distance between the scribing lines [24]..... 20

Figure 4: MFM visualization of magnetic domains shows the decreasing of the domain width (a) sample without treatment (b) sample treated using a 0.6 mJ single pulse [28]. 22

Figure 5: Normarski DIC visualization of surface morphology of laser spots created using 50 mJ single pulse energy within the regimes of: (a) single pulse, (b) 100 pulses, (c) 100 modulated pulses [28]. 22

Figure 6: Iron loss depending on B_{max} and the irradiation pitch PL (B_{max} = 0.1 – 1.1 T) [29] 23

Figure 7: The domain structure of investigated GO steel: (a) without laser scribing and (b) after laser treatment by laser beam in continuous mode with power of 24 W. [30] . 24

Figure 8: The ODF sections at φ = 45° represent the sharpness of Goss texture {110}{001} for sample: (a)taken from industrial line after final box annealing and(b) after treatment by laser beam with power of 24 W . [30] 24

Figure 9: Magnetic domain: (a) Without laser (b) Laser direction is TD (c) Laser direction is RD d) laser direction is TD+RD [29] 25

Figure 10: Pry-Bean model of energy loss, sample geometry [33]. 26

Figure 11: Effect of the grain size the different losses components and on the total loss (Pt). 27

Figure 12: Comparison of relative loss change of electrical sheets scribed with different laser intensities [31]..... 28

Figure 13: Anomaly factor η for untreated electrical sheets in comparison with laser scribed sheets treated with different laser intensities [31] 28

Figure 14: Idealized local configuration in plan walls [17]..... 29

Figure 15: Variation of the permeability (abs($\mu app\mu ref$)) in function of the frequency for different wall density. 30

Figure 16: Variation of the permeability (abs($\mu app\mu ref$)) in function of the frequency for different values of electrical conductivity..... 31

Figure 17: Variation of the permeability (abs($\mu app\mu ref$)) in function of the frequency for different values of the sheet thickness..... 31

Figure 18: Power losses (W/kg.$T2$) in function of the frequency for different values of domains wall density. 32

Figure 19: Power losses (W/kg.$T2$) in function of the frequency for different values of sheet thickness 32

Figure 20: Power losses (W/kg.$T2$) in function of the frequency for different values of electrical conductivity. 33

Figure 21: What is a magnetic structure and a magnetic domain? What are the magnetization mechanisms? What is the link between the magnetic hysteresis and the iron losses and the magnetic structure?..... 36

Figure 22: What is a magnetic wall ? Some walls examples (90° and 180° walls). 37

Figure 23: Laser impacts parameters for the three laser processes: irradiation, scribing, ablation. 38

Figure 24: definition of laser patterns parameters (example with lines) and its impact onto the magnetic structure, especially the magnetic walls spacing L. 39

Figure 25: The five types of interaction between grain boundaries and domain walls, shown in order of increasing magnetic pole density at the grain boundary (Tobin and Paul, 1969 [55]). 40

Figure 26: Closure spike-like 180° and 90° domains around defects and grain boundaries [56]. 41

Figure 27: Surface Lancet 180° and 90° closure domains and « tree pattern » of 90° closure domains [57, 58]..... 41

Figure 28: Surface 180° and 90° closure domains due to laser stress induced anisotropy and magnetostriction [59, 60]..... 41

Figure 29: Scheme of the two magnetic poles example with two distributions a*b and A*B of equivalent magnetic charges. 46

Figure 30: Test case with one magnetic domain. 50

Figure 31: magnetic structure and test cases studied 53

Figure 32: Sensitivity analysis of the energy contributions to the walls spacing L and the line spacing d_{DL}. (J = J_s = 2T, $\mathbf{u}_{an}$ = $\mathbf{u}_{DL}$, e = ζ = 0.23 mm, p = 10 μm, $\delta \approx 0$ μm, θ_{DL} = θ_J = θ_W=90°). : walls energy, -- domains energy, – total energy. 55

Figure 33: Sensitivity analysis of the energy contributions to the walls spacing and the lines depth p. (J_s = 2 T, $\mathbf{u}_{an}$ = $\mathbf{u}_{DL}$, e = ζ = 0.23 mm, d_{DL} = 3 mm, δ = 0 μm, θ_{DL} = θ_J = θ_W=90°). : walls energy, -- domains energy, – total energy..... 55

Figure 34: Sensitivity analysis of the energy contributions to the walls spacing and the walls energy. (Js = 2T, uan = uDL, e = ζ = 0.23 mm, dDL = 3 mm, p = 10 μm, $\delta \approx 0$ μm, θDL = θJ = θW=90°). : walls energy, -- domains energy, – total energy. 56

Figure 35: Sensitivity analysis of the energy contributions to the walls spacing and the sheet thickness. (Js = 2T, uan = uDL, dDL = 3 mm, p = 10 μm, $\delta \approx 0$ μm, θDL = θJ = θW=90°). : walls energy, -- domains energy, – total energy..... 56

Figure 36: Sensitivity analysis of the energy contributions to the walls spacing and the global residual stress along the rolling direction. (J_s = 2T, $\mathbf{u}_{an}$ = $\mathbf{u}_{DL}$, e = ζ = 0.23 mm, d_{DL} = 3 mm, p = 10 μm, $\delta \approx 0$ μm, θ_{DL} = θ_J = θ_W=90°). : walls energy, -- domains energy, – total energy..... 58

Figure 37: Sensitivity analysis of the energy contributions to the walls spacing and the global residual stress transverse to the rolling direction. (J_s = 2T, $\mathbf{u}_{an}$ = $\mathbf{u}_{DL}$, e = ζ = 0.23 mm, d_{DL} = 3 mm, p = 10 μm, $\delta \approx 0$ μm, θ_{DL} = θ_J = θ_W=90°). : walls energy, -- domains energy, – total energy..... 58

Figure 38: Sensitivity analysis of the energy contributions to the walls spacing L and the line spacing d_{DL}. (J = J_s = 2T, $\mathbf{u}_{an}$ = $\mathbf{u}_{DL}$, e = ζ = 0.23 mm, p' = 100 μm, $\delta \approx 0$ μm, θ_{DL} = θ_J = θ_W=90°). : walls energy, -- domains energy, – total energy..... 59

Figure 39: Sensitivity analysis of the energy contributions to the walls spacing and the HAZ depth p'. (J_s = 2T, $\mathbf{u}_{an}$ = $\mathbf{u}_{DL}$, e = ζ = 0.23 mm,d_{DL} = 3 mm, δ = 0 μm, θ_{DL} = θ_J = θ_W=90°). : walls energy, -- domains energy, – total energy..... 59

Figure 40: Sensitivity analysis of the energy contributions to the walls spacing and the walls energy. (J_s = 2T, $\mathbf{u}_{an}$ = $\mathbf{u}_{DL}$, e = ζ = 0.23 mm, d_{DL} = 3 mm, p' = 100 μm, $\delta \approx 0$ μm, θ_{DL} = θ_J = θ_W=90°). : walls energy, -- domains energy, – total energy..... 60

Figure 41: Sensitivity analysis of the energy contributions to the walls spacing and the sheet thickness. (J_s = 2T, $\mathbf{u}_{an} = \mathbf{u}_{DL}$, d_{DL} = 3 mm, p' = 100 μm, $\delta \approx 0$ μm, $\theta_{DL} = \theta_J = \theta_W$=90°). : walls energy, -- domains energy, – total energy. 60

Figure 42: Sensitivity analysis of the energy contributions to the walls spacing and the global residual stress along the rolling direction. (J_s = 2T, $\mathbf{u}_{an} = \mathbf{u}_{DL}$, e = ζ = 0.23 mm, d_{DL} = 3 mm, p' = 100 μm, $\delta \approx 0$ μm, $\theta_{DL} = \theta_J = \theta_W$=90°). : walls energy, -- domains energy, – total energy..... 61

Figure 43: Sensitivity analysis of the energy contributions to the walls spacing and the global residual stress transverse to the rolling direction. (J_s = 2T, $\mathbf{u}_{an} = \mathbf{u}_{DL}$, e = ζ = 0.23 mm, d_{DL} = 3 mm, p' = 100 μm, $\delta \approx 0$ μm, $\theta_{DL} = \theta_J = \theta_W$=90°). : walls energy, -- domains energy, – total energy..... 62

Figure 44: Sensitivity analysis of the energy contributions to the walls spacing and the local residual stress along the rolling direction. (J_s = 2T, $\mathbf{u}_{an} = \mathbf{u}_{DL}$, e = ζ = 0.23 mm, d_{DL} = 3 mm, p' = 100 μm, $\delta \approx 0$ μm, $\theta_{DL} = \theta_J = \theta_W$=90°). : walls energy, -- domains energy, – total energy..... 62

Figure 45: Sensitivity analysis of the energy contributions to the walls spacing and the local residual stress transverse to the rolling direction. (J_s = 2T, $\mathbf{u}_{an} = \mathbf{u}_{DL}$, e = ζ = 0.23 mm, d_{DL} = 3 mm, p' = 100 μm, $\delta \approx 0$ μm, $\theta_{DL} = \theta_J = \theta_W$=90°). : walls energy, -- domains energy, – total energy..... 63

Figure 46: Some heterogeneity and non-uniformity effects. Re-orientation, multiplication and refinement within the microscopic magnetic structure [3-5]. Surface, bulk and non-closure domains examples as a function of the texture, i.e. the crystal axes [m,n,p] and the crystal planes (j,k,l). 66

Figure 47: Calculation of the tensor [V^2] in GO steels with the Finite Element Method (left) and analytical formulae given above (right) with κ_s=0 and τ=0. 76

Figure 48: Calculation of the tensor [V^2] in NGO steels with the Finite Element Method (left) and analytical formulae given above (right) with κ_s=0 and τ=0. 77

Figure 49: Sensitivity analysis of the GO magnetic structure to the macroscopic magneto-crystalline anisotropy (a), the stress induced anisotropy (b), the surface magnetic structure (c) and the eddy currents time delay (d). 78

Figure 50: Relative sensitivity analysis of quasi-static apparent permeability to the magneto-crystalline κ_{an} and stress induced κ_s anisotropies ((a) $\sigma_{11} = \sigma_{22}$ (b) $\sigma_{11} = -\sigma_{22}$).79

Figure 51: Relative sensitivity analysis of quasi-static losses to the coercive reluctivity ν_c and the stress induced κ_s anisotropy with κ_{an} = 100 ((a) $\sigma_{11} = \sigma_{22}$ (b) $\sigma_{11} = -\sigma_{22}$)..... 80

Figure 52: Sensitivity analysis of dynamic apparent permeability to the surface magnetic structure ((a) magnitude and (b) phase) and to the damping time delay ((c) magnitude and (d) phase angle) 81

Figure 53: Sensitivity analysis of total dynamic losses to the surface magnetic structure (a) , to the eddy currents time delay (b) and to the stress anisotropy ((c) and (d)). 82

Figure 54: 2D results on [Λ] aspects for a GO steel with FEM (Finite Element Method).. 83

Figure 55: 2D results on [Λ] aspects for a NGO steel with FEM (Finite Element Method). 84

Figure 56: definition oft he 2D problem to be solved with the TMP formulation. 89

Figure 57: TMP variable for a GOES as a function of the two coordinates in the cross section. 89

Figure 58: TMP variable profile within the sheet thickness as a function space and of frequency..... 90

Figure 59: solution for the total eddy currents that damp the field and generate the losses comparing with the classical formulations. 90

A) Bibliography – State of the Art

Reducing energy losses of electrical machines is a real need in the industrial world to maintain more efficiency and financial economics. These electrical machines mostly incorporate soft magnetic materials used as flux multipliers. Hence any reduction in iron losses of these soft magnetic materials leads to saving the energy in electrical machines. Nowadays, research on soft magnetic materials form an important issue with their different classes, properties and structures. Among these classes, grain-oriented silicon steel achieves a low core losses and high permeability very useful in some electrical machines especially in transformers. The morphology of the magnetic domains is related to the beneficial effects on permeability and coercivity produced by grain-oriented silicon steels [1] . Therefore, we will focus our study on the refinement of magnetic domains by a scribing laser under suitable conditions to reduce iron losses in grain-oriented silicon steel and trying to understand the relationship between magnetic structures of these oriented grains, unidirectional magnetization mechanisms and performance within a closed magnetic circuit.

I. Scalar magnetic models, taking the magnetic structure into account:

For a logical study of the iron losses in grain-oriented silicon steel it is necessary to understand each model of hysteresis and losses predictions. We will focus on the parameters used in each model to relate it with the magnetic structures on the one hand. Also, we will study the relationship between these magnetic structures and conditions of laser-scribing on the other hand, to optimize parameters of the laser scribing process in a way to control the parameters of magnetic structure responsible for the iron losses.

1. Models for prediction of losses:

Steinmetz's Model:

Steinmetz [2] considered the core loss as a result of two components: hysteresis loss and eddy current loss. The total loss is given by an empirical formula:

$$P_{tot} = K_h \,.f.\, B^{\mathrm{n}} \;+\; K_e \,.\, f^2.\, B^2 \qquad \text{(A.1)}$$

where n is the Steinmetz hysteresis loss flux density exponent dependent on the type of material, K_h is the hysteresis coefficient experimentally calculated and K_e is the eddy current loss coefficient proportional to the electrical conductivity σ and the lamination thickness d by the following relationship:

$$K_e = \frac{d^2\,\pi^2\sigma}{6} \qquad \text{(A.2)}$$

This model was limited because it only treats sinusoidal flux waveforms. Later on, many improvements were suggested for the Steinmetz model to overcome different limitations [3] [4] [5]. For several years the Steinmetz's equation has been used for the prediction of iron losses but the equations do not take into account the domain's parameters within the plate, so it will not help us to provide a relationship between the parameters on the macroscale and the magnetic structure.

Bertotti's Model:

Bertotti [6] proposed a model of iron losses, which is widely used nowadays, based on the separation of total losses into three categories: hysteresis losses (static losses), eddy currents losses (classical losses) and excess losses as follows:

$$P = P^{(hyst)} + P^{(class)} + P^{(exc)} = k_{hyst}\, f\, B_m^{\delta} + k_{class}\, f^2\, B_m^2 + k_{exc}\, f^{\beta}\, B_m^{\alpha} \qquad \text{(A.3)}$$

The identification of the hysteresis parameter k_{hyst} and the exponent of the magnetic flux density δ are carried out by DC measurements (Epstein frame). The eddy current parameter k_{class} is identified by the material properties known from the manufacturer's

material sheet and the parameter of excess losses k_{exc} is determined from measurements at very low frequency using the same configuration as for k_{hyst}. He developed a statistical model for interpretation of the eddy current losses [7]; he called Magnetic Objects (MO), the characteristic group of active walls clustered by the effect of the internal wall-to-wall correlation fields, so he considers the domain structure as $\tilde{n}$ statistical independent magnetic object and for grain oriented silicon steel, as our case, a single Bloch wall can be considered as a MO.

Furthermore, Bertotti obtained that the excess power loss $P^{(exc)}$ for most soft magnetic materials (linear material behavior) can be described by the following equation:

$$P^{(exc)} = 8\,(fB_m)^{1.5}\left(\sqrt{\sigma G^{(w)} S H_0}\right) \quad \text{(A.4)}$$

where S is the cross-sectional area of the material, *G* is the damping effect of the eddy current pattern which surrounds the wall, H_0describes the direct pinning effect of lattice defects and σ the conductivity. This model is important because it includes some parameters of the microstructure in the equation to predict the dynamic losses.

Inspired by the model of Bertotti for prediction of losses, some researches tried to figure out the influence of domain width on energy losses in soft magnetic materials [8].

Starting from the equation of dependency of energy losses on magnetic induction and magnetic field frequency in a magnetic material:

$$P = \alpha\,.B^{\beta}\,.f^{\gamma}.\varepsilon' \quad \text{(A.5)}$$

where α, β and γ are deterministic parameters and ε' is a random error. They noticed that as the intensity of the field increases, the width of domains perpendicular to the field decreases, while of those orientated along the field increases. Considering this fact, the domain width D (expressed by the ratio of widths of domains, whose magnetic moment is directed along the field vector, to total sample width D_0) was chosen as the feature characterizing them. They was based on a non-standard statistical analysis of experimental data concerning energy losses in a Metglas 2605 TCA ribbon to express the domain width expected value *E(D|f,B)* as a function of the magnetic induction and the frequency by the following expression:

$$E(D|f,B) = (1.632 + 0.939\,.\,B + 0.664\,.\,B^2)\,.f^{-0.5} \quad \text{(A.6)}$$

Thus, to link energy loss with domain they gave the expressions below for the coefficients α, β and γ depending on domain width expected value *E(D)* and the standard deviation of domain width σ *(D)(* the change of domain width at specified, fixed values of B and f*)* by a nonlinear regression method:

$$\alpha = a + b.[E(D)]^{d} + c.[\sigma(D)]^{e} \quad \text{(A.6a)}$$

$$\beta = l + m.[E(D)]^{p} + n.[\sigma(D)]^{q} \quad \text{(A.6b)}$$

$$\gamma = r + s.[E(D)]^{v} + t.[\sigma(D)]^{w} \quad \text{(A.6c)}$$

where a, b, c, d, e, l, m, p, q, r, s, t, v and w are reel numbers to be determined.

To obtain the following relationship for each parameter:

$$\alpha\,(E(D),\sigma(D)) = 4.67 * 10^{-5} - 1.711 * 10^{-4}.E(D) + 4.088 * 10^{-3}.\,\sigma(D) \quad \text{(A.7)}$$

$$\beta\,(E(D),\sigma(D)) = 2.54 - 2.5 * \sqrt{E(D)} + 0.019\,.\,\frac{1}{\sqrt{\sigma(D)}} \quad \text{(A.8)}$$

$$\gamma(E(D),\sigma(D)) = 3.278 - 2.557 * (\sigma(D))^{0.1} \quad \text{(A.9)}$$

So, they became able to predict the value of the loss based on these three parameters.

2. Model of static hysteresis:

Jiles-Atherton's Model:

The Jiles-Atherton's model [9] is a static hysteresis model based on the physical behavior of magnetic materials, in particular on the energetic considerations in connection with the displacement and deformation of the Bloch walls. The total magnetization considered as two contributions: reversible component M_{rev} due to domain wall bending and the irreversible component M_{irr} due to wall displacement.

$$M = M_{rev} + M_{irr} \tag{A.10}$$

The reversible magnetization can be written as function of the anhysteretic magnetization M_{anh} by the expression:

$$M_{rev} = c\,(M_{anh} - M_{irr}) \tag{A.11}$$

$$M_{anh}\,(H_e) = M_s\,.\boldsymbol{L}\left(\frac{H_e}{a}\right) \tag{A.12}$$

with M_s the saturation magnetization, H_e the effective field: $H_e = H + \alpha M_{anh}$ and $\boldsymbol{L}\left(\frac{H_e}{a}\right)$ the Langevin equation. The variation of the irreversible magnetization is then given by the following equation:

$$\frac{dM_{irr}}{dH_e} = \frac{(M_{anh} - M_{irr})}{k\delta} \tag{A.13}$$

with δ a coefficient of value +1/-1 depending on the evolution of the field. Finally, the variation of the total magnetization is given by the following differential equation:

$$\frac{dM}{dH} = \frac{(1-c)\frac{dM_{irr}}{dH_e} + c\frac{dM_{anh}}{dH_e}}{1-\alpha c\frac{dM_{anh}}{dH_e} - \alpha(1-c)\frac{dM_{irr}}{dH_e}} \tag{A.14}$$

To use this hysteresis model, 5 parameters, with some that are directly related to the microstructure, should be determined:

***α*:** mean field parameter representing interdomain coupling, affect the remanence magnetization, ***M_s*:** saturation magnetization of the material, ***a*:** parameter related to the temperature: a = $\frac{k_B T}{M_s \mu_0}$, affect the shape of the loop, ***c*:** coefficient representing the rate of domain wall bending, affect the initial magnetization, ***k*:** parameter representing the "quasi-static" mobility of the walls (related to the number of pinning sites), affect the width of the loop (coercive field and the remanence magnetization)

The coercivity is determined by the amount of pinning, and hence by the parameter *k*. For this reason, the definition of this pinning parameter in units of A.m^{-1} is preferred since the pinning force acts like a field opposing the prevailing magnetic field H.

Jiles suggested a numerical method [10] for the determination of these parameters calculated from experimental measurements of the coercivity, remanence, saturation magnetization, initial anhysteretic susceptibility, initial normal susceptibility, and the maximum differential susceptibility.

Researchers tried to figure out the influence of microstructure on the parameters of the Jiles-Atherton's model, they observed that a modification of the grain size (ϕ) or the dislocation density (ζ_d)corresponds to a variation of parameters *k* and *a*. The latter must vary both linearly with $\frac{1}{\phi}$ and must both be proportional to $\sqrt{\zeta_d}$, the remaining parameters M_s, $c_j$and α_j must remain constant.

The reason for assuming the parameter *k* as a parameter depending on grain size and dislocation density is that *k* is proportional to the coercivity H_c, and the coercivity predominantly depends on the grain size and the dislocations density. Also for the parameter *a* the dependence is that the parameter *a* should be a constant of the material dependent in part on the microstructure [11]. It should be proportional to the domain density in the demagnetized state and the domain density in the demagnetized state should

be proportional to the pinning site density, which, in turn, is proportional to *k*. This dependence is given by the following equations [12]:

$$k_j = k_{j0}(G_1 + \frac{G_2}{\phi})\sqrt{\zeta_d}) \quad \text{(A.15)}$$

$$a_j = a_{j0}(G_1 + \frac{G_2}{\phi})\sqrt{\zeta_d}\ ) \quad \text{(A.16)}$$

were G_1 and G_2 are constants.

Furthermore, Szczyglowski developed a dynamic extension of Jiles-Atherton [13]; he considered a field component H_d added to the effective field caused by eddy current reactions. The magnetic field of the reaction is calculated from the equation:

$$\overrightarrow{rot}\,\overrightarrow{rot}\,H_d = -\,\sigma\,\frac{\partial B}{\partial t} \quad \text{(A.17)}$$

where *σ* is the material conductivity and *B* is the magnetic induction.

3. Models of dynamic hysteresis:

Loss Surface Model (LS):

The LS's model comes from the work of Chevalier and Kedous-Lebouc [14] , it is a dynamic behavior based on the knowledge of a surface response determined by a large number of measures; it is based on three parameters to represent the magnetic behavior of the sheet: the peak induction, the instantaneous value of the induction and its rate of evolution over time. The measures allow us to build or draw a surface *H(B, B_m, dB/dt)* under triangular induction with different magnitudes, knowing the couples *(B, dB/dt)* it is possible to draw the cycle *B(H).* The next step was a deep analysis of the dynamic phenomena that gives a physical interpretation for the expression of the dynamic magnetic field's variation, the hysteresis cycle is therefore reconstructed by distinguishing a static contribution and a dynamic contribution of the magnetic field as shown in the expression:

$$H(B,\frac{dB}{dt}) = H_{stat}(B,historical) + H_{dyn}(B,\frac{dB}{dt}) \quad \text{(A.18)}$$

where H_{dyn} is an analytical function, approached by portions of polynomials, dependent on $\frac{dB}{dt}$ and *B*, then the iron loss is obtained by a simple integral on the volume region:

$$\int_v H\,dB \quad \text{(A.19)}$$

The comparison between computed hysteresis loops and measured loops gives a good matching. Also, for his importance this model has been implemented in the FLUX 2D/3D post-processing code of finite elements calculation for few types of ferromagnetic materials. However, the differentiation in the dynamic contribution between classical losses caused by macroscopic induction currents and excess losses allocated in the microscopic local induced currents generated by the magnetic domain structure of the material and the displacements of the walls of Bloch is not made.

In the dynamic LS's model, the coefficients of the polynomial function used for the dynamic magnetic field are not easily and physically connected to the microscopic magnetic structure. Some microscopic parameters, such as the grain size, the thickness of the sheet and the domain's size, are very important parameters because they are to be related with the laser-scribing parameters to control the microstructure.

Raulet-Masson's Model:

Raulet and Masson [15] suggested a behavioral model of dynamic properties for magnetic materials called the Dynamic Static Feedback model (DSF model), they introduce a dynamic parameter *γ* related, on the one hand, to the geometry of the sheet and, on the other hand, to the conductive dynamic properties of the magnetic material. The dynamic field is expressed by the equation:

$$H_{dyn} = H_{stat}(B_m) + \gamma.\frac{dB_m}{dt} \quad \text{(A.20)}$$

Afterwards, Raulet improved a model for magnetic diffusion DWM "Diffusion & Wall Motion" [16]. The idea of the DWM model is to replace the static characteristic of the material in the classical magnetic diffusion model by a dynamic characteristic which accounts for the dynamic effects created during walls motion, the magnetic field expression is similar to DSF model but the dynamic parameter β of DWM model is related to the structure of magnetic domains and to walls motion. The dynamic material law is given by the following equation:

$$\frac{\partial B(y,t)}{\partial t} = \frac{1}{\beta}\left[H(y,t) - H_{stat}(B(y,t))\right] \quad \text{(A.21)}$$

where the dynamic parameter β is identified with only one dynamic B(H) characteristic performed in any experimental conditions. Therefore, this material law represents a statistical behavior of the movement of the wall and considers it as isotropic and intrinsic to the material.

Lambda Model:

In his thesis [17], O. Maloberti developed a dynamic hysteresis model in which he supposed that the magnetic structure of the material is due to the superposition of two main mechanisms: the Domain Walls Displacement (DWD) and the Domain Moments Rotation (DMR). The model is called "Lambda Model'' where Lambda (Λ) is the structural dynamic property summarizing the components of the magnetic structure (S_ω , v_ω , η_ω , n_{ω_i} , γ_ω):

S_ω : Wall surface

v_ω: Wall velocity

η_ω: Wall mobility

n_ω : Volume density of walls

γ_ω : Surface energy of walls

After some physical analysis, it is possible de lump the whole microscopic magnetization reversal processes in one dynamic magnetization property Λ. This parameter was introduced in the expression of the magnetic field, a dynamic contribution dependent on Λ added to the static field [18]:

$$H = H_s + \sigma\, \Lambda^2 \partial_t B \quad \text{(A.22)}$$

$$\Lambda = \sqrt{\frac{1}{2\sigma\vartheta J_s n_\omega m_\omega S_\omega}} \quad \text{(A.23)}$$

where J_s is the saturation magnetic polarization, ϑ is a number between 0 and 1 (depending on the polarization direction inside domains), and m_ω the average walls mobility.

To relate this dynamic parameter with the macroscale, the Figure 1 shows the variation of excess losses as a function of the frequency for different values of Λ, it is remarkable that for high frequencies, excess losses increase as a function of the structural dynamic parameter. To relate this model with our goal, we will try to study the effect of the laser-scribing on the factor Λ, which can lead us to decrease this factor in order to decrease the excess losses. We also have to study the effect of this factor on the other loss components (hysteresis and eddy current) knowing that the static hysteresis losses might increase under the effect of the laser-scribing [19].

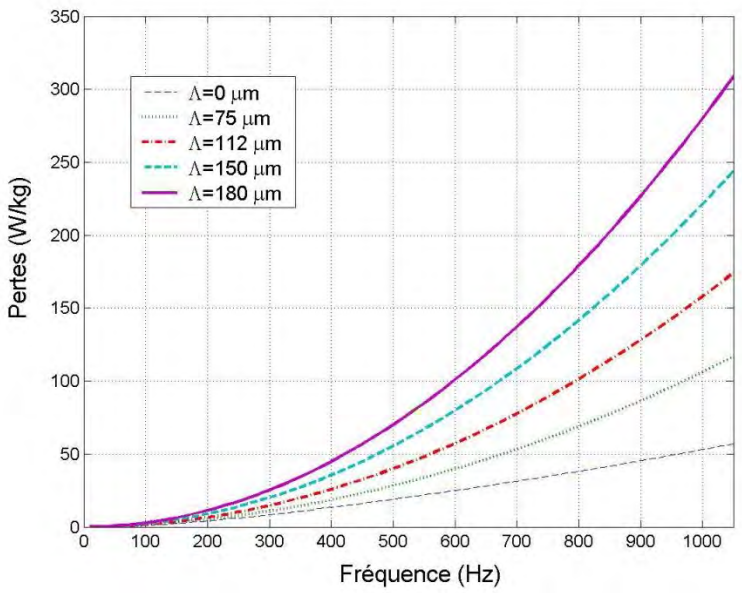

Figure 1: Variation of excess losses for Λ = 0, 75, 112, 150 and180 μm as a function of the frequency [17]

II. Scribing, domains refinement and models of magnetic structures

Grain-oriented steels are formed of large grain size that leads to large magnetic domains. These domains produce losses resulting from the movement of domain walls under the action of the alternative applied field. So, the refinement of domains minimizes the rate of walls motion and then less energy is lost. The first studies on domains refinement were realized by a mechanical scratching method to reduce energy losses of steels. Therefore, researchers have sought to save energy, so they studied different domain refinement techniques (mechanical scratching [20], plasma irradiation [21], spark ablation [22]and laser-scribing) to visualize their influence on energy losses.

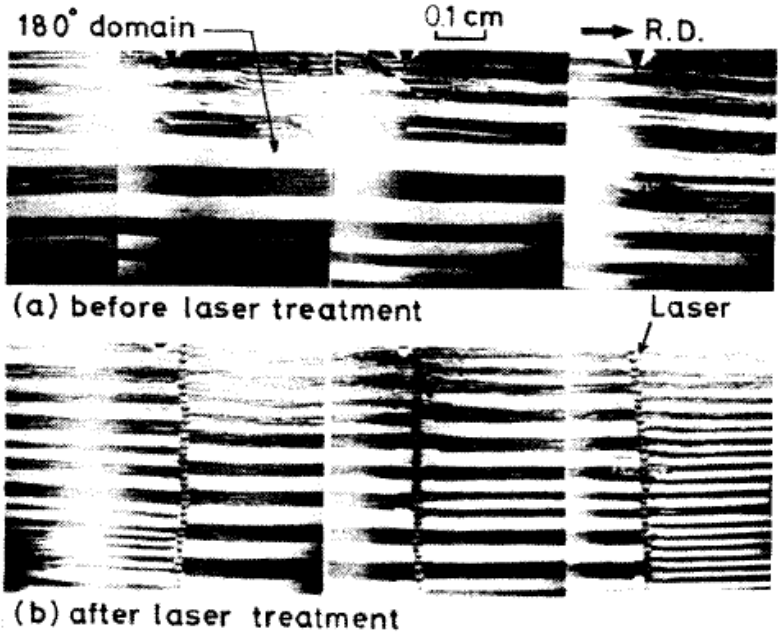

Figure 2: The domains structure of 3% Si-Fe single sheet before and after laser treatment observed by SEM) [23] .

Among these techniques, the laser-scribing is an elegant non-contact method of refinement that shows good results for 180° domain refinement then for reducing the core loss. In 1981, Luchi et al. [8], found a reduction more than 10% in core losses of commercial high permeability grain-oriented silicon steel (3% Si-Fe single sheet) at low frequency. The sheet was treated under optimum conditions of a Q-switched Nd:YAG laser, also the SEM imaging showed a change in the domains structures, in the Figure 2 the domains refinement is clearly visible.

For the sake of selecting the appropriate laser parameters to attain the minimum of core losses, we then expose the different effects of the variation of laser parameters on magnetic structure and losses based on the recent results of researchers.

4. Laser's pulse mode:

Petryshynets et al. [24] showed an improvement of 16% (maximum value) for a grain-oriented Fe-3%Si steel (sheet of 30mm width, 80mm length and 0,28mm thickness) scribed by a fiber laser in pulse regime while the continuous regime gives a better improvement (38% maximum value) for the same scribe lines distances (for line distance 4 mm, Figure 3*).* Noting that the power density of the laser beam in case of continuous regime was in the range from 12W up to 30W with step of 6W, the laser beam spot size was 30µm and the scribing velocity was 100mm/s. For the pulse mode, the input power of laser beam varied from 30 W to 240 W with a pulse duration of 100µs and 100Hz repetition rate. The distance between the neighboring pulses was ΔL=0,3mm.

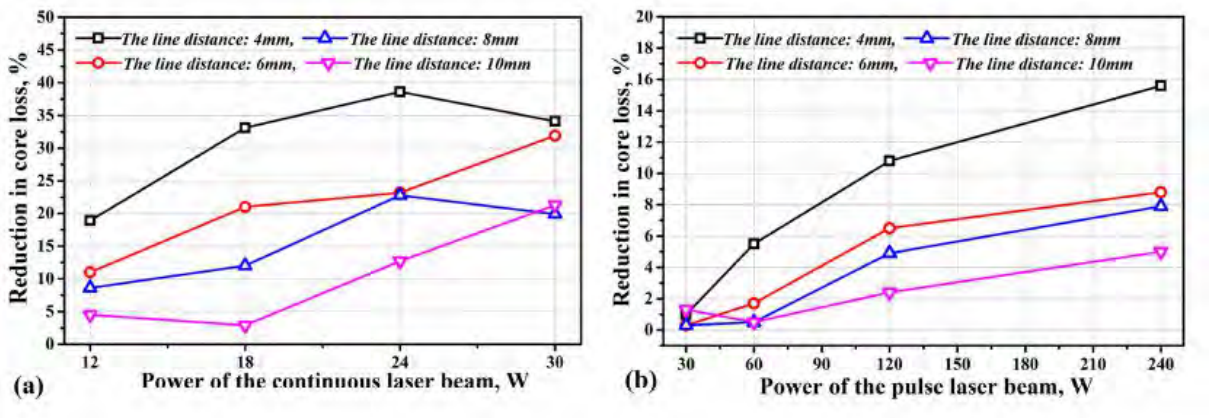

Figure 3: Dependence of the core reduction on (a) continuous and (b) pulse laser beam power and distance between the scribing lines [24].

In a comparison between the use of a continuous CO_2 laser and the use of a pulsed fiber laser for scribing grain oriented electrical steel (sheet dimensions 300mm x 30mm x 0.3mm) *Rauscher et al.* [25] found the reduction in core loss for the sample treated by the pulsed fiber laser (14.5% mean value) higher than for that treated by the continuous CO_2 laser (12.5% mean value) at the same line distances. Using a Nd-YAG laser set to Q-mode, *Huang et al.* [26] verified a reduction rate of 13.12% in core loss for grain-oriented silicon steel (30Q130, thickness 0.3mm) for optimized laser conditions (combination of pulse energy of 2.52 mJ, small point spacing of 0.22 mm, and small scribing spacing of 3.03 mm).

Therefore, *Ponnaluri et al.* [27] demonstrated that the use of an excimer laser scribing process gives beneficial effects in reducing core loss more than the use of Nd-YAG or CO_2 lasers. They were able to achieve a maximum core loss reduction of 26% for a grain-oriented silicon steel (M-4 of thickness 0.3mm) scribed by the excimer laser (energy = 64 mJ, repetition rate =50 Hz, spot size =1.2mmx0.7mm). However, the use of an excimer laser is not favorable due to his multimode aspect also the profile and the beam energy of this type of lasers are usually inhomogeneous, so it makes it hard to get a laser beam

correctly focused.

5. Pulse Energy and Energy rate:

Luchi et al. [23] studied the optimum value of pulse energy of their irradiation laser for better reduction in core loss. So, they figure out an experimental relation between the energy of the pulse and the reduction of core loss by the expression:

$$\Delta W = \frac{c_1 u}{1+c_2 u} - c_3 u \qquad \text{(A.24)}$$

where c_1, c_2 and c_3 are constants, ΔW is the reduction of core loss and u the energy irradiated on the unit area of specimen. The optimum condition of u was between 0.2 and 0.3 J/cm^2 for a reduction in core loss more than 10%. By comparing two laser beam source for the scribing of a grain oriented electrical steel (sheet dimensions 300mm x 30mm x 0.3mm), Rauscher et al. [25] found a slight improvement (3%) of core loss at low laser energy (*E<4 J/m*) as well as at high energy (*E>50 J/m*) for both CO_2 laser and fiber laser source. Therefore, the core loss was reduced by 12.5% (mean value) for the sheet treated by the CO_2 laser and 14.5% (mean value) for the other within the optimal energy E (*5 J/m<E<45 J/m)*. A maximum value of reduction in core loss was attain for an energy *E=13 J/m* and *E= 9 J/m* respectively for the CO_2 laser and the fiber laser.

Huang et al. [26] showed an increasing in the reduction rate of core loss (sheet thickness 0.3 mm) with the increasing of pulse energy and they achieved a maximum reduction rate of 13.12% for a value of pulse energy of 2.52 mJ (at optimum conditions of an Nd-YAG laser Q-mode: 0.22mm point spacing and 3.03 mm scribing spacing).

A newly research done by Puchy et al. [28] on a sample of Fe-3.2Si grain-oriented electrical steel (the samples with dimensions of 30mmx10mmx0.35mm) treated by a fiber laser irradiation with a wavelength of 1064 nm where the scan direction was oriented perpendicularly to the rolling direction shows the effects of the laser-scribing on the microscale (magnetic domain width) and on the macroscale (coercivity) of the sample magnetic structure. In the process of laser-scribing, they used different number of pulses (1, 5, 10, 50 and 100 pulses) and for each number of pulses they varied the single pulse energy. They showed that the increase of the single energy pulse for the same number of pulses increase the magnetic domain width as well as for the coercivity. So, the lowest pulse energy used (0.6 mJ) was the optimum energy for decreasing the magnetic domain width (Figure 4) and coercivity then for decreasing the core loss. Also, they examined the effect of increasing the number of pulses on the sample for the same single pulse energy, for a single pulse a shown in the Figure 5 the surface ablation is negligible while for 100 pulses and for 100 modulated pulses laser regime a significant surface ablation occurs. For a macroscale interpretation, for the same single pulse energy the coercivity decrease by increasing the pulse numbers from single pulse to 5 pulses for an optimum value of 0.035 A/cm at single pulse energy of 0.6mJ (coercivity before laser-scribing was 0.057 A/cm), but then the increasing of the pulse numbers increases the coercivity (as shown in the Table 1).

Pulse number / Single pulse energy	1	5	10	50	100	100* (modulated)
0.6 mJ	0.039	0.035	0.037	0.038	0.055	0.05
5 mJ	0.062	0.065	0.064	0.070	0.084	0.08
50 mJ	0.080	0.070	0.069	0.069	>0.3	0.12

Table 1: The value of coercivity (in A/cm) for samples scribed with different laser conditions [28].

Pulse number / Single pulse energy	1	5	10	50	100	100* (modulated)
0.6 mJ	16±2.1	15±2.0	15±1.9	16±2.5	23±2.9	29±3.1
5 mJ	39±3.8	41±3.9	40±3.7	43±4.3	38±3.6	52±6.5
50 mJ	50±5.5	43±4.3	42±4.2	43±4.7	120±9.1	75±8.1

Table 2: The value of magnetic domain width (in μm) for samples scribed with different laser conditions [28].

In like manner, a microscale interpretation the magnetic domain width decreases by increasing the number of pulses to 5 pulses and 10 pulses for an optimum value of 15±1.9 μm at single pulse energy of 0.6mJ (magnetic domain width before laser-scribing was 45±4.2 μm), but when they increased the number of pulses the decrease in domain width becomes less significant (as shown in the Table 2).

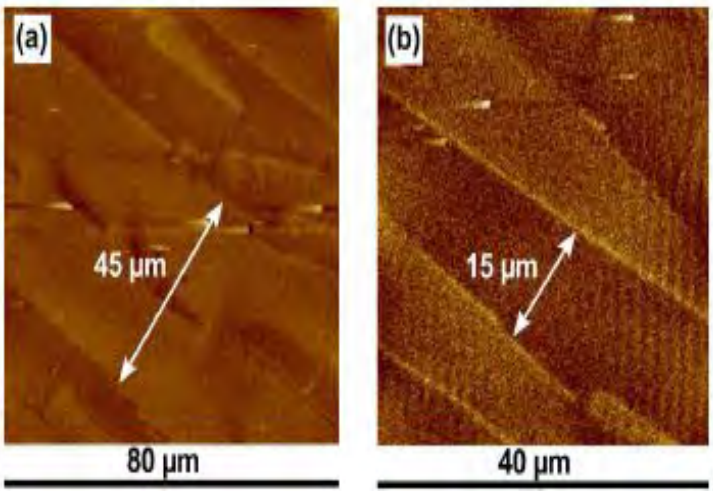

Figure 4: MFM visualization of magnetic domains shows the decreasing of the domain width (a) sample without treatment (b) sample treated using a 0.6 mJ single pulse [28].

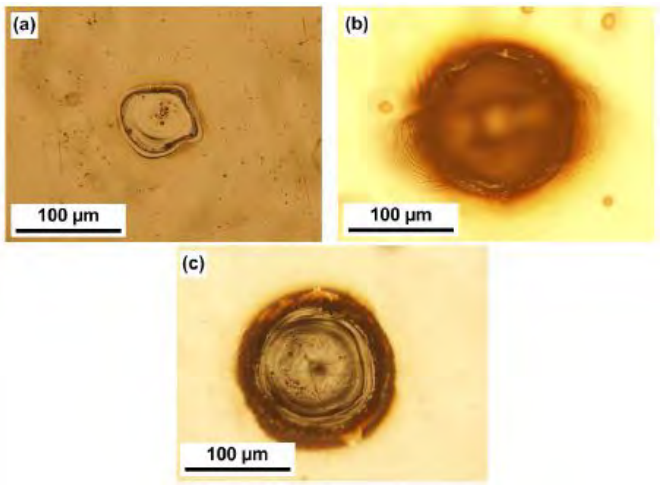

Figure 5: Normarski DIC visualization of surface morphology of laser spots created using 50 mJ single pulse energy within the regimes of: (a) single pulse, (b) 100 pulses, (c) 100 modulated pulses [28].

6. Scribing spacing:

Beside their study on the influence of pulse energy, Huang et al. [26] examined the suitable value of the scribing spacing of the Nd-YAG laser process for a maximum reduction in core loss of a grain-oriented silicon steel (30Q130 sheet thickness 0.3 mm). They found that increasing of the scribing spacing leads to more core loss and they selected scribing spacing of 3.03 mm (pulse energy of 2.52 mJ and point spacing of 0.22 mm) as an optimum value for the reduction of core loss 13.12%.

Using a laser irradiation system, Kajiwara and Enokizono [29] tested the effect of the irradiation pitch on the reduction of the iron loss of oriented electrical steel sheets (thickness 0.35 mm). The results (Figure 6) showed that the rotational iron loss decreased about 30.5% for the sheet irradiated by the laser with an irradiation pitch between 0.25 mm and 0.5 mm.

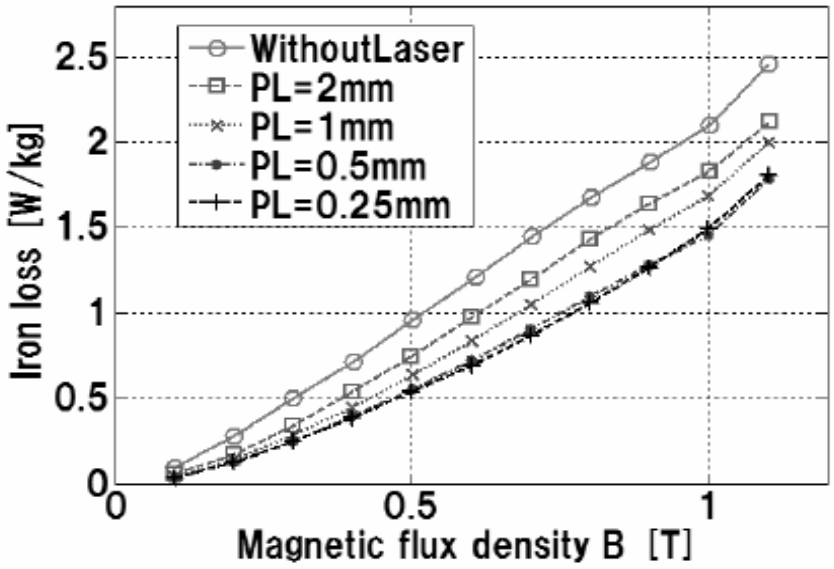

Figure 6: Iron loss depending on B_{max} and the irradiation pitch PL (B_{max} = 0.1 – 1.1 T) [29]

Furthermore, Petryshynets et al. [30] studied the effect of laser-scribing with a fiber laser in continuous mode on magnetic properties of grain-oriented steel. So, they showed a deterioration of coercivity for the sample scribed by the laser with a scribing spacing of 3 mm and that is due to high intensity of thermal stress on the sample. By increasing the scribing spacing the coercivity decrease, the lowest value of coercivity was reached for a scribing spacing of 7.5 mm and laser power beam of 24 W. In the same article, they showed the effect of the laser scribing for these optimal conditions of laser scribing on the refinement of magnetic domains and on the texture of the sample: The Figure 7 shows the formation of complex domain structures in the vicinity of the laser scribed lines and it can be assumed that the degradation of domains walls takes place around the fast-heated zones. On the other hand the sharpness of the Goss texture of the sample showed in figure Figure 8 wasn't significantly affected by the laser-scribing because the laser beam power of 24 W induces a slight variation of substructure parameters on the surface of contact so the texture of the sample after the scribing is still the same.

Figure 7: The domain structure of investigated GO steel: (a) without laser scribing and (b) after laser treatment by laser beam in continuous mode with power of 24 W. [30]

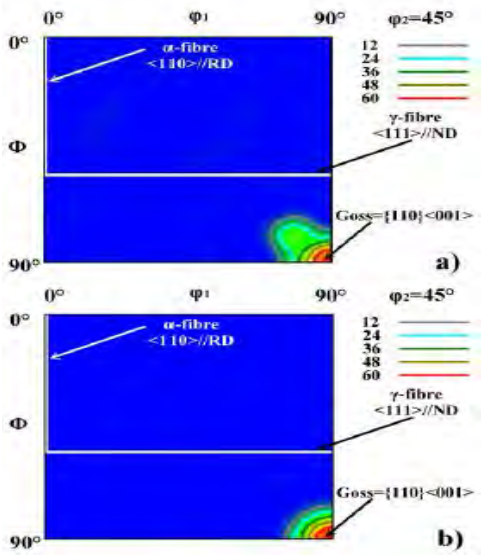

Figure 8: The ODF sections at φ = 45° represent the sharpness of Goss texture {110}{001} for sample: (a)taken from industrial line after final box annealing and(b) after treatment by laser beam with power of 24 W . [30]

But in another article [24], they showed the effect of scribing spacing on core losses: when the scribing distance increase the reduction in core loss decrease and the maximum reduction of core loss achieved was 40% with a laser continuous laser beam of power 24 W for scribing distance 4 mm. Here the challenge is to identify the optimum scribing spacing that decreases the core losses without increasing significantly the coercivity of the sample.

7. Scribing direction:

The scribing of a sample could be realized either in the longitudinal direction it means in the rolling direction of the manufactured sample or in the transversal direction it means perpendicularly to the rolling direction. Ponnaluri et al. [27] examined the effect of each scribing direction of a grain-oriented silicon steel sheet on the reduction of core loss. So, they found that the scribing in the transversal direction improves the core loss much better than in the longitudinal direction.

Also, Kajiwara and Enokizono [29] conclude the same result that the iron loss decreases with using a scribing in the longitudinal direction but this reduction is higher in case of transversal direction. Moreover they tested the effect of the scribing in both directions and they found a better improvement in iron loss up to 12.9%. In the figure below (Figure 9*)* it is clearly visible that the transverse direction (TD) of scribing creates better refinement in domain structures than that in the longitudinal direction (RD).

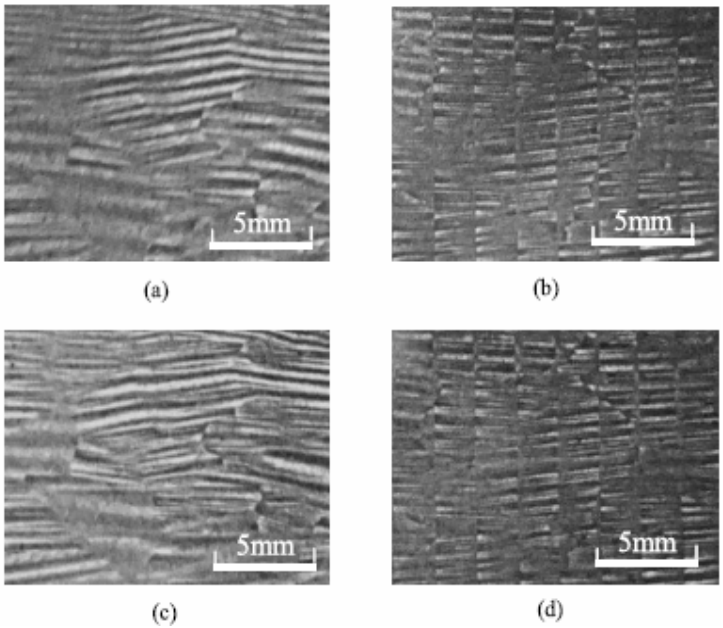

Figure 9: Magnetic domain: (a) Without laser (b) Laser direction is TD (c) Laser direction is RD d) laser direction is TD+RD [29]

In order to investigate the influence of laser scribing on static, dynamic, high and low loss component of laser scribed electrical steel, Weidenfeller and Anhalt [31] proposed a theoretical formula of loss that relates the dynamic losses with the classical losses (eddy currents) with an anomaly factor η dependent on the frequency, the relation is given by:

$$P_{dyn}(f) = \eta\,(f)\,P_{cl}(f) \tag{A.25}$$

The total power loss is the sum of the hysteresis loss, the component independent of the frequency, and the frequency dependent dynamic losses:

$$P\,(f) = P_h + P_{dyn}(f) \tag{A.26}$$

They tested the effect of laser scribing on the behavior of the anomaly factor as a function of the frequency for different intensity of laser beam: for high intensity of laser used for scribing the anomaly factor $\eta(f)$ increases, which increases the dynamic losses generated by domain wall movement. When they reduced the intensity of laser the anomaly factor decreased for the frequency between 1 and 100 Hz but then increase for higher frequency. Also, they showed that the high induction losses which represents the domains wall annihilation-recreation and the rotation of magnetic moments were increased by the laser-scribing while the low induction losses which represents the domain wall mobility was decreased after the laser-scribing at low intensity. So, the reduction of total power losses can be realized when the increase of high induction losses is negligible in front of the decreasing of the low induction losses.

B) First Modelling of the Magnetic Behaviour:

Once we relate the magnetic microstructure and metallurgical structure of the sheet with the macroscale observables on the first hand and the parameters of the laser-scribing with the microstructures on the other hand we become able to control the macroscale observables (iron losses and magnetic permeability) by applying specific laser conditions during the scribing process and also if it possible to suggest specific conditions during the crystallization process.

Therefore, to estimate the influence of the main parameters of the sheet as: thickness, grain size and boundaries, domain size, walls density and mobility and electrical conductivity on the permeability and the core losses; we have selected the Pry and Bean's model [32] as a first simple model. This famous domain model supposes an infinite plane sheet (Figure 10) formed of equal width 180° parallel domains whose magnetization lies in the plane of the sheet whereas their domains walls are perpendicular to it.

Pry and Bean assume also that all domain walls move with the same velocity and they take three boundary conditions: the component of a current density vector normal to the surfaces of the sheet is equal to zero, the component of a current density vector normal to domains walls is continuous on each wall and the difference between tangential component of current density vector across each domain wall is equal to $-2\sigma v_\omega B_s$ where σ is the electrical conductivity, v_ω is the domain wall velocity and B_s is the saturation induction.

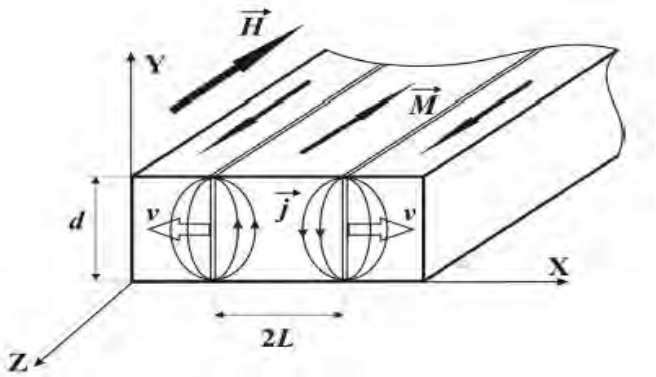

Figure 10: Pry-Bean model of energy loss, sample geometry [33].

A study made by De Campos et al. [34] considers this same model where they found an expression for the optimum grain size to minimize the iron losses.

Considering the total energy as the sum of the magnetostatic energy and of the domain wall energy (γ) per unit volume:

$$E_t = \frac{\beta D \mu_0 M_S^2}{G_S} + \frac{\gamma}{D} \qquad \text{(B.1)}$$

β non-dimensional constant depends on the domain wall configuration [35] .

And by minimizing this energy, they have obtained the domain width (D) in function of grain size G_S:

$$D = \sqrt{\frac{\gamma G_S}{\beta \mu_0 M_S^2}} \qquad \text{(B.2)}$$

Also, they applied loss separation to study the impact of grain size; they considered the total loss as summation of hysteresis loss (P_h), classical loss (P_{cl}) and anomalous loss (P_a). Anomalous loss is related to the classical loss with η the anomalous factor [32]:

$$P_a = (\eta - 1)\ P_{cl} \tag{B.3}$$

$$P_{cl} = \pi^2 \frac{1}{6\rho} e^2 B_{max}^2 f^2 \tag{B.4}$$

with $\eta \backsimeq 1{,}63(D/e)$, e the sheet thickness and ρ the electrical resistivity.

They found that hysteresis loss is inversely proportional to the grain size and the anomalous loss is proportional to the square root of the grain size value, the expressions of losses are as following:

$$P_a = c_1 G_s^{1/2} \frac{1}{\rho} e^2 B_{max}^2 f^{3/2} \tag{B.5}$$

$$P_h = (c_2 + \frac{c_3}{G_s}\ )\ \mathrm{B}_{\mathrm{max}}^{\mathrm{q}}\ f \tag{B.6}$$

c_1, c_2 and c_3 are constants to be experimentally determined.

The dependence of losses on the grain size is shown in the figure below (Figure 11*),* the values of losses are estimated for *e= 0.51 mm, ρ = 20.5 µΩcm, B=1.5 T, f=60 Hz* and for $P_h = 2.52 + 62.5\ (\frac{1}{G_s})$. The optimum value of grain size that gives us the minimum of total loss is between 100µm and 130µm.

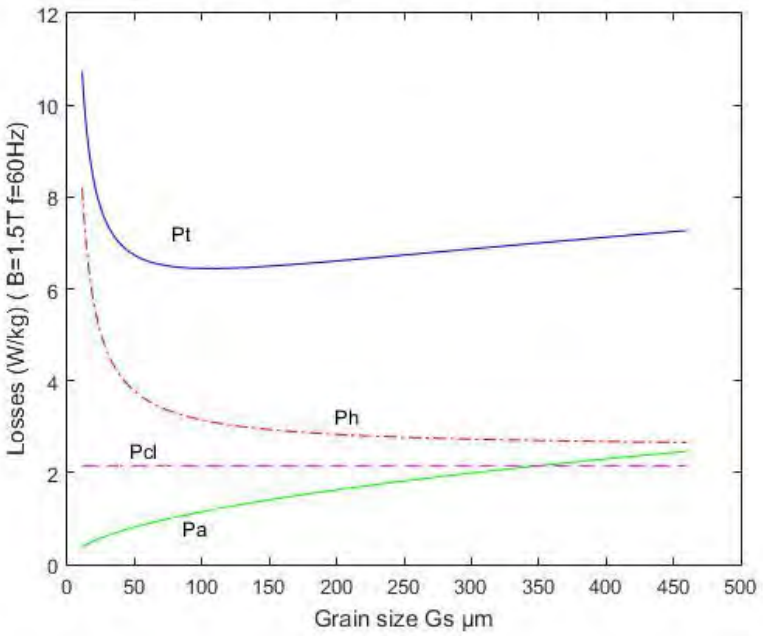

Figure 11: Effect of the grain size the different losses components and on the total loss (Pt).

Looking deeply in this analysis we remark that while we increase the size of grains in order to decrease the losses due to hysteresis we compound anomalous losses coming from large domains which favorite the high mobility of the walls and vice versa. Therefore the reduction of the grain size during manufacturing process should be carefully chosen to maintain a reduction in anomalous loss more important than the useless increase in hysteresis loss.

Furthermore, many study [31] [36] [37] focused on the anomaly factor of Pry and Bean's model which is the factor of proportionality between anomalous loss and classical loss. This factor is dependent on the frequency; the dependence is given by (B.7) [31]:

$$\eta(f) = (\eta_0 - \eta_\infty)e^{-(f/fw)^x} + \eta_\infty \quad \text{(B.7)}$$

with η_0 anomaly factor for frequency f →0 , η_∞ anomaly factor for frequency f→∞ and f_w as the inflexion point of the curve.

They estimated the impact of laser-scribing on the behavior of this factor by comparing the variation of the anomaly factor in function of frequency for three sheets of grain oriented silicon electrical scribed with a Nd:YAG laser. The condition of the laser during scribing were varied for each sheet (pulse energies I_{laser}=*106W/cm²* with line distance of 5mm; I_{laser}= *72W/cm²* with line distances of 7.5mm, and I_{laser}= 9.9*W/cm²*with laser lines distances of 4.0 mm while the diameter of the focal point of laser light on the samples was kept constant at *d= 50μm*).

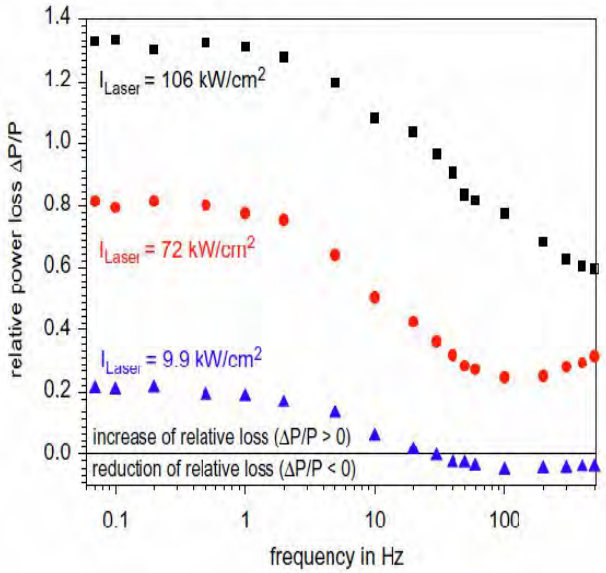

Figure 12: Comparison of relative loss change of electrical sheets scribed with different laser intensities [31]

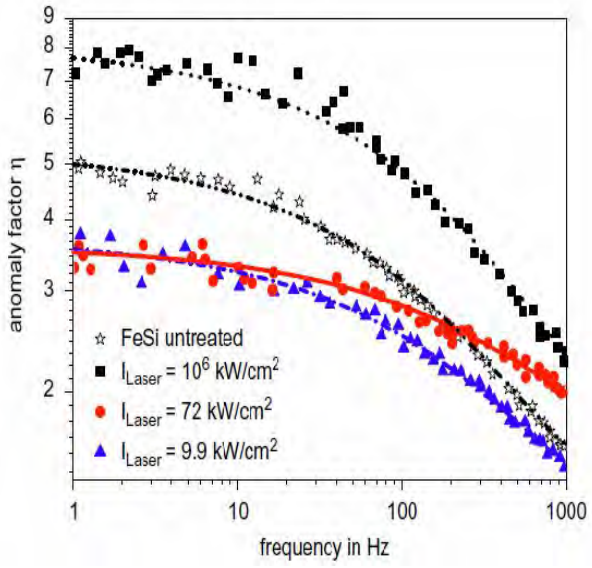

Figure 13: Anomaly factor η for untreated electrical sheets in comparison with laser scribed sheets treated with different laser intensities [31]

As shown in the Figure 12 the relative power loss decreases significantly for the sheet scribed with a laser at lowest frequency (9.9 kW/cm^2 with laser lines distances of 4.0 mm) this decreasing is compatible with the behavior of the anomaly factor *(*Figure 13*)* in function of frequency for the same sheet.

Inspired by the previous researches and in order to estimate the impact of different parameters on macroscale observables, we consider an ideal case of wall distribution in simple sheet geometry equivalent to the configuration of Pry and Bean's model as shown in the Figure 14, the domains are oriented parallel to the field and the walls planes traverses all the thickness ζ of the sheet [17]. Maxwell microscopic equations were used to calculate microscopic induced currents and the diffusion equation of the induced current (j_{eddy}) was deduced as follows:

$$\Delta j_{eddy} = \mu_0 \sigma \partial_t j_{eddy} \quad \text{(B.8)}$$

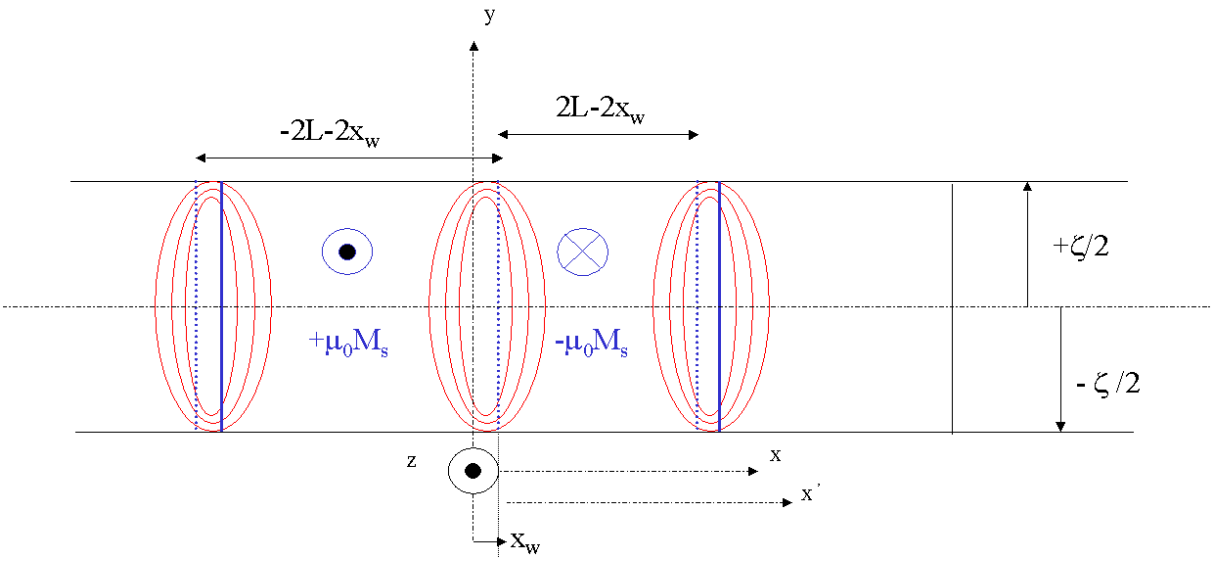

Figure 14: Idealized local configuration in plan walls [17]

Taking into account the three boundary conditions at the edge between two domains:

$$j_x\ (0^+,y,t) = j_x\ (0^-,y,t) \quad \text{(B.9)}$$

$$j_x\ ((-2L-2x_\omega\ )^+,y,t) = +j_x\ ((+2L-2x_\omega)^-,-y,t) \quad \text{(B.10)}$$

$$j_y\ (0^+,y,t) - \ j_y\ (0^-,y,t) = \ -2\sigma v_\omega \mu_0 M_s \quad \text{(B.11)}$$

where j_x , j_y and j_z are the components of the induced current, σ is the electrical conductivity, v_ω is the domain walls velocity and M_s is the saturation magnetization.

Defining η_ω as the wall mobility, the domain walls velocity can be given by the expression:

$v_\omega = \eta_\omega \ . H_a$ with $\eta_\omega = \frac{\Pi^3}{1.05*16\,\zeta\,\sigma\,\mu_0 M_s}$ and H_a is the applied field.

And also the related permeability (μ_{app}) in the harmonic state was calculated as a function of the frequency ω, the static field H_s and the domain wall parameters (the wall mobility η_ω and the wall density per unit length $n_\omega = 1/(2L)$) with the following expression:

$$\mu_{app} = \frac{B}{H_a} = \frac{2\mu_0 M_s n_\omega\, \eta_\omega \left(1-\frac{H_s}{M_s}\right) + j\mu_0\omega}{2n_\omega\, \eta_\omega H_s + \ j\omega} \quad \text{(B.12)}$$

The total loss is as follows:

$$P = \iint (\sigma^{-1}J^2)dx'dy = \iint H_a\ \partial_t B\ dx'dy = 2\ \zeta\ \mu_0 M_s v_\omega H_a \quad \text{(B.13)}$$

We studied the impact of some parameters (electrical conductivity, sheet thickness and wall mobility) on the permeability of the sample and core losses.

The Figure 15 illustrates the variation of this permeability, relative to the static permeability at zero frequency μ_{ref}, as a function of the frequency for different wall densities. It is clear that the increasing in the value of wall density increase the value of the permeability at significant frequency (>25Hz).

The term of conductivity appears in the expression of the wall mobility which is inversely proportional to the conductivity, so when the electrical conductivity σ increases the wall mobility η_ω decreases and then the permeability as a function of the frequency decreases as shown in the Figure 16. Also the wall mobility η_ω is inversely proportional to the thickness of the sheet, the permeability decreases in function of the frequency while increasing the thickness ζ (Figure 17*)*.

Figure 18 shows that the increasing in domain walls density decrease the value of losses as a function of the frequency, therefore increasing the value of the sheet thickness shows an increasing in losses *(*Figure 19*)* also the same conclusion for the dependence of electrical conductivity; losses increases as a function of frequency while increasing the value of the electrical conductivity *(*Figure 20*).*

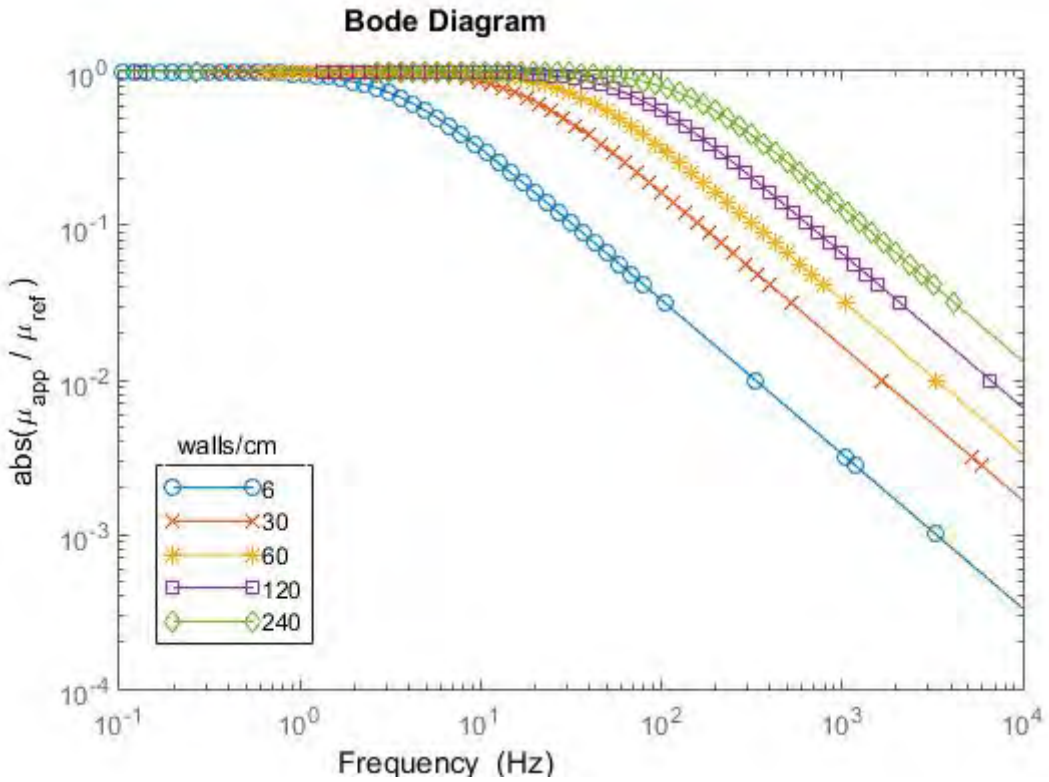

Figure 15: Variation of the permeability (abs($\frac{\mu_{app}}{\mu_{ref}}$)) in function of the frequency for different wall density.

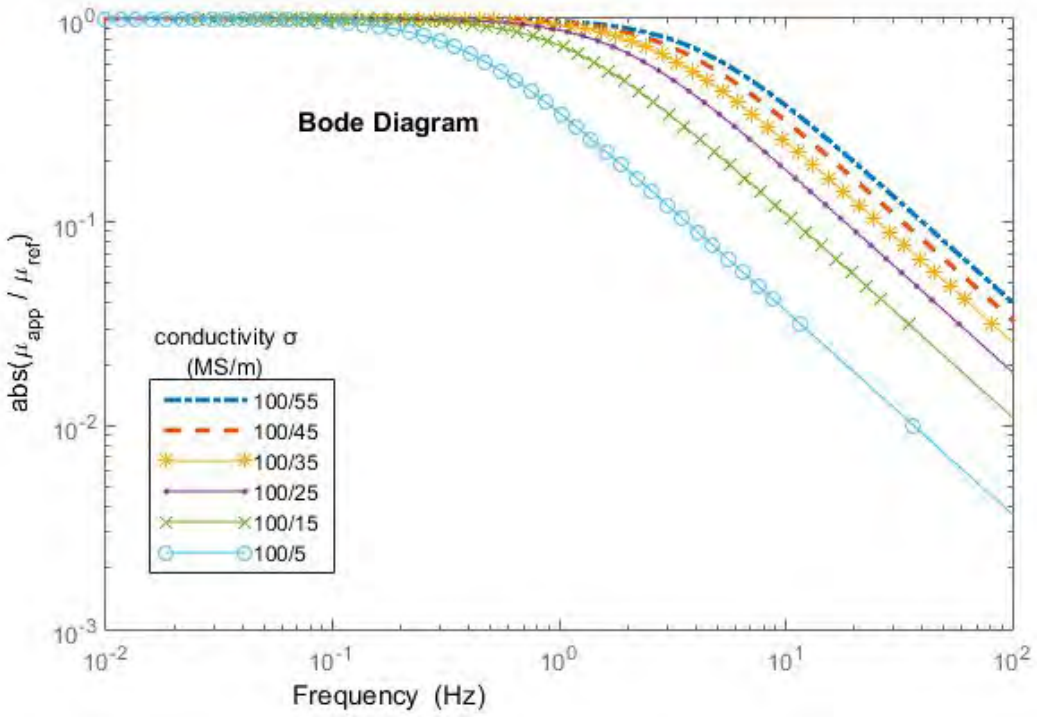

Figure 16: Variation of the permeability (abs($\frac{\mu_{app}}{\mu_{ref}}$)) in function of the frequency for different values of electrical conductivity.

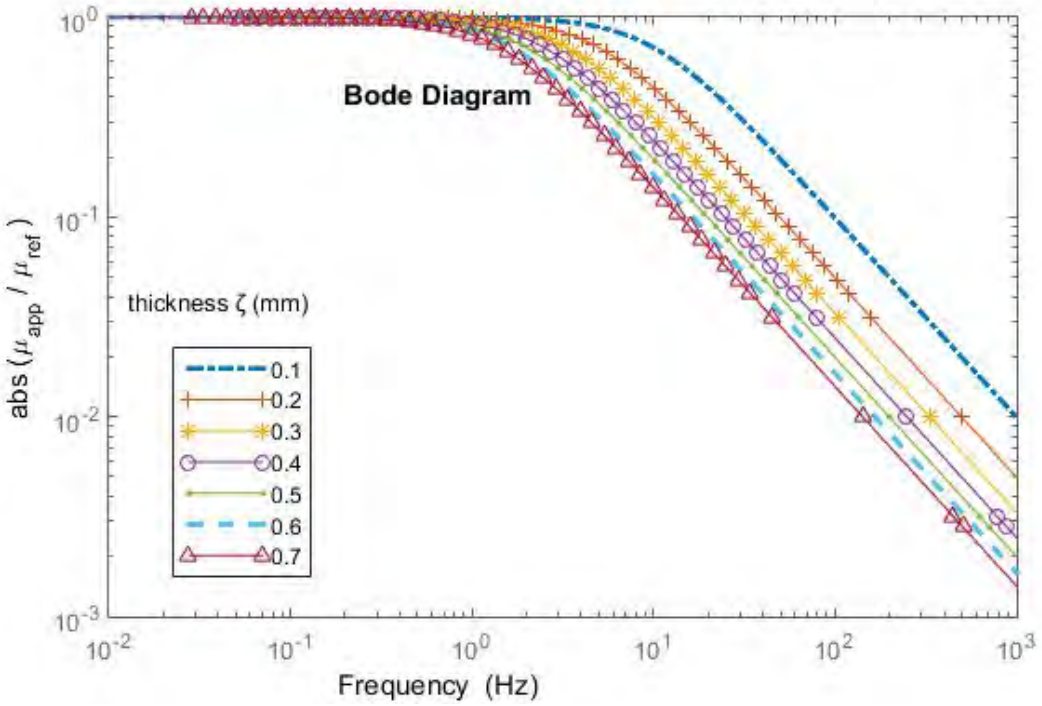

Figure 17: Variation of the permeability (abs($\frac{\mu_{app}}{\mu_{ref}}$)) in function of the frequency for different values of the sheet thickness.

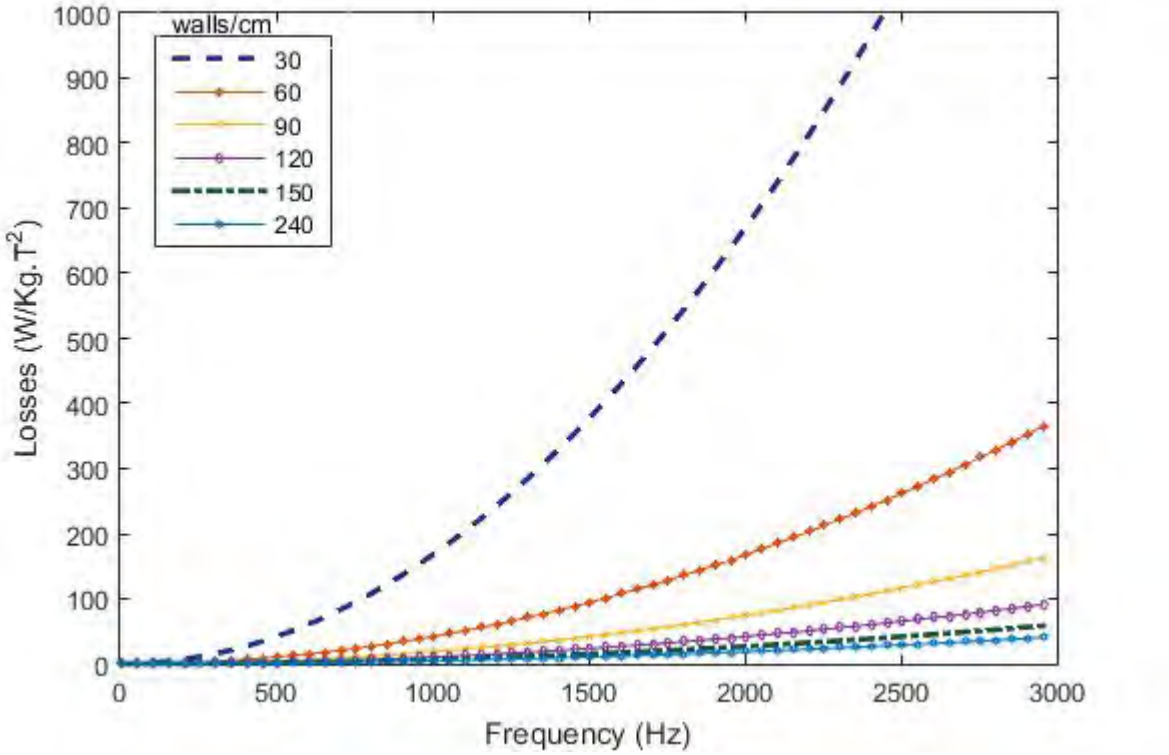

Figure 18: Power losses (W/kg.T^2) in function of the frequency for different values of domains wall density.

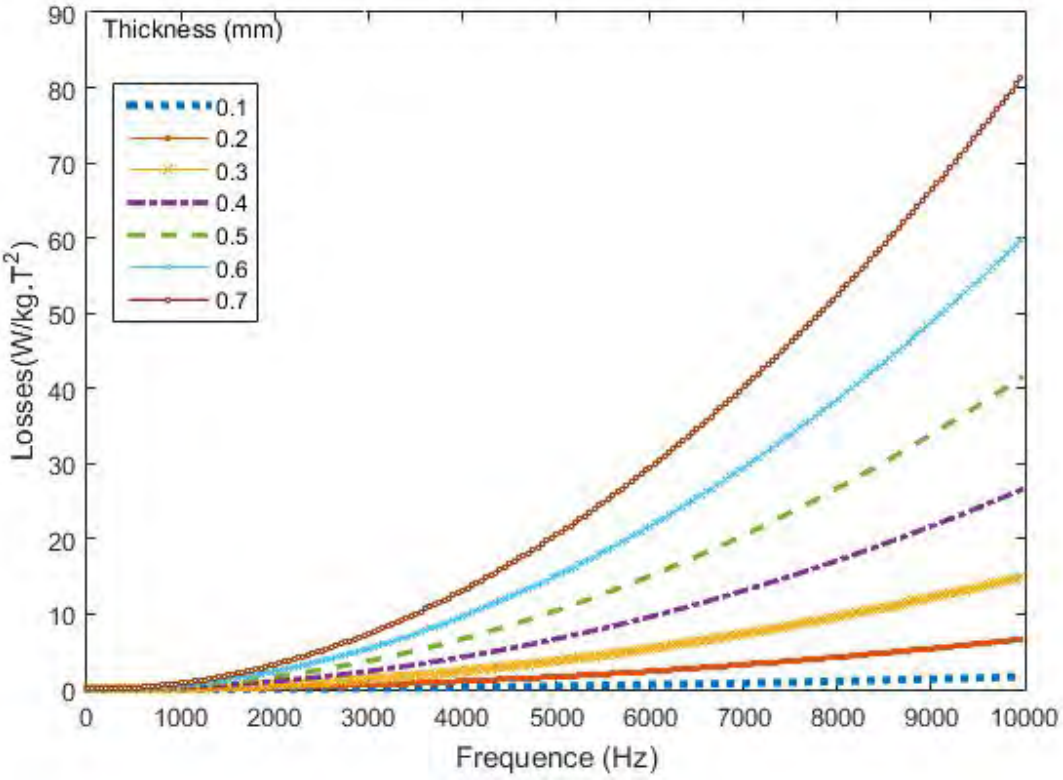

Figure 19: Power losses (W/kg.T^2) in function of the frequency for different values of sheet thickness

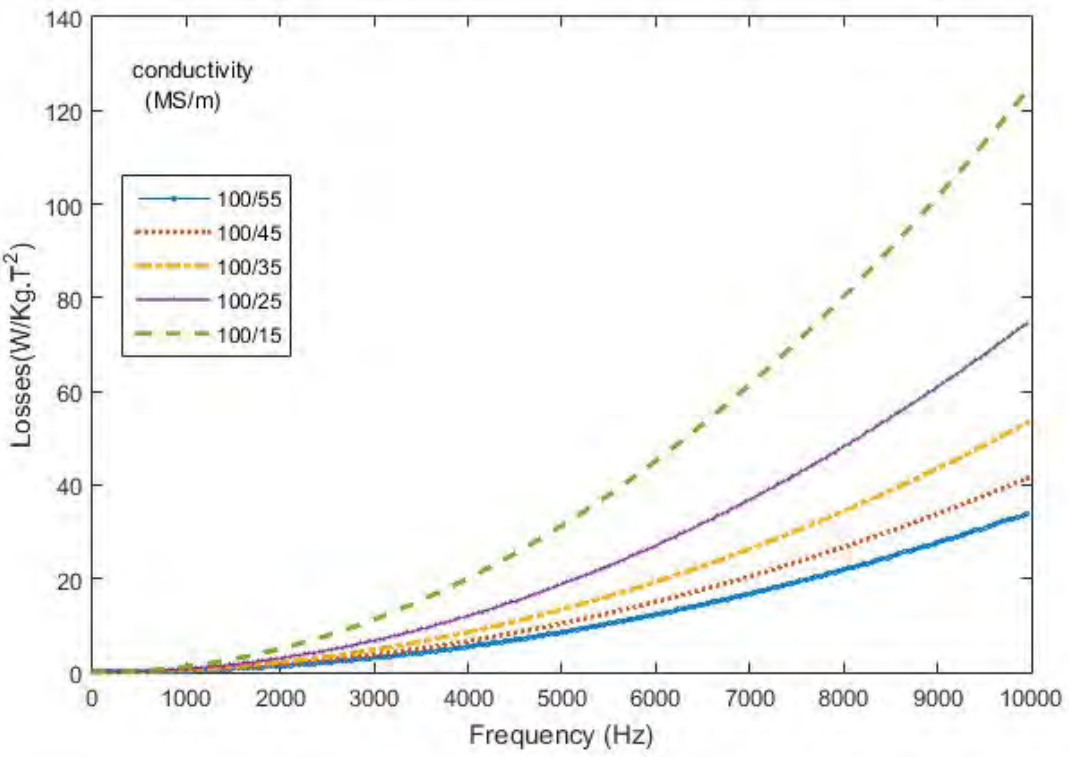

Figure 20: Power losses (W/kg.T^2) in function of the frequency for different values of electrical conductivity.

C) First modelling of the Surface Magnetic Structure – Surface magnetic model 1

I. Context and brief summary of the state of the art for the laser irradiation refinement process

The existence of magnetic domains and walls constituting the magnetic structure of a soft magnetic materials has been demonstrated since approximately 1969, thanks to studies from P. Weiss and Bitter [38] [39] It is well known that magnetization curves, hysteresis and iron losses in soft magnetic materials are due to several magnetization reversal mechanisms, such as the magnetic domains walls pinning, displacement, bowing, multiplication, fusion, nucleation and the domains magnetic rotation. Therefore, the shape and size of magnetic domains and the density, area and mobility of domains walls have got a significant impact onto the magnetic behavior, and especially the iron losses [32].

Research on the laser scribing and irradiation process on electrical steels has started at the end of the 20th century. Some first interesting results showing an impact of the scribing process onto the magnetic domains refinement can be found in [40] [41]. First processes were performed with the mechanical ball scribing [42]. Then, the development of new technologies such as the laser technologies made it possible to improve the scribing process. These technologies must limit the metal deforming or the insulating coating damaging. The laser process has been mainly investigated and implemented for the surface irradiation technique on some GO SiFe materials with specific thicknesses. Various techniques have been proposed, some use continuous lasers [27] [25], the others use pulsed lasers [43] with wavelength around 1 μm and short pulses from 500 fs to 200 ns. In practically, the whole papers, the laser irradiation process is dedicated to the magnetic domains' refinement; and Most of laser patterns investigated correspond to straight lines perpendicular to the rolling direction in GO 3% SiFe alloys.

In the ESSIAL project we would like to:

a) use new monomodal new technologies of pulsed NdYag lasers working in the infrared zone for the magnetic domains' refinement techniques;

b) investigate various laser techniques including the irradiation process (mainly thermal effects), the scribing process (grooves and thermal effects) and the ablation process (mainly creation of grooves). In each case, we identify and estimate the Heat Affected Zone (HAZ) and thermal stress (T), the matter ablation thresholds and material removal zone (MRZ), the Residual Stress Zone (RSZ) and value (m) (see deliverable D2.5. (version 1 at M5) and deliverable D3.1 (version 2 M19));

c) implement the laser scribing concept either before or after the insulating coating process, depending on the laser treatment, when this is possible. This may provide solutions to enhance the benefits of the domains refinement process without damaging the coating (laser refinement process);

d) optimize various laser patterns geometry (1D lines, Spots & 2D lines) dedicated to the located, oriented and selective domains refinement;

e) adapt a laser treatment before the 2nd recrystallization of GO materials to investigate the differential growth of non-oriented or oriented grains (laser texturization process).

f) carry out a sensitivity analysis to the thickness of material and to the nature and quality of various alloys (GNO SiFe or GO SiFe, other non-textured or textured materials).

Control of the process requires to first optimize the laser parameters (spot size, peak power, pulse energy, duration and repetition frequency, scanning speed, …) to get any desired scribing lines [30] [44]. It is then necessary to specify the optimal lines to maximize the dynamic loss reduction due to walls motion and by minimizing the static hysteresis loss increase due to pinning effects [36]but still favoring the walls activation and nucleation [45]. Most studies are essentially practical with magnetic measurements and microscopic observations for various laser parameters [28]. The theory called micro-magnetism [46] can be used to describe the rotation of polarization within a wall, including the calculation of the walls thickness. This method can also be used to describe the domain wall spacing but for very few domains and in a perfect crystal [47] or around small defects [34]. Other authors also experimentally studied the impact of the surface crystallographic texture onto the magnetic structure [48].

In the ESSIAL project, WP3 (Physical studies), task 3a (magnetic studies), we plan to:

1) model the magnetic structure and its relationship to the laser patterns parameters

2) model the magnetic behavior and losses and its relationship to the magnetic structure

3) characterize, measure and identify the useful magnetic properties

4) correlate the theoretical results with the experimental results and validate

5) help the specification of the laser patterns characteristics

In this chapter, we focus on a method to help the specification of the best laser patterns to optimize later the magnetic performances (magnetic permeability, coercive force, power losses). To do so, we investigate a theoretical tool to estimate statistically the impact of a laser scribing or irradiation pattern onto the main parameters that define a magnetic structure at zero external magnetic field, with magnetic domains and walls, more especially the domains wall spacing.

II. Soft magnetic materials and the laser scribing or irradiation process

Before analyzing the impact of any laser scribing or irradiation process, we must understand the magnetic structure of soft magnetic materials. So, we suggest first introducing what a magnetic structure and its origins are. Magnetic domains and walls and the corresponding energies will be briefly defined. Then, we must consider the laser induced modifications within the magnetic material such as the magnetic poles, the closure domains and other walls bowing and pinning effects. Then, in the next section, we will look for a quantified energy formulation that allow a sensitivity analysis according to the typical shapes and dimensions of magnetic domains as a function of both the materials' intrinsic properties, its geometry and more precisely some first laser pattern parameters.

8. Description and origin of the magnetic structure

Soft magnetic materials have got two main characteristics: they can be magnetized and demagnetized very easily with a weak coercive force and they show a very low remanence at zero magnetic field applied. These characteristics cannot be obtained by a homogeneous magnetization or polarization. Due to several energy contributions and the energy minimization principle, the material prefers to organize itself in several volume areas called magnetic domains (see arrows in blue in Figure 21 and Figure 22) homogeneously magnetized in different directions and separated by a thin boundary called magnetic wall (see grey boundaries in Figure 21 and Figure 22) where the polarization rotates.

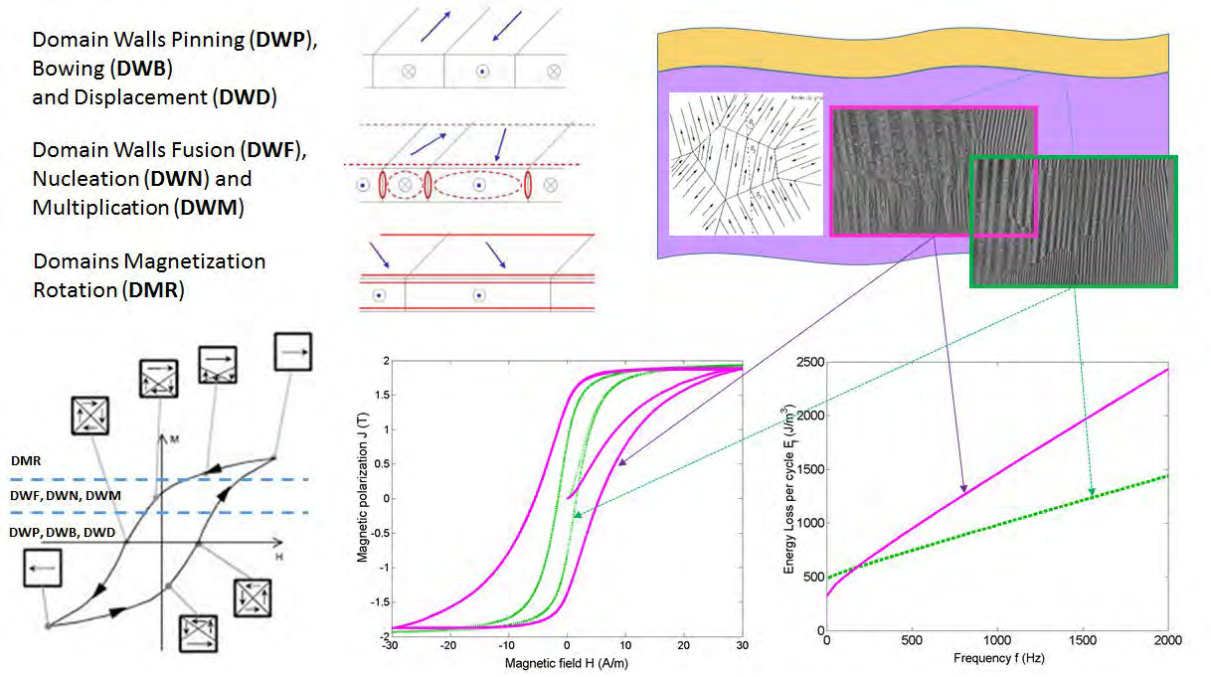

Figure 21: What is a magnetic structure and a magnetic domain? What are the magnetization mechanisms? What is the link between the magnetic hysteresis and the iron losses and the magnetic structure?

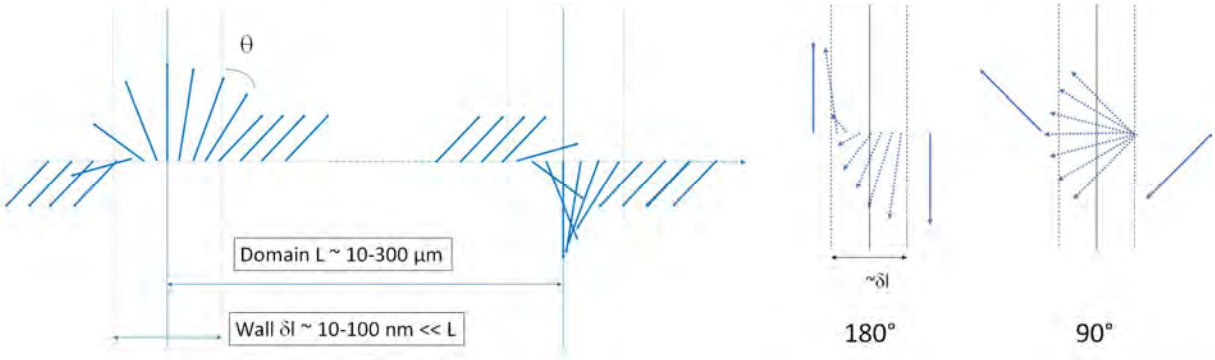

Figure 22: What is a magnetic wall ? Some walls examples (90° and 180° walls).

The main energy contributions that are at the origin of a magnetic structure are called the magneto-crystalline anisotropy energy, the magnetic exchange energy, the magneto-static demagnetizing energy and the magnetoelastic energy [49]. These last will be detailed and used in the present surface model afterwards. In case of non-closure domains configuration with magnetic poles (see Figure 24), The magneto-static demagnetizing energy usually increases with the size of non-closure domains. In the case of closure domains configuration (see Figure 24), The anisotropy energy also increases with the size of domains (see definition of a closure domain in the next sub-section). The sum of the anisotropy and exchange energy increases with the walls number or walls density, which is inversely proportional to the size of domains. As a result, the material chooses a compromise by creating domains and walls with size and density that minimize the global energy. The aim of the first surface magnetic model presented below is to describe this compromise and to analyze the impact of a surface laser treatment on any improvement of this energy balance that should lead to performances enhancement.

9. Role of the laser processes

Then, we consider the effect of the laser treatment on the material at different locations. In parallel to the theoretical study, some experimental trials and characterizations have been carried out to analyze the relationship between some laser parameters (laser power, spot size, laser pulse duration and repetition frequency, scanning speed, …) and its impacts on the topography or/and the stress level with the affected zone and finally the magnetic structure around the laser impacts and the corresponding macroscopic properties (dots or lines, cf Deliverable D2.5. previous sections and Figure 23). Thus, it will be possible to adjust the laser parameters that are able to affect positively the material surface. Selection can be done thanks to complementary analysis carried out by optical, metallurgical and magnetic observations. We suggest first eliminating all the solutions that damage significantly the surface with melted phases and re-deposition of droplets, too large, inaccurate or irregular spots or grooves, too big deformations and flatness damaging or insulator damaging (see deliverable D2.5. for details). The best parameters estimated must be investigated further with additional observations carried out by the metallurgists, physicists and thanks to the XRD, MFM and the MOKE imaging techniques (see deliverables D2.2., D2.3. and D3.2.). At the end, even the parameters selected must be confirmed thanks to macroscopic magnetic measurements of the permeability, the losses and the hysteresis cycles (see deliverable D3.2., measurements done with the SST).

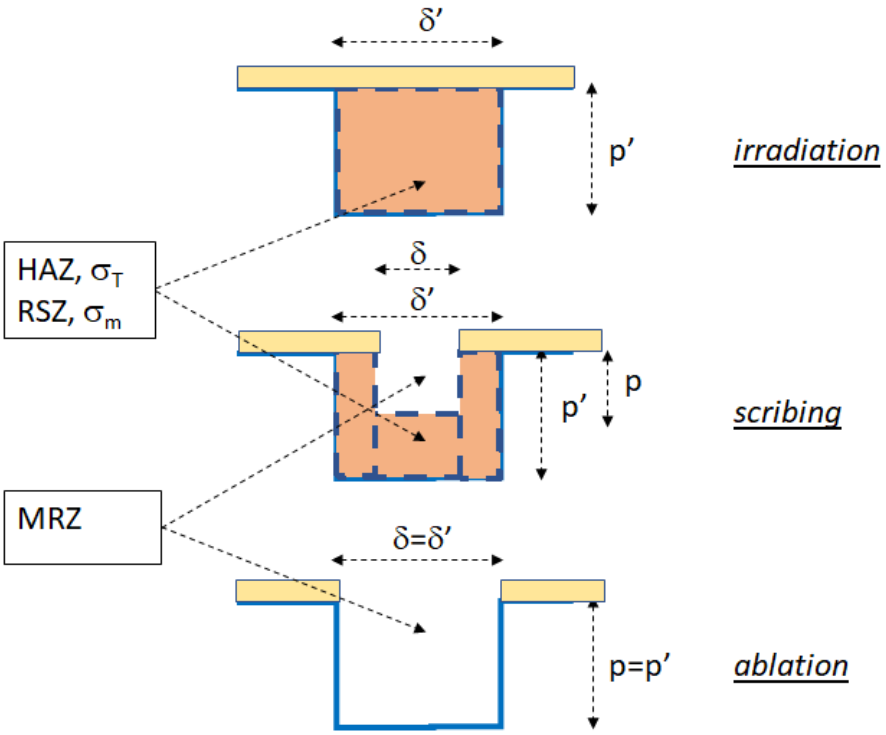

Figure 23: Laser impacts parameters for the three laser processes: irradiation, scribing, ablation.

Then, it will be proposed additional trials with specific patterns and the goal of the present modeling is to help defining the laser process and patterns specifications in case of irradiation (Heat Affected Zone HAZ width δ' and depth p', thermal induced stress σ_T) or in case of scribing/ablation (Material Removal Zone MRZ width δ and depth p, Stress Affected Zone RSZ width δ' and depth p', Laser Induced Shock Wave stress σ_m). To complete the patterns definition, we also have to specify the characteristic size of each pattern: for example, the dots or/and line spacing (d_{DL} for lines perpendicular to the rolling direction and d_{DT} for lines perpendicular to the transverse direction) (see Figure 24).

In the following, we would like to describe the main interesting consequences of the laser scribing zones within the magnetic structure. We assume that the magnetic property inside the treated zone is affected such that the magnetic polarization is either greatly reduced or misoriented. It is thus important to limit the volume of these scribing zones so as neither to weaken significantly the global magnetic saturation of samples nor to jeopardize the insulation properties of the coating. We therefore propose to assume that the laser can affect very locally the magnetic polarization and permeability of the material such that it disturbs the domains and walls by making the two following assumptions:

(i)	**laser « scribes » modify very locally the magnetic properties such that the polarization is greatly reduced (scribing or ablation with MRZ) or disoriented (thermal or mechanical stress induced anisotropy inside the HAZ or the RSZ) inside the affected zone**

(ii)	**laser patterns create located closure domains (mainly due to the stress induced anisotropy) or magnetic poles (mainly due to the creation of grooves) at the vicinity of the lines or the grooves that will define one dimension of surface magnetic domains due to an energy minimization principle.**

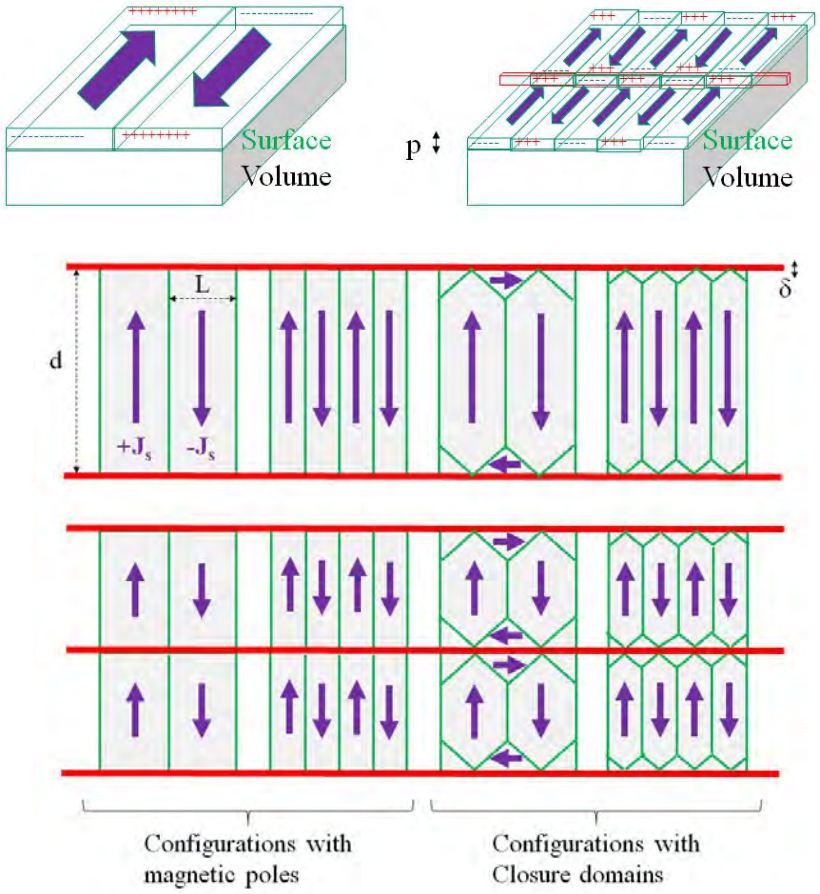

Figure 24: definition of laser patterns parameters (example with lines) and its impact onto the magnetic structure, especially the magnetic walls spacing L.

a. Magnetic poles and equivalent charges

A magnetic pole appears at an interface between two different materials when the angle between the magnetic polarization $\boldsymbol{J}$ and the unit vector $\boldsymbol{n}$ normal to the interface is different from zero. The equivalent magnetic charge J_n is defined as the result of the dot product $\boldsymbol{J}\cdot\boldsymbol{n}$ between $\boldsymbol{J}$ and $\boldsymbol{n}$. When the anisotropy is very strong, the material won't create closure domains that cost a huge amount of energy and it prefers to keep domains oriented along easy axis. As a consequence, magnetic poles J_n can appear at different locations:

i) At the vicinity of grain boundaries between two misoriented grains of angles θ_1 and θ_2 with the boundary normal direction:

$$J_n = J(cos\theta_1 - cos\theta_2) \quad \text{(C.1)}$$

ii) Magnetic poles can also appear at the surface of an electrical sheet if the easy axis of the grains is not tangential to the surface but with an angle θ_s to the normal direction ($\theta_s=\pi/2$ for perfectly oriented grains).

$$J_n = Jcos\theta_s \quad \text{(C.2)}$$

iii) And of course, magnetic poles can appear at the vicinity of the area affected by the laser (see Figure 24). Considering one magnetic domain that goes from one line to another, positive magnetic poles can appear at one extremity against one line and negative magnetic poles will appear at the other extremity against the other line. In case of scribing lines with an angle θ_{DL} against the rolling direction, we've got a succession of positive and negative magnetic poles all along each line.

$$J_n = Jcos(\theta_{DL}) \quad \text{(C.3)}$$

In the following section, we will focus on the magnetic poles generated by the lasers, keeping constant the magnetic poles generated by the grain boundaries and the surface. These last will be included in the 2nd version of the surface magnetic model (next update).

b. Closure domains

Magnetic poles contribute to a certain amount of energy called the magneto-static demagnetizing energy. The latter come from the interaction at long distance between magnetic poles. When the anisotropy of the material is not so high, and the magnetic poles are close to each other, closure domains cost less energy than the demagnetizing energy and then the material prefers to create closure domains (see Figure 25).

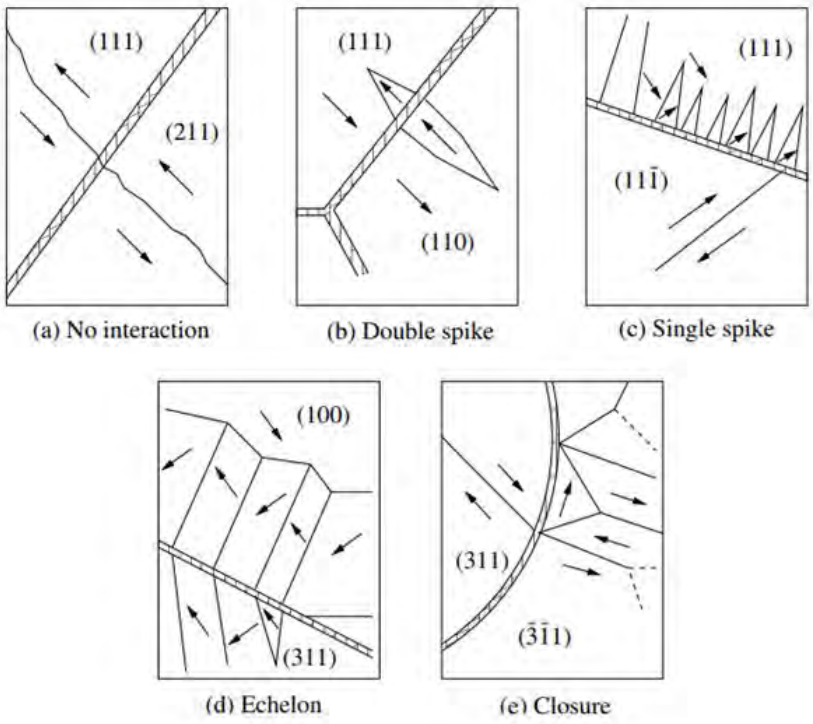

Figure 25: The five types of interaction between grain boundaries and domain walls, shown in order of increasing magnetic pole density at the grain boundary (Tobin and Paul, 1969 [55]).

As a consequence, different kinds of closure domains can appear at different locations:

i) Either 180° or 90° closure domains can appear at the vicinity of grain boundaries between two misoriented grains (see Figure 26)

ii) 180° and 90° Lancet domains can also appear at the surface of an electrical sheet if the easy axis of the grains is not perfectly tangential to the surface but with an angle θ to the normal direction (see Figure 27).

iii) Either 180° or 90° closure domains can finally appear at the vicinity of the area affected by the laser (see Figure 28).

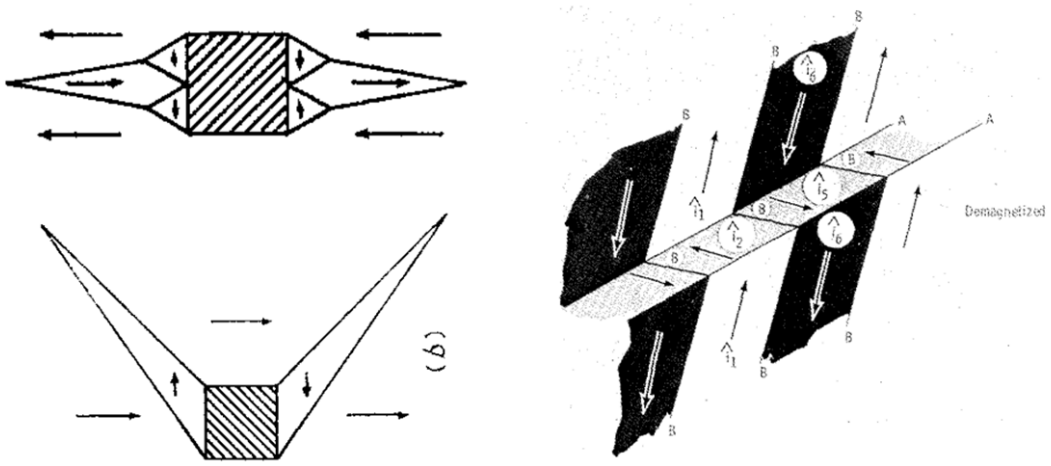

Figure 26: Closure spike-like 180° and 90° domains around defects and grain boundaries [56].

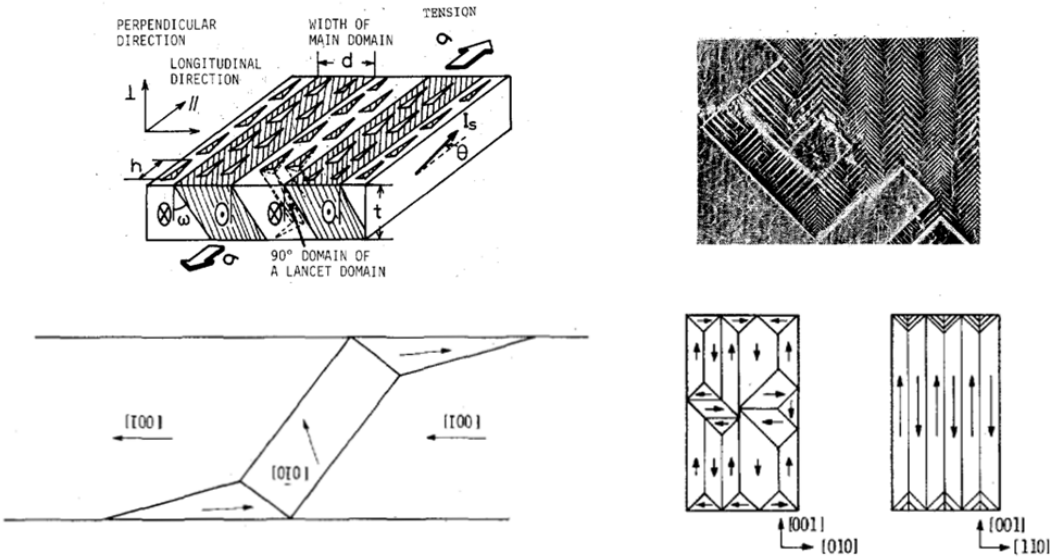

Figure 27: Surface Lancet 180° and 90° closure domains and « tree pattern » of 90° closure domains [57, 58].

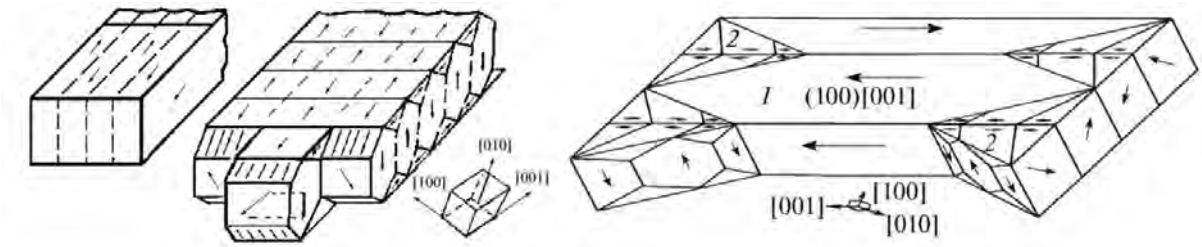

Figure 28: Surface 180° and 90° closure domains due to laser stress induced anisotropy and magnetostriction [59, 60].

In the following section, we will focus on 90° closure domains generated at a specified depth by the laser, due to either the grooves (scribing / ablation) or the thermal effects (irradiation / scribing), keeping constant the effect of surface and grain boundaries. Surface and grain boundaries will be included in the second version of the surface magnetic model (next update).

c. Walls pinning, nucleation and multiplication

Of course, adding some scribed or engraved patterns on the surface of a material may create some defects which will probably affect the static motion of magnetic walls. Defects usually act as pinning sites that prevent the walls to move at low speed and so increase what we call the static hysteresis losses and the static coercive force. At low frequencies, the walls will jump from one defect to another and induce additional loss. At the same time, the walls will require a highest field to detach from one defect and contribute to the magnetization reversal mechanism. On the contrary, some defects can become nucleation or activation sites, *i.e.* the location where walls can be either created by the presence of magnetic poles or activated by the presence of small walls around closure domains. It is then necessary to specify the optimal laser patterns type and geometry (first lines type, width, depth and spacing) to maximize the dynamic loss reduction due to walls motion and by minimizing the static hysteresis loss increase due to pinning effects [36] but still favoring the walls activation and nucleation [45].

Now we will introduce the main energy contributions and corresponding material properties that will be used for our first model. Then a sensitivity analysis to the size of domains (or equivalently the walls spacing and density) will be proposed. Finally, we would like to be able to consider the different patterns of the laser treatment to theoretically estimate its impact on the re-organization of the magnetic structure within the quasi-static working conditions first.

III. Energy contributions and magnetic properties involved

1. Magnetic exchange energy

First of all, the main magnetic ordering property of a material is determined by its exchange interaction energy between magnetic moments carried by the atoms and due to their particles spins at the atomic scale [50]. This interaction is in theory acting at a long distance between the whole magnetic moments of a sample, but it is possible to consider only the interaction between the closest neighbors without loss of generality. In any case, this energy increases when the magnetic polarization is rotating, forming an angle between the neighboring magnetic moments. On the contrary, the exchange energy becomes nil for homogeneous magnetic polarization, i.e. with parallel magnetic moments all orientated in the same direction. That is the reason why soft magnetic materials will create domains with constant magnetic polarization and for which no exchange energy has to be considered. Nevertheless, to be able to achieve a non-magnetized state, the material also creates magnetic walls between the domains, for which the polarization is rotating (see Figure 22) and so the exchange energy has to be considered inside the walls. Thus, for soft ferromagnetic materials with large domains and very thin magnetic walls with only one rotation of freedom, it is possible to approximate the exchange energy density e_{ex} [J.m^{-3}] by the one due to neighboring magnetic moments [47] and given by (C.4). More general expressions can be used with two or three rotations of freedom.

$$e_{ex} = A_{ex}\left(\partial_y \theta\right)^2 \tag{C.4}$$

Where A_{ex} [J.m^{-1}] is called the macroscopic exchange coefficient (linked to an exchange integral calculation), θ is the angle between magnetic moments and one fixed direction along the wall (the magnetic easy axis for example, see next section), y is the direction perpendicular to the wall (see Figure 22). The material property A_{ex} can be related to the Curie temperature T_c [50] thanks to equation (C.5).

$$T_c \approx \frac{Z a_0 A_{ex}}{6 k_B} \tag{C.5}$$

where
T_c is the Curie temperature *(T_c=1043 K for Fe)*
Z is the Atomic number *(Z=26 for Fe)*
a_0 is the lattice parameter *(2.86 Angström for Fe)*
k_B *is the Boltzmann constant (k_B=1.38e $^{-23}$ J.K^{-1})*
This leads to $A_{ex} \approx 1.2e^{-11}\, Jm^{-1}$ for the iron (Fe) (see Table 3)

2. The magneto-elastic and self-magnetostriction energy – Stress induced anisotropy and magnetic induced stress

In most general cases, we will have to consider the magneto-elastic or magnetostriction energy and its corresponding coefficients. There are two kinds of magnetostriction: the self-magnetostriction (Direct magnetostriction Joule effect) and the stress induced magnetostriction (Inverse magnetostriction Villari effect) [61].

The self-magnetostriction corresponds to a magnetization induced strain in a material with free conditions. For fixed limit conditions, like in our case, the strain turns into a magnetization induced stress. It leads to a magneto-elastic contribution $e_{\lambda\varepsilon}$ to the magneto-crystalline anisotropy energy density even without any external stress applied to the material (this effect called the Joule ΔE effect is due to a strain induced by the magnetization). Positive magnetostriction corresponds to a positive strain and negative stress along the magnetization, negative magnetostriction means a negative strain and

positive stress along the magnetization.

$$e_{\lambda\varepsilon} = +\frac{1}{2}\left(\frac{9}{4}\right)\left((C_{11}-C_{12})\lambda_{100}^2\sum_{i=1}^{3}\cos^4\theta_i + C_{44}\lambda_{111}^2\sum_{i=1}^{3}\sum_{j=1\neq i}^{3}\cos^2\theta_i\cos^2\theta_j\right)$$
$$\underbrace{\approx}_{sin\theta<<1}\left(\left(\frac{9}{4}\right)\left((C_{11}-C_{12})\lambda_{100}^2 + C_{44}\lambda_{111}^2\right)\right)\left(\frac{3}{2}-\sum_{i=1}^{3}\sin^2\theta_i\right) \quad (C.6)$$

where
C_{11}, C_{12} and C_{44} are the Hooke elastic constants of the isotropic material [J.m^{-3}≡Pa].
(C_{11} and C_{12} correspond to the tensile constant C_{44} to the shearing constant).
λ_{100} and λ_{111} are the lattice magnetostriction strains in [100] and [111] directions [n.u.].
θi is the angle between the magnetization or polarization and the direction i [rad].

The stress induced magnetostriction corresponds to a change in magnetization due to the stress. It leads to a stress induced anisotropy energy $e_{\lambda\sigma}$ related to magnetostriction (this effect called the Villari effect generates an additional stress induced magnetostriction energy). Positive magnetostriction means that magnetization along an expansive stress costs less energy than transverse to the expansive stress. Thus, magnetization along a compressive stress costs more energy. Magnetic domains along an expansive stress are favored. Negative magnetostriction means that magnetization along an expansive stress costs more energy than transverse to the stress. Thus, magnetization along a compressive stress costs less energy. Magnetic domains along a compressive stress are favored.

$$e_{\lambda\sigma} = -\left(\frac{3}{2}\right)\left(\lambda_{100}\sum_{i=1}^{3}\sigma_{ii}\left(\cos^2\theta_i-\frac{1}{3}\right) + \lambda_{111}\sum_{i=1}^{3}\sum_{j=1\neq i}^{3}\sigma_{ij}\cos\theta_i\cos\theta_j\right)$$
$$\underbrace{\approx}_{\sigma_{ij}\ll}\frac{3}{2}\lambda_{100}\sum_{i=1}^{3}\sigma_{ii}\left(\sin^2\theta_i-\frac{2}{3}\right) \quad (C.7)$$

where
σ_{ii} and σ_{ij} are the mechanical tensile and shearing stresses [Pa].

The whole magnetostriction effects have to be considered

- Before the coating and the surface laser treatment: In the whole material submitted to a rolling process that can generate a residual stress
- After the coating and before the laser treatment: between the metal and the coating that can exert a residual stress due to different thermal expansions
- During and after the surface laser treatment: in the HAZ (Heat Affected Zone) and the RSZ (Residual Stress Zone) where a heat induced stress can gradually change the magnetic properties without cancelling it as is assumed in (i) and (ii).

3. Magneto-crystalline and macroscopic anisotropy energy

The whole possible magnetization directions in a crystal are not equivalent. It is easier to align the magnetic polarization along some specific crystallographic axes called easy axis. Thus, the magneto-crystalline anisotropy energy is minimum in these directions. That's why, most domains contain a positive or negative magnetic polarization which is always aligned to one easy axis. For these well oriented domains, no anisotropy energy has to be considered. On the contrary, closure domains can generate a significant amount of anisotropy energy when the magnetic polarization isn't aligned to one of the easy axis. Nevertheless, to be able to achieve a non-magnetized state, the material also creates magnetic walls between the domains, for which the polarization is rotating (see Figure 22) and so the anisotropy energy has to be considered inside the walls. For example, at the microscopic crystallographic scale, in cubic crystalline grains (Fe and Ni), easy axis correspond to directions of the edges ((100), (010) and (001) for Fe) or directions of the diagonals ((111) for Ni).

(i) Metallography, texture, residual stress and macroscopic anisotropy

Most materials are polycrystalline materials with several misoriented or partially oriented grains with different shapes and dimensions. The crystallographic texture of the material also defines the direction and rate of grains orientation. As we know, significant amounts of energy have to be considered due to the grain boundaries between the grains. These contributions contain both the located magneto-crystalline energy of closure domains and magneto-static energy due to magnetic poles at the boundaries. Thus, these contributions depend on the texture and the grains' shape, orientation and dimension.
Moreover, the metallurgical processes (rolling, flattening and coating processes) may generate residual stresses inside the material despite stress releasing annealing used during the manufacturing. We know from previously that any residual stress can change the magnetic anisotropy energy called magnetostriction stress induced anisotropy.
As a consequence, the effective macroscopic anisotropy energy does not come only from the microscopic magneto-crystalline anisotropy but also from the texture, the grains' shape, orientation and dimension and finally the residual stress induced by the metallurgical process.
In the following, we assume that all microscopic effects can be lumped in an equivalent macroscopic anisotropy coefficient K_{an} that may differ from the first order magneto-crystalline anisotropy constant K due to the texture, metallography and residual stress inside the material. In case of the macroscopic uniaxial anisotropy, K_{an} is approximately given by (C.8)

$$K_{an,1} = K_1 - \frac{9}{4}\left((C_{11} - C_{12})\lambda_{100}^2 + C_{44}\lambda_{111}^2\right) + \frac{3}{2}\lambda_{100}\left(\sigma_{r//} - \sigma_{r\perp}\right) - \chi_d \mu_0^{-1} J_s^2 \qquad \text{(C.8)}$$

where
K_1 is the first order magneto crystalline anisotropy constant
$\sigma_{r//}$ and $\sigma_{r\perp}$ are the manufacturing residual tensile stresses along the magnetic easy axis and perpendicular to the easy axis respectively.
$\chi_d \propto \Delta\theta/g$ is the demagnetization factor dependent on the grains' shape, dimension g and disorientation angle

In some polycrystalline materials and depending on the crystallographic texture (main orientation of grains) such as the GOSS texture, only one equivalent easy axis is more interesting and important than the others; this last can be described with the uni-axial type of anisotropy. For hexagonal crystalline grains (Co), easy axis corresponds to only one direction (001). We call it a uni-axial material.

(ii) Uniaxial anisotropy

For uniaxial soft ferromagnetic materials with one main magnetic easy axis at the macroscopic scale (majority of NGO and GO SiFe steels, polycrystalline Co alloys,), it can be proposed to approximate close to the easy axis the macroscopic anisotropy energy density e_{an} [J.m^{-3}] only by its changeable part and by the equation (C.9).

$$e_{an,micro} = K_1 sin^2\theta + K_2 sin^4\theta \underset{\sin\theta \ll 1}{\Longrightarrow} e_{an} \approx K_{an,1} sin^2\theta \qquad \text{(C.9)}$$

Where $K_{an,1}$ [J.m^{-3}] is called the macroscopic anisotropy constant and θ is the angle between magnetic moments and the most important magnetic easy axis (see Figure 22). For NGO and GO SiFe steels we have approximately $\boldsymbol{K_{an,1} \approx 2e^4\, J.m^{-3}}$ and $\boldsymbol{K_{an,1} \approx 4.5e^4\, J.m^{-3}}$ respectively (see Table 3).

(iii) Cubic anisotropy

For some soft ferromagnetic materials with cubic anisotropy, one main magnetic easy axis (polycrystalline FeNi and FeCo alloys, pure polycrystalline Ni and Fe alloys), it can be proposed to approximate close to the easy axis the magneto-crystalline anisotropy energy density e_{an} [J.m^{-3}] by equation (C.10).

$$e_{an} = K_1\left(\sum_{i\neq j=1}^{3}\cos^2\theta_i\cos^2\theta_j\right) + K_2\left(\cos^2\theta_1\cos^2\theta_2\cos^2\theta_3\right)$$
$$\underset{varying}{\Longrightarrow} e_{an} \approx K_{an,1}\left(\sum_{i=1}^{3}\sin^2\theta_i\right) + K_{an,2}\left(\sum_{i=1}^{3}\sum_{j=1}^{3}\sin^2\theta_i\sin^2\theta_j\right) \quad \text{(C.10)}$$

Where
$K_{an,1}(2K_1\text{-}K_2)$ is called the first order macroscopic anisotropy constant [J.m^{-3}].
$K_{an,1}(-(K_1+K_2)\delta_{ij} + K_2)$ is called the second order macroscopic anisotropy constant [J.m^{-3}].
θ_i is the angle between magnetization and the easy axis i (see Figure 22). For polycrystalline pure Fe and Ni alloys we

(iv) others

For other types of anisotropies, it is necessary to improve the model by taking into account more realistic anisotropy energies with several easy axis.

4. Demagnetizing energy or shape anisotropy energy

The magneto-static demagnetizing energy is closely linked to the internal demagnetizing field created by the magnetization variations in space. The latter can result from two contributions. One comes from the non-divergence free magnetic polarization inside the volume of a material. This energy contribution is always minimized and cancelled inside soft magnetic materials thanks to the domains and the walls. Another contribution comes from the magnetic interaction energy between magnetic poles, analogous to the interaction energy between electric charges. This dipolar magnetic energy acts at a long distance between the whole magnetic poles of a sample, but it is sometimes possible to consider only the interaction between the closest neighbors without loss of generality. Let's consider two distributions of magnetic poles of size a*b and A*B respectively and separated by a distance r = $\sqrt{(X^2+Y^2+Z^2)}$ (see Figure 33).

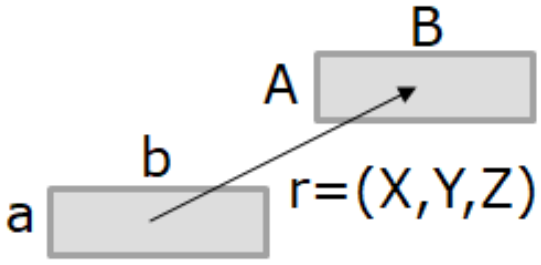

*Figure 29: Scheme of the two magnetic poles example with two distributions a*b and A*B of equivalent magnetic charges.*

Then, the demagnetizing energy between these two magnetic charges distributions is defined by the following integral calculation (see equations (C.11) and (C.12)). J_n and J_n' are supposed to be the magnetic charges of pole a*b and A*B respectively. The constant $\mu_0=4\pi e\text{-}7$ H.m^{-1} is the magnetic permeability of the air. In case of cartesian coordinates and magnetic poles with rectangular shapes, the result can be expressed by (C.13) [51].

$$E_d \approx \frac{1}{2} N_d(X,Y,Z,a,b,A,B) J_n J_n' \quad \text{(C.11)}$$

$$N_d \approx \frac{1}{2\pi\mu_0} \int_{-\frac{a}{2}}^{\frac{a}{2}} \int_{-\frac{b}{2}}^{\frac{b}{2}} \int_{-\frac{A}{2}}^{\frac{A}{2}} \int_{-\frac{B}{2}}^{\frac{B}{2}} \left(\frac{1}{\sqrt{(X+x-x')^2+(Y+y-y')^2+Z^2}} \right) dx'\, dy'\, dx\, dy \quad \text{(C.12)}$$

$$N_d \approx \frac{1}{2\pi\mu_0} \sum_{i=0}^{1} \sum_{j=0}^{1} \sum_{k=0}^{1} \sum_{l=0}^{1} (-1)^{i+j+k+l} \begin{pmatrix} \frac{1}{2} U(V^2 - W^2) ln(R-U) \\ \frac{1}{2} V(U^2 - W^2) ln(R-V) \\ UVW \tan^{-1}\left(\frac{UV}{RW}\right) \\ \left(\frac{15}{4} UV - \frac{1}{2}(U^2+V^2)\right) R \end{pmatrix} \quad \text{(C.13)}$$

where

$U = \mathrm{X} + (-1)^i \frac{A}{2} - (-1)^j \frac{a}{2}$

$V = \mathrm{Y} + (-1)^k \frac{B}{2} - (-1)^l \frac{b}{2}$

$W = Z$

$R = \sqrt{U^2 + V^2 + W^2}$

N_d is called the shape demagnetizing factor. It depends mainly on the geometry formed by the two magnetic poles with magnetic charges distributions a*b and A*B.

5. The Zeeman interaction energy with the external field

It is first proposed to explain the role played by the laser scribing with the magnetic poles and closure domains on their own, even without any external magnetic field applied. The first surface model is dedicated to a zero-field energy minimization principle in order to forecast the magnetic structure at a static equilibrium.
Before including the magnetic field coupling, we must understand the coupling between the volume magnetic structure (see next section) and the surface magnetic structure (see present section and next update). The magnetic field coupling will be then considered thanks to a dynamic limit condition for the surface and volume model (see next update).

6. Magnetic parameters

To sum up, in soft magnetic materials we mainly have to consider the following physical constants and materials properties (see Table 3, Table 4 and Table 5, [57]).

Table 3: magnetic parameters in some polycrystalline magnetic alloys

	$J=J_s$	$K_{an,1}$	$K_{an,2}$	A_{ex}	λ_{100}	λ_{111}
	[T]	[J.m^{-3}]	[J.m^{-3}]	[J.m^{-1}]	*1e^{-6}	*1e^{-6}
GNO SiFe	2.1	1.2-2.25 e^{4}	-	1.19 e^{-11}	23.7	-4
GO SiFe 3%	2.1	3.0-5.4 e^{4}	-	1.19 e^{-11}	23.7	-4
$Ni_{50}Fe_{50}$	1.6	-7000	-40000	tbd	7	28
$Fe_{50}Co_{50}$	2.3	3300	-18000	tbd	125	50
Fe (poly.)	2.19	42000	15000	1.19 e^{-11}	20	-15.7
Ni (poly.)	0.65	-4500	5300	6.74 e^{-12}	-58	-24
$Fe_{30}Co_{70}$	1.8	-45000	5000	1.58 e^{-11}	125	50

Table 4: Magnetic ordering in pure magnetic elements [57]

	Z	a_0 [Angström]	T_c [K]	A_{ex} [J.m^{-1}]
Fe (cc)	26	2.8	1043	1.19 e^{-11}
Ni (cfc)	28	2.75	627	6.74 e^{-12}
Co (hexagonal)	27	2.7	1388	1.58 e^{-11}

Table 5: Magnetocrystalline anisotropy in pure magnetic elements [57]

	$J=J_s$ [T]	K_1 [J.m^{-3}]	K_2 [J.m^{-3}]	A_{ex} [J.m^{-1}]
Fe (cubic)	2.1	54800	1960	1.19 e^{-11}
Ni (cubic)	0.65	-126300	57800	6.74 e^{-12}
Co (hex-c)	1.8	760000	100500	1.58 e^{-11}

We must keep in mind that some significant discrepancies are often observed between the microscopic properties of pure magnetic elements (Fe, Ni, Co) and the macroscopic ones in various alloys or compound made from these elements (GNO SiFe, GO SiFe, Cubic NiFe, NO FeCo). This difference is very sensitive to the composition, grains, residual stress and the texture.

IV. First test case and modelling

First, let's define the reference frame (x,y,z). In the following, we consider the surface of a laminated sample with thickness $e=\zeta$ along x. We focus mainly on what happens on the surface (y,z) of the sample submitted to a homogeneous laser treatment. We will study one laser pattern example and two magnetic structure examples with generalizations if, and when, it is possible. The test case is first introduced. Then, we focus on one domain (single domain configuration). Finally, we extend the calculation to M*N domains (multi-domains configuration), giving more importance to the closest neighboring domains.

1. Test case studied and laser patterns parameters

We suggest first studying the case of lines scribed with a laser and its parameters defined in Table 4. The direction y corresponds to the direction of laser lines. The lines are parallel to each other with a certain line spacing d along z. The lines have got a certain width along z (δ or δ') and depth along x (p or p') (see Figure 23).
In parallel, we consider a magnetic structure with parallelepipedal domains for which the magnetic polarization $\boldsymbol{J}$ is uniform. θ_J is the angle between the laser lines and the magnetic polarization of domains. The main easy axes can be parallel to z but can also have another orientation defined by the unit vector $\boldsymbol{u}_{an}$. For non-closure domains, the first polarization orientation studied is the one parallel to the main easy axes $\boldsymbol{u}_{an}$, so that θ_J is also the angle between the laser lines and the easy axis $\boldsymbol{u}_{an}$ in this case. Magnetic walls between domains can either be orientated like the polarization $\boldsymbol{J}$ (case of classical 180° walls) or in another direction defined by θ_W. The latter is the angle between the laser lines and the direction of walls. We do not detail in this first model the defects, grains, the mean grain size and the grain boundaries. Nevertheless, these metallurgical parameters are considered inside the equivalent macroscopic anisotropy. We assume in this first analysis that everything happens like if each domain would establish itself from one line to another without interruption, but in a material with a macroscopic anisotropy that is different from the one at the microscopic scale between the grain's boundaries. In the following, we estimate the main energy contributions of one typical magnetic structure defined by some geometrical parameters (see Table 6) and represented in Figure 30 (single domain configuration) and Figure 31 (multi domains configuration).

Table 6: laser pattern parameters

Magnetic structure parameter	Laser parameter	Metallurgy	Description
K_{an}	-	σ_r	rolling and coating initial residual stress
K_{an}	-	g	typical grain
K_{an}	-	$\Delta\theta$	texture – disorientation angle
(a)	***MRZ or p***	**-**	**depth of the MRZ (grooves due to laser)**
(a')	***HAZ or p'*** ***RSZ or p'***	**-**	**depth of the HAZ within the laser lines**
	σ_T	**-**	**laser induced stress due to thermal effect**
	σ_m	**-**	**induced stress due to laser shock wave**
(a)	**-**	***e***	**thickness of the sample**
L	***(b)***	**-**	**width of the magnetic domains**
(c)	***d***	**-**	**distance between lines scribed by laser**
(δ)	δ	-	width of the MRZ within the laser lines
(δ')	δ'	-	width of the HAZ or RSZ within the laser lines
θ_J	θ_J	-	angle between lines and the polarization
θ_W	θ_W	-	angle between lines and the walls direction
θ_{DL}	-	θ_{DL}	Angle between lines and the rolling direction

2. Single magnetic objects

Figure 30 shows the geometry and magnetic polarization of one single domain. As previously mentioned, we can add the energy of the walls (exchange energy + anisotropy energy) with the demagnetization energy of the magnetic poles (magneto-static energy) in case of non-closure domain configuration and finally with the energy of closure domains (magneto-crystalline anisotropy energy) in case of closure domain configuration. In the closure domains configuration, the 90° closure domains are represented in-plane, but the following study may stand for out of plane 90° closure domains as well.

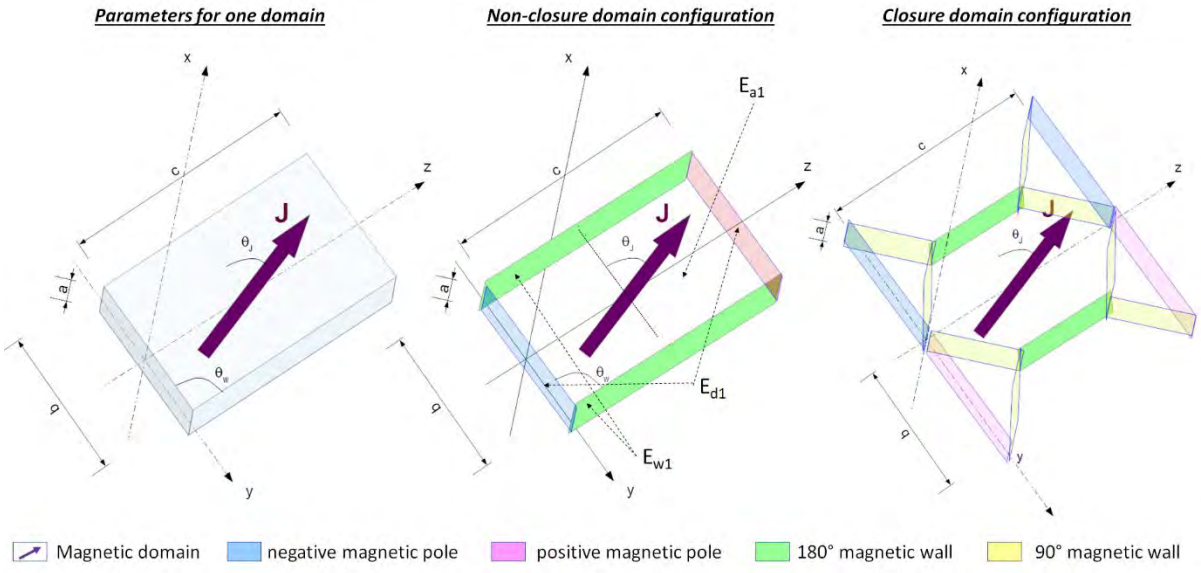

Figure 30: Test case with one magnetic domain.

a. *Magnetic walls*

(i) Magnetic walls without stress

In this section, we give the thickness and the energy of a classical 180° wall (Bloch wall [52]) in a material with uniaxial anisotropy. The same method can be used to find a similar results for other types of walls (180° Néel walls [53], 90° walls [54], …). The wall energy is the sum of the exchange energy and the anisotropy energy given by equation (C.14). In order to minimize the total energy, the material will limit the thickness of the walls such that the angle θ between the magnetization and the easy axis inside the wall is given by (C.15).

$$E_{w1} = \int \left(A_{ex} \left(\partial_y \theta \right)^2 + K_{an} \sin^2 \theta \right) dy \iint dxdz \tag{C.14}$$

$$\overset{min}{\Leftrightarrow} \left(\partial_y \theta \right)^2 = \frac{K_{an}}{A_{ex}} \sin^2 \theta$$

$$\Rightarrow \cos \theta = -\tanh\left(\sqrt{\frac{K_{an}}{A_{ex}}} y \right) \tag{C.15}$$

This result leads to the approximate thickness of the walls, given by (C.16).

$$\delta y = \sqrt{\frac{K_{an}}{A_{ex}}} \tag{C.16}$$

$\delta y \approx 30\, nm$ for Fe, $\delta y \approx 50\, nm$ for Ni and $\delta y \approx 5\, nm$ for Co.

Finally, the total energy of 180° Bloch walls can be calculated, which gives $\boldsymbol{E_{w1}}$ equation (C.17) for one wall.

$$E_{w1} = 4\sqrt{A_{ex}K_{an}} \iint dxdz = 4ac\sqrt{A_{ex}K_{an}} \quad \text{(C.17)}$$

Example of the 180° Bloch wall

a = e/sin(θ_{wa}) is the width or depth of the wall.
c = d/sin(θ_{wb}) is the length of the wall.

with
θ_{wa} the wall's inclination in the (x,y) plane.
θ_{wb} the wall's inclination in the (y,z) plane.

Example of the 90° Néel Wall

a = p' the HAZ or RSZ is the width or depth of the wall.
c = (y+z)

with
y=b/√(1+(cot(β/2))²)
z=b/√ (1+(tan(β/2))²)
b = L/sin(β)
β = π/2-(θ_{DL}-θ_{wb})

(ii) Magnetic walls with laser induced stress

Due to the inverse magnetostriction Villari effect, the laser induced stress will add a magnetostriction energy to the walls and modify both the exchange and anisotropy energy inside the walls due to the stress induced anisotropy.

$$E_{w1} \approx 4ac\sqrt{A_{ex}K_{an,\sigma}} - ac\sqrt{\frac{A_{ex}}{K_{an,\sigma}}}\lambda_{100}\left(\sigma_{zz} - \frac{\sigma_{yy}+\sigma_{xx}}{2}\right) \quad \text{(C.18)}$$

Example of the 180° Bloch wall

$$K_{an,\sigma,180} \approx K_{an} + \frac{3}{2}\lambda_{100}(\sigma_{zz} - \sigma_{xx}) \quad \text{(C.19)}$$

Example of the 90° Néel Wall

$$K_{an,\sigma,90} \approx K_{an} + \frac{3}{2}\lambda_{100}(\sigma_{zz} - \sigma_{yy}) \quad \text{(C.20)}$$

We think that 90° Bloch walls inside the volume should have an energy density similar to that of the 90° Néel walls with a modified anisotropy similar to that of the 180° Bloch walls.

b. Magnetic domain and poles

(i) Non-closure domains configuration

In case of a non-closure domain, no anisotropy energy must be considered in the domain. The maximum energy is due to the demagnetizing energy E_{d1} (C.21) due to the interaction between the magnetic poles of the domain.

$$E_{d1} \approx \frac{1}{2} N_d(0,0,c,a,b,a,b) J^2 \quad \text{(C.21)}$$

In case of a laser induced stress $[\sigma_{ij}]$ that penetrates inside the main 180° domains, its total energy must include the inverse magnetostriction energy E_{s1} (C.22)

$$E_{d1} \approx \frac{1}{2} N_d(0,0,c,a,b,a,b) J^2 + E_{s1}$$
$$E_{s1} = \left(\frac{3}{2}\right)\left(\lambda_{100} \sum_{i=1}^{3} \sigma_{ii}\left(\frac{1}{3} - \alpha_i^2\right) - \lambda_{111} \sum_{i=1}^{3} \sum_{j=1 \neq i}^{3} \sigma_{ij} \alpha_i \alpha_j\right) abc \quad \text{(C.22)}$$

$\alpha_i = cos\,\theta_i = J_i/|J|$ is the cosines of the angle between the main 180° domain's polarization and the direction i.

(ii) In-plane Closure domains configuration

In case of a closure domain, the anisotropy energy has to be considered in the domain. In case of a 90° closure domain, we can estimate the anisotropy energy thanks to the following equation (C.23).

$$E_{a1} \approx K_{an} sin^2\left(\theta_{DL} - \theta_J\right) ayz \quad \text{(C.23)}$$

In case of a laser induced stress $[\sigma_{ij}]$ that penetrates inside the closure 90° domains, its total energy must include the inverse magnetostriction energy E_{s1}, similar to a stress induced anisotropy energy (C.24)

$$E_{a1} \approx K_{an} sin^2\left(\theta_{DL} - \theta_J\right) ayz + E_{s1}$$
$$E_{s1} = \left(\frac{3}{2}\right)\left(\lambda_{100} \sum_{i=1}^{3} \sigma_{ii}\left(\frac{1}{3} - \alpha_i^2\right) - \lambda_{111} \sum_{i=1}^{3} \sum_{j=1 \neq i}^{3} \sigma_{ij} \alpha_i \alpha_j\right) ayz \quad \text{(C.24)}$$

$\alpha_1 = 0$, $\alpha_2 = cos(\pi/2 - \theta_{DL})$ and $\alpha_3 = cos(\theta_{DL})$.

We think that in the out-of-plane 90° closure domains configuration the total anisotropy energy density should be similar to that of the in-plane 90° closure domains.

(iii) Lancet tranverse Closure domain configuration

The Lancet domains configuration happens in GO SiFe materials. It is due to slight misorientation of grains out of plane. Dipolar magnetic energy due to magnetic poles at the sheet surface can be reduced either thanks to the 180° main domains refinement or thanks to the Lancet configuration that consists in in plane 180° closure domains at the surface and out-of-plane 90° closure domains inside the volume (see Figure 27). This last configuration costs sometimes less energy than the domains refinement, which increase the dynamic iron losses but may contribute to an increase in the static permeability probably thanks to more walls nucleation centers, smaller walls that can be activated by a lower magnetic fields and with a low probability to meet a defect. In order to reduce the iron losses, the manufacturing process can be improved thanks to a tensile residual stress along the rolling direction that makes the Lancet configuration energy bigger than the main fine 180° domains configuration. However, this strategy is not able to improve both the static permeability and the losses. One stake of the laser process is to reduce the width of main 180° domains and increase the walls nucleation and activation centers at the same time.

3. M*N domains and walls

Now, we would like to estimate the total energy density per unit surface, considering a surface of M*N magnetic domains (see Figure 31).

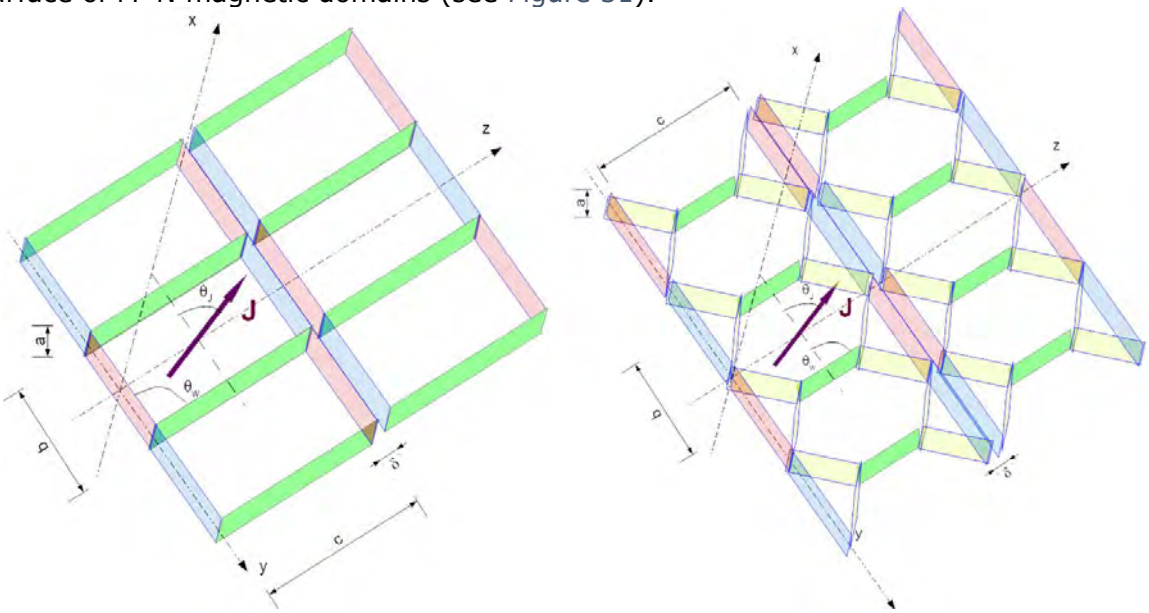

Figure 31 : magnetic structure and test cases studied

a. *Magnetic walls*

Finally, the total energy density of the walls e_w, considering M*N walls, can be calculated thanks to equation (C.25).

$$e_w = \sum_m \sum_n \frac{e_{w1}}{MNbc} \tag{C.25}$$

b. *Magnetic domains and poles*

(i) Non-closure domains configuration

In case of a non-closure domains, the total domains' energy density e_d due to the interaction between the whole 2*M*N magnetic poles of the domains and the stress induced magnetostriction energy is given by (C.26).

$$e_d = \frac{1}{2}\sum_{m1}\sum_{n1}\sum_{m2}\sum_{n2}\frac{N_d(0,(m2-m1)b,(n2-n1)c,a,b,a,b)J^2}{MNbc} + \sum_m \sum_n \frac{e_{s1}}{MNbc} \tag{C.26}$$

(ii) In-plane Closure domains configuration

In case of 90° closure domains (the minority), the total anisotropy energy density e_a in the domains can be estimated thanks to equation (C.27).

$$e_a = \sum_m \sum_n \frac{e_{a1}}{MNbc} \tag{C.27}$$

(iii) Lancet tranverse Closure domains configuration

The Lancet domains configuration is a secondary magnetic structure that can exist in parallel to the previous ones. It is then necessary to define additional magnetic structure parameters that would represent the lancet domains size and density.

V. Sensitivity analysis with constraints

In this section we would like to analyze the impact of different manufacturing and patterns parameters of the laser treatment on the re-organization of the surface magnetic structure within the quasi-static working conditions but without any external magnetic field. Modelling the action of the magnetic field will be possible only once the volume model is developed (see next section) and the coupling between the volume and the surface is modelled. It will also be possible to compare between the non-closure domains configuration and the closure domains configuration and to identify any correlation between the laser process (irradiation, scribing or ablation mode) and the domains configuration chosen by the material, *i.e.* the one that costs the lowest energy. A first hypothesis consists in relating:

- the irradiation process to the closure domains configuration,
- the ablation process to the non-closure domains configuration,
- The scribing process to a mix of the two configurations above.

The laser parameters should play the role of input parameters (patterns, lines spacing, width, depth, length, …). The magnetic structure parameters should play the role of output parameters (domains size, walls spacing, walls density, … and later, the mobility / pinning, nucleation properties). However, for a sensitivity analysis, both laser and magnetic parameters are considered as input parameters. The outputs are the energy contributions and the total energy of domains and walls.

In the following analysis, we will assume the correspondences below:

- $a = p$ or p' (depth of the grooves or the HAZ, RSZ due to the laser)
- $b = L$ (width of magnetic domains, the walls spacing)
- $c = d$ (distance between lines scribed by the laser, the lines spacing)
- $\delta <<$ (width of the grooves due to the laser scribing / ablation)
- $\theta_J = 90°$ (angle between lines and the magnetic polarization of domains)
- $\theta_w = 90°$ (angle between lines and the walls direction)
- $\sigma = \sigma_T$ (induced residual stress due to the laser thermal effect)

Before carrying out calculations, we introduce an additional parameter, the one that corresponds to the rolling and transverse directions of a laminated sample. Let's name $\boldsymbol{u}_{DL}$ the unit vector along the rolling direction DL. θ_{DL} is the angle between the laser lines and the rolling direction. The latter often corresponds to the easy magnetic axis $\boldsymbol{u}_{an}$.

The sensitivity analysis that follows in this section will focus on five parameters:

- d_{DL}: line spacing with lines perpendicular to the rolling direction (3 mm by default)
- p or p': depth of the grooves or HAZ respectively (10 μm and 100 μm by default)
- K_{an}: macroscopic anisotropy constant (54 000 J/m^3 by default)
- ζ: magnetic sheet thickness (0.23 mm by default)
- σ: induced residual stress (0 MPa by default)

While using the following values by default for the other fixed variables:
$J=[0,0,2\ T]$ (the polarization vector)
$\theta_{DL} = \theta_J = \theta_W = 90°$ ()
$e = \zeta = 0.23\ mm$ (the sheet thickness)
$\boldsymbol{u}_{an} = [0,0,1]$ (the macroscopic anisotropy direction)
$\theta_W = [\pi/2, \pi/2]$ (the main walls inclination)
$A_{ex} = 1.2e^{-11}\ J.m^{-1}$ (macroscopic magnetic exchange coefficient)
$\lambda_{100} = 2.6e^{-5}$ (first order magnetostriction coefficient in direction [100])
$\lambda_{111} \approx 0$ (second order magnetostriction coefficient in direction [111])

4. Non-Closure domain configuration without stress

We think that this domains configuration may happen for laser treatments with grooves and small HAZ and RSZ, *i.e.* weak thermal effects and induced residual stress. The corresponding laser process is the ablation process with ultra-short pulses for which the thermal diffusion and the induce shock wave have no time to penetrate the material.

a. Without induced stress

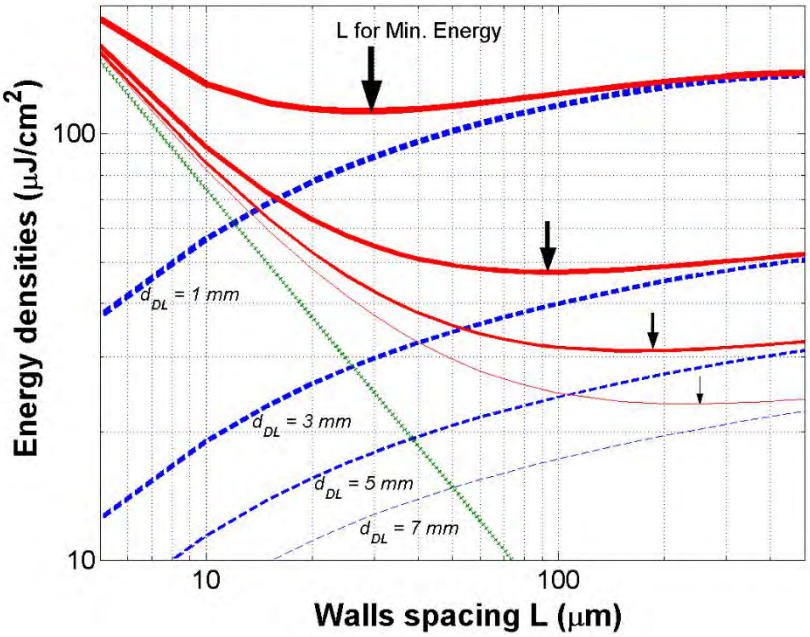

Figure 32: Sensitivity analysis of the energy contributions to the walls spacing L and the line spacing d_{DL}. ($J = J_s = 2T$, $\mathbf{u}_{an} = \mathbf{u}_{DL}$, $e = \zeta = 0.23$ mm, $p = 10$ μm, $\delta \approx 0$ μm, $\theta_{DL} = \theta_J = \theta_W = 90°$). : walls energy, -- domains energy, – total energy.

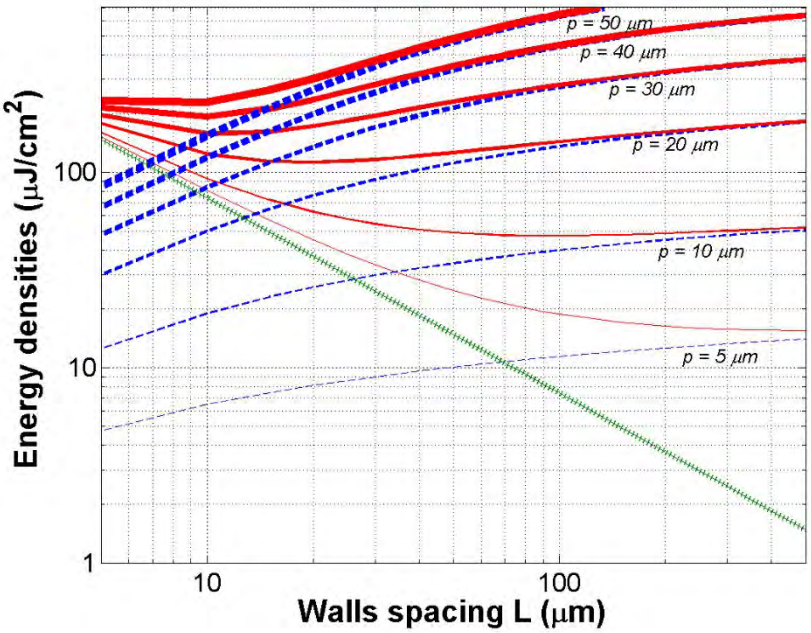

Figure 33: Sensitivity analysis of the energy contributions to the walls spacing and the lines depth p. ($J_s = 2$ T, $\mathbf{u}_{an} = \mathbf{u}_{DL}$, $e = \zeta = 0.23$ mm, $d_{DL} = 3$ mm, $\delta = 0$ μm, $\theta_{DL} = \theta_J = \theta_W = 90°$). : walls energy, -- domains energy, – total energy.

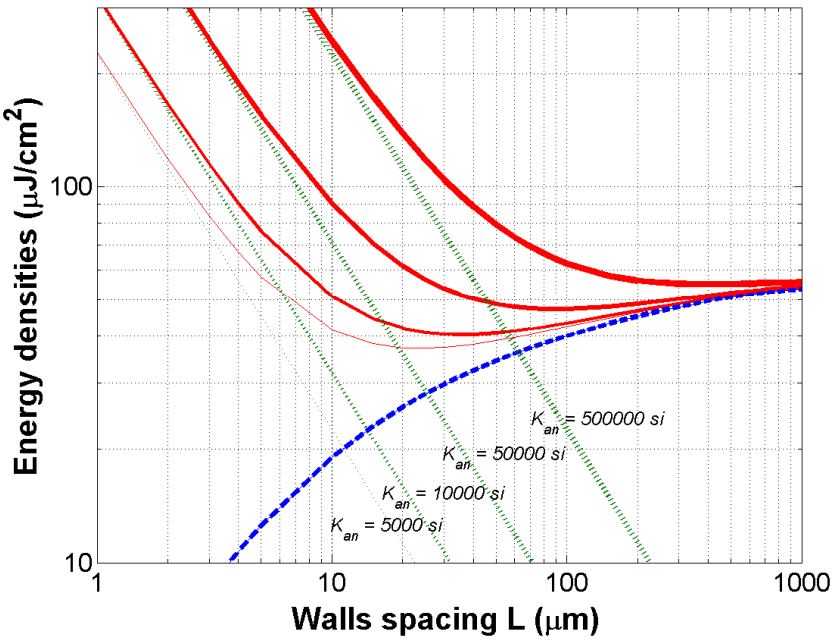

Figure 34: Sensitivity analysis of the energy contributions to the walls spacing and the walls energy. (Js = 2T, uan = uDL, e = ζ = 0.23 mm, dDL = 3 mm, p = 10 μm, δ ≈ 0 μm, θDL = θJ = θW=90°). : walls energy, -- domains energy, – total energy.

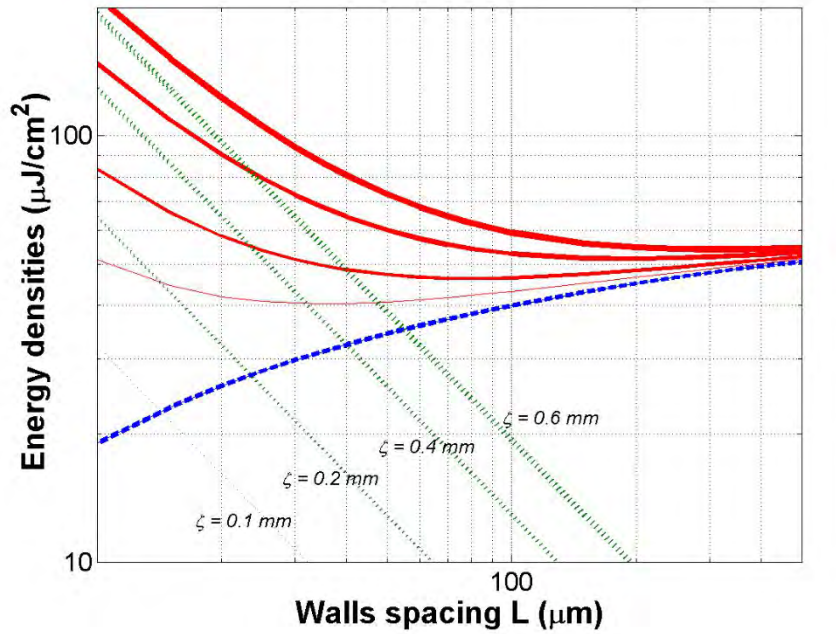

Figure 35: Sensitivity analysis of the energy contributions to the walls spacing and the sheet thickness. (Js = 2T, uan = uDL, dDL = 3 mm, p = 10 μm, δ ≈ 0 μm, θDL = θJ = θW=90°). : walls energy, -- domains energy, – total energy.

In Figure 32-Figure 35, only non-closure domains are considered. We also assume that the depth of walls equals the thickness $a = \zeta = e_p$ of the sample. At the same time, the domains energy due to laser induced magnetic poles is estimated with the laser lines depth $a = p$. As expected, the walls energy increases when the walls spacing decreases (the number of walls increases). At the same time, the main 180° domains demagnetizing energy decreases when the walls spacing decreases (the magnetic poles become smaller).

Therefore, it is coherent to find an optimal wall spacing which minimize the total energy and corresponds to the best compromise found by the material.
In Figure 32, the walls energy does not depend on the line spacing. At the same time, the domains demagnetizing energy increases when the line spacing decreases (shorter distance between magnetic poles). The material has no other choice to refine its magnetic structure in order to limit the increase in the total energy when scribing lines onto the surface. However, the minimum energy becomes higher when the line spacing decreases and may be in competition against another configuration energy.
In Figure 33, the walls energy does not depend on the line depth. At the same time, the domains demagnetizing energy increases when the line depth increases (bigger magnetic poles). The material has no other choice to refine its magnetic structure in order to limit the increase in the total energy when scribing lines onto the surface. However, the energy minimum becomes also higher when the line spacing decreases and may be in competition against another configuration energy.
In Figure 34, the domains demagnetizing energy does not depend on the macroscopic anisotropy. At the same time, the walls energy increases when the anisotropy increases (this can be due to an increase in the inverse magnetostriction stress or bigger grain size). The stronger the anisotropy, the larger the domains in order to reduce the number of walls and therefore the total walls energy. This time the energy minimum becomes smaller when the anisotropy decreases.
In Figure 35, the domains demagnetizing energy does not depend on the sheet thickness. At the same time, the walls energy increases when the thickness increases (walls go deeper in the thickness). The bigger the thickness, the larger the domains in order to reduce the number of walls and therefore the total walls energy. This time the energy minimum becomes smaller when the thickness decreases.

b. *With induced stress*

The manufacturing process can induce stresses in the whole material or its all surface. On the contrary, the laser process can induce stresses only locally at the vicinity of the laser impact (the HAZ or the RSZ). The ablation process does not generate any significant thermal induced stresses. The non-closure domains configuration is sensitive mainly to global stresses induced by the manufacturing process but not significantly to the located laser induced stresses. In fact, the effect should be like but weaker than the effect of a global residual stress. In this section, we suggest analyzing the effect of a global residual stress induced by the manufacturing processes (rolling and coating processes) along the rolling direction 2 and the transverse direction 3 respectively.
In Figure 36-Figure 37, the walls energy does not depend significantly on the residual stress. At the same time, the main 180° domains magnetostriction energy decreases for tensile stress and increases for compressive stress in the rolling direction (positive magnetostriction). On the contrary, but at a lesser extent, the main 180° domains magnetostriction energy increases for tensile stress and decreases for compressive stress in the transverse direction (positive magnetostriction). However, without considering any other domains or misorientations, the walls spacing that minimizes the total energy does not significantly depend on the residual stress. Nevertheless, the decreasing minimum energy must be considered when comparing to another domains' configuration with residual stress.
We think that the rolling and coating processes exerts a global tensile stress to the surface of the material, which contributes to the main 180° domains refinement. Both the ablation and scribing processes damage the coating to create the grooves. This may cancel the benefit from the tensile stress, while allowing the domains refinement by another and more efficient way: reduction of the demagnetizing field generated at the vicinity of laser patterns. Moreover, the patterns may be considered as new defect that can act as new nucleation and activation centers for the magnetic walls.

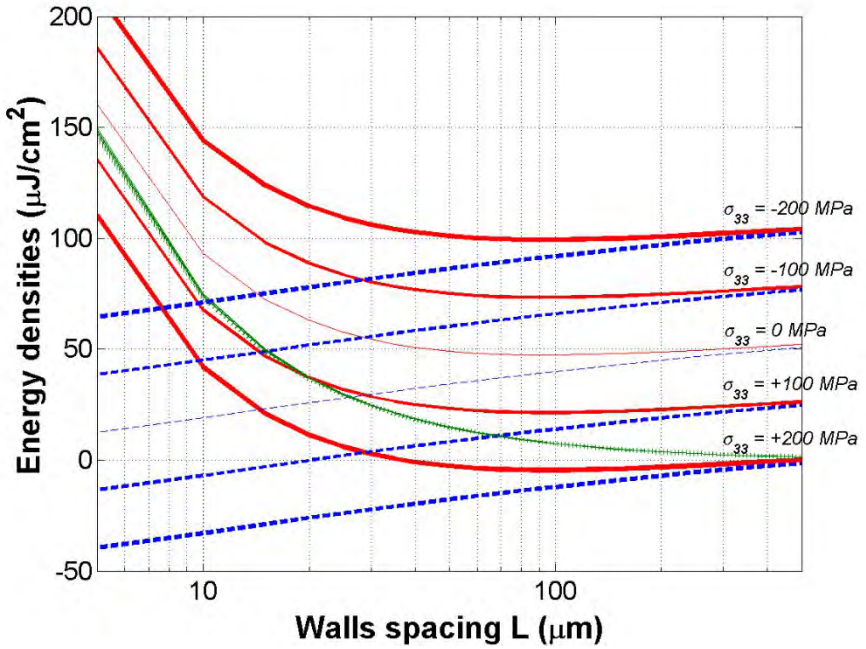

Figure 36: Sensitivity analysis of the energy contributions to the walls spacing and the global residual stress along the rolling direction. (J_s = 2T, $\mathbf{u}_{an} = \mathbf{u}_{DL}$, e = ζ = 0.23 mm, d_{DL} = 3 mm, p = 10 μm, δ ≈ 0 μm, $\theta_{DL} = \theta_J = \theta_W$=90°). : walls energy, -- domains energy, – total energy.

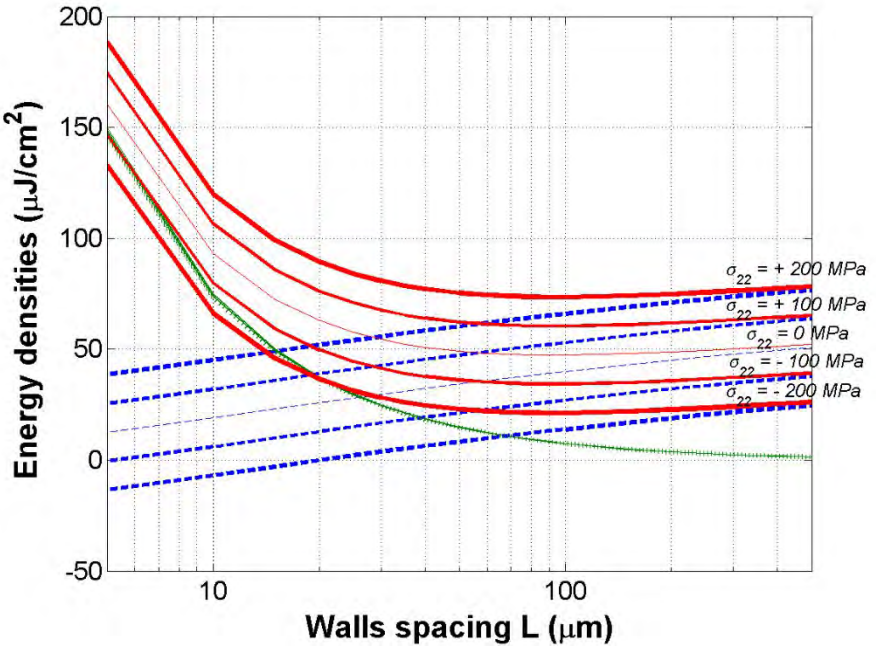

Figure 37: Sensitivity analysis of the energy contributions to the walls spacing and the global residual stress transverse to the rolling direction. (J_s = 2T, $\mathbf{u}_{an} = \mathbf{u}_{DL}$, e = ζ = 0.23 mm, d_{DL} = 3 mm, p = 10 μm, δ ≈ 0 μm, $\theta_{DL} = \theta_J = \theta_W$=90°). : walls energy, -- domains energy, – total energy.

5. In-plane closure domains' configuration

We think that this domains configuration may happen for laser treatments with strong thermal effects and induced residual stress. The irradiation process with long pulses for which the peak power is insufficient to create any grooves can rather generate a heat that diffuses deep inside the material. We also think that the scribing process heat can penetrate the material and should thus induce closure domains at the vicinity of the laser grooves.

a. Without induced stress

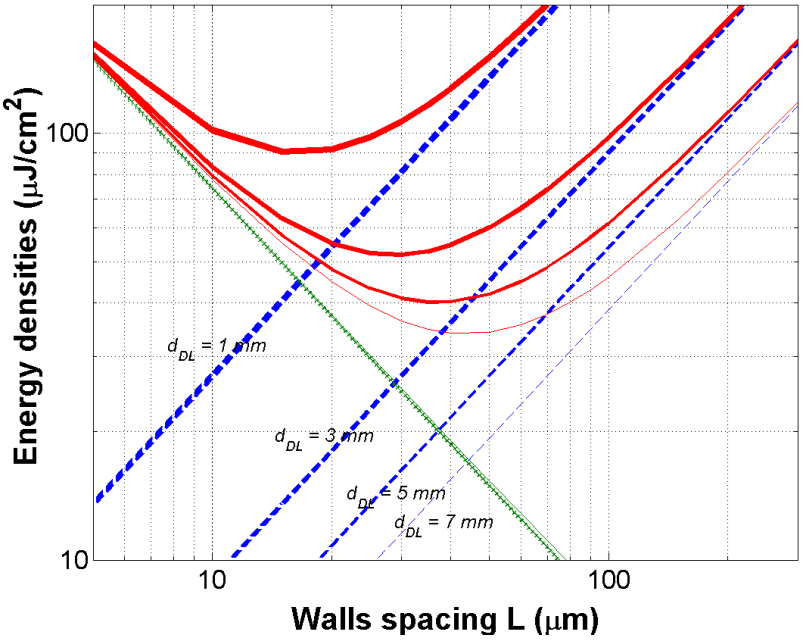

Figure 38: Sensitivity analysis of the energy contributions to the walls spacing L and the line spacing d_{DL}. ($J = J_s = 2T$, $\mathbf{u}_{an} = \mathbf{u}_{DL}$, $e = \zeta = 0.23$ mm, $p' = 100$ μm, $\delta \approx 0$ μm, $\theta_{DL} = \theta_J = \theta_W = 90°$). : walls energy, -- domains energy, – total energy.

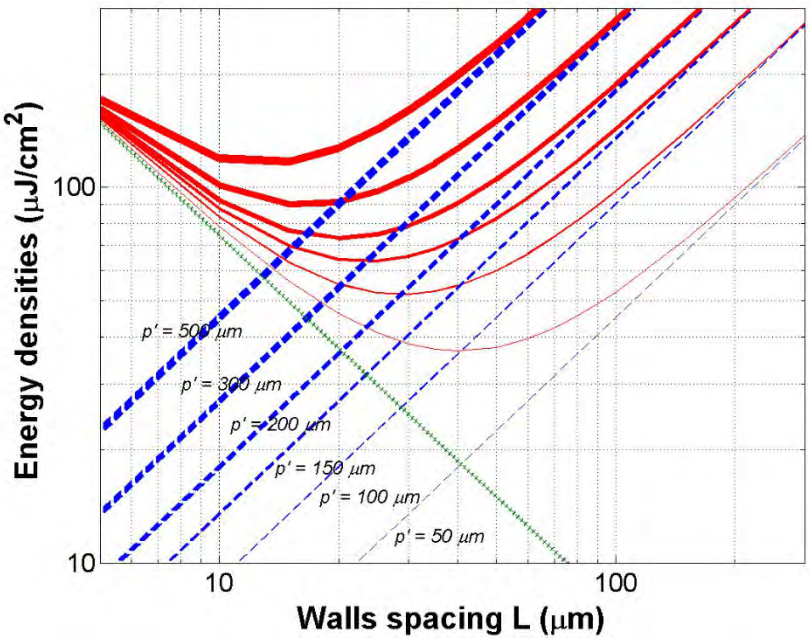

Figure 39: Sensitivity analysis of the energy contributions to the walls spacing and the HAZ depth p'. ($J_s = 2T$, $\mathbf{u}_{an} = \mathbf{u}_{DL}$, $e = \zeta = 0.23$ mm, $d_{DL} = 3$ mm, $\delta = 0$ μm, $\theta_{DL} = \theta_J = \theta_W = 90°$). : walls energy, -- domains energy, – total energy.

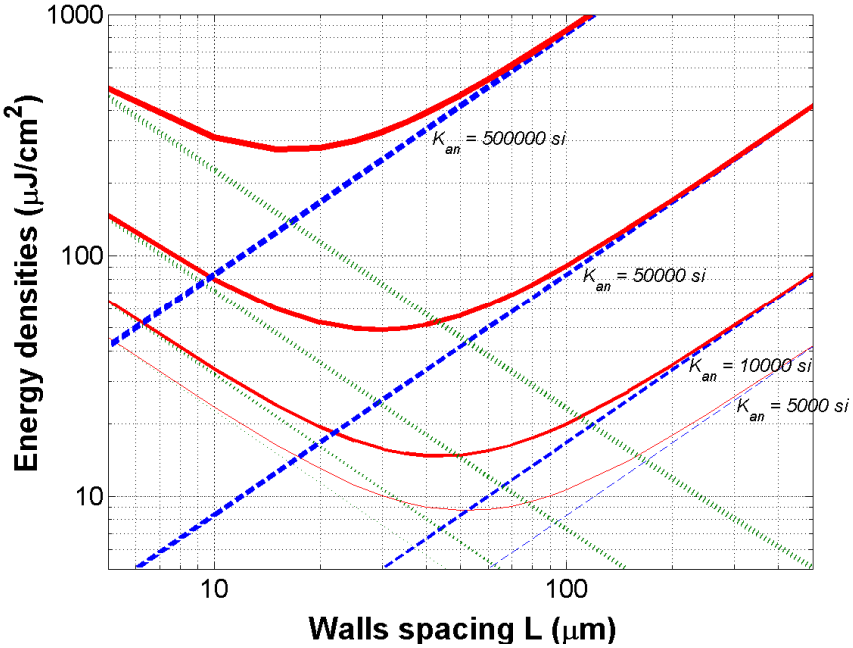

Figure 40: Sensitivity analysis of the energy contributions to the walls spacing and the walls energy. (J_s = 2T, $\mathbf{u}_{an} = \mathbf{u}_{DL}$, $e = \zeta$ = 0.23 mm, d_{DL} = 3 mm, p' = 100 μm, $\delta \approx 0$ μm, $\theta_{DL} = \theta_J = \theta_W$=90°). : walls energy, -- domains energy, – total energy.

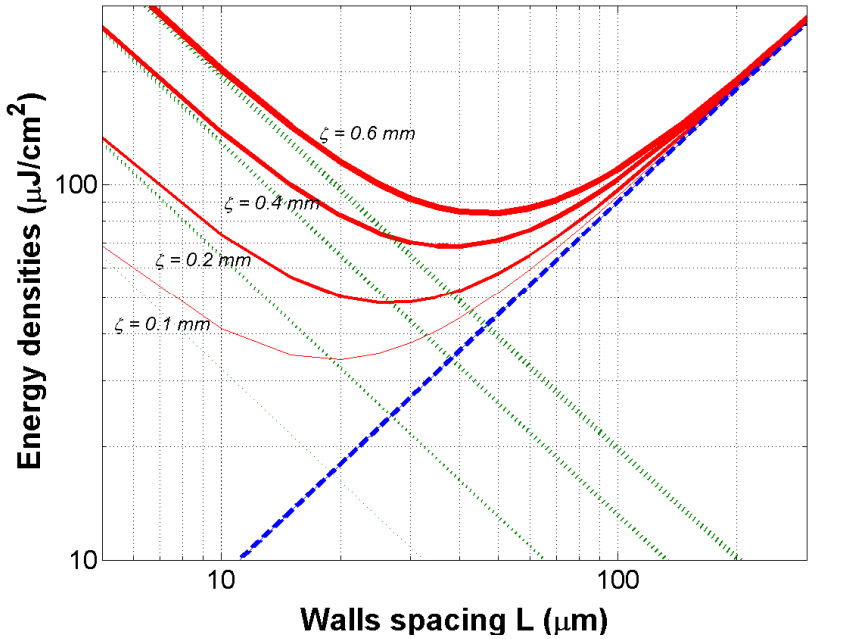

Figure 41: Sensitivity analysis of the energy contributions to the walls spacing and the sheet thickness. (J_s = 2T, $\mathbf{u}_{an} = \mathbf{u}_{DL}$, d_{DL} = 3 mm, p' = 100 μm, $\delta \approx 0$ μm, $\theta_{DL} = \theta_J = \theta_W$=90°). : walls energy, -- domains energy, – total energy.

In Figure 38-Figure 41, only closure domains are considered. We still assume that the depth of 180° Bloch walls equals the thickness $a = \zeta = e_p$ of the sample. At the same time, the 90° closure domains anisotropy energy due to laser induced stresses is estimated with the heat affected zone $a = p' = \delta'$. As expected, the walls energy increases when the walls spacing decreases (the number of walls increases). Meanwhile, the 90° closure domains anisotropy energy decreases when the walls spacing decreases (the closure domains become smaller). Therefore, it is coherent to find an optimal wall spacing which minimize the total energy and corresponds to the best compromise found by the material.

In Figure 38-Figure 39-Figure 41, the effect of the line spacing, the line depth and the sheet thickness on the closure domains' configuration is similar to that of the non-closure domains' configuration. The value of the minimum total energy can be either bigger or smaller than the one of the non-closure domains configuration, which determines the most probable magnetic structure chosen by the material.
On the contrary, in Figure 40, both the domains anisotropy energy and the walls energy increase when the macroscopic anisotropy constant increases. Consequently, the stronger the anisotropy, the finer the domains in order to reduce the size and volume of closure domains and therefore the total domains' energy. Naturally, the total energy minimum becomes higher when the anisotropy increases.

b. With induced stress

The closure domains configuration is sensitive either to global stresses induced by the manufacturing process or to the local laser induced stresses. However, the effects should be different due to the positive magnetostriction on 90° closure domains only.
In this part, we suggest analyzing the effect of a residual stress either induced by the manufacturing processes (rolling and coating processes) or the laser process (thermal induced stress) along the rolling direction 2 and the transverse direction 3 respectively.

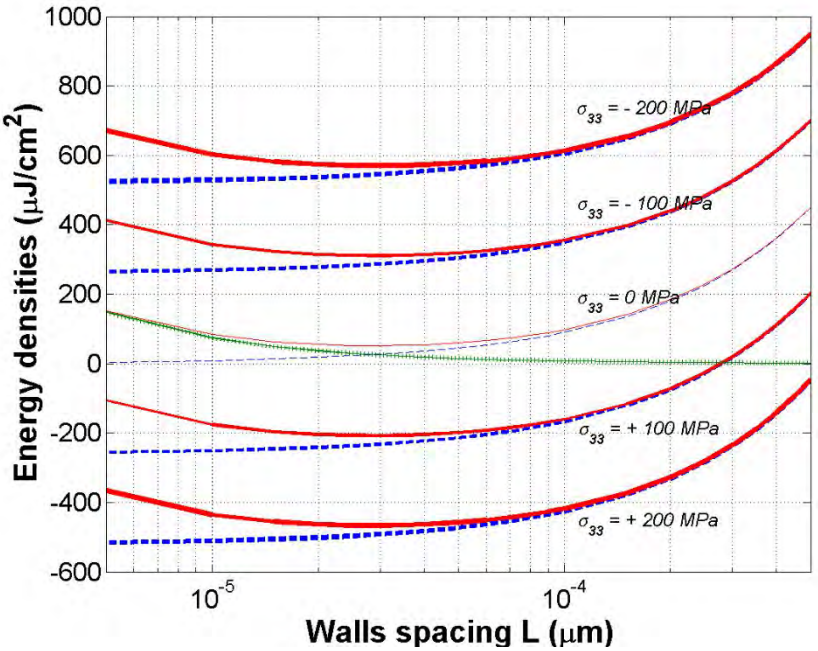

Figure 42: Sensitivity analysis of the energy contributions to the walls spacing and the global residual stress along the rolling direction. (J_s = 2T, $\boldsymbol{u}_{an} = \boldsymbol{u}_{DL}$, $e = \zeta$ = 0.23 mm, d_{DL} = 3 mm, p' = 100 μm, $\delta \approx 0$ μm, $\theta_{DL} = \theta_J = \theta_W$=90°). : walls energy, -- domains energy, – total energy.

In Figure 42-Figure 43, the walls energy does not depend significantly on the residual stress. The effect of the global residual stress in both directions 2 and 3 on the closure domains' configuration is similar to that of the non-closure domains' configuration, because the main 180° domains occupy the biggest volume of the material affected by the residual stress. The domains magnetostriction energy decreases for tensile stress and increases for compressive stress in the rolling direction 3. It increases for tensile stress and decreases for compressive stress in the transverse direction 2. In Figure 44-Figure 45, the effect of the local residual stress in both directions 2 and 3 on the closure domains' configuration is opposite to the effect of a global residual stress, because the only the 90° closure domains are affected by the residual stress. The domains magnetostriction energy increases for tensile stress and decreases for compressive stress in the rolling direction 3. It decreases for tensile stress and increases for compressive stress in the transverse direction 2.

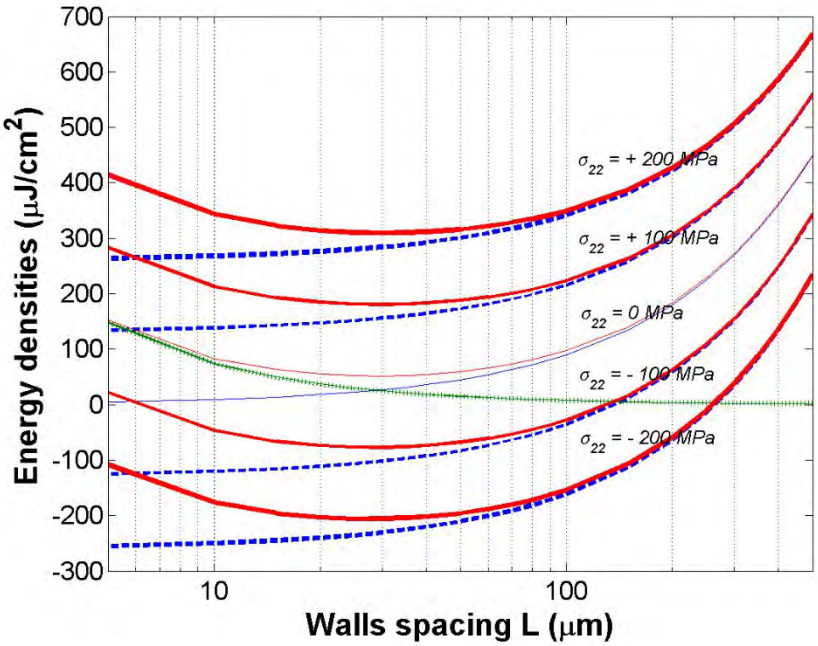

Figure 43: Sensitivity analysis of the energy contributions to the walls spacing and the global residual stress transverse to the rolling direction. (J_s = 2T, $\mathbf{u}_{an} = \mathbf{u}_{DL}$, e = ζ = 0.23 mm, d_{DL} = 3 mm, p' = 100 μm, δ ≈ 0 μm, $\theta_{DL} = \theta_J = \theta_W$=90°). : walls energy, -- domains energy, – total energy.

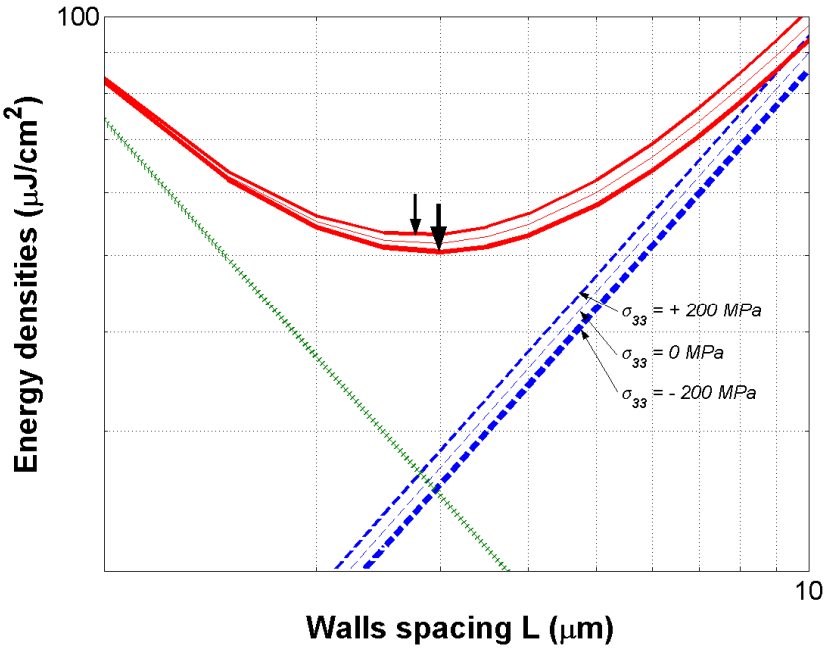

Figure 44: Sensitivity analysis of the energy contributions to the walls spacing and the local residual stress along the rolling direction. (J_s = 2T, $\mathbf{u}_{an} = \mathbf{u}_{DL}$, e = ζ = 0.23 mm, d_{DL} = 3 mm, p' = 100 μm, δ ≈ 0 μm, $\theta_{DL} = \theta_J = \theta_W$=90°). : walls energy, -- domains energy, – total energy.

We think that any local residual stress induced by the laser process either in direction 3 (rolling direction) or in direction 2/1 (direction transverse to the rolling direction) is likely to be a compressive stress. Thus, the latter will also cancel the benefit from any tensile stress used in purpose during the prior manufacturing processes. However, Both the irradiation and scribing processes can induce the domains refinement by another and more efficient way: reduction of the anisotropy field generated at the vicinity of laser impacts. In that case, the value of the local compressive stress will play an important role in the natural selection of the magnetic domains configuration that will take place in the material.

The latter is not necessarily the ones that corresponds to the finer domains but the lower total energy. Finally, the laser patterns may still be considered as new defect that can act as new nucleation and activation centers for the magnetic walls.

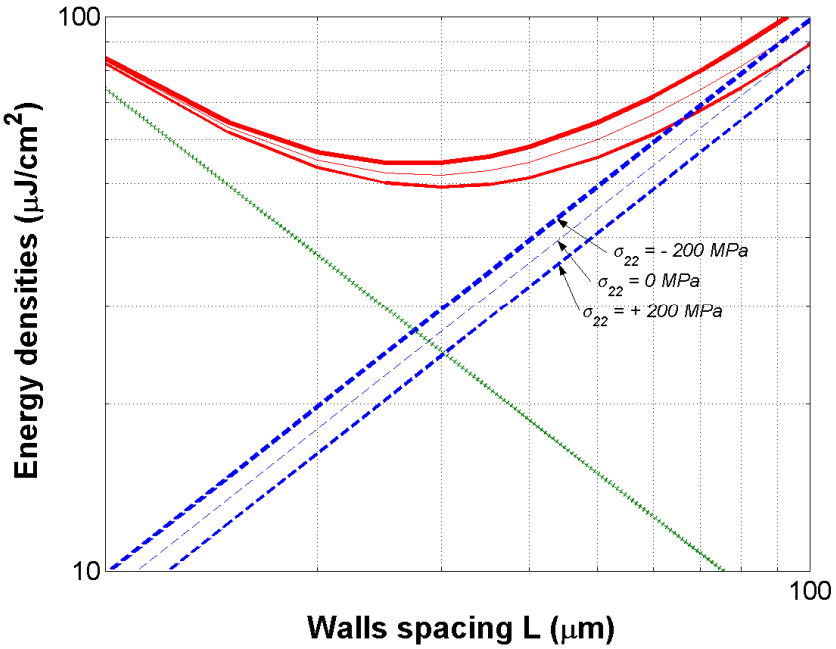

Figure 45: Sensitivity analysis of the energy contributions to the walls spacing and the local residual stress transverse to the rolling direction. (J_s = 2T, $\mathbf{u}_{an} = \mathbf{u}_{DL}$, e = ζ = 0.23 mm, d_{DL} = 3 mm, p' = 100 μm, $\delta \approx 0$ μm, $\theta_{DL} = \theta_J = \theta_W$=90°). : walls energy, -- domains energy, – total energy.

6. Conclusion and laser patterns proposals

Results seem coherent, but the equations written in a software programs can be compared to mathematical references and experimental observations done with AFM/MFM and MOKE imaging techniques (see deliverable D3.2.).
A finer magnetic structure should help to reduce the iron losses thanks to a higher walls' density, providing that the walls surface and mobility are unchanged or improved. Unfortunately, there will probably be a limitation to the reduction of domains size. In fact, the higher the lines and walls densities, the stronger the probability that the walls are pinned by the defects.

The present modeling might help us specify the laser patterns and parameters. Specifications sheets will be designed and completed according to first the experimental plan for investigations, then the proof of concept samples and finally the requirements of each specific prototype. It is proposed to vary only one parameter of the list in Table 6 at a time. The experimental plan is separated in four parts depending on the process (irradiation, scribing or ablation) and the dimensions (1D or 2D patterns).

7. Discussions

The present model can help us illustrate the impact of the laser treatments and different simple patterns on a classical and ideal magnetic structure with domains and walls. However, previous studies deserve further investigations, developments and improvements to consider some important additional aspects and answer the following questions:

1. How to be independent on the arbitrary choice of domains' shape?
2. How to describe more complex domains shape and magnetic objects?
3. What is the mutual influence of the volume and the surface?
4. What happens when adding the coupling with the external field?
5. How to inverse the model by defining the goal criteria and ease the determination of the optimal laser pattern and parameters?

So, the next steps are to address all these questions and to confront the theory against the experiment (see Deliverables D3.2. (version 2 at M24) and D3.1. (version 3 at M30)).

However, this method might be always confronted to serious limitations due to the huge number of degrees of freedom, considering the infinite variety of magnetic structures. Another solution based on structural but statistical state variables will be investigated in the next section of this report.

D) First modelling of the Volume Magnetic Structure – Tensor Magnetic Phase theory

I. Context and brief summary of the state of the art

Most of existing material representations [62], even including the dynamic hysteresis and iron losses [63], ignore local microscopic non uniformities. These concern the magnetic structure (domains and walls [64]) and are mainly due to surface effects, anisotropy and exchange. This structure has its origin in the possibility of lowering the energy of a system by going from a saturated configuration with high magnetic energy to a domains configuration, with a lower energy. The domains structure found are partially induced by the presence of the external surfaces of the crystal, and it is therefore not unexpected to find that it may be altered radically by changes in these surfaces. The size of a domain is not a fundamental length of physics, but rather sensitive to geometry and material in hand [65-68]. The microscopic scale is associated to the walls and domains; at the macroscopic scale we consider the geometry entirely. We will investigate the possibility to account for the sensitivity of the magnetic structure and its characteristic length to the macroscopic geometry at an intermediate scale called the mesoscopic one.

II. Tensor State Variable

1. Magnetic structures: Domains and walls

The drawings of Figure 46 have been made with the help of experimental observations [65-68] and micro magnetic arguments [67,68]. It is hard to imagine being able to identify this natural heterogeneity with the help of only one macroscopic global measurement, except if we preliminary know the way the structure will establish itself (The use of deterministic methods may moreover permit to limit the number of measurements needed). The dilemma is the same as the one that consists of distinguishing two different subdivisions, that cannot be separated by looking at one macroscopic quantity only. Unfortunately, we clearly feel that if we fix the property of a material previously homogenised, we may predict the response of one specimen, but we also might not be able to do it for another geometry [69,70]. Magnetic objects have got typical and characteristic topological and physical properties that we propose to describe thanks to one tensor state variable $[\Lambda^2]$, statistically gathering every microscopic information

$$\left[\Lambda^2\right] = \begin{bmatrix} \Lambda^2_{11} & \Lambda^2_{12} & \Lambda^2_{13} \\ \Lambda^2_{21} & \Lambda^2_{22} & \Lambda^2_{23} \\ \Lambda^2_{31} & \Lambda^2_{32} & \Lambda^2_{33} \end{bmatrix}, \begin{Bmatrix} \Lambda^2_{ii} \propto \lambda_j \lambda_k;\ \ j,k \neq i \ \ and \ \ i = 1..3 \\ \Lambda^2_{ij} \propto \lambda^2_k;\ \ k \neq j \neq i \ \ and \ \ i,j = 1..3 \end{Bmatrix} \qquad (D.1)$$

Where λ_i, λ_j and λ_k might correspond (with some topological, interaction and averaging corrections) to the typical shape and size of each cell constituting the magnetic structure.

$$\lambda_j \ \lambda_k \approx \left(S_{w,jk}\sqrt{2\sigma J_s n_{w,j} n_{w,k} m_{w,j} m_{w,k}}\right)^{-1} \propto length^2 \qquad (D.2)$$

J_s is the saturation magnetic polarisation, n_w is the walls volume density, m_w is the walls mobility and S_w is the walls surface.

Each factor of this tensor is homogeneous to a squared length, linked to walls density, surface, mobility, domains size, … [71,72]. The model is inspired from the Néel domains phase model.

Of course, using one degree of freedom for three dimensions microscopic objects, we still may not discern different magnetic structures that have got comparable space variations and mesoscopic properties. However, it should have no consequence because it contains a minimum required information concerning the resulting geometry dependent vector behaviour. Phenomena that we aim to consider. Finally, we will need to use the inverse tensor $[V]$ of $[\Lambda]$ (such that $[V]= [\Lambda]^{-1}$ with $[\Lambda^2]= [\Lambda]^2$ and $[V^2]= [V]^2$)

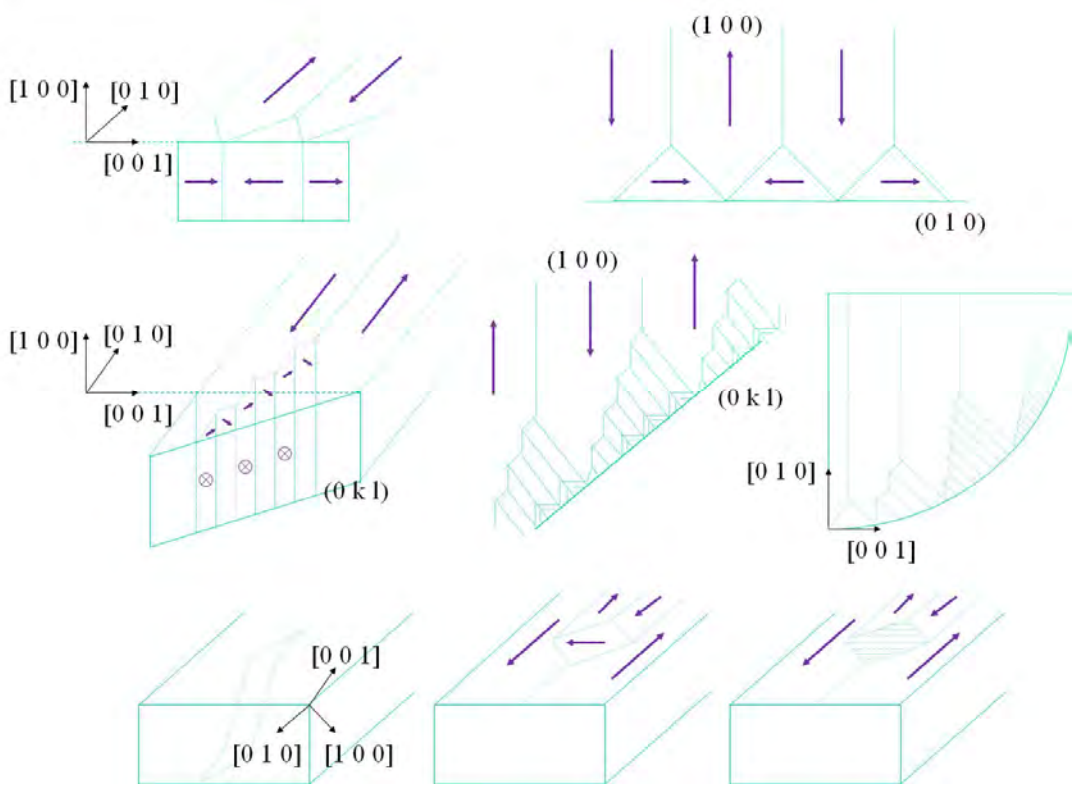

Figure 46: Some heterogeneity and non-uniformity effects. Re-orientation, multiplication and refinement within the microscopic magnetic structure [3-5]. Surface, bulk and non-closure domains examples as a function of the texture, i.e. the crystal axes [m,n,p] and the crystal planes (j,k,l).

In the next section, we propose a theory that may provide an alternative to foresee and calculate this mesoscopic diversity.

2. Magnetic polarization

Microscopic magnetic objects have got typical and characteristic topological and physical properties that we have proposed to describe thanks to one tensor state variable $[\Lambda^2]$, statistically gathering every microscopic information [82]. It is closely related to mean length of one pair of domains, and so it can be viewed as the sum (D.3) of two new tensor variables $[\Lambda\uparrow^2]$ and $[\Lambda\downarrow^2]$ in order to account for the actual organisation with opposite neighbouring domains

$$[\Lambda^2] = \left[\Lambda_\uparrow{}^2\right] + \left[\Lambda_\downarrow{}^2\right] \tag{D.3}$$

Equation (D.3) looks like a volume conservation law. Each factor of these tensors is homogeneous to a squared length, linked to walls density, surface, mobility, domains size, … and so on … Thus, they vary in space and time like $[\Lambda^2]$; They will be our degrees of freedom. We will then define the magnetic polarisation of a soft material with these two tensors and with the natural saturation polarisation (the one carried by each domain of constant magnetisation). J_s being the saturation magnetic polarisation, we can define the local magnetic polarisation $\boldsymbol{J}(\boldsymbol{x},t)$ by (D.4)

$$\begin{aligned} [\Lambda^2]\vec{J} &= \left(\left[\Lambda_\uparrow{}^2\right] - \left[\Lambda_\downarrow{}^2\right]\right)\vec{J_s} \\ \Leftrightarrow \vec{J} &= [\Lambda^2]^{-1}\left(\left[\Lambda_\uparrow{}^2\right] - \left[\Lambda_\downarrow{}^2\right]\right)\vec{J_s} \end{aligned} \tag{D.4}$$

We saw that the three tensors involved are symmetrical and written with real coefficients [82]. They are so diagonalisable [83] (see above (D.1) definition of $[\Lambda^2]$). We can also show that the basis in which $[\Lambda\uparrow^2]$ and $[\Lambda\downarrow^2]$ are diagonal might exactly be the same and at every point $(\boldsymbol{x},t)$, even if it can be different from point to point. This assertion simply comes from the fact that there exist an anisotropy and identical easy axes for polarisation vectors that are in opposite directions [84]. When (D.4) is written in the basis B_d that makes all the tensors diagonal, then $\boldsymbol{J_s}$ writes $\boldsymbol{J_s} = J_s(1,1,1)^T$. Moreover, even if $[\Lambda\uparrow^2]$ and $[\Lambda\downarrow^2]$ vary in space and time with different values for magnetized materials, as for $[\Lambda^2]$ and $\boldsymbol{J}$, a magnetic state will be defined with $[\Lambda^2]\vec{J} = \left(\left[\Lambda_\uparrow{}^2\right] - \left[\Lambda_\downarrow{}^2\right]\right)\vec{J_s}$ somehow a constant vector in space (without any divergence nor rotational properties). If we know the temporal and spatial evolutions of tensor $[\Lambda^2]$, then we can easily deduce the magnetic polarisation $\boldsymbol{J}$ thanks to Equation (D.4).

III. Quasi-Static Energy tendencies

The natural structuring and its space variations come from a competition between several energy terms [75]. The contributions proposed are all expressed in [J.m^{-3}] (volume energy density), except $\boldsymbol{e_{dm}}$ which is homogeneous to a surface energy density ([J.m^{-2}]) (the operators $\cdot$, $\times$, $[\nabla\times]$, $\vec{\cdot}$ and $\vdots$ are explained in the **Appendix A** [76]).

1. The mesoscopic magnetic exchange energy

The interaction between neighbouring domains and walls involves an amount of energy that we propose to write as follows

$$\vec{e}_{ex} = C_{ex}\frac{\gamma_w^6}{K_{an}^5}\left([\nabla] \times [\Lambda^2]^{-1} \right)^{\vec{\cdot}2} \qquad \text{(D.5)}$$

γ_w is the walls energy density [J.m^{-2}].

$K_{an}=|\boldsymbol{K_{an}}|=|\vec{\mathrm{K}}_{an}|$ is the module of the macroscopic anisotropy vector [J.m^{-3}].

C_{ex} is a magnetic exchange coefficient without any dimension [n.u.].

This energy vector describes a natural tendency of the material (called *Mesoscopic Exchange Energy*) to make homogeneous its magnetic structure and magnetization. This effect may be even more important since the wall energy is strong (γ_w >>) and the anisotropy is weak ($K_{an}=|\vec{\mathrm{K}}_{an}|$<<). $[\nu]=[\nabla]\times[\Lambda^2]^{-1}$ corresponds to a non-divergent current of exchanging walls, that takes part to the energy.

2. The mesoscopic magnetic anisotropy energy

This second energy vector describes another tendency (called *Mesoscopic Anisotropy Energy*) that leads the material to orientate its domains and walls along one or several directions, determined by the most favourable mesoscopic anisotropy axes. The latter, involved in $\boldsymbol{K_{an}}$, depend on both the crystallographic texture and metallographic assembly in grains, including the defects [77,78]. This energy depends on the difference between natural and actual directions, weighted by walls equivalent density (Λ^{-2}) and the ratio (γ_w/K_{an}) to take the walls energy, partly due to the microscopic anisotropy, into account.

$$\vec{e}_{an} = C_{an}\frac{\gamma_w^4}{K_{an}^3}\left([\Lambda^2]^{-1} - \left(\frac{\vec{K}_{an}\cdot\left([\Lambda^2]^{-1}\cdot\vec{K}_{an}\right)^T}{|\vec{K}_{an}|^2} \right)^T \right)^{\vec{\cdot}2} \qquad \text{(D.6)}$$

$\vec{\mathrm{K}}_{an}=\boldsymbol{K_{an}}$ is the macroscopic anisotropy vector [J.m^{-3}].

C_{an} is a macroscopic anisotropy coefficient without any dimension [n.u.].

3. The mesoscopic magnetoelastic anisotropy energy

a. *The self-magnetostriction energy*

This energy vector describes another tendency (called *Mesoscopic Self Magnetostriction Energy*) that leads to a magnetization induced strain in the material and thus a magneto-elastic energy. The directions of the magneto-strictive strains are determined by the orientations of the polarized domains (each domain carries a magnetic polarization which corresponds to the saturation polarization in a direction given by the domain orientation). The magnitude of the strains and the energy depend on the magnetostriction coefficients λ_{100} and λ_{111} in directions *[100]* and *[111]* respectively, the magnetoelastic properties of the material, and the equivalent size Λ of domains.

$$\vec{e}_{\lambda\varepsilon} = +\frac{9}{4} C_\lambda \frac{\gamma_w^4}{K_{an}^4} [\Lambda^2]^{-1} \vec{\cdot} \left([\lambda^2] \div [C] \div [\Lambda^2]^{-1} \right) \tag{D.7}$$

[λ] is the magnetostriction tensor with *[100]* for the diagonal and *[111]* for the non-diagonal terms. *[C]* is a stiffness tensor containing the linear elastic properties of an orthotropic or isotropic material.

$$[\lambda^2] = \begin{bmatrix} \lambda_{100}^2 & \pm\lambda_{111}^2 & \pm\lambda_{111}^2 \\ \pm\lambda_{111}^2 & \lambda_{100}^2 & \pm\lambda_{111}^2 \\ \pm\lambda_{111}^2 & \pm\lambda_{111}^2 & \lambda_{100}^2 \end{bmatrix} \text{ and } [C] = \begin{bmatrix} C11 - C12 & C44 & C55 \\ C44 & C22 - C23 & C66 \\ C55 & C66 & C33 - C13 \end{bmatrix} \tag{D.8}$$

C_λ is a magnetostriction coefficient without any dimension.

b. *The magnetostriction stress induced anisotropy energy*

This energy vector (called *Stress Induced Anisotropy Energy*) describes the change in anisotropy and in the magnetization due to an external stress. The directions of the stresses define the new directions to be considered in the total macroscopic anisotropy. The magnitude of the energy depends on the magnetostriction coefficients λ_{100} and λ_{111}, the stress value and the equivalent size Λ of domains in each stress direction.

$$\vec{e}_{\lambda\sigma} = -\frac{3}{2} C_\lambda \frac{\gamma_w^4}{K_{an}^4} [\Lambda^2]^{-1} \vec{\cdot} \left([\lambda] \div [\sigma] \div [\Lambda^2]^{-1} \right) \tag{D.9}$$

[σ] is the stress tensor [Pa].

4. Microscopic eddy currents

Any physical mechanism that leads to a new magnetic structure costs some energy. We know that any change in the magnetic structure is not reversible, but rather dissipative with losses. The latter mainly come from eddy currents induced around the walls in motion and in magnetic domains with rotating magnetization. Let's assume that any change in the global magnetic energy minimum, which is responsible for the change in magnetization

and magnetic structure, can only increase in time due to eddy current losses induced by the time variations of $[\Lambda^2]$.

$$\vec{e}_\tau = +\frac{\gamma_w^4}{K_{an}^3}\tau\partial_t[\Lambda^2]^{-1}\vec{:}\,\delta[\Lambda^2]^{-1} \qquad \text{(D.10)}$$

τ is a time delay due to eddy currents *[ms]*. It is closely related to the time delay given by previous models $\tau \propto \sigma\Lambda^2\mu$. And due to microscopic eddy currents, both around walls and inside domains. This effect can be considered as a damper equivalent to a dynamic induced anisotropy always perpendicular to the directions given by $[\Lambda^2]$.

5. Demagnetizing energy

Finally, the last energy term is mainly due to the surface dipolar magnetic energy.

$$\vec{e}_{dm} = C_{dm}\frac{K_{an}^4}{\gamma_w^3}\left(\vec{n}\cdot\left([\Lambda^2]\cdot\vec{n}\right)^T\right)^{\cdot 2} \qquad \text{(D.11)}$$

n is the unit vector normal to the outer surface of the geometry considered.

C_{dm} is a metallurgical parameter that can depend on the grain's boundary spacing and the surface laser treatment (laser lines depth and spacing)

This vector tends to orientate the magnetic moments [66], multiply and refine the domains, in order to create as few poles as possible. It is different from zero on the surface only (the material often manages to create a minimum charge within the bulk, even if it cannot avoid it onto the surface) [63,64]. This energy even more important that the surface domains are big, the anisotropy is strong, and the walls energy is weak. In one of the next sections and in the next deliverable update, we will propose to develop a surface and coupling model to describe the surface magnetic structure, minimizing the energy terms that correspond to this surface. C_{dm} is one of the key parameters that determines Λ at the surface.

IV. Formulation

In this last sub-section, we clarify better and interpret longer the effects of the different tendencies. Finally, we propose and discuss a governing equation (D.12).

1. Energy minimization principle

As a conclusion, the magnetic structure will establish itself by minimising the total following energy of the system {volume Ω, outer surface $\partial\Omega$}

$$\vec{\mathrm{E}}_\mathrm{m} = \iiint_\Omega (\vec{\mathrm{e}}_\mathrm{m})\mathrm{d}^3x = \iiint_\Omega (\vec{\mathrm{e}}_\mathrm{ex} + \vec{\mathrm{e}}_\mathrm{an} + \vec{\mathrm{e}}_{\lambda\epsilon} + \vec{\mathrm{e}}_{\lambda\sigma} + \vec{\mathrm{e}}_\tau)\mathrm{d}^3x$$
$$+ \iint_{\partial\Omega}(\vec{\mathrm{e}}_\mathrm{m} + \vec{\mathrm{e}}_\mathrm{dm})\mathrm{d}^2\mathrm{x} \quad \text{to be lowered} \qquad \text{(D.12)}$$

This description can be developed thanks to additional contributions due to miscellaneous parameters (volume charges, temperature, stresses, …). Finally, each contribution appears here quasi-static without any field interactions. The coupling with the quasi-static magnetic field can be considered with a border static condition. The dynamic diffusion and the coupling with the time varying field may be taken afterwards into account with the Maxwell Equations [63,71], or with the volume dynamic term $\boldsymbol{e_\tau}$ and with a border's dynamic condition (see [72] and [81]).

2. Non divergence condition

We study first the ensemble {Exchange, Anisotropy, Magnetostriction, Eddy current losses} weakly varying the tensor $[\Lambda^2]$ (see **Appendix A** for usual identities). We assume that the material has succeeded in minimising its magnetic charges, by orientating most of its domains and walls tangentially to the surface, or by multiplying and refining them. So, we also have:

$$\iint_{\partial\Omega}[\Lambda^2]\cdot\vec{n}d^2x=\iint_{\Omega}\vec{\nabla}\cdot[\Lambda^2]d^3x=\vec{0}\Leftrightarrow\vec{\nabla}\cdot[\Lambda^2]=\vec{0}\ and\ \vec{\nabla}\cdot[V^2]=\vec{0} \tag{D.13}$$

The divergence of $\boldsymbol{J}=\vec{\mathrm{J}}$ is closely linked to the one of $[\Lambda^2]$ (D.13) ($\left[\vec{\nabla}\otimes\vec{\mathrm{J}}_s\right]=[0]$, explanations given in **Appendix A** of [82])

$$\vec{\nabla}\cdot\vec{J}=\vec{\nabla}\cdot\left([\Lambda^2]^{-1}\left(\left[\Lambda_\uparrow{}^2\right]-\left[\Lambda_\downarrow{}^2\right]\right)\right)\vec{J}_s \tag{D.14}$$

The non-divergence condition on $[\Lambda^2]$ is so closely linked to the one acting on $\boldsymbol{J}=\vec{\mathrm{J}}$. In fact, we have the obvious and certain following implication (with (D.14) and $\vec{\nabla}\cdot\vec{\mathrm{J}}=0$, we can show that the reciprocal relation of (D.15) is also true.)

$$\vec{\nabla}\cdot\left([\Lambda^2]^{-1}\left[\Lambda_\uparrow{}^2\right]\right)=\vec{\nabla}\cdot\left([\Lambda^2]^{-1}\left[\Lambda_\downarrow{}^2\right]\right)=0\Leftrightarrow\vec{\nabla}\cdot\vec{J}=0 \tag{D.15}$$

The variational principle applied onto the action E_m seems to give us two interesting clues [79] (see next sub-sections).

3. Limit conditions

First the matrix $[\mathrm{n}]\otimes\left([\nabla\times]\left[\Lambda^2\right]^{-1}\right)$ keeps constant at each interface of $\partial\Omega$. It does not exist in substances without any domains and walls; it will therefore be nil at the edge between such a classical material and a structured one. It means that the rotational evolutions within the magnetic structure stop against the outer surface along its normal unit vector.

It seems that the non-divergence condition on $[\Lambda\uparrow^2]$ and $[\Lambda\downarrow^2]$ implies the absence of volume charges because then $\vec{\nabla}\cdot\vec{\mathrm{J}}=0$ (D.15). However there can always exist surface charges depending on the direction of $\vec{\mathrm{J}}$ and polarisations of surface domains relative to

the normal vector of the enclosing surface, even if the divergence theorem [69] tells us that the global surface integrals $\oiint_{\partial\Omega}\left([\Lambda^2]\cdot[\mathrm{n}]\right)\mathrm{d}^2\mathrm{x}$ and $\oiint_{\partial\Omega}\left(\vec{\mathrm{J}}\cdot\vec{\mathrm{n}}\right)\mathrm{d}^2\mathrm{x}$ equal thus 0 [65].

4. Tensor PDE

Secondly, the tensor property into Ω obeys the following partial differential equation

$$[\Delta]\ [\mathrm{V}^2]\text{-}\vec{\nabla}\left(\vec{\nabla}.[\mathrm{V}^2]\right)\text{-}\frac{\mathrm{C_{an}}}{\mathrm{C_{ex}}}\left(\frac{\mathrm{K_{an}}}{\gamma_\mathrm{w}}\right)^2\left([\mathrm{V}^2]\text{-}\left(\frac{\vec{\mathrm{K}}_{\mathrm{an}}\left([\mathrm{V}^2]\vec{\mathrm{K}}_{\mathrm{an}}\right)^{\mathrm{T}}}{\mathrm{K}_{\mathrm{an}}^2}\right)^{\mathrm{T}}\right)$$
$$+\frac{3}{2}\frac{C_\lambda}{C_{ex}}\left(\frac{K_{an}}{\gamma_w}\right)^2\left(\frac{[\lambda]\vdots[\sigma]}{K_{an}}\vdots[V^2]\right)\text{-}\frac{9}{4}\frac{C_\lambda}{C_{ex}}\left(\frac{K_{an}}{\gamma_w}\right)^2\left(\frac{[\lambda^2]\vdots[C]}{K_{an}}\vdots[V^2]\right)\text{-}\left(\frac{K_{an}}{\gamma_w}\right)^2\tau\partial_t[V^2]=[0] \qquad \text{(D.16)}$$

We call this equation the tensor structuring equation for the magnetic structure.

We define κ *[mm^{-2}]* the squared ratio between the total anisotropy (either magneto-crystalline, magneto-strictive or stress induced) and the magnetic exchange:

$\kappa = \kappa_{an} + \kappa_{\lambda\varepsilon} - \kappa_{\lambda\sigma}$

$=(C_{an}/C_{ex})*(K_{an}/\gamma_w)^2 + (C_\lambda/C_{ex})*(K_{an}/\gamma_w)^2(9\lambda^2C/4K_{an}) - (C_\lambda/C_{ex})*(K_{an}/\gamma_w)^2(3\lambda\sigma/2K_{an})$

determines the space variations of $[V^2]=[\Lambda^2]^{-1}$ *(structuring depth).*

$\kappa_{\lambda\varepsilon}$ is always positive and corresponds to an equivalent negative compressive stress.

$\kappa_{\lambda\sigma}$ can contain the manufacturing stress or/and the laser induced stress. $\kappa_{\lambda\sigma}$ is positive for negative compressive stress and negative for positive tensile stress.

Let's define $\kappa_s = \kappa_{\lambda\varepsilon} - \kappa_{\lambda\sigma r}$ the natural magnetostriction anisotropy due to either self-magnetostriction and manufacturing stress (σ_r being the residual stress) and $\kappa_{si} = -\kappa_{\lambda\sigma i}$ the laser induced stress anisotropy ($\sigma_r = \sigma_T$ or σ_m being the laser induced stress).

V. Static and dynamic Magnetization

1. Vector magnetic behaviour

When a varying magnetic field is applied to the material, some memory effects (called hysteresis) and eddy currents are induced within the microscopic mechanisms around defects and magnetic walls. It manifests itself in a magnetic behaviour, characterised by a delayed relationship between the magnetic field ***H*** and the flux density ***B***.

a. Origin of Static Hysteresis

This hysteresis is mainly due to hampering and jumps of magnetic walls [85] around defects, grains joints, … and local microscopic unavoidable magnetic charges. Changes in the applied magnetic field can make the walls move when a threshold is excited to counterbalance the opposition of the charges. Then the walls irreversibly jump, inducing eddy currents and losses. It naturally depends on the history of the material (existing structure and hampered walls on defects plus succession of field applied [86]).

b. Origin of Dynamic Hysteresis

The dynamic hysteresis is mainly due to eddy currents induced with time varying fields and polarisations at the mesoscopic scale within domains and at the microscopic scale around moving domain walls [87]. They can be homogenised and included in a behavioural model, dedicated to the magnetic field damping and involving the tensor variable $[\Lambda^2]$.

c. Magnetic behavioural law

All these phenomena "delay" the flux density or the induction $\boldsymbol{B} = \mu_0\boldsymbol{H}+\boldsymbol{J} = \mu_0(\boldsymbol{H}+\boldsymbol{M})$ such that the magnetic field $\boldsymbol{H}$ (D.17) becomes the sum of the quasi-static magnetic field $\boldsymbol{H_M}$ ([10], the excess static hysteresis field $\boldsymbol{H_s(B)}$ due to hysteresis and the dynamic field $\boldsymbol{H_{dyn}(B,\partial_t B)}$ due to motion of domain walls (see (D.17))

$$\begin{aligned}\vec{H}(\vec{B}, History, \partial_t\vec{B}) &= \vec{H}_M(\vec{B}) + \vec{H}_s(\vec{B}, History) + \vec{H}_{dyn}(\vec{B}, \partial_t\vec{B})\\ \vec{H}_M(\vec{B}) &= \nu\vec{B} = \mu^{-1}\vec{B}\\ \vec{H}_s(\vec{B}) &\approx \nu_c\vec{B}\\ \vec{H}_{dyn}(\vec{B}, \partial_t\vec{B}) &= \sigma_e[\Lambda^2](\vec{B}, \partial_t\vec{B})\partial_t\vec{B}\end{aligned} \quad \text{(D.17)}$$

$\mu=\nu^{-1}$ and ν are the quasi-static magnetic permeability and reluctivity respectively [H/m].

ν_c is the complex coercive reluctivity (static hysteresis field other flux density) [m/H]

σ_e is the electrical conductivity [S/m]

$\mu_0=4\pi.e\text{-}7$ H/m is the vacuum magnetic permeability.

The equivalent relationship between the fils $\boldsymbol{H}$ and the magnetic polarization $\boldsymbol{J}$ becomes:

$$\left(\left(1-(\nu+\nu_c)\mu_0\right)-\sigma_e[\Lambda^2]\mu_0\partial_t\right)\vec{H} = ((\nu+\nu_c)+\sigma_e[\Lambda^2]\partial_t)\vec{J} \quad \text{(D.18)}$$

2. Coupling with the magnetic field $\boldsymbol{H}$ – magnetic polarization $\boldsymbol{J}$

Coupling the volume structuring model and the magnetic field consists in using the behavioral law (D.17) at the surface of the material, involving the surface magnetic structure $[\Lambda_0^2]=[\Lambda^2]_{surf}$, which represents the limit condition of the model. We suggest analysing the magnetic behaviour with the help of Bode diagrams (see Figure 52). We assume that $[V_0^2]$ is known (next sections for examples) and that $[\Lambda^2]\boldsymbol{J}=[\Lambda_0^2]\boldsymbol{J_{surf}}$ is a constant vector, independent from z, that we can determine using (D.18) at the surface for time harmonics with angle velocity ω ($\boldsymbol{H_a}=\boldsymbol{H_{surf}}$, $\boldsymbol{H_s}\sim\boldsymbol{0}$ neglected, $\mu=\mu_0\mu_r=\mu_0(1+\chi)$).

$$\vec{J} = [V^2]\left[\Lambda_0^2\right]\frac{\left[\left(\frac{\chi}{1+\chi}-\nu_c\mu\right)-j\sigma_e\left[\Lambda_0^2\right]\mu_0\omega\right]}{\left[(1+\nu_c\mu)+j\sigma_e\left[\Lambda_0^2\right]\mu\omega\right]}\mu\overrightarrow{H_a} \xrightarrow[\mu_0\ll\mu]{\nu_c\mu\ll1} \vec{J} \approx [V^2]\left[\Lambda_0^2\right]\left[1+j\sigma_e\left[\Lambda_0^2\right]\mu\omega\right]^{-1}\mu\overrightarrow{H_a} \quad \text{(D.19)}$$

Whatever the experimental tool used, we can *a priori* only measure and access the magnetic field $\boldsymbol{H_a}$ applied onto the enclosing surface and the mean flux density $\langle\boldsymbol{B}\rangle_r$, averaged inside the volume Ω considered. In some usual and convenient configurations

(closed magnetic circuit), the mean magnetic polarisation $<\boldsymbol{J}>_{\boldsymbol{r}}$ can also be determined. $\boldsymbol{J}$ checks (D.19) and $\boldsymbol{H}$ can be given by (D.18). It is so finally possible to build the magnetic behaviour $<\boldsymbol{B}>_{\boldsymbol{r}}(\boldsymbol{H_a})$ and the averaged total loss density $<<p>_{\boldsymbol{r}}>_t=<\boldsymbol{H_a}<\partial_t\boldsymbol{B}>_{\boldsymbol{r}}>_t$.

3. Apparent permeability

To study the magnetic response, we examine the reduced apparent permeability defined in our case by (D.20):

$$\frac{\vec{\mu}_{app}}{\mu}=\frac{\langle\vec{J}\rangle_r}{\mu H_a}=\frac{1}{\zeta}\int_{-\zeta/2}^{+\zeta/2}\frac{\vec{J}}{\mu H_a}dz \qquad \text{(D.20)}$$

4. Total iron losses

The mean total power loss density becomes the sum of two contributions:

$$\begin{aligned}\ll p >_r>_t&=< \vec{H}_{surf} < \partial_t\vec{J} >_r>_t=\ll p_{stat} >_r>_t +\ll p_{dyn} >_r>_t\\ &=< \vec{H}_{s,surf} < \partial_t\vec{J} >_r>_t +< \vec{H}_{dyn,surf} < \partial_t\vec{J} >_r>_t\end{aligned} \qquad \text{(D.21)}$$

The fields acting are applied onto the enclosing surface. $<.>_{\boldsymbol{r}}$ means a volume average in space and $<.>_t$ means a time average operation. No classical losses appear here. All the contributions due to varying induced "diffusion" are supposed to be included in the dynamic term (see (D.21) and Figure 53), where $\boldsymbol{H_{dyn,surf}}$ and $<\partial\boldsymbol{J}>_{\boldsymbol{r}}$ contain every damping effect due to heterogeneous and non-uniform domain walls motion and eddy currents as well.

VI. Computation and theoretical results – test cases

1. 1D static and magneto-harmonic testcases

Let's consider a magnetic sheet of thickness ζ. Let's use the *(x,y,z)* or *(1,2,3)* reference frame for which axis 1 or *x* corresponds to the rolling direction, 2 or *y* corresponds to the transverse direction and *z* corresponds to the thickness. The 1D approximation consists in assuming no space variation in directions *x* and *y* but only in direction z. We also consider only time harmonics variations. The Partial Differential Equation PDE (D.16) becomes:

$$\begin{aligned}&\partial_z^2\,[\mathrm{V}^2]-\frac{\mathrm{C_{an}}}{\mathrm{C_{ex}}}\left(\frac{\mathrm{K_{an}}}{\gamma_w}\right)^2\left([\mathrm{V}^2]-\left(\frac{\vec{\mathrm{K}}_{\mathrm{an}}([\mathrm{V}^2]\vec{\mathrm{K}}_{\mathrm{an}})^{\mathrm{T}}}{\mathrm{K}_{\mathrm{an}}^2}\right)^{\mathrm{T}}\right)\\ &+\frac{3}{2}\frac{C_\lambda}{C_{ex}}\left(\frac{Kan}{\gamma_w}\right)^2\left(\frac{[\lambda]\div[\sigma]}{Kan}\div[V^2]\right)-\frac{9}{4}\frac{C_\lambda}{C_{ex}}\left(\frac{Kan}{\gamma_w}\right)^2\left(\frac{[\lambda^2]\div[C]}{Kan}\div[V^2]\right)-j\left(\frac{Kan}{\gamma_w}\right)^2\tau\omega[V^2]=[0]\end{aligned} \qquad \text{(D.22)}$$

Let's work with a perfectly (GO) or partially (GO) oriented material of mass density *d*, linear properties (magnetic permeability $\mu=\nu^{-1}=\mu_r\mu_0$ and electric conductivity $\sigma_e=\rho^{-1}$). We will focus onto the average magnetic polarisation and the mean power losses within time

harmonics (frequency *f* and $\omega=2\pi f$). We will highlight the role played by both the geometry and the magnetic structure on these global quantities.

a. *Calculation of the magnetic structure*

(i) GO SiFe

For GO SiFe materials, we assume that the magnetic structure can be approximately described with a diagonal tensor $[V^2] = [\Lambda^2]^{-1}$.

$$[V^2] = \begin{bmatrix} V_{11}^2 & 0 & 0 \\ 0 & V_{22}^2 & 0 \\ 0 & 0 & V_{33}^2 \end{bmatrix} \tag{D.23}$$

we use the following input parameters and limit conditions:

$\zeta=0.5\ mm$ and $\kappa_{an} = \frac{C_{an}}{C_{ex}}\left(\frac{K_{an}}{\gamma_w}\right)^2 = (4/\zeta)^2\ mm^{-2}$ with $\boldsymbol{u_{an}}=(1,0,0)^T$.

$\Lambda_{110}=100\mu m$, $\Lambda_{220}=\Lambda_{330}=200\mu m$, $\Lambda_{120}=\Lambda_{130}=\Lambda_{230}=10000\mu m$ >> at the surface.

The PDE corresponding to the three unknowns V_{ii}^2 (i=1..3) are:

$$\left(\partial_z^2 . - \kappa_{ii}(1+\tau_{ii}\partial_t .)\right)V_{ii}^2 = 0 \tag{D.24}$$

With

$\kappa_{11} = \kappa_{s,11}$ and $\kappa_{ii} = \kappa_{an} + \kappa_{s,ii}$ for i=2,3

$$\kappa_{s,ii} = \frac{C_\lambda}{C_{ex}}\left(\frac{K_{an}}{\gamma_w}\right)^2\left(\frac{3\lambda_{100}}{2K_{an}}\right)\left(\frac{3}{2}\lambda_{100} - \sigma_{ii}\right), \sigma_{ij} = 0$$

$$\tau_{ii} = \left(\frac{K_{an}}{\gamma_w}\right)^2 \tau \Big/ \kappa_{ii}$$

The time harmonic solutions with angle velocity ω are given by:

$$V_{ii}^2(z) = V_{ii0}^2 \frac{cosh\left(\sqrt{\kappa_{ii}(1+j\tau_{ii}\omega)}z\right)}{cosh\left(\frac{\sqrt{\kappa_{ii}(1+j\tau_{ii}\omega)}\zeta}{2}\right)}, \quad i = 1,2,3 \tag{D.25}$$

The model can be implemented either with analytical formulae (linear 1D testcases only) or the finite element method (useful for larger dimensions).

Results are shown in Figure 47.

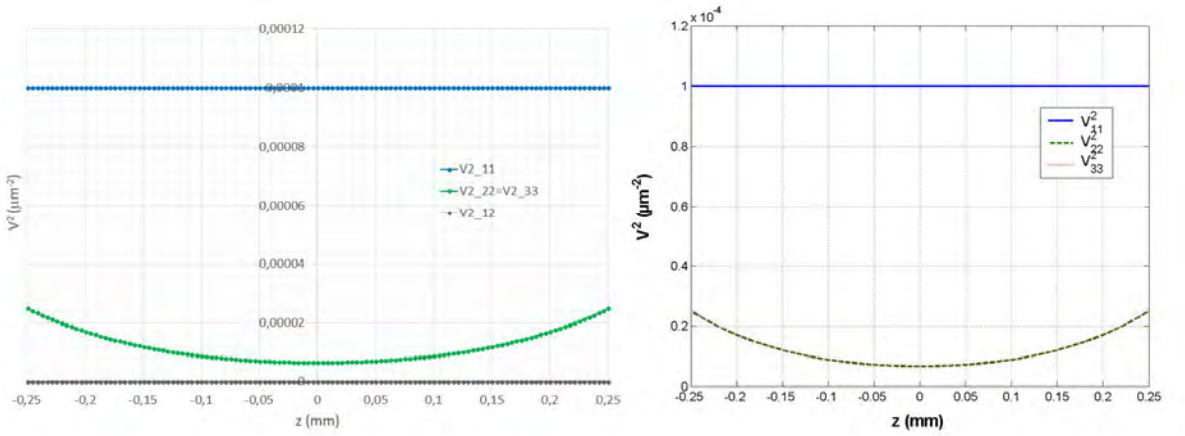

Figure 47: Calculation of the tensor [V²] in GO steels with the Finite Element Method (left) and analytical formulae given above (right) with κ_s=0 and τ=0.

(ii) NGO SiFe

For NGO SiFe materials, we assume that the magnetic structure can be approximately described with a non-diagonal tensor $[V^2] = [\Lambda^2]^{-1}$.

$$[V^2] = \begin{bmatrix} V_{11}^2 & V_{12}^2 & 0 \\ V_{21}^2 & V_{22}^2 & 0 \\ 0 & 0 & V_{33}^2 \end{bmatrix} \tag{D.26}$$

we use the following input parameters and limit conditions:

ζ=0.5 mm and $\kappa_{an} = \frac{c_{an}}{c_{ex}}\left(\frac{K_{an}}{\gamma_w}\right)^2 = (4/\zeta)$ mm^{-2} with $\boldsymbol{u_{an}}=(a=\sqrt{(2/3)},b=\sqrt{(1/3)},0)^T$.

$V^2_{120}= V^2_{210}=-(0.75/300)^2$, $V^2_{130}= V^2_{230}=-(1/10000)^2$, $V^2_{110}=(2/300)^2$, $V^2_{220}=(1/300)^2$, $V^2_{330}=(0.5/300)^2$ μm^{-2} at the surface.

The PDE corresponding to the four unknowns V_{ii}^2 and V_{12}^2 are:

$$\begin{Bmatrix} \left(\partial_z^2 . - \kappa_{ii}(1+\tau_{ii}\partial_t .)\right)V_{ii}^2 + \kappa_{an} ab V_{ij}^2 \\ \left(\partial_z^2 . - \kappa_{ij}(1+\tau_{ij}\partial_t .)\right)V_{ij}^2 - \kappa_{an} ab V_{ii}^2 \end{Bmatrix} = \begin{Bmatrix} 0 \\ 0 \end{Bmatrix} \tag{D.27}$$

With

$\kappa_{11} = \kappa_{an}(1-a^2) + \kappa_{s,11}$

$\kappa_{22} = \kappa_{an}(1-b^2) + \kappa_{s,22}$

$\kappa_{33} = \kappa_{an} + \kappa_{s,11}$

$\kappa_{12} = \kappa_{an}(2-b^2-a^2)$

$$\kappa_{s,ii} = \frac{C_\lambda}{C_{ex}}\left(\frac{K_{an}}{\gamma_w}\right)^2\left(\frac{3\lambda_{100}}{2K_{an}}\right)\left(\frac{3}{2}\lambda_{100} - \sigma_{ii}\right), \sigma_{ij} = 0$$

$$\tau_{ij} = \left(\frac{K_{an}}{\gamma_w}\right)^2 \tau \Big/ \kappa_{ij}$$

The time harmonic solutions with angle velocity ω are shown in Figure 48.

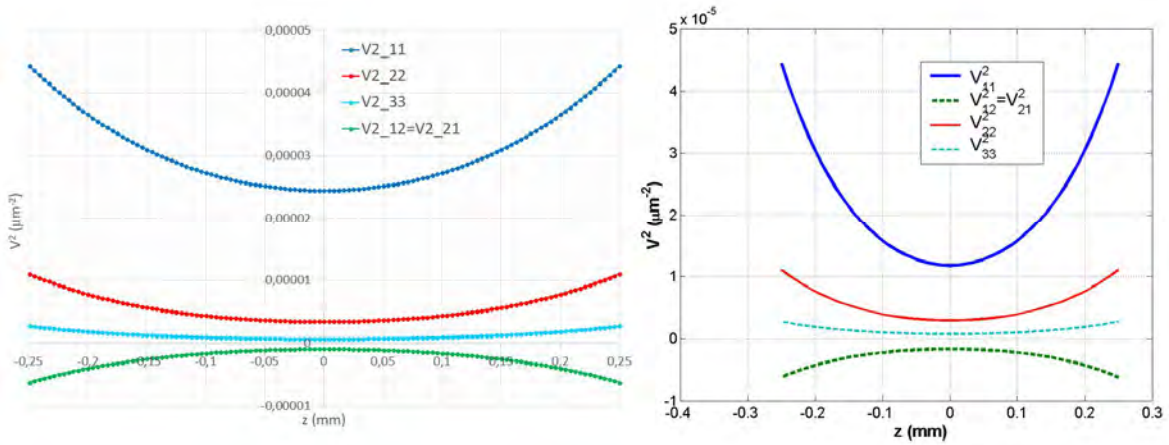

Figure 48: Calculation of the tensor [V^2] in NGO steels with the Finite Element Method (left) and analytical formulae given above (right) with κ_S=0 and τ=0.

(iii) Sensitivity analysis

The Figure 49 shows the results of a sensitivity analysis to the main physical parameters κ_{an} (macroscopic magneto-crystalline anisotropy), κ_s (stress induced anisotropy), $\Lambda_0 = \Lambda_{surf}$ (surface magnetic structure) and τ (eddy current damping time delay).

The default values of the input parameters used are as follow:

$\zeta = 0.23 - 0.5\ mm$ (sheet thickness)

$J_s = 2.1\ T$ (saturated magnetic polarization)

$\rho = \sigma_e^{-1} = 48\ \mu\Omega.cm$ (electrical resistivity)

$\mu = 20\ 000\mu_0$ (quasi-static permeability)

$d = 7650\ kg.m^{-3}$ (volume mass density)

$\kappa_{an} = 10\text{-}100\ mm^{-2}$ (macroscopic magneto-crystalline anisotropy coefficient, $\boldsymbol{u_{an}}=(1,0,0)^T$)

$\kappa_s = \kappa_{s,11} = \kappa_{s,22} = \kappa_{s,33} = -100\ldots+100\ mm^{-2}$ (stress induced anisotropy)

$\tau = 1\ ms$ (eddy current damping time delay)

$\omega = 2*pi*300$ (time harmonic angle velocity)

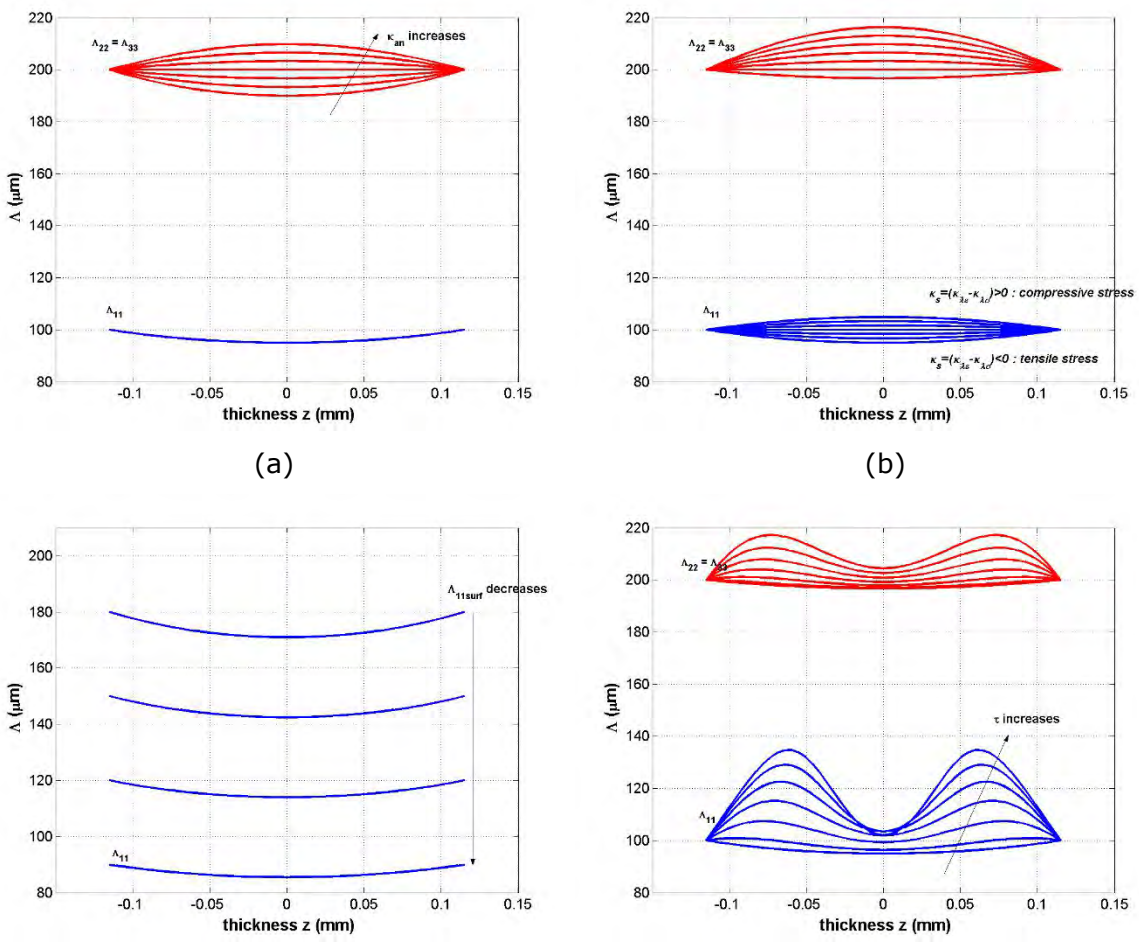

Figure 49: Sensitivity analysis of the GO magnetic structure to the macroscopic magneto-crystalline anisotropy (a), the stress induced anisotropy (b), the surface magnetic structure (c) and the eddy currents time delay (d).

b. *Calculation and sensitivity analysis of observables – case of GO SiFe*

(i) quasi-static properties

quasi-static permeability

By using (D.19) with $\omega = 0$, $\mu >> \mu_0$ and $\boldsymbol{B} \approx \boldsymbol{J}$, (D.20) becomes

$$\frac{\vec{\mu}_{app}}{\mu} = \frac{1}{\zeta}\left(\int_{-\frac{\zeta}{2}}^{+\frac{\zeta}{2}} [V^2] dz\right)[\Lambda_0^2]\frac{\vec{H}_a}{H_a}$$

$$\mu_{app,i} = \frac{\tanh\left(\frac{\sqrt{\kappa_{ii}}\zeta}{2}\right)}{\left(\frac{\sqrt{\kappa_{ii}}\zeta}{2}\right)}\mu \qquad \text{(D.28)}$$

$\boldsymbol{H_a}/H_a$ gives the direction of the magnetic field applied on the surface. In this model μ is a scalar, the anisotropy is determined by the magnetic structure, the shape and orientation of magnetic domains and so the tensor $[\Lambda^2]$. However, it is possible to take non-linearities and additional microscopic anisotropy considerations within a tensor $[\mu]$.

Due to a positive magnetostriction (>0), Figure 50 shows that a global tensile stress σ_{ii} increases the quasi-static apparent permeability in direction i and that a compressive stress σ_{jj} decreases quasi-static apparent permeability in the direction j.

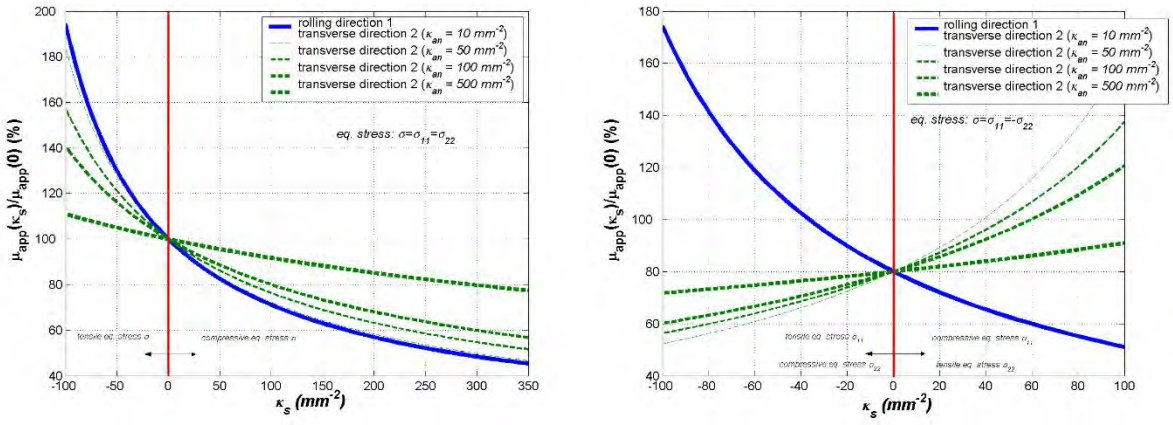

Figure 50: Relative sensitivity analysis of quasi-static apparent permeability to the magneto-crystalline κ_{an} and stress induced κ_s anisotropies ((a) $\sigma_{11} = \sigma_{22}$ (b) $\sigma_{11} = -\sigma_{22}$).

Quasi-static losses

The general definition of the mean power loss density for any periodic signal is given by (D.21). For time harmonics, the corresponding quasi-static energy loss $<<\xi_{stat}>_{\boldsymbol{r}}>_t$ per cycle and per Tesla^2 becomes then (in W.s.T^{-2}.kg^{-1} or J. T^{-2}.kg^{-1})

$$\ll \xi >_r>_t = \frac{\pi \ll p >_r>_t}{d\omega \left| < \vec{J} >_r \right|^2} = \ll \xi_{stat} >_r>_t + \ll \xi_{dyn} >_r>_t$$

$$\xi_s = \ll \xi_{stat} >_r>_t = Re\left(-j \frac{\pi \vec{\underline{H}}_{s,surf} < \vec{\underline{J}} >_r^*}{d \left| < \vec{\underline{J}} >_r \right|^2} \right) = \sum_i \xi_{si}$$

$$\xi_{si} = \frac{\pi}{d} \left| real\left(-j \nu_c \frac{\tanh\left(\frac{\sqrt{\kappa_{ii}}\zeta}{2}\right)}{\left(\frac{\sqrt{\kappa_{ii}}\zeta}{2}\right)} \right) \right| \qquad \text{(D.29)}$$

The relative variation of quasi-static losses as a function of the anisotropies are exactly the same as the ones for the quasi-static apparent permeability given in Figure 50. Due to a positive magnetostriction (>0), a global tensile stress σ_{ii} increases the quasi-static losses in direction i and a compressive stress σ_{jj} decreases quasi-static losses in the direction j. As a consequence, except if the coercive reluctivity depends on the stress, a tensile stress cannot reduce the quasi static losses but rather the dynamic losses (see Figure 53).

Figure 51 gives results of the sensitivity analysis to the coercive reluctivity. The quasi-static losses are proportional to ν_c, but the slope depends on the anisotropies and especially on the stress induced anisotropy.

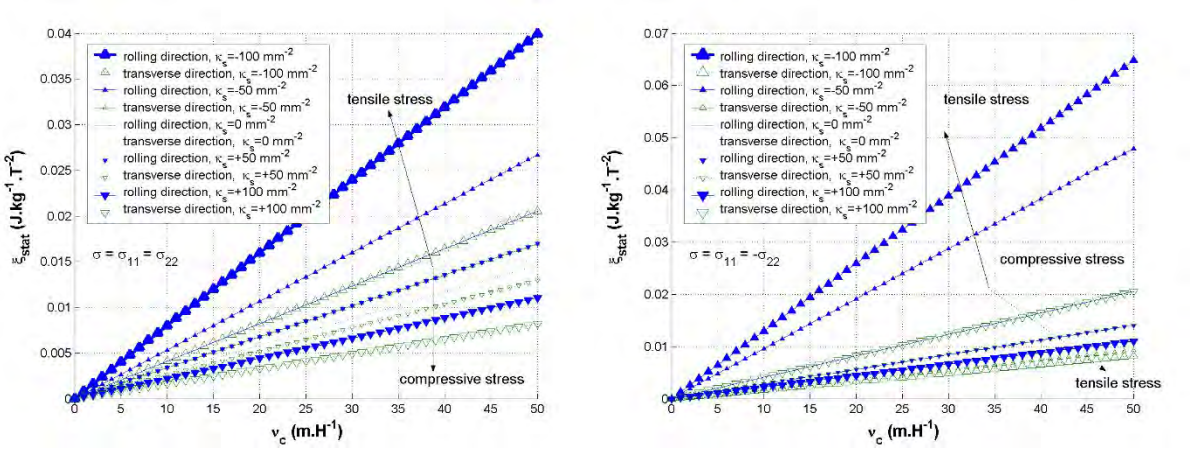

(a) (b)

Figure 51: Relative sensitivity analysis of quasi-static losses to the coercive reluctivity ν_c and the stress induced κ_s anisotropy with κ_{an} = 100 ((a) $\sigma_{11} = \sigma_{22}$ (b) $\sigma_{11} = -\sigma_{22}$).

(ii) dynamic magnetization

linear dynamic permeability

By using (D.19) with $\omega \neq 0$, $\mu >> \mu_0$ and $\boldsymbol{B} \approx \boldsymbol{J}$, (D.20) becomes

$$\frac{\vec{\mu}_{app}}{\mu} = \frac{1}{\zeta} \left(\int_{-\frac{\zeta}{2}}^{+\frac{\zeta}{2}} [V^2] dz \right) [\Lambda_0^2] \left[[1] + j\sigma_e [\Lambda_0^2] \mu\omega \right]^{-1} \frac{\vec{H}_a}{H_a}$$

$$\mu_{app,i} = \left(\frac{\tanh\left(\frac{\sqrt{\kappa_{ii}(1+j\tau_{ii}\omega)\zeta}}{2} \right)}{\left(\frac{\sqrt{\kappa_{ii}(1+j\tau_{ii}\omega)\zeta}}{2} \right)} \right) \left(\frac{1}{1+j\sigma_e \Lambda_{0,ii}^2 \mu\omega} \right) \mu \qquad \text{(D.30)}$$

The low pass filtering behaviour of the apparent magnetic permeability with time harmonics is well described by the model (see Figure 52). Eddy currents damping can come from the domains magnetic rotation (contribution of τ) or the walls motion (contribution of Λ^2)

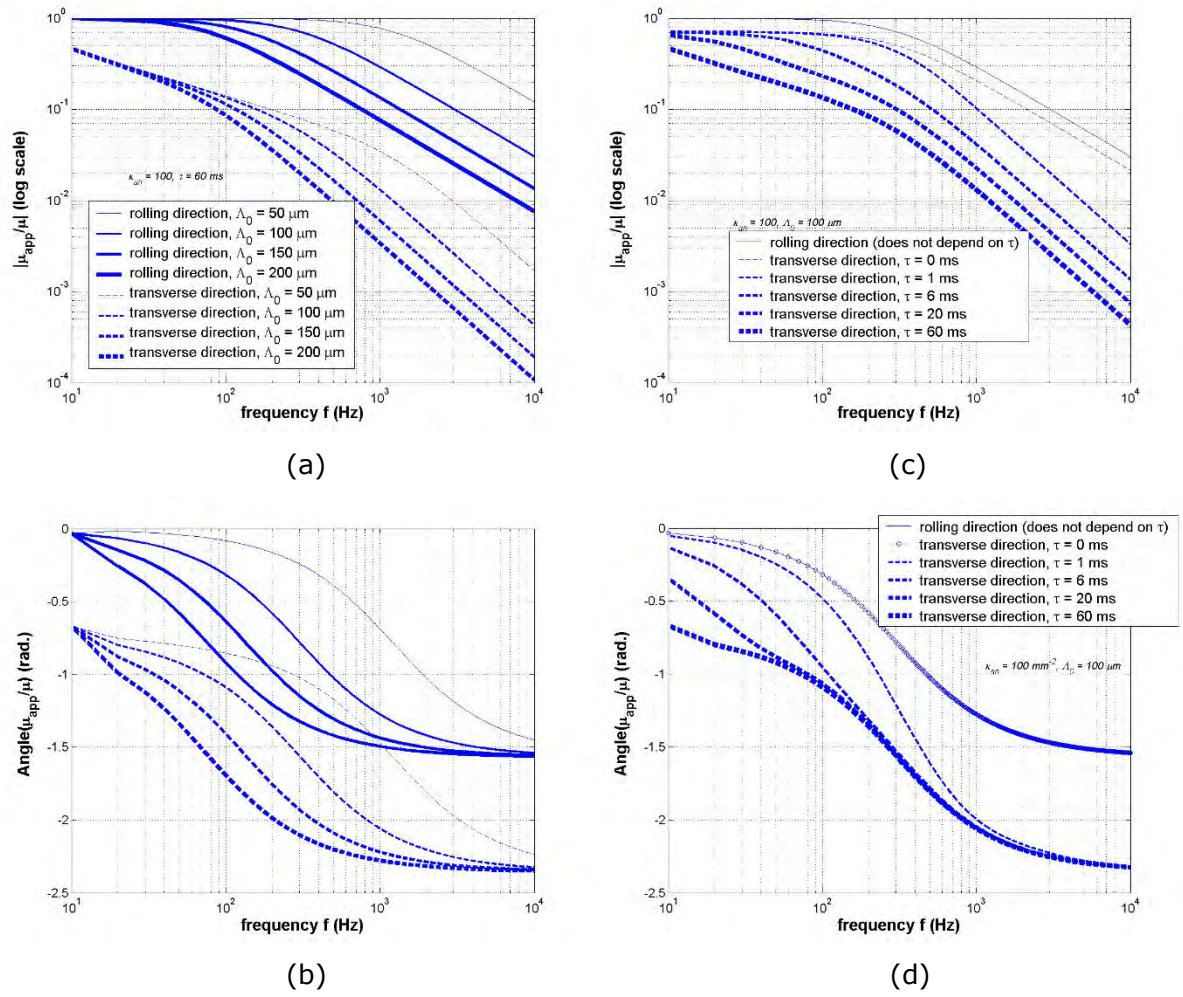

Figure 52: Sensitivity analysis of dynamic apparent permeability to the surface magnetic structure ((a) magnitude and (b) phase) and to the damping time delay ((c) magnitude and (d) phase angle)

linear dynamic losses

The general definition of the mean power loss density for any periodic signal is given by (D.21). For time harmonics, the corresponding energy $\ll\langle\xi\rangle_r\rangle_t$ per cycle and per Tesla^2 becomes then (in W.s.T^{-2}.kg^{-1} or J. T^{-2}.kg^{-1}):

$$\ll \xi >_r>_t = \frac{\pi \ll p >_r>_t}{d\omega \left| < \vec{J} >_r \right|^2} = \ll \xi_{stat} >_r>_t + \ll \xi_{dyn} >_r>_t$$

$$<< \xi_{dyn} >_r >_t = + Re\left(\frac{\pi\sigma\left[\Lambda_{surf}^2\right]\omega \underline{\vec{J}}_{surf} < \underline{\vec{J}} >_r^*}{d \left| < \underline{\vec{J}} >_r \right|^2} \right) = \sum_i \xi_{di}$$

$$\xi_{di} = \frac{\pi\sigma_e \Lambda_{0,ii}^2 \omega}{d} \left| real\left(\frac{\left(1+j\sigma_e \Lambda_{0,ii}^2 \mu\omega\right)\left(\frac{\sqrt{\kappa_{ii}(1+j\tau_{ii}\omega)}\zeta}{2}\right)}{\tanh\left(\frac{\sqrt{\kappa_{ii}(1+j\tau_{ii}\omega)}\zeta}{2}\right)} \right) \right| \qquad \text{(D.31)}$$

The Figure 53 shows that the total iron losses at frequencies up to the quasi-static conditions (*f > 10 Hz*) are driven mainly by the dynamic losses that can only increase with the frequency (eddy currents losses around walls and inside the domains).

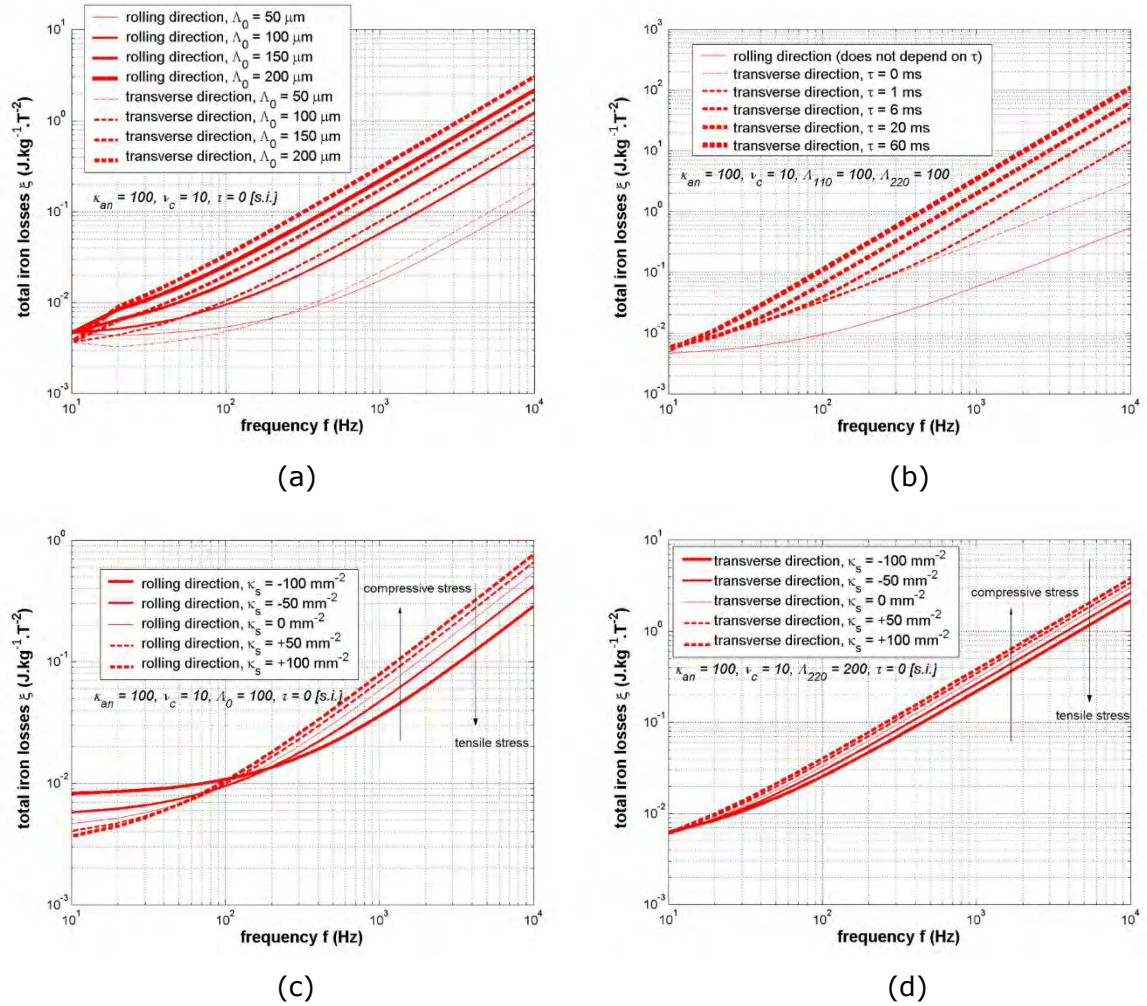

Figure 53: Sensitivity analysis of total dynamic losses to the surface magnetic structure (a) , to the eddy currents time delay (b) and to the stress anisotropy ((c) and (d)).

2. 2D testcases

Let's consider the magnetic sheet of thickness ζ and width *W*. Let's use the *(x,y,z)* or *(1,2,3)* reference frame for which axis 2 or *y* corresponds to the rolling direction, 1 or *x* corresponds to *W*, i.e. the transverse direction and *z* corresponds to the thickness. The 2D approximation consists in assuming no space variation in direction *x* but only in directions *x* and *z*. We also consider only the steady state with neither time variations nor external magnetic field. The Partial Differential Equation PDE (D.16) becomes:

$$\begin{Bmatrix} \partial_x^2 V_{11}^2 + \partial_z^2 V_{11}^2 - \kappa\left(V_{11}^2 - u_{an,1}.\left(V_{11}^2.u_{an,1} + V_{12}^2.u_{an,2} + V_{13}^2.u_{an,3}\right)\right) \\ \partial_x^2 V_{22}^2 + \partial_z^2 V_{22}^2 - \kappa\left(V_{22}^2 - u_{an,2}.\left(V_{21}^2.u_{an,1} + V_{22}^2.u_{an,2} + V_{23}^2.u_{an,3}\right)\right) \\ \partial_x^2 V_{33}^2 + \partial_z^2 V_{33}^2 - \kappa\left(V_{33}^2 - u_{an,3}.\left(V_{31}^2.u_{an,1} + V_{32}^2.u_{an,2} + V_{33}^2.u_{an,3}\right)\right) \\ \partial_x^2 V_{12}^2 + \partial_z^2 V_{12}^2 - \kappa\left(V_{12}^2 - u_{an,1}.\left(V_{21}^2.u_{an,1} + V_{22}^2.u_{an,2} + V_{23}^2.u_{an,3}\right)\right) \\ \partial_x^2 V_{13}^2 + \partial_z^2 V_{13}^2 - \kappa\left(V_{13}^2 - u_{an,1}.\left(V_{31}^2.u_{an,1} + V_{32}^2.u_{an,2} + V_{33}^2.u_{an,3}\right)\right) \\ \partial_x^2 V_{23}^2 + \partial_z^2 V_{23}^2 - \kappa\left(V_{23}^2 - u_{an,2}.\left(V_{31}^2.u_{an,1} + V_{32}^2.u_{an,2} + V_{33}^2.u_{an,3}\right)\right) \end{Bmatrix} = \begin{Bmatrix} 0 \\ 0 \\ 0 \\ 0 \\ 0 \\ 0 \end{Bmatrix} \quad \text{(D.32)}$$

a. GO steels

Let's first work with a perfectly oriented material defined by:

$$\begin{Bmatrix} \vec{u}_{an} = \frac{\vec{K}_{an}}{K_{an}} = \begin{pmatrix} 0 \\ 1 \\ 0 \end{pmatrix} \\ V_{ij0}^2 = V_{ij}^2(z = \pm\zeta/2) \end{Bmatrix} \quad \text{(D.33)}$$

Numerical results in Figure 54 show the both the space variations and refinement of main domains but also the orientation and space variations of closure domains.

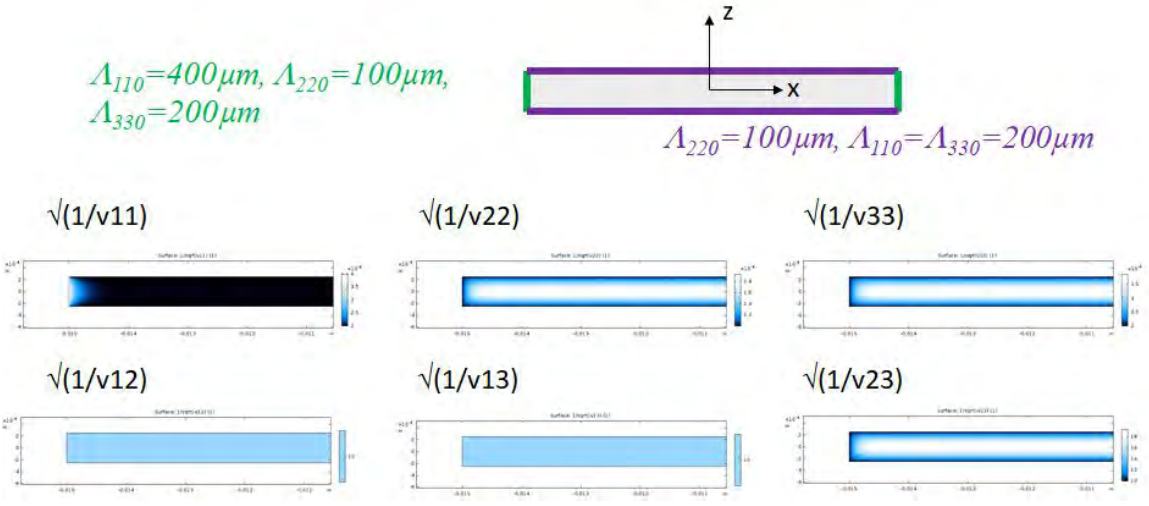

Figure 54: 2D results on [Λ] aspects for a GO steel with FEM (Finite Element Method).

b. NGO steels

Let's first work with a non or partially oriented material defined by:

$$\left\{ \begin{array}{l} \vec{\boldsymbol{u}}_{an} = \frac{\vec{K}_{an}}{K_{an}} = \begin{pmatrix} a \\ b \\ 0 \end{pmatrix} \\ V_{ij0}^2 = V_{ij}^2(z = \pm\zeta/2) \end{array} \right\} \qquad \text{(D.34)}$$

Numerical results in Figure 55 show the both the space variations and refinement of main domains but also the orientation and space variations of closure domains.

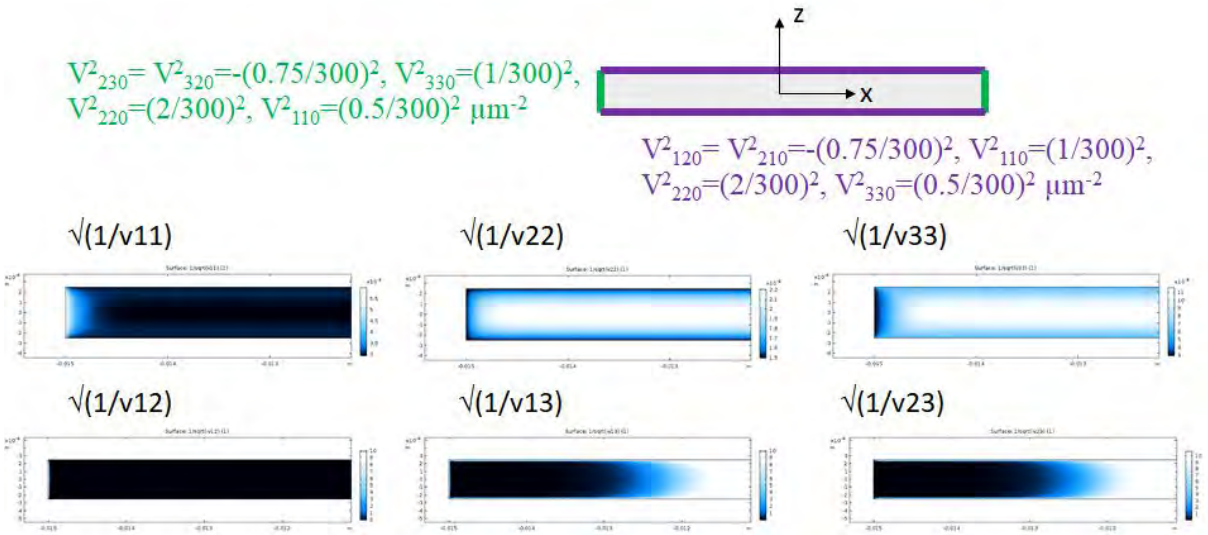

Figure 55: 2D results on [Λ] aspects for a NGO steel with FEM (Finite Element Method).

VII. Partial conclusions, critics and forthcomings

The present model does not make any arbitrary assumption concerning the type and topology of domains. It can also take complex domains shapes statistically into account, thanks to its cross-sectional areas and its walls mobility and density. Thus, this method is no more confronted to serious limitations due to the huge number of degrees of freedom, considering the infinite variety of magnetic structures. The latter might be statistically described thanks to the infinite possible values of the 6 terms present in $[V^2]$. This solution based on structural but statistical state variables has been investigated including the effect of Zeeman type modified interaction with the external field, taking the grains, grains size and grains boundaries in the macroscopic anisotropy into account

This new model can help us illustrate the impact of the laser treatments and different patterns on the magnetic structure with domains and walls only if further investigations, developments and improvements are carried ou

t to answer the following questions:

1. What is the mutual influence of the volume and the surface?
2. How to inverse the model by defining the goal criteria and ease the determination of the optimal laser pattern and parameters?

In the next update of this deliverable we will add a section on a second modelling of the Surface Magnetic Structure, that will act as the necessary limit condition for the volume model, still coupling the material to the external field. This additional section will address the following subjects:

- Energy minimization, formulation: Non divergence and limit conditions
  - Non divergence
  - Limit condition
- Surface Energy densities
  - Exchange
  - Magnetic anisotropy
  - Magnetoelastic anisotropy
  - Demagnetizing energy
    - Geometry, thickness
    - Grains
    - Laser patterns
    - Laser induced stress
- Energy minimization, surface formulation and magnetic structure

E) Tensor Magnetic Phase Formulation and couplings (TMP) – Coupling between the volume and the surface magnetic structure

I. State variable

$$[\Lambda^2] = \begin{bmatrix} \Lambda_{11}^2 & \Lambda_{12}^2 & \Lambda_{13}^2 \\ \Lambda_{21}^2 & \Lambda_{22}^2 & \Lambda_{23}^2 \\ \Lambda_{31}^2 & \Lambda_{32}^2 & \Lambda_{33}^2 \end{bmatrix}, \quad \begin{Bmatrix} \Lambda_{ii}^2 \propto \lambda_j \lambda_k; \ j,k \neq i \ and \ i = 1..3 \\ \Lambda_{ij}^2 \propto \lambda_k^2; \ k \neq j \neq i \ and \ i,j = 1..3 \end{Bmatrix}$$

Each factor (λ_i, λ_j and λ_k) is homogeneous to a squared length, linked to walls density, surface, mobility and density for each direction.

The model is inspired from the Néel domains phase model.

II. Governing Equations

The formulation is based upon the Energy minimization principle (see previous part)

$$Min\left\{\vec{E}_m = \iiint_\Omega (\vec{e}_{ex} + \vec{e}_{an} + \vec{e}_{\lambda\epsilon} + \vec{e}_{\lambda\sigma} + \vec{e}_{\tau})d^3x + \iint_{\partial\Omega} (\vec{e}_m + \vec{e}_{dm})d^2x\right\}$$

A new Tensor State Variable is then defined: the inverse of $[\Lambda^2]$, closely linked to the magnetic objects' density per unit cross sections in the whole directions of space:

$$[\boldsymbol{V^2}] = [\boldsymbol{\Lambda^2}]^{-1}$$

The energy minimization principle leads to the following governing PDE:

$$\Rightarrow [\Delta]\,[V^2] - \vec{\nabla}(\vec{\nabla}.[V^2]) - \frac{C_{an}}{C_{ex}}\left(\frac{K_{an}}{\gamma_w}\right)^2\left([V^2] - \left(\frac{\vec{K}_{an}([V^2]\vec{K}_{an})^T}{K_{an}^2}\right)^T\right)$$

Magnetic exchange *Divergence condition* *Magnetic anisotropy*

$$+\frac{3}{2}\frac{C_\lambda}{C_{ex}}\left(\frac{K_{an}}{\gamma_w}\right)^2\left(\frac{[\lambda]\div[\sigma_s]}{K_{an}}\div[V^2]\right) - \frac{9}{4}\frac{C_\lambda}{C_{ex}}\left(\frac{K_{an}}{\gamma_w}\right)^2\left(\frac{[\lambda^2]\div[C]}{K_{an}}\div[V^2]\right) - \left(\frac{K_{an}}{\gamma_w}\right)^2\tau\partial_t[V^2] = [0]$$

Self magnetostriction *Stress anisotropy* *Micro-currents*

III. Bulk and Boundary conditions

1. Bulk conditions

Volume Conservation

$$[\boldsymbol{\Lambda^2}] = [\boldsymbol{\Lambda_\uparrow^2}] + [\boldsymbol{\Lambda_\downarrow^2}]$$

Up-down Polarization

$$[\Lambda^2]\vec{J}_{\uparrow\downarrow} = [\Lambda_{\uparrow\downarrow}{}^2]\vec{J}_s = \frac{1}{2}[\Lambda^2](\vec{J}_s \pm \vec{J})$$

With

$$\vec{J}_s = \begin{pmatrix} Jsat \\ Jsat \\ Jsat \end{pmatrix}$$

Magnetic Polarization

$$\vec{\boldsymbol{J}} = \vec{J}_{\uparrow} - \vec{J}_{\downarrow}$$

2. Non-divergence condition

Magnetic flux conservation principle – closure domains generation principle

$$\vec{\boldsymbol{\nabla}} \cdot \vec{\boldsymbol{B}} = \vec{\boldsymbol{\nabla}} \cdot \vec{\boldsymbol{J}} + \boldsymbol{\mu_0}\vec{\boldsymbol{\nabla}} \cdot \vec{\boldsymbol{H}} \approx \vec{\boldsymbol{\nabla}} \cdot \vec{\boldsymbol{J}} = \vec{\boldsymbol{\nabla}}([\boldsymbol{\Lambda_{\uparrow}}^{\boldsymbol{2}}] - [\boldsymbol{\Lambda_{\downarrow}}^{\boldsymbol{2}}])\vec{\boldsymbol{J}}_{\boldsymbol{s}} = \boldsymbol{0}$$

3. Boundary conditions

Magnetic structure at boundaries?

$$[\boldsymbol{\Lambda}^{\boldsymbol{2}}_{\boldsymbol{surf}}] = [\boldsymbol{\Lambda}^{\boldsymbol{2}}_{\boldsymbol{0}}]$$

IV. Coupling formulations: *TMP(MF) couplings*

1. surface energy minimization principle

Proposal of a coupling boundary equation, which provide a relationship between the TMP state variable and the classical field variables at the external surface of a magnetic material:

$$\forall i,j:\ C_{ex}\frac{\gamma_w^3}{K_{an}^2}V_{ij}^2 + C_{an}\frac{\gamma_w^3}{K_{an}^2}\left(V_{ij}^2 - k_{ani}\left(\sum_k V_{jk}^2\, k_{ank}\right)\right) + \frac{9}{4}\lambda_{ij}^2 C_{ij} V_{ij}^2 - \frac{3}{2}\lambda_{ij}\sigma_{sij}V_{ij}^2$$

Magnetic exchange — *Magnetic anisotropy* — *Self magnetostriction* — *Stress anisotropy*

$$-C_z\frac{\sigma_e}{2}\frac{K_{an}}{\gamma_w}\begin{pmatrix} B_i\sum_k \Lambda_{jk}^4 j\omega B_k \\ B_j\sum_k \Lambda_{ik}^4 j\omega B_k \end{pmatrix} - \sqrt{C_{dmi}C_{dmj}}\frac{K_{an}^2}{\gamma_w}\frac{B_iB_j}{B_{sat}}\Lambda_{jk}^4 = 0$$

Zeeman field interactions — *Demagnetizing stray energy*

With

$$C_{dm1} \propto \sqrt{\frac{cos^2\theta_{g1}}{g_2 g_3}}$$

$$C_{dm1} \propto \sqrt{\frac{\boldsymbol{sin^2\theta_{L2}}}{\boldsymbol{p_L d_L}} + \frac{\left(sin\theta_{g1} sin\theta_{g3}\right)^2}{g_1 g_3}}$$

$$C_{dm1} \propto \sqrt{\frac{\boldsymbol{sin^2\theta_{L3}}}{\boldsymbol{p_L d_L}} + \frac{\left(sin\theta_{g1} cos\theta_{g3}\right)^2}{g_1 g_2}}$$

θ_{gi} : Grains orientation angles (texture)

g_i : Grains size

θ_{gi}, d_L, p_L: Laser patterns (angle, spacing, depth)

σ_{sij}: residual or/and induced stress

C_z is not completely determined.

2. Non-divergence condition

Case of quasi-static polarization J_M with classic equations, satisfying the Laplace equation:

$$\Delta[\Lambda_\uparrow{}^2] = \Delta[\Lambda_\downarrow{}^2] \Rightarrow \vec{\Delta}([\Lambda_\uparrow{}^2] - [\Lambda_\downarrow{}^2])\vec{J}_s = [\Lambda_0^2]\vec{\Delta}(\overrightarrow{J_M}) = \vec{0}$$

1. Boundary conditions

Quasi-static polarization driven by the surface structure, as if no magnetic phase:

$$\overrightarrow{J_{M_{surf}}} = \overrightarrow{J_{surf}} = \overrightarrow{J_0}$$

V. Observables

1. Mean polarization (T):

$$\vec{J} = [V^2]([\Lambda_\uparrow{}^2] - [\Lambda_\downarrow{}^2])\vec{J}_s = [V^2]\,[\Lambda_0^2]\,\overrightarrow{J_M}$$

2. Applied field (A/m):

$$\vec{\Delta}(\overrightarrow{H_a}) = \vec{0},\ \overrightarrow{H_{a_{surf}}} = \overrightarrow{H_0}$$

3. Apparent relative permeability:

$$\frac{(\mu_{app})_{ij}}{\mu} = \frac{< J_i >_r}{\mu H_{0,j}}$$

4. Losses (W/m³):

$$\ll \xi >_r>_t = < \vec{H}_a < \partial_t \vec{J} >_r>_t$$

VI. Result: 2D test case with GO material

The TMP formulation has been put to the test with a user interface of COMSOL multiphysics, enabling the programming of any new physical formulation.

The definition of the problem can be explained thanks to .

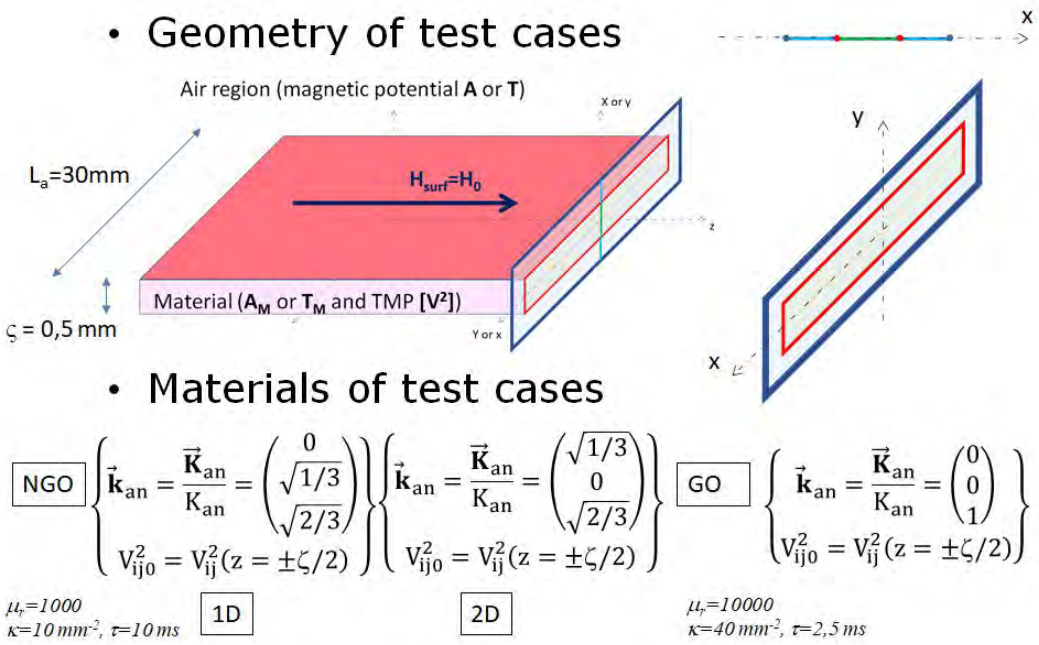

Figure 56: definition oft he 2D problem to be solved with the TMP formulation.

We chose a particular GO material (GOES) and we computed the TMP variable as a function of space coordinates in the cross section of a sheet (Figure 57), its evolution within the thickness and dependent on the frequency (Figure 58) and the resulting eddy currents comparing to the classical T or T_M formulations given by [86] (Figure 59).

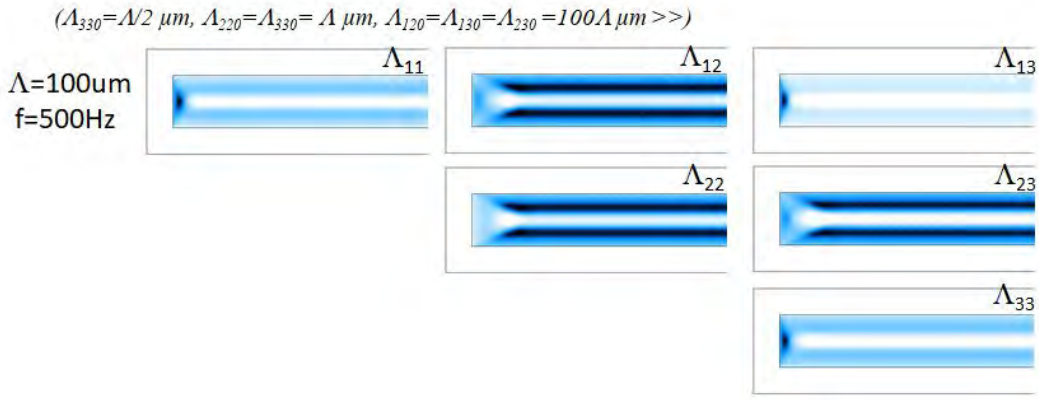

Figure 57: TMP variable for a GOES as a function of the two coordinates in the cross section.

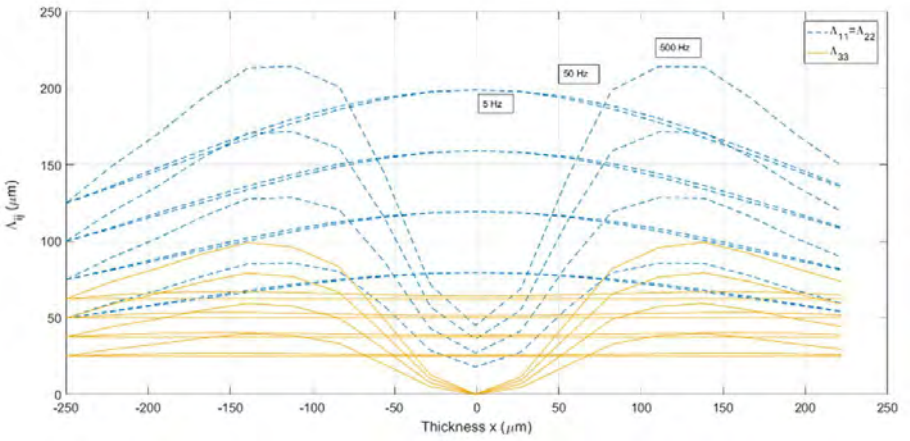

Figure 58: TMP variable profile within the sheet thickness as a function space and of frequency.

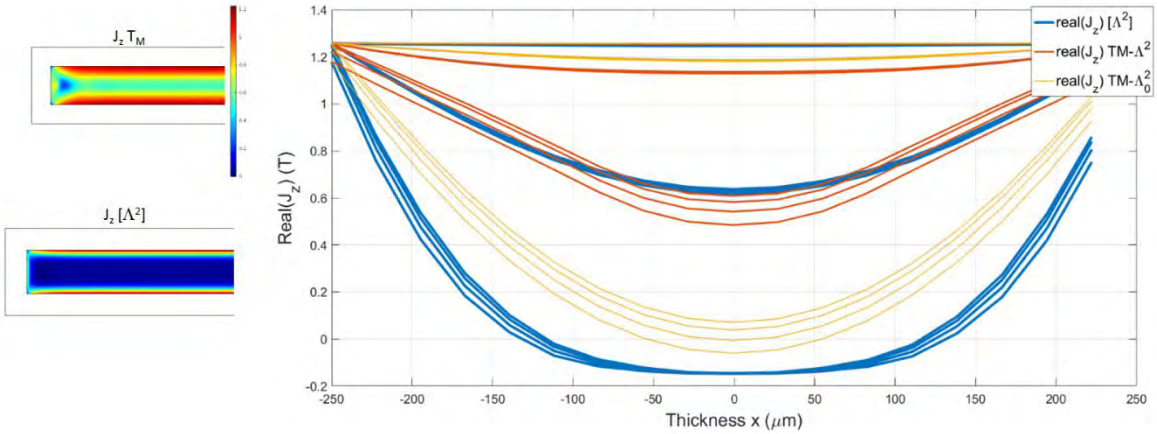

Figure 59: solution for the total eddy currents that damp the field and generate the losses comparing with the classical formulations.

VII. FORTHCOMING

Sensitivity, parametric identification and analysis of (Λ_0, $\kappa_s(\sigma)$, τ, C_{dm} ...)

Comparisons to magnetic measurements varying:

- **The laser power**
  - **surface tensor, volume model identification**
  - **comparison to the theory – surface identifications**
- **the laser pattern**
  - **surface tensor, volume model identification**
  - **comparison to the theory – surface identifications**
- **the laser spot**

…

Bibliography

[1] F.Fiorillo, G. Bertotti, C. Appino, M. Pasquale, "Soft magnetic materials," *J. Webster (ed.), Wiley Encyclopedia of Electrical and Electronics Engineering. Copyright #1999 John Wiley & Sons, Inc.*

[2] C. P. Steinmetz, "On the law of hysteresis," *Proceedings of the IEEE, vol. 72, no. 2*, pp. 197– 221, Feb. 1984.

[3] J. Reinert ; A. Brockmeyer ; R.W.A.A. De Doncker, "Calculation of losses in ferro- and ferrimagnetic materials based on the modified Steinmetz equation," *IEEE Transactions on Industry Applications*, vol. 37, pp. 1055-1061, Jul-Aug. 2001.

[4] J. Li, T. Abdallah, C. R. Sullivan, "Improved calculation of core loss with nonsinusoidal waveforms," in *Conference Record of the 2001 IEEE Industry Applications Conference, 2001. Thirty-Sixth IAS Annual Meeting*, vol. 4, vol. 4, pp. 2203–2210, 2001, pp. 2203–2210.

[5] K. Venkatachalam; C.R. Sullivan ; T. Abdallah; H. Tacca, "Accurate prediction of ferrite core loss with nonsinusoidal waveforms using only Steinmetz parameters," *Computers in Power Electronics, 2002. Proceedings. 2002 IEEE Workshop on*, pp. 36-41, 3-4 Jun. 2002.

[6] G. Bertotti, "General properties of power losses in soft ferromagnetic materials," *IEEE Transactions On Magnetics*, vol. 24, no. 1, pp. 621-630, jan. 1988.

[7] G. Bertotti, "Physical interpretation of eddy current losses in ferromagnetic materials.I:Theoretical considerations," *Journal of Applied Physics*, vol. 57, p. 2110, 1985.

[8] M. Najgebauer, K. Chwastek, J. Szczyglowski, P. Kopciuszewski, "Influence of magnetic domain structure on energy losses in soft magnetic materials," in *Conference: Soft Magnetic Materials 16*, Düsseldorf, Sep. 2003.

[9] D.C. Jiles , D.L. Atherton, "Theory of ferromagnetic hysteresis," *Journal of Magnetism and Magnetic Materials*, vol. 61, pp. 48-60, 1986.

[10] D. C. Jiles, J. B. Thoelke., M. K. Devine, "Numerical Determination of Hysteresis Parameters for the Modeling of Magnetic Properties Using the Theory of Ferromagnetic Hysteresis," *IEEE Transactions On Magnetics*, vol. 28, no. I, pp. 27-35, Jan. 1992.

[11] M. J. Sablik and D. C. Jiles, "Coupled Magnetoelastic Theory of Magnetic and Magnetostrictive Hysteresis ," *IEEE Transactions on magnetics*, vol. 29, no. 3, 1993.

[12] L Dupré, M J Sablik, R Van Keer, J Melkebeek, "Modelling of microstructural effects on magnetic hysteresis properties," *Journal of physics D: app. physics*, vol. 35, pp. 2086-2090, 2002.

[13] J. Szczyglowski, "Influence of eddy currents on magnetic hysteresis loops in soft magnetic materials," *Journal of Magnetism and Magnetic Materials*, vol. 223, pp. 97-102, 2001.

[14] T. Chevalier, A. Kedous-Lebouc, B. Cornut, C. Cester, "A new dynamic hysteresis model for electrical steel sheet," *Physica B: Condensed Matter*, vol. 275, pp. 197-201, Jan. 2000.

[15] M.A. Raulet, J.P. Masson, D. Gaude, "Presentation and experimental validation of a behavioral model of dynamic properties for magnetic materials," *J. Phys. IV France* , vol. 08, pp. Pr2-619-Pr2-622, 1998.

[16] M.A. Raulet, "Contribution à la modélisation des matériaux magnétiques liés à leur environnement en génie électrique," Lyon, 2011.

[17] O. Maloberti, "Contribution à la modalisation de la dynamique d'aimantation dans les matériaux magnétiques doux: Caractérisation et simulation ," Grenoble, 2006.

[18] O. Maloberti, A. Kedous-Lebouc, O. Geoffroy, G. Meunier, V. Mazauric, "Field diffusion-like representation and experimental identification of a dynamic magnetization property," *Journal of Magnetism and Magnetic Materials*, vol. 304, pp. e507-e509, Sep. 2006.

[19] S. Patri, R. Gurusamy, P. A. Molian, M. Govindaraju, "Magnetic domain refinement of silicon-steel laminations by laser scribing," *Journal of materials science* , vol. 31, pp. 1693-1702, 1996.

[20] P. Beckley and D. Snell , "Low-Cost, High-Speed Domain Refinement without Damage to Insulative Coatings ," *Journal of Materials Engineering and Performance*, vol. 3(2), pp. 209-213, Apr. 1994.

[21] K. Sato, M. Kurosawa, B. Fukuda and T. Kan, "Investigation on the domain refining effect in grain-oriented silicon steel," *Journal of magnetism and magnetic materials*, vol. I 12, pp. 183-185, 1992.

[22] P. Beckley, D. Snell, and C. Lockhart, "Domain control by spark ablation," *Journal of Applied Physics* , vol. 57, p. 4212, 1985.

[23] T. Iuchi, S. Yamaguchi, T. Ichiyama, M. Nakamura, T. Ishimoto, K. Kuroki, "Laser processing for reducing core loss of grain oriented silicon steel," *Journal of Applied Physics* , vol. 53, pp. 2410-2412, 1982.

[24] I. Petryshynets, F. Kovac, V. Puchy, M. Sebek, J. Fuzer, P. Kollar, "Magnetic losses reduction in grain oriented silicon steel by pulse and continuous fiber laser processing," *AIP Advances*, vol. 8, no. 047604, 2018.

[25] P. Rauscher, J. Hauptmann, E. Beyer, "Lasers in Manufacturing Conference 2013: Laser scribing of grain oriented electrical steel under the aspect of industrial utilization using high power laser beam sources," *Physics Procedia* , vol. 41, pp. 312-318, 2013.

[26] W. Ming, M. Li, Y. Liu, J. Guo, J. Li, X. Shao, S. Wang Y. Huang, "Parameter optimization of Nd:Yag laser scribing process on core loss of grain-oriented magnetic silicon steels," *The international journal of advanced manufacturing technology*, vol. 70, pp. 1-9, Jan. 2014.

[27] S. V. Ponnaluri, R.Cherukuri, P.A. Molian, "Core loss reduction in grain-oriented silicon steels by excimer laser scribing Part I: experimental work," *Journal of materials processing technology*, vol. 112, pp. 199-204, 2001.

[28] L. Falat, I. Petryshynets, R. Dzunda, M. Sebek V. Puchy, "The Influence of Fiber Laser Pulse Processing on Coercivity and Nanohardness of Fe–3.2Si Grain-Oriented Electrical Steel in relation with its Surface Changes and Magnetic Domains Modifications," *Acta Physica Polonica A*, vol. 131, no. 6, pp. 1445-1449, 2017.

[29] T. Kajiwara, M. Enokizono, "Effect of Laser Stress on Vector Magnetic Properties of Electrical Steel Sheets," *IEEE Transactions on magnetics*, vol. 5, no. 4, Apr. 2014.

[30] I. Petryshynets, V. Puchy, F. Kovac, M. Sebek, "Effect of laser scribing on soft magnetic properties of conventional grain-oriented silicon steel," *Acta Physica Polonica A*, vol. 131, no. 4, pp. 777-779, 2017.

[31] B. Weidenfeller, M. Anhalt, "Effect of laser treatment on high and low induction loss components of grain oriented iron-silicon sheets," *Journal of Magnetism and Magnetic Materials*, vol. 322, pp. 69-72, 2010.

[32] R. H. Pry and C. P. Bean, "Calculation of the energy loss in magnetic sheet materials using a domain model," *Journal of applied physics*, vol. 29, no. 3, pp. 532-533, 1958.

[33] M. Najgebauer, "Models for prediction of energy loss in soft magnetic materials," in *XII International PhD Workshop OWD 2010*, Wisła, 23-26 Oct. 2010.

[34] M.F. de Campos, J.C. Teixeira, F.J.G. Landgraf, "The optimum grain size for minimizing energy losses in iron," *Journal of Magnetism and Magnetic Materials*, vol. 301, pp. 94-99, 2006.

[35] J. Shilling, G. Houze, "Magnetic properties and domain structure in grain-oriented 3% Si-Fe," *IEEE Transactions on magnetics*, vol. MAG-10, no. 2, p. 195, 1974.

[36] B. Weidenfeller, W. Riehemann, "Frequency dependence of loss-improvement of grain oriented silicon steels by laser scribing," *Journal of Magnetism and Magnetic Materials*, vol. 133, pp. 177-179, 1994.

[37] B. Weidenfellera, W. Riehemann, "Polarization-dependent fractional loss improvement of laser scribed GO FeSi steels," *Journal of Magnetism and Magnetic Materials*, vol. 320, pp. e661–e664, 2008.

[38] P. WEISS, "L'HYPOTHÈSE DU CHAMP MOLÉCULAIRE ET LA PROPRIÉTÉ FERROMAGNÉTIQUE," *J. Phys. Theor. Appl.*, vol. 6, no. 1, pp. 661-690, 1907.

[39] F. Bitter, "On Inhomogeneities in the Magnetization of Ferromagnetic Materials," *Phys. Rev.*, vol. 38, p. 1903, 1931.

[40] T. Luchi, S. Yamaguchi, T. Ichiyama, M. Nakamura, T. Ishimoto and K. Kuroki, "Laser processing for reducing core loss of grain oriented silicon steel," *Journal of Applied Physics*, vol. 53, pp. 2410-2412, 1982.

[41] M. Nakamura et al, *Transactions on Magnetics*, vol. MAG-23, no. 5, 1987.

[42] H. Wang, *H. Wang, Acta Metall. Sin. (Engl. Lett.)*, vol. 26, no. 5, pp. 618-622, October 2013.

[43] S. Patri, R. Gurusamy, P. A. Molian, M. Govindaraju, "Magnetic domain refinement of silicon-steel laminations by laser scribing," *Journal of Materials Science*, vol. 31, no. 7, pp. 1693-1702, Jan 1996.

[44] Seungjoon Ahn et al., "Investigation of core loss characteristics of 3% SiFe using the laser scribing method," *physica status solidi b* , vol. 241, no. 7, pp. 1641-1644, 2004.

[45] B. Weidenfeller, W. Riehemann, "Domain refinement and domain wall activation of surface treated FeSi sheets," *Journal of Magnetism and Magnetic Materials*, vol. 160, pp. 136-138, 1996.

[46] William Fuller Brown Jr., "Domains, micromagnetics, and beyond: Reminiscences and assessments," *Journal of Applied Physics*, vol. 49, p. 1937, 1978.

[47] L. LANDAU, E. LIFSHITS, "ON THE THEORY OF THE DISPERSION OF MAGNETIC PERMEABILITY IN FERROMAGNETIC BODIES," *Phys. Zeitsch. der Sow.*, vol. 8, pp. 153-169, 1935.

[48] M. Bisran, *Journal of magnetism and magnetic materials*, vol. 164, pp. 300-304, 1996.

[49] A. Corciove, "On the calculation of magnetostatic energies associated to domain structures in ferromagnetic thin films," *Journal de Physique*, no. 2-3, pp. 408-409, Colloque C 1, Tome 32 1971.

[50]] S. Chikazumi, *Physics of Ferromagnetism*.: Oxford university Press, 1997, 655 pages.

[51] G. Akoun, J-P. Yonnet, *IEEE Transactions on Magnetics*, vol. MAG-20, no. 5, pp. 1962-1964, 1984.

[52] F. Bloch, *Z. Physik*, vol. 74, p. 295, 1932.

[53] L. Néel, *C. R. Acad. Sc.*, vol. 241, p. 533, 1955.

[54] J. Kaczer, *Le journal de Physique et le Radium*, p. 120, Tome 20 1959.

[55] Tobin, A., & Paul, D. (1969). Stability of ferromagnetic domain structures at grain boundaries. *Journal of Applied Physics, 40*, 3611.

[56] P.F. Davis, “A theory of the shape of spike-like magnetic domains”, *British Journal of Applied Physics,* vol. 2, ser. 2, 1969

[57] J.W. Shilling, JR. L. Houze, “Magnetic properties and domain structure in grain-oriented 3% Si-Fe”, *Transactions on Magnetics*, vol. MAG-10, no. 2, pp. 195, June 1974.

[58] Masaaki Inamura, “AC magnetostriction in Si-Fe single cristal close to (110)[001]”, IEEE Transactions on Magnetics”, vol. MAG-19, no. 1, january 1983.

[59] V.I. Pudov, Yu.N. Dragoshanskii, « Domain structure and magnetic losses in laminated magnetic circuits upon laser treatmen”, The physics of metals and metallurgy, vol. 116, no. 6, pp. 538-543, 2015.

[60] V.I. Pudov, Yu.N. Dragoshanskii, « Magnetic domain structure and thermal stabilization of laser treatment zones in soft magnetic materials”, Physics of of the solid state, vol. 58, no. 2, pp. 258-265, 2016.

[61] Marcelo J. Dapino, “A magneto-elastic modelfor Villari magnetostrictiver”.

[62] M-A. Raulet, B. Ducharne, J-P. Masson, and G. Bayada, “The magnetic field diffusion equation including dynamic hysteresis”, *IEEE Transactions on Magnetics*, 2004, vol. 42, n°2, pp. 872–875.

[63] O. Maloberti, V. Mazauric, G. Meunier, A. Kedous-Lebouc, O. Geoffroy, “An Energy-Based Formulation for Dynamic Hysteresis and Extra Losses”, *IEEE Transactions on Magnetics*, 2006, vol. 42, n°4, pp. 895-898.

[64] A. Hubert, R. Schafer, *Magnetic Domains*, Springer Verlag, 2000.

[65] D.H. Martin, “Surface Structures and Ferromagnetic Domain sizes”, *Proc. Phys. Soc.*, 1956, vol. 70, pp. 77-84.

[66] Y. A. S. Shur, YU. N. Dragoshanskiy, ”The shape of closure domains inside silicon iron crystals”, *Fiz. Metal. Metalloved*, 1966, vol. 22, n°5, pp. 702-710.

[67] L. Néel, “Les lois de l’aimantation et de la subdivision en domaines élémentaires d’un monocrystal de Fer”, *Journal de Physique et le Radium*, 1944, Tome 5, série 8(11), pp. 241-251.

[68] C. Kittel, “Physical Theory of Ferromagnetic Domains”, *Reviews of Modern Physics*, 1949, vol. 21, n°4, pp. 541-583.

[69] G. Bertotti, *Hysteresis in Magnetism*, Academic Press, 1998, pp. 391-430, pp. 129-162.

[70] G. Lochak, *La Géométrisation de la Physique*, Flammarion, 1994.

[71] O. Maloberti, A. Kedous-Lebouc, O. Geoffroy, G. Meunier, and V. Mazauric, "Field Diffusion-Like Representation and Experimental Identification of a Dynamic Magnetization Property", *Journal of Magnetism and Magnetic Materials*, 2006, vol. 304, pp. e507-e509.

[72] O. Maloberti, *Contribution à la Modélisation des Effets Dynamiques dans les Matériaux Magnétiques Doux : Caractérisation et Simulation*, PhD ed. EEATS/INPG Grenoble, Septembre 2006.

[73] H.A.M. Van Den Berg, A.H.J.V.D. Brandt, "Self-Consistent Domain Theory in Soft Ferromagnetic Media II: Basic domains structures in thin film objects", *Journal of Applied Physics*, 1986, vol. 60, n°3, pp. 1105-1113.

[74] H.A.M. Van Den Berg, A.H.J.V.D. Brandt, "Self-Consistent Domain Theory in Soft Ferromagnetic Media III: Composite domains structures in thin film objects", *Journal of Applied Physics*, 1987, vol. 62, n°5, pp. 1952-1959.

[75] A. De Simone, "Energy Minimizers for Large Ferromagnetic Bodies", *Arch. Rat. Mech. Anal.*, 1993, vol. 125, pp. 99-143.

[76] J. Hladik, P.E. Hladik, *Le Calcul Tensoriel en Physique*, Dunod 3rd ed., Paris, 1999.

[77] E.A. Wood, *Crystals and Light*, Dover Pub. Inc., New York, 1977.

[78] M.I. Darby, E.D. Isaac, "Magnetocrystalline Anisotropy of Ferro- and Ferrimagnetics", *IEEE Transactions on Magnetics*, June 1974, vol. MAG-10, n°2, pp. 259-299.

[79] T.L. Gilbert, "A Phenomenological Theory of Damping in Ferromagnetic Materials", *IEEE Transactions on Magnetics*, November 2004, vol. 40, n°6, pp. 3443-3449.

[80] J.B. Passioura, "Simulation Models: Science, Snake-Oils, Education or Engineering", *Agronomy Journal*, 1996, vol. 88, pp. 690-694.

[81] O. Maloberti, A. Kedous-Lebouc, G. Meunier, V. Mazauric, "How to Formulate Soft Materials Heterogeneity? 2. Hysteresis, Dynamic Motions and Diffusion", *submitted to J.M.M.M.*, conference SMM'18 in Cardiff 2007

[82] O. Maloberti, G. Meunier, A. Kedous-Lebouc, V. Mazauric, “How to Formulate Soft Materials Heterogeneity? *1. Quasi-Static Equilibrium and Structuring*”, *submitted to J.M.M.M.*, conference SMM’18 in Cardiff 2007.

[83] J. Hladik, P.E. Hladik, *Le Calcul Tensoriel en Physique*, Dunod 3rd ed., Paris, 1999.

[84] G. Bertotti, *Hysteresis in Magnetism*, Academic Press, 1998, chapter 5, pp. 129-162.

[85] D.C. Jiles, D.L. Atherton, “Theory of Ferromagnetic hysteresis”, *Journal of magnetism and Magnetic Materials*, 1986, vol. 61, pp. 48-60.

[86] O. Maloberti, *Contribution à la Modélisation des Effets Dynamiques dans les Matériaux Magnétiques Doux : Caractérisation et Simulation*, PhD ed. EEATS/INPG Grenoble, Septembre 2006.

[87] H. Williams, W. Shockley, C. Kittel, “Studies of the propagation velocity of a ferromagnetic domain boundary”, Physical Review, 1950, vol. 80, n°6, pp. 1090-1094.

Appendix A. *Mathematical Tools*

Operators

$[Y] = [\vec{Y}_1, \vec{Y}_2, \vec{Y}_3] = \begin{bmatrix} Y_{11} & Y_{12} & Y_{13} \\ Y_{21} & Y_{22} & Y_{23} \\ Y_{31} & Y_{32} & Y_{33} \end{bmatrix}$, $[n] = [\vec{n}, \vec{n}, \vec{n}]$: $[Y]^{\top}$ means to transpose the matrix [Y]

$[\vec{\nabla}](\vec{A}) = [\vec{\nabla} \otimes \vec{A}], \left[[\vec{\nabla}](\vec{A})\right]_{ij} = [\vec{\nabla} \otimes \vec{A}]_{ij}$: tensor gradient on a vector,

$\vec{\nabla} \cdot [Y] = \left(\vec{\nabla} \cdot \vec{Y}_1\ , \vec{\nabla} \cdot \vec{Y}_2, \vec{\nabla} \cdot \vec{Y}_3\right)^T$: vector divergence on a tensor,

$[\vec{\nabla}] \times [Y] = [\vec{\nabla} \times][Y] = \left[\vec{\nabla} \times \vec{Y}_1, \vec{\nabla} \times \vec{Y}_2, \vec{\nabla} \times \vec{Y}_3\right]^T$: tensor rotational on a tensor,

$[\Delta][Y] = \left[\vec{\Delta}(\vec{Y}_1), \vec{\Delta}(\vec{Y}_2), \vec{\Delta}(\vec{Y}_3)\right]^T$: tensor laplacian on a tensor,

$\vec{\nabla} \cdot = (\partial_1 \cdot, \partial_2 \cdot, \partial_3 \cdot)^T$: Nabla operator,

$\vec{\Delta} \cdot = (\partial_1\partial_1 \cdot, \partial_2\partial_2 \cdot, \partial_3\partial_3 \cdot)^T$: Laplacian operator.

Operations

$\left[\vec{A} \otimes \vec{B}\right], \left[\vec{A} \otimes \vec{B}\right]_{ij} = A_i B_j$: tensor product between two vectors.

$\left[[Y] \div [Z]\right], \left[[Y] \div [Z]\right]_{ij} = Y_{ij} Z_{ij}$: tensor product type 1 between 2 tensors.

$\left[[Y] \times [Z]\right] = \left[\vec{Y}_1 \times \vec{Z}_1, \vec{Y}_2 \times \vec{Z}_2, \vec{Y}_3 \times \vec{Z}_3\right]^T$: tensor product type 2 between 2 tensors.

$([Y] \vec{\bullet} [Z]) = \left(\vec{Y}_1 \cdot \vec{Z}_1, \vec{Y}_2 \cdot \vec{Z}_2, \vec{Y}_3 \cdot \vec{Z}_3\right)^T$, $\left([Y]^{\vec{\bullet}2}\right) = ([Y] \vec{\bullet} [Y])$: vector product between 2 tensors.

$[Y] \circ [Z] = Y_{ij} Z_{ij}$: scalar product between two tensors.

Derivative and integral properties

$$[\vec{\nabla}\times][\vec{\nabla}\times][Y] = [\vec{\nabla}](\vec{\nabla}\cdot[Y]) - [\Delta][Y]$$

$$[X]\vec{\bullet}([Y]\times[Z]) = [Z]\vec{\bullet}([X]\times[Y]) = [Y]\vec{\bullet}([Z]\times[X])$$

$$\vec{\nabla}\cdot\left([Y]\vec{A}\right) = \left(\vec{\nabla}\cdot[Y]\right)\cdot\vec{A} + [Y]\circ\left[\vec{\nabla}\otimes\vec{A}\right]$$

$$\iiint_{\Omega}\left(\vec{\nabla}\cdot\vec{A}\right)d^3x = \oiint_{\partial\Omega}\left(\vec{A}\cdot\vec{n}\right)d^2x$$

$$\iiint_{\Omega}\left(\vec{\nabla}\times\vec{A}\right)d^3x = \oiint_{\partial\Omega} -\left(\vec{A}\times\vec{n}\right)d^2x$$

$$\iiint_{\Omega}\left(\vec{\nabla}\cdot[Y]\right)d^3x = \oiint_{\partial\Omega}\left([Y]\vec{\bullet}[n]\right)d^2x$$

$$\iiint_{\Omega}\left([\vec{\nabla}]\times[Y]\right)d^3x = \oiint_{\partial\Omega} -([Y]\times[n])d^2x$$

$$\iint_{\Sigma}\left([\vec{\nabla}]\times[Y]\right)d^2x = \oint_{\partial\Sigma}\left([Y]\vec{\bullet}[n]\right)dx$$